

AD-A156 674

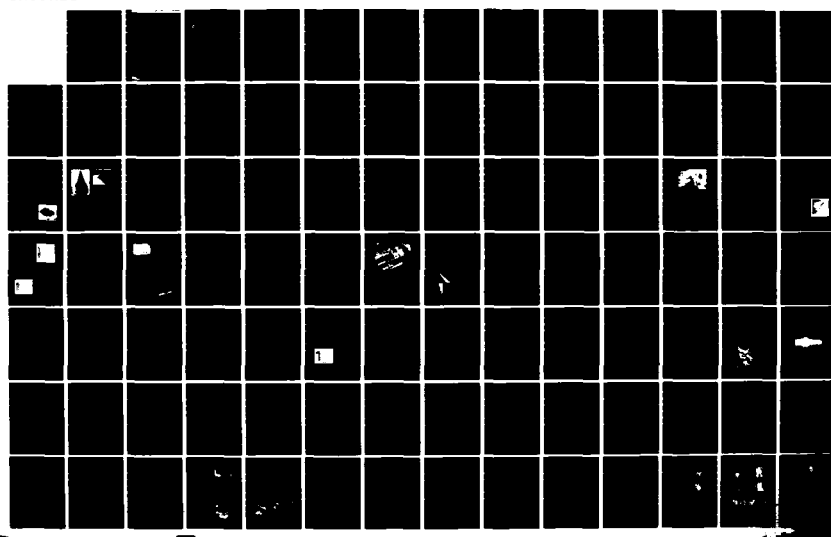
DEVELOPMENTS IN SCIENCE AND TECHNOLOGY(U) JOHNS HOPKINS 1/2
UNIV LAUREL MD APPLIED PHYSICS LAB 1983 JHU/APL/DST-11

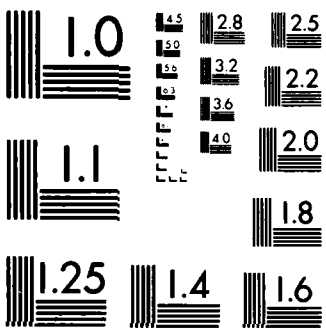
N00024-83-C-5301

UNCLASSIFIED

F/G 5/2

NL





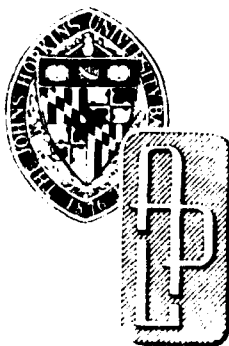
MICROCOPY RESOLUTION TEST CHART
NATIONAL BUREAU OF STANDARDS 1963 A

2627

JHU APL DST 11
FISCAL YEAR 1983

01

AD-A156 674



APPLIED PHYSICS LABORATORY

DEVELOPMENTS IN SCIENCE AND TECHNOLOGY

4 DTIC

JUL 16 1985

A

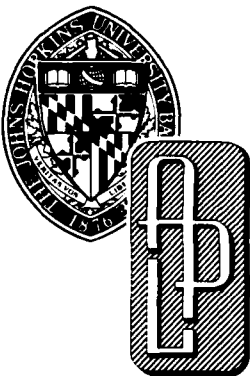
Approved for public release; distribution unlimited

DTIC FILE COPY

THE JOHNS HOPKINS UNIVERSITY • APPLIED PHYSICS LABORATORY
Johns Hopkins Road, Laurel, Maryland 20723
Operating under Contract N00024-83-C-5301 with the Department of the Navy

85 5 23 113

JHU/APL DST-11
FISCAL YEAR 1983



APPLIED PHYSICS LABORATORY

DEVELOPMENTS IN SCIENCE AND TECHNOLOGY

Approved for public release; distribution unlimited.

H-1

THE JOHNS HOPKINS UNIVERSITY • APPLIED PHYSICS LABORATORY
Johns Hopkins Road, Laurel, Maryland 20707
Operating under Contract N00024-83-C-5301 with the Department of the Navy



Technical Coordinators

*Chairman, R. C. Morton
C. B. Bargeron
J. R. Champion
H. K. Charles, Jr.
M. Gussow
E. T. Marley
R. H. Peery
J. W. Walker
W. P. Willis, Jr.*

Managing Editor

M. B. Gilbert

Associate Editor

A. L. Machurek

Staff Artist

D. L. George

UNCLASSIFIED

FOREWORD

The Applied Physics Laboratory (APL), a division of The Johns Hopkins University, is located in Howard County, Maryland, midway between Baltimore and Washington. Its work is carried out under contractual agreements between the University and the federal, state, and local governments. APL employs a staff of more than 2700 including 1430 professional scientists and engineers, of whom more than half have advanced degrees. Their ideas are implemented and extended through several field activities and a network of associate contractors and collaborators from coast to coast.

The primary mission of APL is to enhance national security by applying advanced science and technology to the solution of problems important to national objectives. The Laboratory conducts programs in fundamental and applied research, exploratory and advanced development, component engineering, systems engineering and integration, and test and evaluation of operational systems. Approximately 85% of the Laboratory's effort is for the Department of Defense (76% for the Navy and 9% for other DoD agencies). The remaining 15% is devoted to nondefense areas, including space research.

The current programs at APL cover a wide range of activities. Many are broad in scope, long term, or highly classified, and therefore not reportable herein. The articles for this document are solicited annually from the whole Laboratory. The writers are individuals or small groups who have been personally involved in particular efforts and are motivated to report to a wider audience than they usually communicate with. For these reasons, this publication does not necessarily represent all the accomplishments of APL during fiscal year 1983 (1 October 1982 through 30 September 1983).

APL was organized in 1942 under the auspices of the Office of Scientific Research and Development to develop a proximity (VT) fuze for antiaircraft defense; that was the principal effort during World War II. The era of emerging guided-missile technology extended from about 1944 to 1956. During that time, APL concentrated on providing better air defense for the Fleet by developing a family of shipborne surface-to-air missiles. The Navy-sponsored "Bumblebee" program pioneered many basic guided-missile technologies later used in other air, surface, and submarine missile programs.

The era of weapons systems engineering began in 1956 with the commissioning of the first guided-missile cruiser. The experience gained during that period has found application in many systems of interest to the Navy in various warfare areas and to other branches of the government. Significant activities are proceeding in areas of special APL competence, including advanced radar techniques, missile propulsion, missile guidance, countermeasures, and combat systems integration.

Of the newer weapon system programs, the Aegis Shipbuilding Project is of major importance. USS *Iwo Jima* (CG-47), now in the Fleet, is the first ship in a new class of multimission guided missile cruisers that will carry the Aegis surface-to-air weapon system. The Laboratory is Technical Advisor to the Navy in the design and development of the Aegis system. APL now has the broader challenge of integrating the system into the operations of the battle group. This effort, for which APL is Technical Direction Agent, includes the design and development of the Battle Group Antiair Warfare Coordination System exploiting the operation of Aegis cruisers with other ships and aircraft of the battle group. Other areas of tactical systems support involve aviation countermeasures as well as the improved effectiveness of the Harpoon cruise missile. The Laboratory has recently been made Technical Direction Agent of the Tomahawk cruise missile program. APL has a major role in the conceptualization of future command, control, and communications (C³) systems to facilitate the operation of Naval forces. Both strategic and tactical aspects of the C³ process are being examined. An important increasing effort at APL involves assessing the integrated performance of all the above systems.

The Laboratory continues to provide technical evaluation of the operational Fleet Ballistic Missile (FBM) System. Quantitative test and evaluation procedures are applied to every newly commissioned ballistic missile submarine. Similarly, APL currently provides precise evaluation of the Army's Pershing missile programs. Significant programs are also under way for Naval strategic communications and tactical targeting. Since 1970, APL has had the responsibility for planning and conducting a significant technical program to ensure the security of the FBM submarine fleet against possible technological or tactical countermeasures. The approach is to quantify all physical and tactical means that might be developed to detect, identify, and track our submarines and to propose and evaluate suitable countermeasures and tactics.

APL has a significant space program. It started with the Navy Navigation Satellite System, originally known as Transit, one of the Laboratory's most important accomplishments since the wartime proximity fuze and the surface-to-air missile program. APL invented the concept, designed and built the initial satellite constellation, and set up and operated a worldwide satellite tracking network. The APL Space Program has greatly expanded and is now applied to the design and construction of a broad range of scientific satellites and spaceborne scientific experiments for NASA and the DoD.

With the encouragement of the DoD, APL is applying its talent and the experience developed in DoD programs to a number of government-sponsored civil programs. Some examples of the areas to which attention has been devoted in recent years are biomedical research and engineering; power plant location; in-

tegration of national ocean service surveys; navigation aids; reduction of pollution of the biosphere; ocean thermal, geothermal, and flywheel energy systems; and advanced education.

Through the extensive and intensive use of integrated circuits and microprocessor logic in satellites, in radar and other naval systems, and in biomedical engineering and other civil areas, APL has become a recognized leader in the area of computer technology. Furthermore, it continues to pioneer in innovative applications of computers of all sizes to problems of national importance. This trend is underscored throughout the document by the frequent references to computing as an integral part of most of the accomplishments reported herein.

To support its R&D activities through knowledge and experience in advanced research, the Laboratory performs fundamental research in biological, chemical, mathematical, and physical sciences related to its various missions. Through unique applications of system engineering, science, and technology to the needs of society, APL has enhanced the University's tradition of excellence while gaining worldwide recognition of its own.

.....

Dr. Robert C. Morton, Chairman of the Coordinating Committee for the past two issues of the APL Selected Accomplishments, died on February 9, 1984. What he has left behind is much more enduring than the many memories that his friends and co-workers will always carry with them. Something of his spirit lives on in all who knew him. But perhaps his most significant legacy is the extraordinarily capable and successful team of people – numbering in the hundreds – who today carry on the tradition of professional excellence and service for which he stood.

CONTENTS

WEAPON SYSTEMS DEVELOPMENT

Introduction	12
Battle Group Antiair Warfare Coordination <i>C. C. Phillips and R. T. Lundy</i>	14
The Tactical Electronic Warfare Support Center <i>G. S. Gealy</i>	16
Semicoherent Processing - A Unique Method of Processing Radar Doppler Data <i>R. E. Thurber</i>	19
Simulation of the Vertical Launch of Tomahawk from the SSN 688 Class Submarine <i>J. S. O'Connor</i>	22
Design and Development of a Modular Six-Degree-of-Freedom Digital Simulation for the Tomahawk Cruise Missile Program <i>G. B. Stupp and F. W. Riedel</i>	24
Rain Damage Effects on Hypersonic Missile Radomes <i>R. K. Frazer</i>	27
Development of Computational Codes for the Analysis of Supersonic Flowfields <i>M. E. White, M. D. Griffin, and D. M. Van Wie</i>	30

SPACE SCIENCE AND TECHNOLOGY

Introduction	34
The HILAT Satellite <i>K. A. Potocki, S. D. Baran, and L. H. Schwerdtfeger</i>	38
Ultraviolet Imager of Atmospheric Emissions and Daylight Global Auroral Imagery from Space <i>C.-I. Meng and F. W. Schenkel</i>	41
Digital Signal Processor for the Geosat-A Radar Altimeter <i>J. A. Perschy and S. F. Oden</i>	44
RF Section of the Geosat-A Radar Altimeter <i>E. G. Weiermiller and J. Daniels</i>	47
Upgrade of the APL 60-ft Dish Antenna Control System <i>R. L. Konigsberg, V. F. Neradka, and T. M. Rankin</i>	50
Alternate Fine Guidance Sensor for the Space Telescope <i>M. D. Griffin, T. E. Strikwerda, and D. G. Grant</i>	53
NASA Ground Terminal Fault Isolation and Monitoring System <i>D. E. Buchholz, A. J. Cote, Jr., and P. J. Grunberger</i>	58

Reentry Thermal-Response Predictions for the General-Purpose Heat Source <i>P. T. Brenza and D. W. Conn</i>	63
---	----

COMPUTER TECHNOLOGY

Introduction	68
Implementation of a SAR Processor on a VAX 11780/FPS-164 System <i>B. E. Raff, R. N. McDonough, and J. L. Kerr</i>	70
Side-Look Sonar Image Exploitation <i>D. C. Doty and C. A. Twigg</i>	74
Development of Powerful Space-Qualified Computers <i>B. W. Ballard, R. M. Henshaw, and T. Zaremba</i>	77
Text Processing Prompters for the IBM 4341 VM/CMS System <i>S. M. Schaaf</i>	80
The Computervision CADDS 4 Finite Element Modeling Package <i>D. F. Persons</i>	82

OCEAN SCIENCE AND TECHNOLOGY

Introduction	89
A New Technique for the Encapsulation of Thermistors <i>C. W. Anderson and G. J. Farruggia</i>	90
Model for the Assessment of Antisubmarine Acoustic Surveillance Systems <i>J. I. Bowen and R. E. L. Johnson, Jr.</i>	93

BIOMEDICAL SCIENCE AND ENGINEERING

Introduction	99
Retinal Vascular Development in Kitten and Puppy Eyes <i>R. W. Flower (APL) and D. S. McLeod, G. A. Lutty, B. Goldberg, and S. D. Wajer (JHMI)</i>	100
SEM Study of the Hyaloid Vascular System in Newborn Mice Exposed to Oxygen <i>P. M. Bischoff and S. D. Wajer (JHMI) and R. W. Flower (APL)</i>	104
Stromal Damage in Rabbit Corneas Exposed to CO ₂ Laser Radiation <i>R. L. McCally, C. B. Bergeron, W. R. Green (JHMI), and R. A. Farrell</i>	107
Motion Noise Reduction in Neuromagnetic Measurement Systems <i>H. W. Ko, J. S. Hansen, and D. A. Bowser</i>	109

Sutureless Vascular Anastomosis System <i>J. J. Wozniak</i>	112
A System to Inhibit Self-Injurious Behavior <i>A. L. Newman</i>	115

ENERGY, ENGINEERING, AND CIVILIAN TECHNOLOGY

Introduction	121
Geothermal Energy Assessment at East Coast Naval Facilities <i>R. W. Newman</i>	122
Tape-X Data Recording System <i>R. A. Quinnell, R. L. Nelson, and C. A. Twigg</i>	125
A Network Management Simulation of AGRT Systems Under Vehicle-Follower Control <i>H. Y. Chiu, D. L. Kershner, and P. J. McEvaddy</i>	127
Epoxy Characterization and Qualification Studies <i>H. K. Charles, Jr., E. S. Dettmer, J. A. Weiner, and R. C. Benson</i>	129
Ball-Bond Shear Testing <i>H. K. Charles, Jr., C. V. Clatterbaugh, J. A. Weiner, and G. D. Wagner</i>	135
Custom Large-Scale Integrated Circuit <i>R. C. Moore and R. E. Jenkins</i>	139

FUNDAMENTAL RESEARCH

Introduction	145
Photoelectrolysis of Water by Modified Transition Metal Oxides <i>T. E. Phillips, J. C. Murphy, K. Moorjani, and T. O. Poehler</i>	146
Nondestructive Testing and Evaluation of Metals and Ceramics Using Photothermal Imaging <i>L. C. Aamodt and J. C. Murphy</i>	150
Oldroyd Fluids Oscillating in Rectangular Ducts <i>V. O'Brien and L. W. Ehrlich</i>	153
Boundary Conditions and Reversibility in Diffusion Controlled Reactions <i>L. Monchick</i>	157

PATENTS	160
----------------	-----

PUBLICATIONS AND PRESENTATIONS	164
---------------------------------------	-----

AUTHOR INDEX	174
---------------------	-----

WEAPON SYSTEMS DEVELOPMENT

INTRODUCTION

In response to the Kamikaze threat of World War II, the U.S. Navy's Bureau of Ordnance requested APL to conduct research and development in all phases of guided missilery and to analyze the effectiveness of new systems in an appropriate environment. The Laboratory did so with the assistance of a group of associated contractors having expertise in various areas of science and technology. That team developed the new technology and resources required to put the Terrier, Talos, and Tartar surface-to-air missiles into operational service and advised the Navy on doctrinal matters. The Terrier was introduced in USS *Boston* in 1955; that event was followed by the introduction of Talos on USS *Galveston* in 1958. Subsequently, Tartar went to sea on USS *Adams* in 1960.

In succeeding years, APL supported the Navy with an aggressive program to give the Fleet an effective defense against an ever-increasing threat. That program has produced Standard Missile in addition to Terrier, Talos, and Tartar. In time, APL's scope of activities broadened to include fire control, acquisition, and surveillance radar systems. Working first with analog and then with digital electronic computational techniques, the Navy produced tactical data and weapon systems that relieve weapons personnel of much of the routine associated with a fighting ship and also greatly reduce reaction time. APL has made and continues to make important contributions in this evolution. In addition, the Laboratory has brought to the Navy weapon community an understanding of the potential capabilities of the emerging world of electronic computation and automation.

In its effort to help develop the basic structure of shipboard combat systems, APL has defined the functions of sensor, command, support, and weapon elements for those very complex systems. Such consistency in basic structure has favored technical interchange among major developments in which APL has played a role, e.g., the Aegis Combat System, Terrier and Tartar New Threat Upgrades, and, most recently, the new multimission DDG-51 Combat System.

In keeping with these trends, APL's current emphasis in antiair warfare is to enhance the effectiveness of a battle group by integrating, at the battle group level, the information available to individual ships and by coordinating the responses of the individual ships. The Aegis ship plays a key role in achieving this objective and is particularly valuable as the number of attackers increases and the countermeasures environment worsens.

In addition to the enhancement of battle group ~~AAW~~ resources, APL is conducting naval warfare analysis to improve the coordination of ships, aircraft, submarines, and sensors including satellites—an activity called composite warfare analysis. Composite warfare is the combat use of maritime forces in the principal areas of antiair, antisurface, antisubmarine, and electronic warfare against enemy systems. Intrinsic to composite warfare are the attributes of force coordination among the warfare areas. Coordination includes factors of time and force

position relationships, communications, combat system interfaces and interactions, tactics, doctrine, and training. By means of coordination, an attempt is made to achieve battle synergism among the warfare areas.

As a result of the surface missile experience, the Laboratory was able to assist the Naval Air Systems Command with its upgrade of the Sparrow Missile to the AIM-7M model, the Army with its development of the Improved Hawk and Patriot systems, and the Air Force in its current development of AMRAAM.

In the area of strategic missile systems, the Laboratory has helped develop and conduct an independent evaluation program for the Navy's Fleet Ballistic Missile (FBM) Weapon System. The program requires continuing technical and operational testing throughout the operational lives of various models of the weapon system, i.e., Polaris, Poseidon, and Trident I. It also includes the future Trident II. For those systems, APL derives quantified estimates of performance under operational conditions, identifies sources of system inaccuracy and unreliability for corrective action or future improvement, and assesses weapon system readiness for operational deployment.

In the mid-1960's, in response to an Army request, the Laboratory expanded its strategic evaluation effort to include the Pershing Weapon System and its strategic role in Europe. The program uses the evaluation techniques developed for the Navy's FBM Weapon System. It continues today and relies on data collected and analyzed from test exercises at "alert" sites in Europe as well as from Operational Tests conducted in the United States.

In addition to its testing and evaluation of antiair-warfare and ballistic missile systems, APL has participated in the conception, development, and testing of cruise missile projects. Much of the early work was associated with Harpoon, an antiship missile developed by the Navy in response to the 1967 sinking of an Israeli destroyer by antiship missiles. The APL effort for the Tomahawk missile has recently been expanded to cover a broad range of technical topics and to include an active role in program management. APL continues to support both the Harpoon and Tomahawk programs.

In recent years, the Laboratory's contributions to command, control, and communications (C³) have been increasing. From an initial task to assess the effectiveness of communications with strategic missile submarines, the effort has grown to include participation in a broad assessment of Navy C³ capabilities and technical planning for future systems.

Although the selection has been limited by security requirements, the following summaries of current tasks illustrate the diversity of APL tasking in weapon systems development. The tasks range from technical development and operations analysis at the battle group level to the development of theory and the conduct of tests applicable to small subsystems.

BATTLE GROUP ANTI AIR WARFARE COORDINATION

C. C. Phillips and R. T. Lundy

The Battle Group Anti Air Warfare Coordination Program has evolved as a battle group systems engineering program at APL under the direction of the Aegis Shipbuilding Project Manager, PMS-400. Its objective has been to improve the effectiveness of anti air warfare by building on the capabilities of Aegis and other fleet combat systems to provide improved weapons coordination. Many studies conducted throughout the 1970's had identified major benefits to battle groups that could act as a single, closely integrated force. With such a force, it is possible to acquire data from a wide variety of force sensors and to integrate the data to form a unified coherent air picture from which coordinated responses to battle group threats could be developed.

DISCUSSION

The Battle Group Anti Air Warfare Coordination (BGAWC) Program is a very broad application of the combat system disciplines that have been built up in Terrier, Tartar, Standard Missile, and Aegis. The significant distinction is that BGAWC engineering is at the battle group level. The BGAWC system is distributed over a wide variety of surface and air combatants with considerably different capabilities in terms of mobility, weapons, reaction times, and automation. The system configuration consequently is required to accommodate a large, indefinite number of variants because any change in the battle group represents a configuration change in the battle group's system for conducting warfare.

The BGAWC plan envisions the use of a central command system aboard an Aegis cruiser to support the needs of the AAW Commander. The system provides the computers, displays, and decision aids for an orderly conduct of coordinated AAW. The plan further provides the basis in other ships and aircraft for detecting, tracking, and transferring accurate fire control data across standard Navy links to support coordinated engagements.

The upgrading requires modifications to anti air warfare combatants in order to facilitate coordinated data exchange and weapons use. The principal functional requirements to be met in a Fleet modification upgrade effort are listed in Table 1. Specific coordination capabilities to be achieved include the following:

1. The ability to convey a complete and reliable air picture within the battle group. Radar

Table 1 — Functional requirements for a BGAWC system.

Control Unit
Aegis Combat System
Build battle group track data base
Share Aegis tracks with battle group
Antiair Warfare Command support
Display antiair warfare situation
Assimilate extra-force data
Promulgate antiair warfare doctrine and operations
Control antiair warfare engagements
Participating Units
Gridlock to Aegis
Respond to force doctrine
Accept engagement orders
Report engagement status
Data Links
Connect all units in all environments
Transmit tracks, status, doctrine, and commands

data from Aegis ships will be usable on other combatants for all the normal internal decision-making processes.

2. The ability of the AAW Commander to designate targets to other ships and aircraft in the battle group.
3. The ability to designate a target directly to the fire control and launching systems of a remote ship or aircraft.
4. The ability to designate a missile launch from a remote ship using guidance and/or illumination supplied by another ship or aircraft.

Early engineering efforts within the BGAWC Program identified a number of deficiencies in current systems that had to be resolved. Those efforts resulted in the identification of near-term (Phase I) and long-term (Phase III) objectives and resulted in a phased development plan (Fig. 1) that provides the basis for improved weapons coordination in the near term by means of new displays for the AAWC in the Aegis cruisers and by the resolution of long-standing information exchange problems such as gridlock.* automatic

*Gridlock is the process of accurately registering remote data into a ship's own coordinate system. It removes or minimizes navigation radar alignment errors and translates data differences between coordinate reference systems.

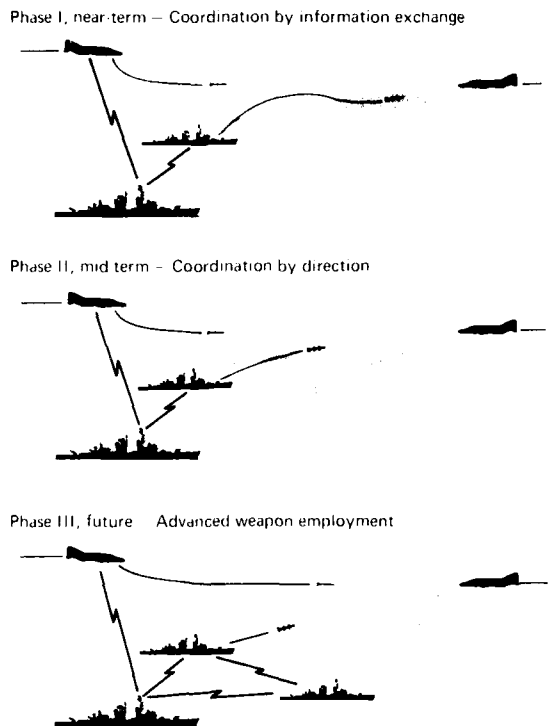


Figure 1 — The three-phase development plan for the BGAAWC Program provides for systematic growth in capabilities. The near-term goal is the improvement of command capabilities by aiding information exchange. Longer-range goals are improved data links and more sophisticated coordination techniques for future weaponry.

local-to-remote track correlation, and improvements in automatic detection and tracking systems. (Two of these efforts are reported in companion articles.) All of these problems will be resolved by 1985 or 1986.

Phase II, scheduled for the late 1980's, will deal more specifically with the AAW weapons coordination command problem. It will provide additional display and decision aids within Aegis cruisers and better information flow among combatant units. Many routine decisions by the AAW Commander will be automated under the concepts of doctrine management algorithms within the computer complex that drive the AAWC display system (in the Aegis cruiser). The integration of new tactical data links (JTIDS and OTCIXS[†]) will provide the improved command capabilities.

[†]JTIDS, in its current definition, is a data link that provides substantial improvements in performance and data capacity over existing links. It is intended to augment the current Naval Tactical Data System links. OTCIXS is the satellite communication link that serves the needs of the Officer in Tactical Command.

Phase III deals with specifics of advanced weapon employment and will resolve the details of the engagement problem for (a) very-long-range intercepts using the techniques of "forward pass" of surface-launched weapons to targeting aircraft, (b) the remote launch of weapons from launchers other than the Aegis ship, and (c) control of the SM-2(N) weapon in conjunction with other surface and aircraft-launched weapons.

SUMMARY

The BGAAWC Program grew out of the effort to apply the automated weapon concepts in Aegis to the coordination of anti-air warfare in battle groups. The advanced capabilities of Aegis combat and command control systems make it readily applicable to this endeavor. Coordinating anti-air warfare involves numerous challenges, including

1. Enhancing the ability of all ships and aircraft in a BGAAWC system to gridlock, correlate, and accept tactical direction;
2. Improving communications to maintain essential connectivity despite countermeasures;
3. Supporting the AAW Commander by means of command displays and decision aids;
4. Defining procedures and tactics to carry out the assigned mission of the battle group successfully.

The AAWC problem transcends the scope of Aegis alone. Consideration must be given to the interactions of other new AAW capabilities, such as the AN/SPS-48E radar, which is part of the Terrier New Threat Upgrade Program. Consequently, the BGAAWC program is developing into a broad-based Fleet modernization program that provides the requisite command support, intercommunications, and interoperability of ships and aircraft for the most effective employment of the Fleet's modern radars and weapons.

THE TACTICAL ELECTRONIC WARFARE SUPPORT CENTER

G. S. Gealy

The Tactical Electronic Warfare Support Center, a computer-based capability, has been developed by APL to produce tactical documents for the Air Warfare Program at the Laboratory. Data bases for tactical aircraft of the Navy (EA-6B, E-2C, F-14) and Air Force (EF-111A) are implemented and maintained with primary emphasis on electronic warfare as it relates to those systems. In addition to that use, the facility is used to integrate threat intelligence and tactical electronic warfare data for the production of EA-6B and EF-111A electronic warfare tactics guides. Specialized software has been developed to perform (a) the integration of mission threat data and electronic warfare tactics, (b) data base management, and (c) the user-defined formatting of tactics guide outputs. The software is currently being expanded to provide the data manipulation and processing required to make the threat data base interface compatible with the Navy's Tactical EA-6B Mission Support System.

BACKGROUND

The Laboratory has been involved in the development of electronic warfare (EW) tactics for 18 years - originally through Project F/O 210 and, more recently, through a number of different projects in the Air Warfare Program. Those projects contribute to the development, test, and evaluation of operational tactics for Navy tactical aircraft and airborne EW equipment, including the EA-6B, E-2C, and F-14 systems. Since 1981, the program has also included similar efforts for the Air Force's EF-111A Tactical Jamming System.

A Tactical Electronic Warfare Support Center (TEWSC) was developed to provide a capability dedicated to specific projects of the Air Warfare Program. It was recognized that a computer-based system was needed for data base maintenance, storage, and retrieval because of the dynamics and growth of the threat in recent years. The expanding data bases must be maintained with the highest standards of quality control while minimizing manpower costs. The Support Center facility has been certified by the Defense Investigative Service for the processing of classified material that has restricted access.

DISCUSSION

The TEWSC Facility

The TEWSC is built around a Wang 2200 computer system. It is dedicated to supporting EW-related projects of APL's Air Warfare Program. Figure 1 is a schematic of the facility. Table 1 lists various input/output software functions and the associated hardware. The Wang operating system uses the BASIC computer language, which is easy for both professional and non-professional programmers to use and has sufficient flexibility and speed to support advanced software requirements.

The original system had a 32K byte random-access-memory central processing unit (CPU), a display/keyboard, a line printer, a daisy wheel report printer, and a triple floppy disk drive. It has been upgraded to include a flatbed plotter/digitizer, an additional 32K byte random access memory for the CPU, high-speed hard-disk storage, and a nine-track tape unit.

Operational Support for EW Tactics

The principal users of the TEWSC are the EA-6B and EF-111A tactical employment projects, which require that related mission threat data and optimum EW tactics data be maintained in order to produce guides for the EA-6B and EF-111A Tactical Jamming Systems. Specialized software developed at the Laboratory for data base management is used to maintain and manipulate the threat and tactics data. The *EA-6B OPTEVFOR Tactics Guide* and the *EF-111A Employment Guide* provide the data directly to Navy and Air Force users. Also, a nine-track data tape is generated for use by Marine Corps EA-6B squadrons in mission planning.

The purpose of the tactics guides is to provide the mission planners with a single source of data on mission threats, optimized EW tactics, and tactical jamming system effectiveness. The documents are specifically designed to support and be compatible with the operational capabilities of the aircraft. The information in the guides is obtained by evaluating data received from a wide variety of sources. As new data become available, the APL analysts evaluate the significance of any changes, including their effect on EA-6B or EF-

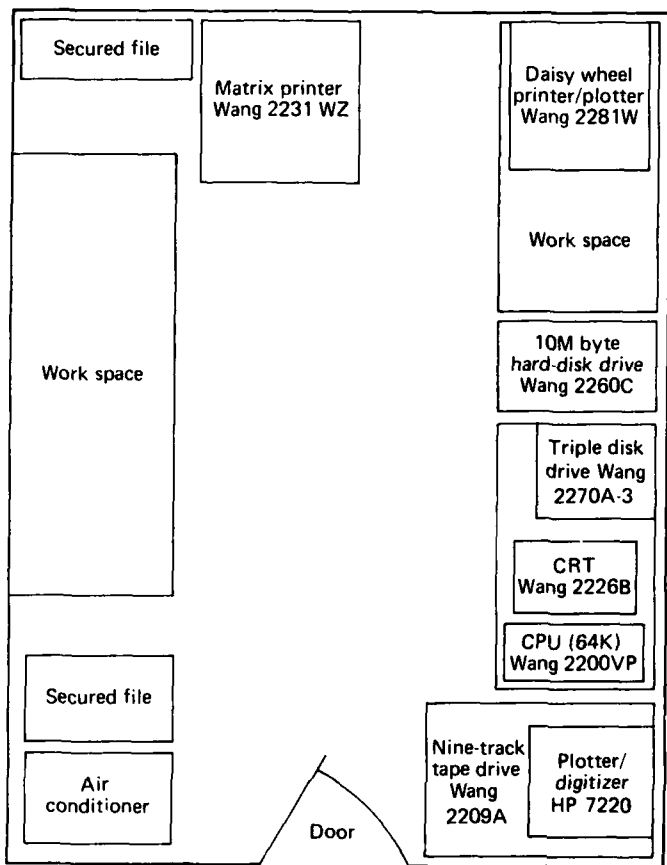


Figure 1 — The physical layout of the Tactical Electronic Warfare Support Center.

111A mission effectiveness and survivability. The Support Center enables the rapid generation of hard-copy or magnetic-tape updates and, if the new information warrants it, an immediate response in support of the EA-6B or EF-111A user.

In addition to those capabilities, software has been developed that allows the merged mission threat, tactics, and effectiveness data to be printed on an off-line laser printer, via nine-track magnetic tape. Because the laser printing capability provides an approximate hundredfold increase in speed over that of the TEWSC Wang daisy wheel printer, significant cost savings in manpower are realized.

A recent demand upon the Support Center is to provide data base support for the EA-6B ICAP II aircraft, which will be deployed soon. This version of the EA-6B provides significant increases in overall jamming system capabilities, with attendant greater sophistication of on-board system software. The compatible Wang software development effort, which is nearly

complete, will generate the required ICAP II data tape.

Electronic Countermeasures Analysis

Software has been developed to evaluate the relative effectiveness of random pulse jamming and noise jamming. It is used to calculate the ratio of peak signal to mean noise power that is required for detection by the radar receiver, as a function of jamming parameters. It can be used, for example, when evaluating U.S. systems to optimize a jamming response for two different types of radars that could be jammed with a single modulation because of their overlapping frequency ranges.

The TEWSC also has been used extensively to analyze the capabilities and limitations of the F-2C and F-14 aircraft in multiple-jamming-platform environments. The F-14 analysis uses a dynamic simulation, in-

Table 1 — Input/output functions of TEWSC hardware.

Hardware	Input Function	Output Function
CRT display and keyboard	TEWSC software* Mission threat data**‡ Jamming modulations and computer lists†‡ ECM analysis inputs* Modulation analysis inputs†‡	
Matrix printer		Software maintenance listings* Mission threat data maintenance listings†‡ Modulation analysis output ECM analysis output
Daisy wheel printer		EA-6B and EF-111A Tactics Guide repro†‡ EA-6B TACAIID repro†
Triple floppy disk drive	Mission threat data†‡ Externally generated software* CPU operating system*	Fleet compatible software***
Plotter-digitizer	Radar and jammer patterns*	ECM analysis graphics**§
Nine-track tape	EA-6B and EF-111A mission threat data†‡	Marines EA-6B data tape† EA-6B TEAMS threat libraries†§ Source tape for laser printer†‡
Hard-disk drive	EA-6B and EF-111A mission threat data exchange†‡	

*EA-6B, EF-111A, F-2C, F-14

**F-20

†EA-6B

‡EF-111A

cluding up to four F-14 aircraft, against up to 30 hostile jamming platforms.

FUTURE DEVELOPMENTS

The TEWSC facility's hardware and software will be upgraded continually as appropriate to meet the changing Air Warfare Program requirements. Extensive software development tasks eventually will provide better routines for processing the EA-6B and EF-111A mission threat data and will provide output in virtually any user-defined format. Also, it is anticipated that the Support Center will be expanded within the next few years to include a Tactical EA-6B Mission Support System (TEAMS). The Texas Instruments TI/990 computer, 100M byte hard-disk storage, magnetic tape interfaces, and multiple color graphics features for TEAMS will represent a significant improvement in TEWSC capabilities and will allow the Laboratory to continue its leadership in the development of EW tactics.

This work was supported by the USAF Tactical Air Command and the U.S. Navy Operational Test and Evaluation Force.

SEMICOHERENT PROCESSING – A UNIQUE METHOD OF PROCESSING RADAR DOPPLER DATA

R. E. Thurber

A method of processing radar data coherently by sampling and digitizing the radar IF at the information bandwidth has been demonstrated. This technique simplifies the hardware required for Doppler processing of radar data. An experimental system was constructed and evaluated in a live radar environment.

BACKGROUND

Doppler processing has been applied extensively in shipboard, land based, and airborne radars for two main purposes:

1. Improvement in signal-to-clutter ratios for detection and position estimation processes,
2. Estimation of target radial velocity.

For radars with fully coherent exciter and transmitter stages, digital Doppler processing is typically achieved through quadrature-phase detection, analog-to-digital (A-D) conversion, and vector processing. However, the implementation of Doppler processing in radars using a noncoherent transmitter (such as a magnetron) is more complex because the pulsed oscillator transmitter produces a random phase on each pulse. This fact has limited the application of Doppler techniques in several important classes of radars, including shipboard surface surveillance, coastal surveillance, and ship collision-avoidance systems. By means of the latest advances in high speed conversion and digital timing circuits, a simpler way to extract Doppler data from noncoherent systems has been devised, making Doppler processing for these systems more cost effective.

DISCUSSION

The Semicoherent Technique

Doppler processing of radar data is accomplished by filtering the data for several consecutive transmissions to enhance the range samples that exhibit a phase change caused by the Doppler effect of a moving target. The amplitude and phase of a given range cell must be measured precisely for several radar transmissions, which implies that the exact amplitude and phase of the transmitted energy pulse are known. This is not the case for radars that use a pulsed high power oscillator as a transmitter. The amplitude is well

controlled, but the phase of the transmitted signal is random from transmission to transmission.

In the past, Doppler processing for these types of radars used a device called a coherent oscillator (COHO), a stable oscillator at the radar IF that is phased locked to the transmitted signal every transmission (see Fig. 1). The COHO output is used to translate the IF return signal to in-phase and quadrature base band signals where they are amplified and converted to digital words for filtering by the moving target indicator (MTI) filter. The performance of the system is limited by the stability and balance of the COHO and the quadrature video processing and conversion circuits. In order to obtain adequate data to separate true moving targets from clutter, these circuits necessarily are complex and costly.

By using recent signal processing component technology, the need for a COHO and quadrature video processing circuits can be eliminated. (See the technique illustrated in the lower portion of Fig. 1.) Sample and hold circuits with extremely small aperture times (< 30 ps) and high speed (> 30 MHz) A-D converters make it possible to sample the return signals at the radar IF and convert them to digital words for filtering without going through the quadrature video processing step. The quadrature data for each range sample are developed by taking two samples of the IF time spaced by 90 electrical degrees of the IF. The samples are taken for every range resolution cell, i.e., at the system information bandwidth.

To establish coherence, the sample clocks must be phase locked precisely to the transmitted signal by means of very-high-speed emitter-coupled logic circuits to form a control loop to phase lock a stable oscillator to a sample of the transmitted pulse. Locking accuracies of better than 100 ps are achieved. The in-phase and quadrature digital samples thus derived are put directly into the MTI filter for Doppler processing. This technique has eliminated all coherent IF and quadrature video processing and has replaced it with one high-speed conversion device and a precision phase locked clock. Two-channel stability requirements for keeping the system balanced are completely eliminated.

Performance Considerations

The performance of any Doppler processing system is limited by the accuracy to which the amplitude

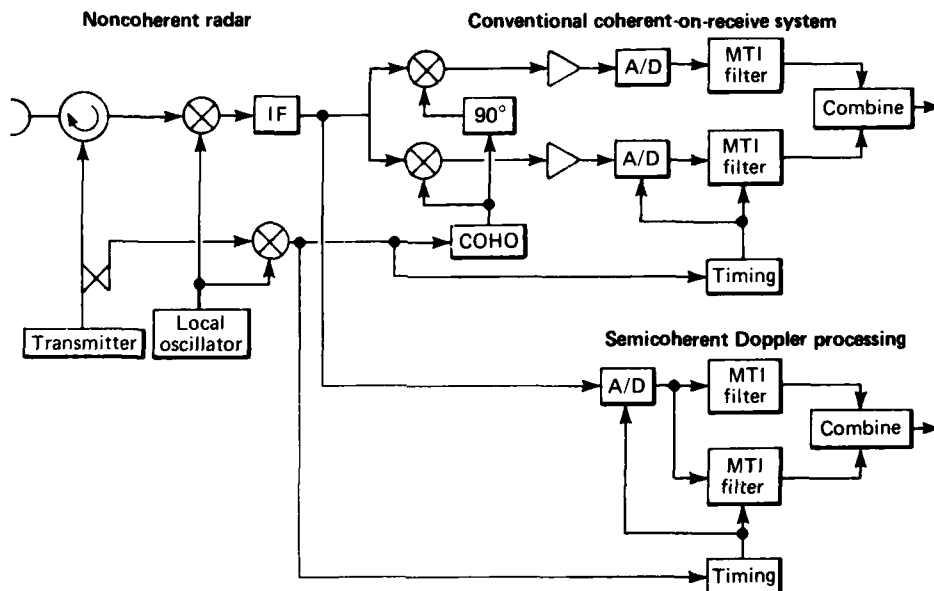


Figure 1 — Doppler processing techniques that were used to process data coherently from a radar with a noncoherent transmitter.

and phase of the data are measured. The accuracy determines to what extent the clutter signals can be separated from targets containing Doppler signals, and this can be expressed as decibels of clutter attenuation.

The semicoherent processing technique is limited by the accuracy with which the sample clock is phase locked to the transmitted signal and by the time jitter between the nonsimultaneous in-phase and quadrature samples. This is in addition to the quantization accuracy and amplitude stability of the system plus environmental effects, all of which are common to every Doppler processor. For typical radar receiver parameters, the accuracy obtained from the sampling and clock circuits permits clutter attenuation in excess of 50 dB. This was the design goal of the system and is not an inherent limitation of the technique.

Experimental Evaluation

A signal processing unit that contained the quadrature time phase direct I/Q sampling circuits was designed and constructed. The unit took the radar I/Q and a reference for locking the sampling timing and produced in-phase and quadrature digital data for every radar resolution cell. In order to analyze these data, a recording interface was built into the processor. Because there are several million data samples every radar scan, the data volume was limited for recording by setting up a window for data collection that could be placed around returns of interest (targets, land, sea, etc.).

The unit, a Coherent Radar Digital Data Collector (CRDDC), was used to record data from an L-band two-dimensional surveillance radar located on the coast of California. The data collection effort verified the performance of the CRDDC and provided a base of coherent radar data for analysis. Figure 2 shows the instrumentation used to collect data with the CRDDC. The region over which data were to be recorded was chosen by viewing the movable sector on the plan position indicator display. The size and location of the window were selected by front panel switches on the CRDDC.

In order to verify the coherence and obtain a measure of the coherent processing gain, the data col-

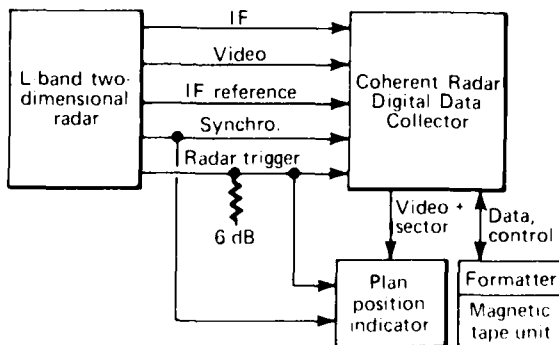


Figure 2 — Instrumentation used to collect data with the Coherent Radar Digital Data Collector.

lected were spectrum analyzed with a fast Fourier transform (FFT) algorithm. $N = 2^7$ points were used in bearing at the same range cell in the FFT processing, and successive FFT's jumped by $N/2$ points to allow 50% overlap. This FFT processing was performed at each range cell within the limits defined by the recording window. For the given radar parameters, a 32-point FFT (i.e., $N = 32$, $m = 5$) was appropriate. It yielded a Doppler resolution of approximately 6.5 kt with ambiguities separated by 205 kt. Hamming weighting was used so that FFT filter sidelobes are down by about 43 dB from the peak value.

Figure 3 illustrates data collected on an aircraft target. This plot is the Doppler filter power response for

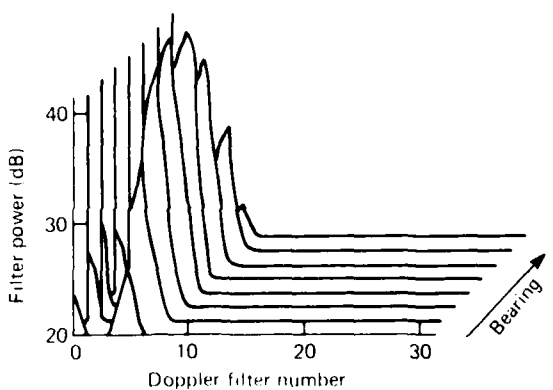


Figure 3 — FFT output of data collected on a 235-kt aircraft target using IF sampled data from a noncoherent radar.

a given range cell for eight successive 32-point transforms as the radar scanned past the target. Also analyzed were data from ship and helicopter targets and sea and land clutter.

CONCLUSIONS

A way to extract Doppler data by directly sampling the radar IF signal has been demonstrated. The technique allows a simpler hardware implementation of Doppler processing for noncoherent radars than has been possible in the past. Although there are performance limitations because of hardware accuracies, the method is adequate to meet many radar processing requirements.

ACKNOWLEDGMENTS

The success of this project was due to the contributions of several staff members. In particular, R. Rzemien and R. J. Clevering provided an excellent hardware design for the CRDDC. F. R. Castella and E. R. Thews developed the programs and analyzed both the technique and the data collected.

This work was supported by Independent R&D.

SIMULATION OF THE VERTICAL LAUNCH OF TOMAHAWK FROM THE SSN 688 CLASS SUBMARINE

J. S. O'Connor

A digital computer code (STEP/688) has been written to simulate the nonlinear dynamics of an underwater, vertical launch of a Tomahawk cruise missile from the SSN 688 capsule launch system (CLS). The simulation is an engineering tool for use in the design phase for evaluating gas generator designs against the performance requirements of the SSN 688 CLS vertical launch system. The simulation uses the predicted pressure/time history of the gas generator, the thermodynamic characteristics of the combustion products, and the geometry of the Tomahawk and CLS to calculate acceleration, velocity, and displacement histories of the missile and the pressure and temperature histories of the ejection chamber. The simulation has been verified by comparison with test data and has been used to predict the performance of the recently redesigned Tomahawk Phase IC gas generator.

BACKGROUND

The Tomahawk missile is ejected vertically from the 688 class submarine by means of a gas generator contained within the capsule launch system (CLS). Pressure resulting from the combustion in the gas generator forces the missile out of the CLS. A set of six ring seals in the CLS maintains the pressure behind the missile (Fig. 1). As the missile clears the sixth and final seal, the hot pressurized gas in the CLS chamber is released inside the submarine fairing. To protect the fairing covering the hull of the submarine, NAVSEA has specified that the pressure at the muzzle of the CLS at the time of missile exit should not be more than 40 psi above the ocean ambient pressure. Also, to ensure the stability of the Tomahawk missile, General Dynamics/Convair states that the muzzle pressure of the CLS should not be less than ocean ambient pressure. The contractor also stipulates that the velocity of the missile at tube exit should stay between 40 and 100 ft/s.

The conditions in the ejection chamber at the time of missile exit are nonlinear functions of launch depth, missile weight, friction between the missile and the CLS, and the rate at which the gas generator supplies energy to the ejection chamber. The simulation uses the predicted pressure-time history of the gas generator, the thermodynamic characteristics of the combustion products, and the geometry of the Tomahawk and CLS to calculate longitudinal acceleration, velocity, and displacement histories of the missile and the pressure and temperature histories of the ejection

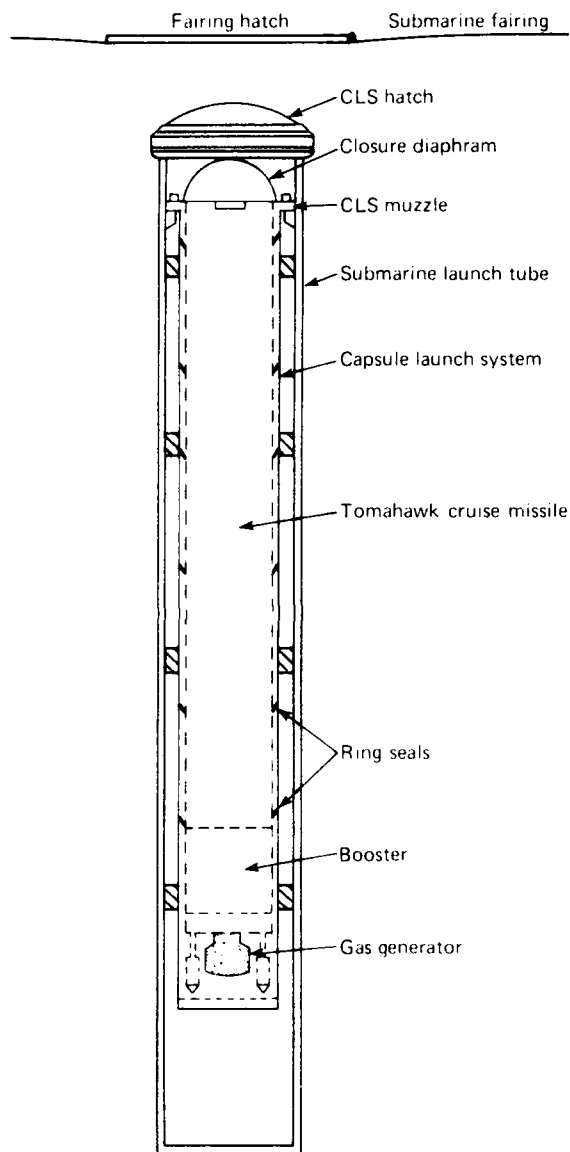


Figure 1 — The Tomahawk capsule launch system.

chamber. Because the equations are nonlinear, they cannot be solved in closed form. To obtain a solution, it is necessary to assume that the nonlinear variables remain linear over a short period of time, Δt (usually 0.001 s), and to solve the equations for each Δt during the entire launch.

DISCUSSION

A CLS gas generator is a device with a characteristic mass flow history that is essentially independent of launch depth. The hot gas always flows into the ejection chamber the same way, regardless of other launch parameters. Some of the energy from the hot gas heats the walls and contents of the ejection chamber, some does work (in the thermodynamic sense) by lifting the missile against the forces restraining it, and the remainder increases the internal energy (temperature and pressure) of the gas already in the chamber. The hydrostatic force of the ocean tending to retard forward motion of the missile is the largest of the component forces used to calculate the thermodynamic work; that component can vary by a factor of 3 between shallow and deep launches. This fact leads to a wide range of temperatures and pressures in the launch chamber for launches conducted at different depths but otherwise identical.

The thermodynamic theory used in the STEP/688 code assumes isentropic flow from the gas generator and ideal gas behavior in the CLS ejection chamber.¹ The energy entering the chamber, the work performed by the gas in the chamber, and the heat lost between times t_i and t_{i+1} are calculated using values for chamber pressure, temperature, and volume and for missile acceleration, velocity, and displacement at t_i . The result is the change in internal energy between t_i and t_{i+1} that is used to calculate the new chamber temperature, T_{i+1} . Using the ideal gas law, the pressure, P_{i+1} , is calculated. The ejection force (P_{i+1} times the missile cross-sectional area) is summed with the retarding forces (hydrostatic, hydrodynamic, friction, and capsule closure rupture) and divided by the missile mass to give the acceleration at t_{i+1} . The acceleration is integrated numerically to yield missile velocity and displacement. When all the system variables have been calculated at t_{i+1} , the simulation uses them as initial values and repeats the process for t_{i+2} .

The simulation was validated by comparing calculated and experimental results for three dynamic test launches and one stationary launch of a boost flight vehicle. Figure 2 shows the comparison of calculated and experimental missile velocities for one dynamic test launch. Reference 2 provides complete theoretical and experimental results, the derivation of the simulation equations, and a simulation user's guide.

APPLICATIONS

The flow rate (burn rate) of a gas generator varies from the design value in a random manner because of manufacturing tolerances. In addition, it varies predictably, depending on the temperature of the

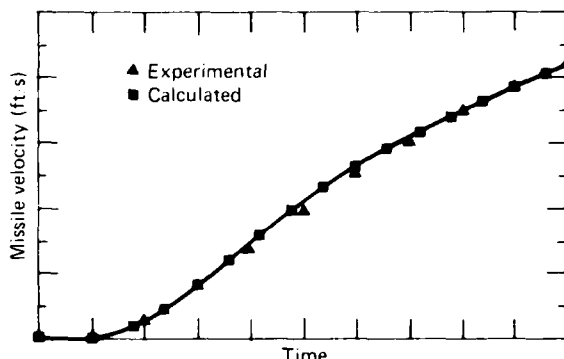


Figure 2 — Comparison of calculated and experimental missile velocities.

gas generator grain at ignition. A parametric analysis was conducted using the STEP/688 code to determine the maximum allowable deviation from the nominal flow rate of the proposed Phase IC gas generator, based on specified muzzle pressure requirements. The parametric analysis considered variations in missile weight, missile/CLS friction, capsule closure load, and gas generator flow rate. The results of that analysis were reported in Ref. 3. STEP/688, is currently being used to determine the limits of allowable launch depth that will meet the system requirements.

ACKNOWLEDGMENT

The author would like to thank R. Kelly Frazer for his assistance in developing the thermodynamic equations for the gas generator flow.

REFERENCES

- 1 J. B. Jones and G. A. Hawkins, *Engineering Thermodynamics*, John Wiley & Sons (1963).
- 2 J. S. O'Connor, *APL/Tomahawk SSN 688 Gas Generator Simulation and Validation Results*, JHU/APL BBE/EM 5118 (27 Apr 1983).
- 3 J. S. O'Connor, *Parametric Analysis of the SSN 688 CLS Gas Generator*, JHU/APL BBE/EM 5117 (3 May 1983).

This work was supported by the Joint Cruise Missile Project Office.

DESIGN AND DEVELOPMENT OF A MODULAR SIX-DEGREE-OF-FREEDOM DIGITAL SIMULATION FOR THE TOMAHAWK CRUISE MISSILE PROGRAM

G. B. Stupp and F. W. Riedel

An all-digital simulation of the Tomahawk missile has been developed. To facilitate simulating different members of the Tomahawk family or different levels of complexity of subsystem models, a modular architecture was developed that allows the use of a high-order integration routine. The simulation is currently being used to analyze the dependence of the Tomahawk antiship missile impact point on the aim-point model.

BACKGROUND

In its role as Technical Direction Agent for the Tomahawk Cruise Missile Program, APL needs a flexible simulation of the missile round to provide understanding and perspective on issues affecting the dynamic performance of the missile. The Tomahawk missile is actually a family of similar missiles, each having its own mission but differing from the others in order to fulfill that mission. Even for a particular missile variant, the range of questions to be investigated can require significantly different levels of complexity for various subsystem models. It is important to have a modular simulation that can be reconfigured easily for the different members of the Tomahawk family and for different subsystem models.

Modularity, by itself, is not a difficult feature to design into a simulation. Each state can be integrated as its derivative is calculated. However, a high-order integration routine, with all elements of the state vector updated from a single subroutine call, was selected for accuracy and efficiency. A simulation methodology was developed for the program that permits the use of a high-order integration routine and still provides the modularity required for the Tomahawk round simulation. Run documentation is automatic so that the output from any run can be identified as to the subsystem models used and the parameter values for those models. In addition, a flexible, easy-to-use plot program was written to facilitate interpretation of the simulation results.

DISCUSSION

The simulation of the Tomahawk missile round is currently configured to represent the terminal guidance portion of a Tomahawk antiship missile flight, although its modularity would allow

reconfiguration to represent other members of the Tomahawk family. The six-degree-of-freedom homing model is shown in Fig. 1. Each box is represented in the simulation by one or more model definition subroutines that implement the functional characteristics of that part of the missile system. The computations performed in most of the subroutines depend on the results from other routines. All of the subroutines are under the control of a main program and several intermediate subprograms.

Figure 2 is a block diagram of the general simulation architecture that implements the model shown in Fig. 1. A central subroutine (INTEG) is used to perform the integration of all states (the vector $\dot{\mathbf{X}}(t)$ in the figure). This subroutine calls other subroutines (XDOT, SUB1, SUB2, etc.) to compute the derivatives ($\dot{\mathbf{X}}(t)$) of the state variables. These low-level derivative subroutines usually represent the various missile subsystems, such as the autopilot and sensors shown in Fig. 1. The simulation was developed with the aim that the model definition subroutines be "plug-in" modular. In other words, any individual subroutine can be modified or even replaced without requiring changes in other parts of the system.

The conventional simulation approach is to have the state and state-derivative vectors defined in the main program to be exactly n elements long, corresponding to the n states of the total system. These vectors are passed to the model definition (derivative) subroutines. Within the subroutines, variables are associated in a one-to-one manner with the n elements of the state and derivative vectors. Thus, in the conventional approach, each subroutine must know which positions within the state vector are allocated for that subroutine's states. Modularity is lost because modifying a particular subroutine (i.e., changing the number of states) would change the positions of the other subroutines' states within the state vector.

The Tomahawk round simulation avoids those problems. First, an initialization procedure is executed during which each model definition subroutine is queried to determine how many states are required. From that information, a state vector is constructed. Changing the number of states of a particular subroutine is handled at program initialization without affecting any of the other model definition routines. Second, all intersubroutine communication takes place using

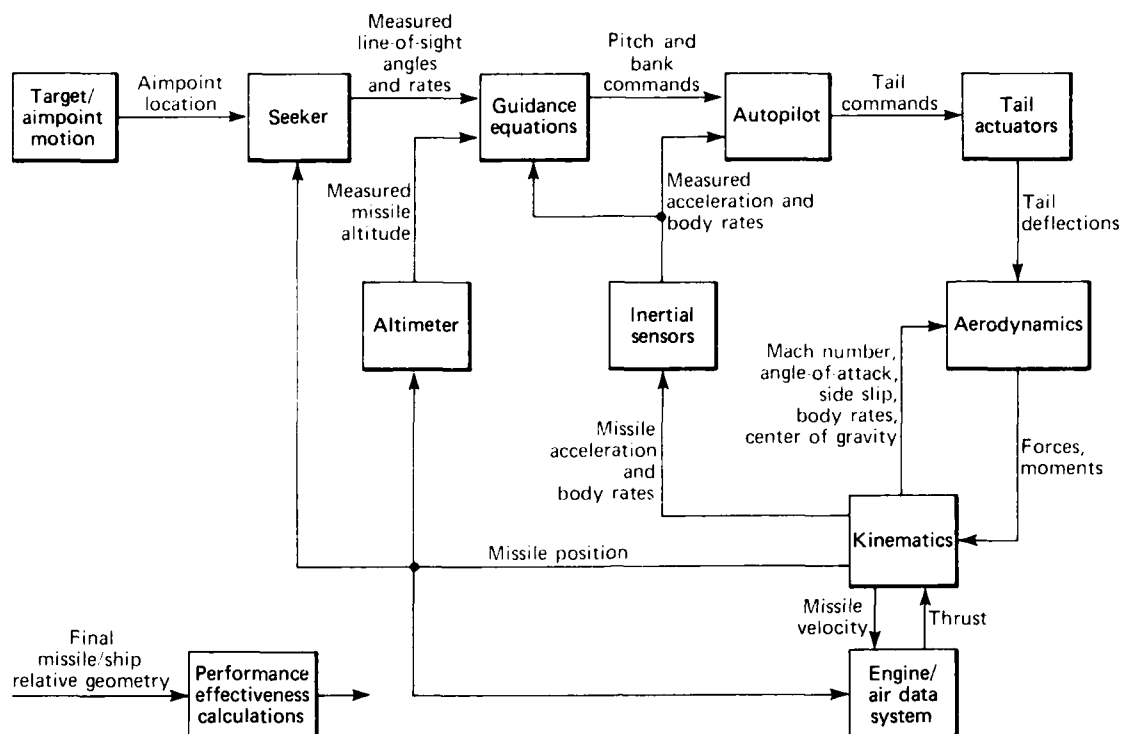


Figure 1 — Six-degree-of-freedom terminal homing model for the Tomahawk antiship missile.

functional inputs and outputs that do not change from model to model. However, because these computer variables are distinct from elements of the state vector, it is necessary to update them after the state has been updated by the integration routine. In the Tomahawk round simulation, this is handled by special assignment calls.

Another modularity problem with the conventional simulation approach involves parameter changes. Typically, input parameter changes are read in through the main program and passed to the appropriate model definition subroutine. This approach requires that the main program know the parameters that might change, and they, of course, change as models are changed. As part of the initialization procedure in the Tomahawk round simulation, the parameters needed to define and initialize an individual subroutine for a given simulation run (or Monte Carlo run series) are read as inputs by the subroutine that needs them. Thus, no change is required in the main program.

This high level of modularity requires the simulation to be self-documenting. The program output functions have been structured so that the output for every run clearly indicates which version of a subroutine is used to make that run and which program input parameters have been changed from their nominal

values. When the initialization entry point of each model definition subroutine is called to return the number of states, the subroutine also writes statements to a run summary listing and to a detailed run data file that give the subroutine name and version number. In addition, the model default parameters are output to the detailed data file. When a subroutine reads its program input for a given run (or Monte Carlo series), parameters that have been changed from their default values are written by the subroutine to the detailed data file and to the summary listing. The detailed data file is formatted like a page of printout. Thus, a user of the simulation may view the run results on a time-sharing terminal and/or create a hard copy for later review. An interactive plotting routine was created to allow easy interpretation of the detailed simulation output.

SIMULATION VERIFICATION AND APPLICATION

Three steps were taken for simulation verification. First, as part of the simulation development, a linear analysis model was constructed. Stability derivative data (generated by perturbing aerodynamic data) were compared to those from the airframe contractor's simulation. A frequency analysis of the linear analysis

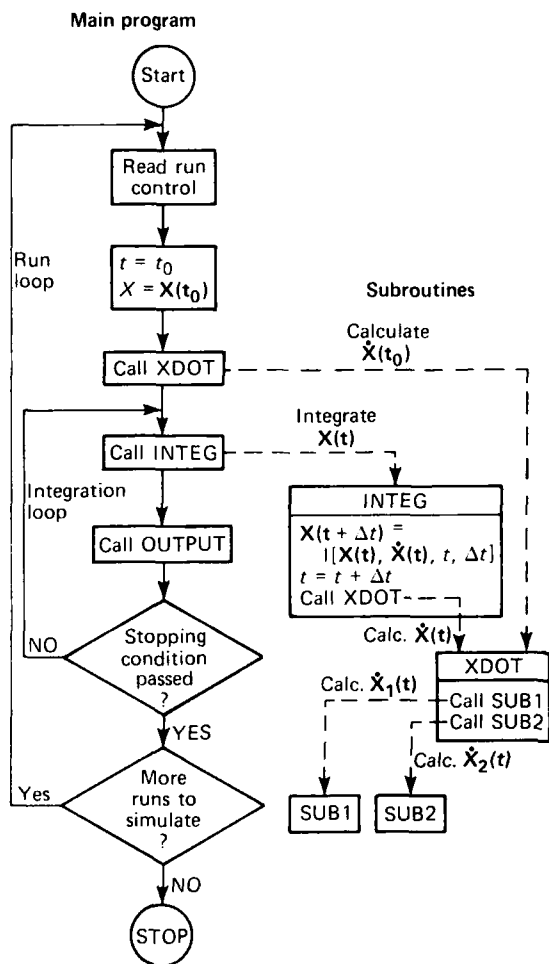


Figure 2 — General program architecture for the numerical integration of dynamic equations.

model was used to verify autopilot gains, stability margins, etc. Step responses from the nonlinear six-degree-of-freedom simulation were then compared to the linear model.

The second step was to compare the autopilot step responses to those from the airframe contractor's simulation. Initial differences were resolved, and the remaining slight differences were shown to have resulted from known differences in propulsion models. In the last step, closed-loop terminal guidance runs were compared to the guidance contractor's simulation. Again, the slight differences that were observed were attributed to differences in propulsion models. Those differences are not important for the first planned use of the simu-

lation and, because of the simulation's modularity, can be removed by using a more detailed engine model.

The Tomahawk simulation was programmed in IBM Fortran IV on the Laboratory's IBM 3033 computer system. The antiship missile configuration runs were at approximately half of real time and used a numerical integration step size of 0.005 s. The time step is determined by seeker filters and may be increased for simulating Tomahawk land-attack variants.

The successful use of the simulation's modularity features has been demonstrated repeatedly. As part of the verification process, a stability-derivative aerodynamics subroutine was substituted for the original detailed aerodynamics routine on several occasions. The instrumentation subroutine has been upgraded. A substitute seeker model was tested easily. The aimpoint subroutine has been changed from a single-shift model to a stochastic bimodal aimpoint model. The latter model has been used to demonstrate the relative sensitivity of the missile impact point to vertical and horizontal aimpoint probability distribution functions.

ACKNOWLEDGMENTS

The essential work contributed by B. E. Kuehne to the simulation, including a principal role in the development of simulation philosophy and structure and the development and programming of key simulation routines, should be noted. Credit should also be given to A. S. Gilbert for programming various subsystem description routines.

REFERENCES

- ¹B. E. Kuehne, *Tomahawk Round 6-DOF Simulation Summary*, JHU/APL FIC(1)83-U-027 (May 1983).
- ²B. E. Kuehne, *Tomahawk 6-DOF Digital Simulation: KINEM, WINDS, WINDV, and Program Control Subroutines*, JHU/APL FIC(1)83-U-033 (Jul 1983).
- ³A. S. Gilbert, *Subroutines for Tomahawk 6-DOF Digital Simulation: AIMPT, INSTR, AT TMR, GUDL, and GUDF*, JHU/APL FID(1)83-U-015 (31 Aug 1983).
- ⁴A. S. Gilbert, *Subroutines for Tomahawk 6-DOF Digital Simulation: INSTR, FINAL, AIMPT, GAUSS, and URAND*, JHU/APL FID(1)83-U-039 (29 Sep 1983).

This work was supported by NAVMIA/SYSCOM, JPM-3.

RAIN DAMAGE EFFECTS ON HYPERSONIC MISSILE RADOMES

R. K. Frazer

An experimental test program has been conducted to demonstrate the effects of raindrop impact on tactical missile radomes in the flight regime between Mach 3.5 and 5.0. The experiments involved exposing three full-size radome samples to a calibrated rain field for distances of 1000 to 6000 ft, followed by a safe recovery. The data on material loss generated in this test constitute a unique record of the rain erosion phenomenon in slip-cast fused silica as it varies with axial location. The results will serve as a basis for obtaining empirical correlations to predict the effects of rain on the erosion of such radomes during operational flights of advanced missile systems.

BACKGROUND

The Navy's Advanced Wide Area Defense Concept includes, as a fundamental part, a surface-launched missile capable of ranges far beyond the radar horizon and traveling at hypersonic speeds. When all-weather performance and high-precision target homing are included as system requirements, the radome material and the physical design become critical, performance-limiting issues. The overall goal of the rain damage program is to provide a reliable way to predict missile system degradation resulting from changes in the radome caused both by aerodynamic heating and by physical damage from raindrop impacts. These environmental effects can alter a radome's RF transmission characteristics to the point where the missile cannot effectively close on the target. The current effort concentrates on testing the rain erosion performance of slip-cast fused silica (SCFS), a material with excellent thermomechanical characteristics but that suffers material loss during supersonic flight through rain. The performance data generated by the tests will be valuable in developing predictive techniques.

In the early 1960's, refinements in the processing of high-purity SCFS (SiO_2) led to the production of prototype radomes that showed excellent potential for hypersonic missile applications.¹ Although it is structurally weak compared to other ceramics, its very low coefficient of thermal expansion ($0.3 \times 10^{-6}/^{\circ}\text{F}$ versus $4.0 \times 10^{-6}/^{\circ}\text{F}$ for alumina, Al_2O_3) and low elastic modulus (4.0×10^{10} psi versus 40×10^{10} psi for Al_2O_3) provide ideal thermal shock resistance. A low dielectric constant partially compensates for the low mechanical strength by allowing relatively thick wall sections to be used. Moreover, the dielectric properties have a low dependence on temperature, allowing extended operation

at high heating conditions. On the other hand, the material's slight porosity and low hardness value leave it susceptible to impact damage by raindrops with a normal velocity component larger than about 1500 ft/s.

Early screening tests² provided a basis for comparison with other materials but produced little data useful for full-size radome design. Recent work of Letson³ has provided a consistent body of erosion rate data for SCFS; incidence angles between 19 and 35° and velocities near 5500 ft/s are covered. Letson's data were gathered using small conical samples about 1.5 to 2.0 in. long as opposed to the earlier screening studies in which small flat plates were used. Unfortunately, none of the tests has provided information about the erosion rates that would occur along the length of a full-size surface. It is expected that the aerodynamic flow field along the radome's length and the presence of water in the boundary layer would have a mitigating effect on a drop's potential for damage aft of the tip region. Because local changes in wall thickness on the order of 0.010 in. will have a significant effect on a radome's boresight error, estimating the erosion rate at various stations is crucial to an accurate prediction of missile system performance. The important issue here is not whether the radome survives but that changes in wall thickness tend to reduce RF performance. The present effort provides data on erosion versus station on full-size prototype radomes that will be correlated with an empirical model.

DISCUSSION

The development of a rain erosion model and the supporting test efforts have five major goals: (a) conducting a literature search to provide an overview of the state of technology for both experimental and theoretical developments,⁴ (b) developing a correlation method for handling full-size sample tests,⁵ (c) procuring and preparing the test items, (d) conducting the tests, and (e) correlating the erosion rate data with theory and developing an improved rain-erosion model.

The first four goals have been met, and the test data are being analyzed. The literature survey revealed that only the experimental work of Letson³ and Balageas⁶ could be used effectively in a correlation scheme. Subsequently, a method for predicting SCFS erosion rates along the radome was proposed that accounts for variations in the intensity of the rain field, the local incidence angle, and the shielding of the sur-

face by water and/or eroded material within the boundary layer. The method assumes that the erosion rate near the tip follows the empirical relationship of Letson's data. Erosion rates aft of the tip are modulated by the effects of changing incidence angle and debris shielding. In functional form, the relationship is

$$\dot{e}(x) = (A g(x) + B h(x)) f(x_0)$$

where

- $\dot{e}(x)$ is the erosion rate at any radome station x ;
- $f(x_0)$ is the erosion rate occurring at the tip location (x_0) and has parametric variation with radome shape, velocity, and rain rate;
- $g(x)$ is the amount of water in the boundary layer at station x ;
- $h(x)$ is the amount of eroded material similarly swept along the radome surface;
- A and B are empirically determined constants.

The experiment, designed to determine the station-dependent erosion effects, has used the Holloman AFB Test Track. The facility can accelerate various size payloads to speeds beyond Mach 5 and then decelerate them to a safe stop. The 10-mi-long track has a 6000-ft section equipped with sprinklers that can approximate rain storms at rates of about 2.5 in./h. Three SCFS radome samples were procured in cooperation with a separately funded API program, and preparations were made to test them at Mach 3.5 and 5.0. Two of the samples were shaped ramjet-nose-inlet compression surfaces with base diameters of 19 in. They were suitable for testing only up to Mach 4.0. The third sample was a 20° half-angle cone with a diameter of 11 in. The absence of the high-incidence-angle aft section on this latter sample allowed it to be tested at Mach 5.0.

The test preparations⁷ involved the design and manufacture of two vibration isolation systems capable of withstanding up to 30,000 lb of axial drag force while isolating the radome from average lateral accelerations of around 100 g at frequencies up to 2000 Hz. After extensive static and dynamic testing at API's environmental test lab,^{8,9} the hardware was shipped to the Holloman test track and mounted to the appropriate rocket sleds. A checkout run using a simulated radome made of steel verified the structural integrity of the vibration isolation system and the rocket sled performance. The rocket motors provided a peak velocity of 3740 ft/s, and the braking system brought the sled to rest intact. Accelerometers mounted to the sled and

radome showed that an overall attenuation in the vibration environment of -17 dB was achieved by the isolation system.

Each large-diameter radome sample was tested at a peak velocity of about 3800 ft/s; one experienced 1000 ft of rain-field exposure while the other went through 4000 ft. Figure 1 is a high-speed photograph of one radome in the rain field at 3775 ft/s. The figure shows the overall character of the flow field around the radome and the presence of water streaks from drop impacts at the radome surface. Figure 2 is a closeup of the surface of the radome that experienced 4000 ft of rain. The damage sites closely resemble those observed in laboratory tests conducted on plate samples impacted by single drops.¹⁰ The large size of the damage sites and their infrequent distribution indicate that only the largest rain drops contributed to the damage. The potentially damaging effect of the more numerous smaller drops has been attenuated by the flow around the radome structure ahead of the damaged section.

Figure 3 shows the small-diameter conical test sample during testing. The peak velocity was 5300 ft/s and the total rain exposure was 6000 ft. Unfortunately, this test item was not recovered intact at the end of the run because of a structural failure that occurred very near the end of the run, when the sled was traveling at about 800 ft/s. Photographic coverage showed the test sample to be intact after leaving the rain field and to have suffered significant erosion over its entire surface. The recovered fragments (representing about one-half of the test sample) indicated that material was removed over the entire surface by impacts with drops of all sizes and that there is a station-dependent effect. Efforts to quantify these observations will depend on assembling

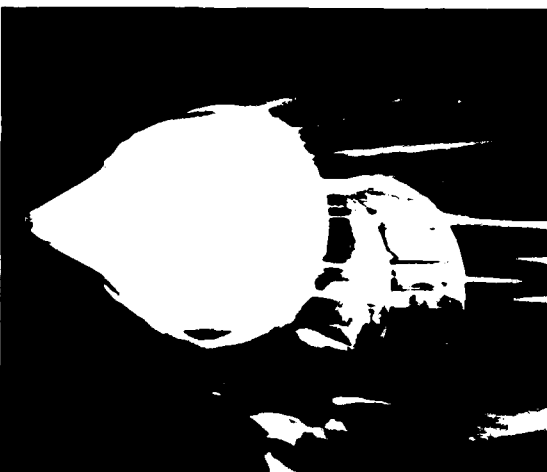


Figure 1 — A radome in the rain field, traveling 3775 ft/s.

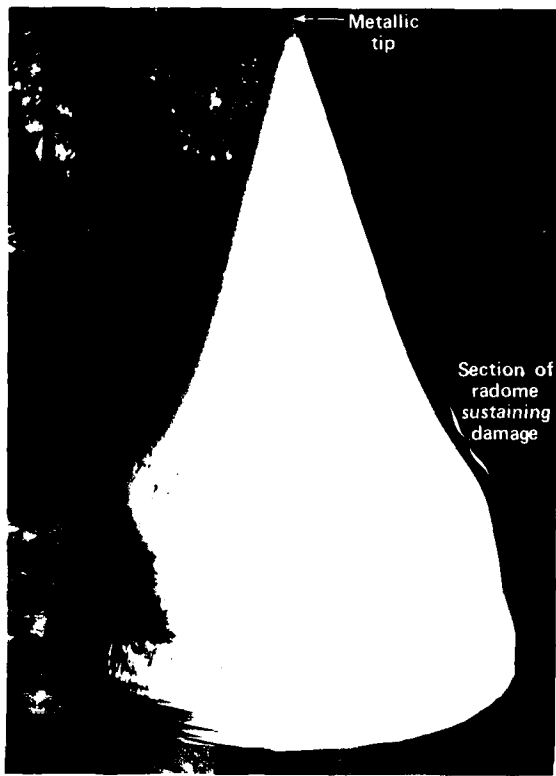


Figure 2 — Closeup of damaged surface of a radome that experienced 4000 ft of rain.

the fragments and making erosion depth versus station measurements.

CONCLUSION

The experimental test program described here has provided a unique set of rain erosion data on full-size SCES radome samples. The availability of these data for correlation with predictive techniques provides a credible foundation for further theoretical development. The two API-built vibration isolation systems provided a structurally adequate "soft" ride for the relatively fragile ceramic samples. Moreover, an increase in the reliability of rocket sled testing of weak ceramic radomes has been demonstrated. The test samples show a significant attenuation of rain damage at stations downstream of the tip, verifying a fundamental assumption in the proposed correlation scheme. Furthermore, the attenuation phenomenon appears to vary with raindrop size. Follow-on efforts will be di-



Figure 3 — The small-diameter conical test sample during testing.

rected at quantifying the erosion experienced in the tests and developing the parametric erosion model for use in preliminary missile design.

REFERENCES

- ¹L. B. Weckesser and R. K. Frazer, "Evaluation of Radomes for Hypersonic Flight," AIAA Fourth Thermophysics Conf. (23-25 Jul 1969).
- ²G. F. Schmit and A. H. Krahill, *Velocity Erosion Rate Relationships of Materials in Rain at Supersonic Speeds*, AFML-TR-70-44 (Oct 1970).
- ³K. N. Larson and W. G. Burlon, *Final Evaluation of Rain Erosion Sled Test Results at M3.7 to 5.0 for Slip Cast Fused Silica Structures*, U.S. Army Missile Research and Development Command Technical Report T-79-42 (Mar 1979).
- ⁴L. K. Fryberger, *Radome Rain Erosion Literature Survey*, JHU API BBE EM-4950 (Jul 1980).
- ⁵J. L. Stadler, "An Approximate Method for Predicting Rain Erosion of Slip Cast Fused Silica Radomes," in *Proc. 16th Symp. on Electromagnetic Windows*, G. K. Huddleston, ed., Georgia Institute of Technology (Jun 1982).
- ⁶D. I. Balageas, "Rain Erosion of Slip Cast Fused Silica," in *Proc. 5th International Conf. on Erosion by Solid and Liquid Impact*, Cambridge, England (Sep 1979).
- ⁷R. K. Frazer, *Test Plans for Rain Erosion Performance Measurements on Three Slip Cast Fused Silica Radome Samples*, JHU API BBE EM-5090 (Jun 1983).
- ⁸H. L. Donnelly and J. R. Bittner, *Radome Rain Erosion - Load Deflection Tests of Full Size Radome Isolation Assembly*, JHU API BBE EM-5110 (Nov 1982).
- ⁹H. L. Donnelly, *Rain Erosion Test - Inertial Properties and Vibration Tests of the Steel Radome and Isolation System*, JHU API BBE EM-5128 (Jun 1983).
- ¹⁰W. F. Adler, *Single Particle Impact Testing of Silica Material*, General Research Corp. CR83-1162 Quarterly Report to NSWC White Oak (6 Apr 1983).

This work was supported by NAVSEA SYSCOM, SEA-062R.

DEVELOPMENT OF COMPUTATIONAL CODES FOR THE ANALYSIS OF SUPERSONIC FLOWFIELDS

M. E. White, M. D. Griffin, and D. M. Van Wie

Recent advancements in computer speed, storage capacity, and algorithmic sophistication have enabled techniques in the field of computational fluid dynamics to become powerful design tools for ramjet engines. In particular, modern computational methods have proven to be very valuable in the analysis of complex supersonic flowfields that are typical of ramjet inlets. This article discusses the development of computational codes for the solution of both inviscid and viscous inlet flowfields.

BACKGROUND

Computational fluid dynamics is the direct numerical solution of the governing partial differential equations that are appropriate for the particular fluid dynamic regime of interest. Once determined, the solution may be processed in order to obtain performance parameters that are important to vehicle design. In the design of ramjet inlets, inexpensive supersonic inviscid flow codes have been developed to obtain flowfield solutions permitting the calculation of inlet additive drag and air capture and the qualitative prediction of inlet efficiency. In addition, supersonic viscous flow codes have been developed to obtain internal inlet flowfield solutions that result in detailed flowfield "pictures" and the calculation of quantitatively accurate inlet efficiencies.

DISCUSSION

Inviscid Flow Code Development

Two- and three-dimensional finite-difference codes have been developed for the solution of steady supersonic inviscid flows. The codes essentially use a steady-state Euler marching technique such as that described by Kutler.¹ Once the flowfield is obtained, the data are processed to yield inlet performance parameters such as air capture, additive drag, cowl wave drag, and kinetic energy efficiencies.²

Figure 1 is a schematic of a typical supersonic inlet for a ramjet missile. When the engine is operating at low angles of attack at Reynolds numbers typical of ramjet applications, the external flowfield is basically inviscid in nature. That is, viscous effects are effectively confined to the thin boundary layer on the compression surfaces. Therefore, it is reasonably accurate and eco-

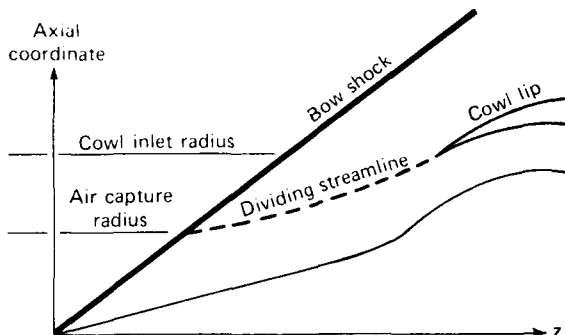


Figure 1 — Axisymmetric inlet flowfield at zero angle of attack.

nomicly efficient to use an inexpensive inviscid marching code for the calculation of this external supersonic flowfield.

The important performance parameters relating to the external inlet flowfield are calculated as appropriate. Figure 2 is an artist's conception of a chin inlet operating at small angle of attack. The additive axial force, often loosely referred to as additive "drag," is obtained by a program developed to trace the streamlines impinging on the cowl lip back to their point of intersection with the bow shock. The additive drag is then calculated by integrating the pressure along the surface of the capture stream tube and multiplying by the tube's projected axial area. The additive normal force is determined by multiplying the pressure by the normal projection of the stream tube. If additive forces are calculated as described above, the axial projection of the capture envelope determines the air capture. However, if only air capture is desired, a mass integration routine is applied at the inlet plane so that the relatively expensive streamline tracing routine can be avoided.

One of the most important inlet performance parameters is the kinetic energy efficiency, which is essentially a measure of how much of the flow's total energy is recoverable as total pressure at the inlet diffuser exit (i.e., the combustor entrance). Although viscous effects play an important role in the internal inlet flowfield, much of the inlet flowfield's total pressure loss occurs because of the internal shock system. In order to analyze those losses, a three-dimensional inviscid marching code has been developed to solve the inlet's internal supersonic flow.³ From such a solution, the qualitatively accurate inviscid kinetic energy efficiency

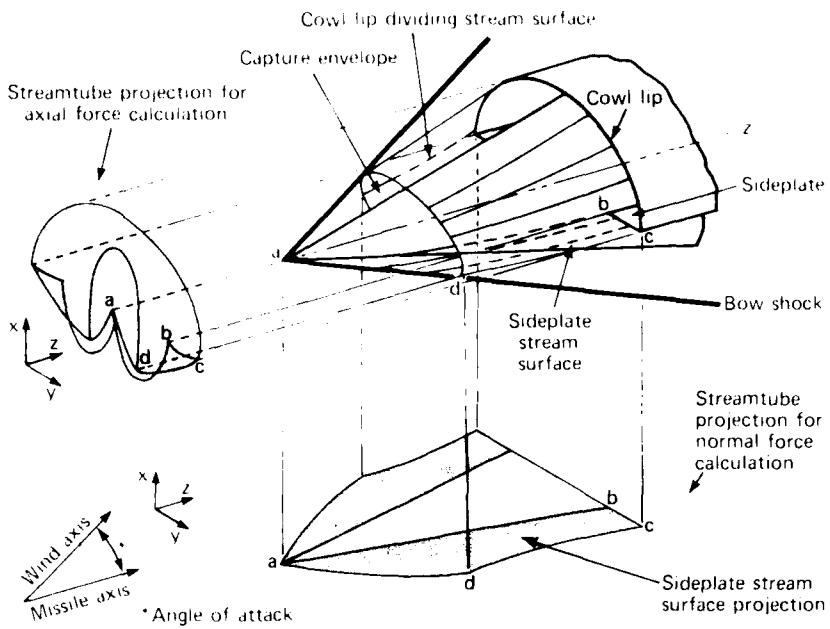


Figure 2 — Chin inlet at angle of attack.

is calculated. This capability has proved to be very valuable as an inexpensive screening tool with which to eliminate inefficient inlet designs.

Viscous Flow Code Development

Purely inviscid analyses have great utility, as can be seen from the above discussion, but also possess severe limitations for the analysis of internal flows. As one might expect, viscosity plays a major role in an internally ducted flow; in fact, the boundary layer may span the entire flow at stations far aft in the duct. In addition, shock-wave boundary-layer interactions will alter the internal shock structure. Therefore, it is always true that viscous effects alone will reduce inlet efficiency, and a viscous analysis capability is necessary to predict internal properties accurately. Such a capability has been developed for two-dimensional and axisymmetric inlet geometries. It is based on approximations to the Navier-Stokes equations that remove their ellipticity and make them parabolic in nature.⁴ The analysis provides a supersonic flowfield solution of the steady-state equations using a relatively inexpensive, spatially marched, finite-difference scheme. Avoided is the enormous expense of a time-dependent solution of the unsteady equations, which requires several hours of execution time on even the most advanced computers. Such a technique is economically impractical for use as a design tool with the present state of computers.

The parabolized Navier-Stokes (PNS) code was originally developed for external flow applications

whereas our primary area of concern is to estimate the losses resulting from internal viscous effects. Accordingly, a NASA Ames version of the external PNS code⁵ was adapted and extended to handle internal flows. PNS results have been obtained for several ramjet inlet designs; they compare favorably with results obtained using a time-dependent solution to the full Navier-Stokes equations and with experimental measurements. An example of such a comparison is shown in Fig. 3, which presents the pressure distribution for a ramjet inlet. The experimental results were obtained from a wind-tunnel test of a one-third-scale inlet model, and the Navier-Stokes solution was obtained for the fully three-dimensional inlet configuration using a NASA Langley computer code. The PNS solution was generated for an axisymmetric approximation of a three-dimensional internal flow where the viscous effects of the sidewall are not taken into account. As can be seen in Fig. 3, this approximation results in less dissipation of the inlet shock system; however, the overall agreement is good.

Table 1 compares the inlet kinetic energy efficiency (η_{in}) for an inviscid flowfield solution with that for a PNS solution at various stations in an axisymmetric ramjet inlet.

Note in the table that the viscous η_{in} is significantly lower than the inviscid η_{in} and that the difference between the two becomes greater at stations farther aft in the duct. At the exit, the difference corresponds to a 12% increase in total pressure loss resulting

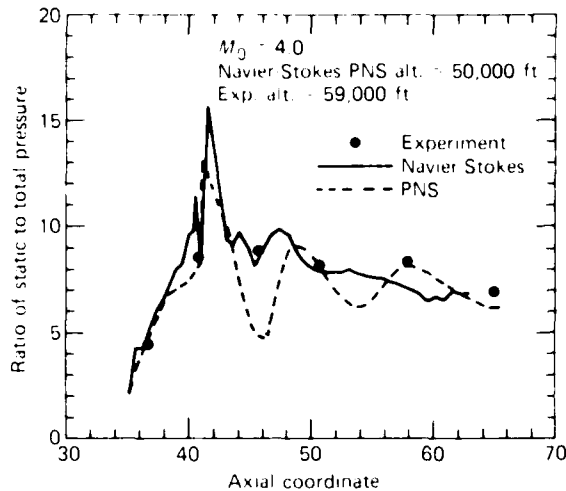


Figure 3 — Pressure distribution for a scramjet inlet.

Table 1 — Mass averaged η_{ke} for the axisymmetric ramjet inlet.

	Cowl Lip	Throat η_{ke}	Midstation	Exit
PNS	0.989	0.981	0.969	0.969
Inviscid	0.996	0.991	0.985	0.984

from viscous effects. It is obvious that viscous losses can make up a substantial amount of the total inlet losses. This fact highlights the importance of a viscous analysis capability for the accurate calculation of ramjet inlet performance.

The current PNS capability can solve flowfields in ramjet inlets with axisymmetric geometries; however, most of the inlet designs currently being studied are complex three-dimensional configurations. Efforts are currently under way to further extend the internal flow PNS code so that solutions can be obtained for inlets with three-dimensional geometries.

REFERENCES

- ¹P. Kutler, "Computation of Three-Dimensional Inviscid Supersonic Flows," in *Springer-Verlag Lecture Notes in Physics, Vol. 41, Progress in Numerical Fluid Dynamics*, pp. 287-374 (1975).
- ²M. D. Griffin, E. S. Billig, and M. F. White, "Applications of Computational Techniques in the Design of Ramjet Engines," in *Proc. 6th International Symp. on Air Breathing Engines*, (1982).
- ³M. D. Griffin, *Inviscid Internal Flowfield Computations for Generalized Hypersonic Inlet Geometries*, JHU API BBP 83-2 (16 Jan 1983).
- ⁴L. B. Schiff and J. L. Steger, "Numerical Simulation of Steady Supersonic Viscous Flow," *AIAA J.* **18**, 1421-1430 (Dec 1980).
- ⁵D. S. Chaussee and J. L. Steger, *Three Dimensional Viscous Flow Field Program, Part 2: Parabolized Navier Stokes Program*, ESI Report 80-06 (Dec 1980).

This work was supported by NAVSEA-SYSCOM, SEA-62R2.

SPACE SCIENCE AND TECHNOLOGY

INTRODUCTION

The Laboratory's involvement in space programs began in the postwar years when Aerobee and captured V-2 rockets carried Geiger tubes, magnetometers, and optical spectrometers high above the earth's surface. The flights provided the first high-altitude measurements of cosmic rays, the geomagnetic field, and atmospheric constituents such as ozone and were conducted by James A. Van Allen, John J. Hopfield, and S. Fred Singer (who were then APL staff members). In 1946, a V-2 rocket carried a camera, installed by Clyde T. Holliday of APL, for the first look at the earth from an altitude of 100 miles. From those beginnings, APL's record of accomplishments proceeds, and includes the conception, design, and development of the Transit Navigation Satellite System and the Satrack Missile Tracking System for the Navy.

Space activities at APL have been supported by an active program of basic research directed toward understanding the chemical and physical processes involved in the earth's atmosphere, ionosphere, and magnetosphere and in interplanetary phenomena. Laboratory achievements include the design and construction of one of the longest-lived scientific satellites ever launched (1963-38C), the discovery of heavy ions trapped in the earth's radiation belts, the experimental confirmation of large-scale field-aligned currents in the auroral regions, the discovery that plasma in the magnetospheres of Jupiter and Saturn has a higher temperature (300 to 700 K) than any other plasma yet observed in nature, and the development of radio astronomy techniques for predicting geomagnetic storms that can disturb terrestrial radio transmissions. Advances in remote sensing include design concepts for future satellite-borne radar altimeters, the derivation of large-scale ocean wave characteristics from satellite-borne radar data, and the development of RF and light frequency radars to monitor crop damaging insects. In addition, APL has developed techniques to predict the disruptive effects of tropospheric phenomena, such as rain, on earth-satellite communications.

In addition to the work reported in this issue of the *APL Selected Accomplishments*, there are a number of space activities presently under way at the Laboratory. The following list is far from inclusive but is intended to provide examples of current efforts.

- APL is collaborating with the Max-Planck Institute on the Active Magnetospheric Particle Tracer Experiment. By creating and monitoring an artificial ion cloud within the distant magnetosphere, the experiment will yield information on the mechanisms responsible for the formation of the Van Allen radiation belts. Launch is scheduled for August 1984.
- Work has begun at APL on the Polar Beacon and Auroral Research (Polar Bear) Satellite Program. The satellite will carry several scientific instruments: an ultraviolet imager for observing the auroral disk and a

magnetometer for measuring the polar magnetic field. Those instruments will permit a unique analysis of auroral phenomena on a global basis.

- The Laboratory is collaborating with the Max-Planck Institute in the development of an energetic particle detector for the NASA Galileo mission. The instrument will be integrated into the Galileo spacecraft scheduled to orbit Jupiter in 1990.
- An APL-built instrument to measure energetic charged particles in the heliosphere will be aboard the International Solar Polar spacecraft scheduled to pass over the sun's poles at the end of this decade.
- APL continues to participate in planning for the Voyager encounter with Uranus in 1986.
- APL is supporting NASA in the design of spacecraft to map simultaneously the earth's gravitational and magnetic field with unprecedented precision.

Eight articles have been chosen for inclusion in this edition of the *APL Selected Accomplishments*.

The first article describes the polar orbiting satellite, HILAT, that was launched on June 27, 1983. HILAT was designed and built by APL and carried experiments by APL, the Air Force Geophysics Laboratory, and SRI International for the Defense Nuclear Agency.

The next article describes APL's ultraviolet imaging instrumentation aboard HILAT that was used to make the first daylight observations of the global auroral display over a polar region.

The Geosat-A satellite being built by APL will carry out radar altimetry to obtain worldwide oceanographic data and a more precise determination of the geoid. Key components of the altimeter are discussed in the third and fourth articles.

In the fifth article, the redesign of the drive and control system for the APL 60-foot parabolic dish antenna is discussed. The system was upgraded to meet the pointing requirements for the reception of S-band frequency energy from Geosat-A.

The sixth article reports on the preliminary system design and integration study of an alternate fine guidance sensor to control and stabilize the Hopkins Space Telescope. The requirement that the Space Telescope maintain a pointing

stability of 0.007 arcsecond with respect to guide stars made this effort particularly challenging.

The next article describes the Fault Isolation and Monitoring System designed by APL for NASA. The system monitors both the quality and the quantity of communication between the Tracking and Data Relay Satellite ground station at White Sands, N. Mex., and the Network Control Center at the Goddard Space Flight Center.

Finally, to support the Galileo mission, APL scientists have examined the thermal response of the spacecraft's nuclear heat source in the event of an off-normal reentry. The results will be used to assess the safety margin of the design.

THE HILAT SATELLITE

K. A. Potocki, S. D. Baran, and L. H. Schwerdtfeger

The HILAT satellite was launched successfully on June 27, 1983 into an 800 by 807 km elliptical orbit with an 82.0° inclination. The objective of this mission is to provide in situ and remote-sensing observations of the plasma density irregularities in the high-latitude ionosphere and of their effects on RF propagation.

BACKGROUND

Naturally occurring radio wave scintillation caused by structured plasmas in the ionosphere can hinder Department of Defense communications and surveillance systems. The Defense Nuclear Agency, which investigates these effects, has sponsored ionospheric research to measure and characterize such phenomena as signal fading, temporal and frequency coherence, etc. This article describes the HILAT (high-latitude ionospheric research) satellite, which was built for the Defense Nuclear Agency to provide measurements of both ionospheric parameters and RF propagation effects.

SPACECRAFT DESCRIPTION

HILAT, designated P83-1 and depicted in Fig. 1, is an operational-class, U.S. Navy Transit navigation satellite modified by API to carry the instrumentation listed in Table 1. To measure high-latitude plasma structure, it carries a unique complement of experiments to perform in situ and remote-sensing observations of the ionosphere. These experiments include (a) radio beacons to measure scintillations caused by ionospheric irregularities; (b) in situ detectors to observe precipitating electron fluxes, plasma density, electric fields, and magnetic fields; and (c) an ultraviolet imaging system with visible photometers to provide global views of the auroral regions.

In order to provide a stabilized platform for imaging, HILAT was three-axis stabilized by means of the Transit gravity-gradient boom and an added momentum wheel for yaw stabilization. There is no on-board data storage. The in situ and imaging data are formatted and telemetered in real time at 4098 bits/s on the coherent beacon experiment transmission to ground receiving stations. The actual ground coverage depends upon the location of the receiving stations and on the spacecraft orbit. Measurements will be made from Sondre Stromfjord, Greenland; Kiruna, Sweden;

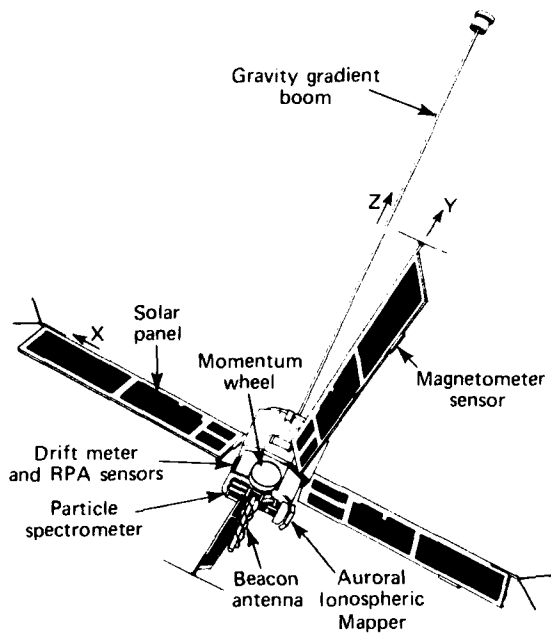


Figure 1 — The orbital configuration of the HILAT satellite. Earth is always in the -Z direction.

Tromsø, Norway; Bellevue, Wash.; and Churchill, Canada.

It is important to the HILAT objectives that the various experiments operate simultaneously. However, the spacecraft's solar arrays and batteries cannot sustain such operation continuously. Therefore, a timer, designed to control the experiments, allows simultaneous operation for one-fourth of an orbit. The orbital phase of the timer is adjustable by ground command to permit operation over any desired 90° sector of the earth. Control of HILAT is provided through the Transit Auxiliary Command System. Experiment mode selection, timer adjustments, and housekeeping telemetry monitoring are performed by the Navy Astro-nautics Group.

Prior to launch, HILAT underwent an extensive test and environmental qualification program. After integration of the spacecraft and the experiments, electromagnetic compatibility and vibration tests were performed at API, and magnetism calibration and thermal vacuum testing were performed at the Goddard Space Flight Center. Figure 2 shows HILAT in preparation for testing at API. All of these tests supported a ready-

Table 1 — HILAT experiments

Instrument	Observations	Operating Characteristics	Experimenters
Coherent beacon	Scintillation Total electron content	Phase coherent radio wave signals at 138, 390, 413, 536, 1239 MHz; right-hand circular polarization	Fremouw (Physical Dynamics Lab.) Rino (SRI International)
Plasma monitor	Total ion concentration Dominant species Ion temperature Electric field	Langmuir probe; spectral density of concentration irregularities at 3, 10, 35, 500, 750 m wavelengths Retarding potential analyzer; ion concentration, 3.5 km resolution; temperature and mass of dominant ion Ion drift meter; cross track electric field with 880 m resolution	Rich (Air Force Geophysics Lab.) Heelis, Hanson (University of Texas, Dallas)
Vector magnetometer	Magnetic field Electric current along magnetic field lines	Three-axis fluxgate; 12 nT quantizations, 400 m resolution	Potemra (JHU/APL)
Electron spectrometer	Electron flux and energy spectra	Energy range: 20 eV to 20 keV; three look directions: up, down, 45° from zenith Three modes, spatial resolution 300, 600, and 1800 m	Hardy (Air Force Geophysics Lab.)
Auroral ionospheric mapper	Night and day aurora E-layer emissions	1150-2000 Å imaging spectrophotometer 3914 and 6300 Å nadir-viewing photometers Wavelength resolution = 30 Å; spatial resolution in E (F) layer is $5 + 20(3 + 13)$ km at nadir	Huffman (Air Force Geophysics Lab.) Meng (JHU/APL)

ness review prior to shipment of the spacecraft to the Vandenberg Air Force Base, Calif.

On June 27, 1983, HILAT was launched successfully on a NASA Scout rocket into an 800 by 807 km elliptical orbit with an 82.0° inclination. That altitude was selected because it was high enough for imager global viewing and low enough for the various in situ measurements. The 82.0° inclination was chosen to give some overhead passes along the geomagnetic meridian

at the ground receiving stations. Ground measurements after launch indicated that all spacecraft subsystems were operating properly and that all of the experiments were meeting their technical objectives.

ACKNOWLEDGMENTS

The HILAT spacecraft is a U.S. Navy navigation Transit satellite originally designed and fabricated

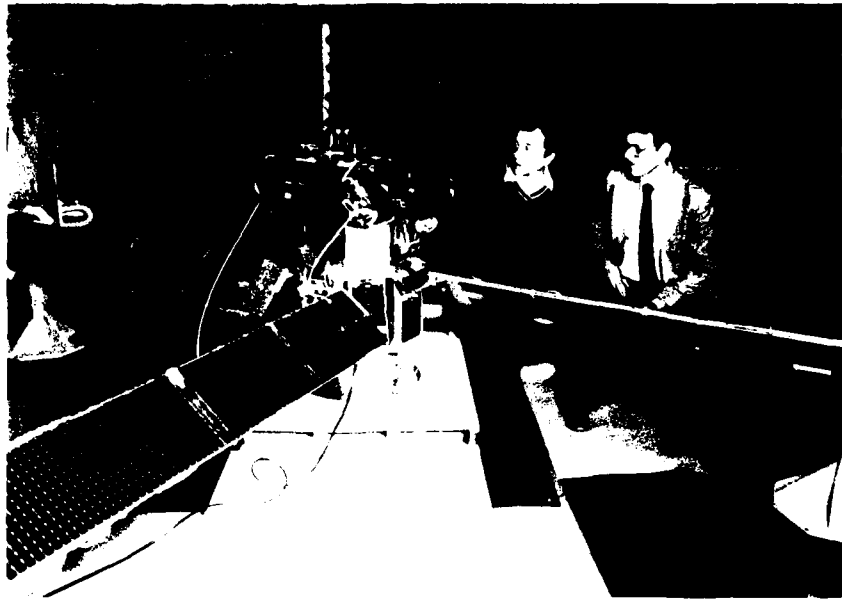


Figure 2 — HILAT being prepared for electromagnetic compatibility tests at APL

and subsequently modified by APL. The engineering success of HILAT is due to all members of the APL staff who were part of the Transit and HILAT teams. HILAT was funded by the Defense Nuclear Agency, and launch activities were coordinated by the U.S. Air Force Space Division. The beacon experiment was built by the Stanford Research Institute, International; the plasma monitor and the electron spectrometer experiments were provided by the Air Force Geophysics Laboratory; the vector magnetometer experiment was built

by APL; and the Auroral Ionospheric Mapper experiment was built by APL for the Air Force Geophysics Laboratory.

REFERENCE

¹The HILAT Science Team, "The HILAT Program," *EOS* **64**, 163-170 (1983).

This work was supported by the Defense Nuclear Agency.

ULTRAVIOLET IMAGER OF ATMOSPHERIC EMISSIONS AND DAYLIGHT GLOBAL AURORAL IMAGERY FROM SPACE

C.-I. Meng and F. W. Schenkel

The global auroral display over the north polar region has been imaged for the first time in full sunlight. This was accomplished by means of the Auroral Ionospheric Mapper, designed and built by APL in collaboration with the Air Force Geophysics Laboratory. The instrument was launched on 27 June 1983 aboard a low-altitude, polar-orbiting, high-latitude research satellite (HILAT, P83-1) as a joint venture of the Defense Nuclear Agency and the USAF Space Test Program.

BACKGROUND

The spatial and temporal variations of the global auroral display reveal extensive information concerning the configuration and dynamics of the magnetosphere. Because the polar auroral phenomenon is the only "visible" consequence of the solar-wind/magnetosphere interaction that can be sensed remotely, the monitoring and understanding of it has been of major interest to geophysicists and space physicists. The ability to observe aurora on the sunlit hemisphere will add important information to the understanding of solar terrestrial processes.

Auroral atmospheric emissions cover very broad wavelength ranges, from infrared to extreme ultraviolet and the short-wavelength bremsstrahlung X rays. In the visible and near-ultraviolet ranges, the most intense auroral brightness can reach a few hundred kilorayleighs (kR) per nanometer, while the Rayleigh scattering of the solar radiance by the atmosphere is about 10^6 kR/nm, making it impossible to detect optical auroral emissions in the sunlit hemisphere. Fortunately, the atmospheric effect is drastically different at slightly shorter wavelengths. Radiation below about 200 nm is totally absorbed by atmospheric molecules and atoms. Thus, the corresponding solar radiations can neither penetrate the earth's atmosphere nor be reflected by it.

Auroral optical emission below 300 nm was found in 1960 by Fastie, Crosswhite, and Markham during a sounding rocket experiment. Subsequently, it has been demonstrated that vacuum ultraviolet (VUV) auroral emissions are sometimes detectable in full sunlight and that the maximum contrast between the aurora and the dayglow background is in the 135 to 155 nm band. Therefore, it should be possible to image the global auroral distribution and activity over the polar regions in both sunlit and dark hemispheres by moni-

toring atmospheric emissions of the proper VUV wavelengths. The first successful attempt to do this was made by the VUV imager aboard the HILAT satellite, which was launched on 27 June 1983 into an 830 km circular polar orbit with 82° inclination.

DISCUSSION

Imaging Experiment

Figure 1 is a schematic diagram of the Auroral Ionospheric Mapper on the three-axis-stabilized HILAT. The mirror shown in the nadir viewing position can scan 67.2° in either direction perpendicular to the satellite's flight path. The light input from the mirror is focused on the entrance slit of the VUV spectrometer by an off-axis parabolic telescope. The spectrometer is a 1/8-m Ebert-Fastie type and the detector is an EMR 510G photomultiplier tube with a cesium iodide photocathode and a magnesium fluoride window. The entrance slit of the spectrometer is 1.5 mm, which corresponds to a spectral resolution of 3 nm; the spectrometer covers the wavelength range from about 110 to 190 nm. The advantage of using the spectrometer as the sensor of this imager instead of a more common photomultiplier tube with a filter wheel is in its ability to provide measurements with a narrower wavelength passband.

With this combination of scan mirror, telescope, and spectrometer, the imager can be operated in three different modes. In the imaging mode, the instrument provides global-scale imagery of atmospheric emission at a selected wavelength in the VUV band. The pictorial swath of about 5000 km width is produced by the combination of the 3-s cross-track horizon-to-horizon scan and the forward motion of the spacecraft, similar to the raster scan of a television tube. The spatial resolution near nadir is about 20 km along the satellite track and 4 km perpendicular to it, and it expands to about 90 by 20 km near the horizon. There are two other modes of operation when the scan mirror is locked in the nadir direction — the photometer mode with the spectrometer fixed at a selected wavelength and the spectrometer mode in which the grating rotates.

In addition to this VUV imaging device, there are two nadir-pointing photometers at visible wavelengths (391.4 and 630 nm) with a 1-nm passband (full-width, half-maximum). Their field of view is a 25-km-

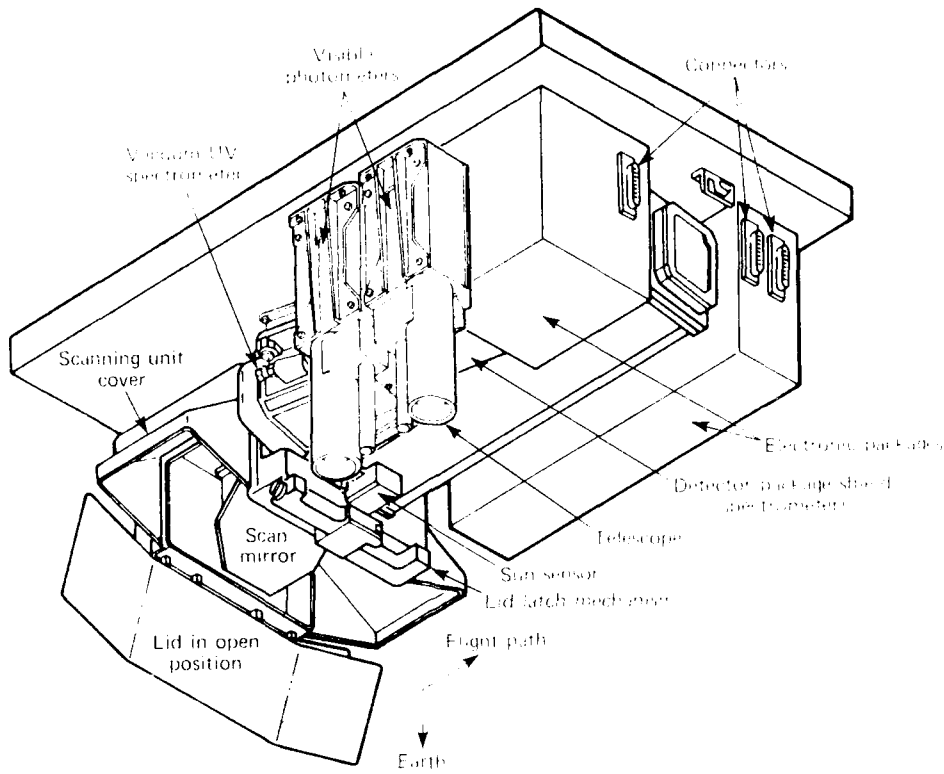


Figure 1 — Schematic of the Auroral Ionospheric Mapper on the HILAT satellite

diameter circle that is sampled once per second. These two well-known auroral wavelengths have been chosen in order to monitor the total energy deposition and the spectral characteristics of precipitating electrons. The visible photometers operate only in the dark hemisphere and are controlled automatically by sensing the earth's albedo brightness.

Daylight Auroral Imagery

The auroral imagery presented here was collected over the northern hemisphere in July 1983 near summer solstice when the major part of the northern auroral oval was under full sunlight. The orbital plane of the satellite is in the dawn-dusk meridian. Figure 2 is an example of an evening pass tracked at API on 18 July 1983 at about 2300 UT. It images the atmospheric atomic oxygen emission at 135.6 (± 1.5) nm over the eastern part of the North American continent and the western part of the Atlantic Ocean from Cuba to the Hudson Strait.

The picture covers an area more than 4000 km wide. It is presented in false color with the color bar on the right indicating relative brightness from very intense (white) to no detectable signals below 28 Rayleighs

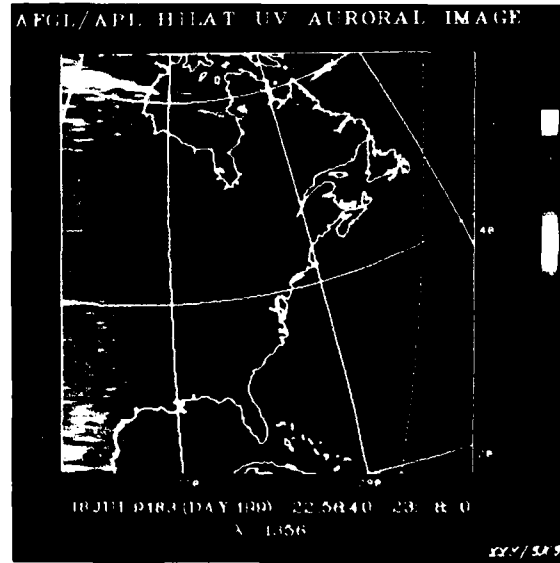


Figure 2 — Evening pass of HILAT tracked at API showing the aurora oval

(black). The light blue background is the dayglow emission caused by the interaction between atmospheric molecules and atoms and the photoelectrons generated

by solar UV radiation. The dark blue and black on the right correspond to the transition into the dark hemisphere. The calculated geometric terminator on the earth's surface is shown for reference by a vertical dotted line. The yellowish green on the left is associated with the limb brightening phenomenon of dayglow because of enhanced volume per solid angle as the imager's field of view moves toward the horizon. The most exciting part, the observation of the evening auroral oval extending across Hudson Bay, is shown as yellowish-green structures above the dayglow background. The structures are clearly identifiable even in the limb-brightening region. These optical auroral features are detected more than 3000 km into the daylight region; they are shown enlarged in Fig. 3. The main feature is a degenerated westward traveling auroral surge that appears as a knot with two parallel arcs along the oval. The dimension of the surge is about 200 km, and the discrete arcs are about 20 km wide and 20 km apart.

The second example (Fig. 4) is an image of the major part of the auroral oval detected on 23 July 1983 at about 1600 UT. The data on this satellite pass were received at Kiruna, Sweden. The entire auroral oval was in daylight. The atmospheric emissions monitored were at 149.3 (± 1.5) nm, from both atomic and molecular nitrogen. In this picture, the sun is toward the left. The auroral oval from afternoon to midnight was imaged above the dayglow background; its display indicates the progress of a weak auroral substorm. Active auroras were over central and west Siberia near the Arctic coast of the Soviet Union. Faint discrete and diffuse auroras extended along the afternoon and evening oval. These observed VUV auroral features in the sunlit polar region are similar to auroral features of the visible wave-

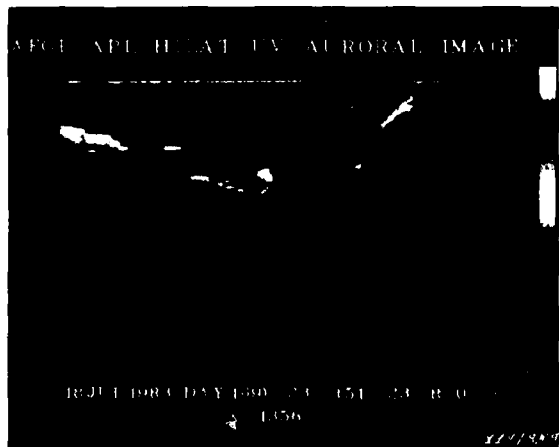


Figure 3 — Enlargement of the central image in Fig. 2.

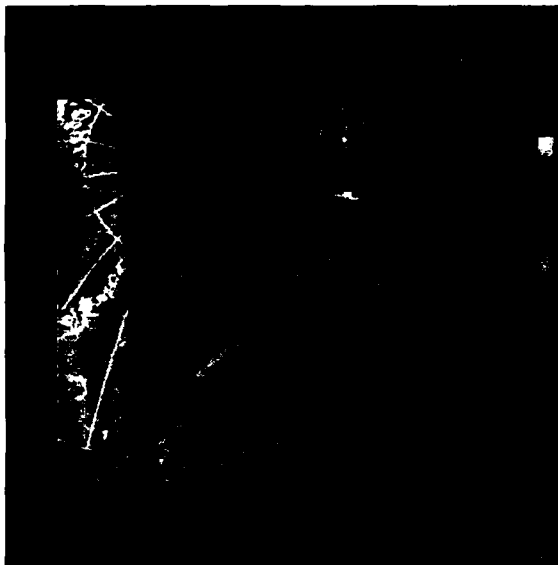


Figure 4 —An image of the major part of the auroral oval, indicating the progress of an auroral substorm.

lengths commonly observed over dark polar regions by earlier spacecraft.

CONCLUSIONS

The VUV imager on board HII-A1 clearly demonstrates that the global auroral display in the local summer polar region under sunlit conditions can be imaged by using properly chosen wavelengths. The earth's albedo and the dayglow background caused by solar radiation previously have prevented auroral observations in the visible and near UV ranges. That is not a formidable obstacle to the described optical measurement. It is believed that this was the first successful attempt to image the auroral display in full daylight and that continuous and complete auroral monitoring is possible from space platforms.

REFERENCE

- W. G. Eastie, H. W. Crowther, and L. P. Maserjian, "The violet Auroral Spectra with a Rocket," *J. Space Res.*, **1**, 111 (1961); *Ann. Geophys.*, **17**, 1094 (1961).

The work was supported by grants A-1366 and E-1366.

DIGITAL SIGNAL PROCESSOR FOR THE GEOSAT-A RADAR ALTIMETER

J. A. Perschy and S. F. Oden

A 13.5-GHz pulse compression radar altimeter to be orbited on board the Geosat-A spacecraft in late 1984 will provide worldwide oceanographic data, including sea-state information and ocean topography. The digital signal processor portion of the altimeter digitizes radar video returns and performs all necessary processing to accomplish real-time tracking of the ocean's surface and to derive selected oceanographic data.

BACKGROUND

The signal processor for the Geosat-A radar altimeter is an extension of the Seasat-A radar altimeter design.¹ The transmit pulse length of the altimeter was increased from 3.2 to 102.4 μ s to accommodate a more reliable but lower-power traveling-wave-tube transmitter. To accommodate this change, the dispersive delay line used for Seasat-A to generate a 3.2 μ s linear FM chirp pulse was replaced by a digital design that generates a 102.4 μ s chirp pulse. The continuous wave (CW) acquisition mode detection circuit was redesigned and moved from the synchronizer to the waveform sampler. The synchronizer was redesigned to accommodate the new long-pulse radar timing requirements. The longer

mission requirements of Geosat-A required a review of parts reliability and radiation environment survivability. The waveform sampler unit was completely redesigned to make use of large-scale integrated circuits. The radiation-sensitive 8080 microprocessor in the Seasat-A adaptive tracker unit was replaced by the less sensitive 8085 microprocessor. The acquisition, track, and calibration algorithms in the adaptive tracker unit were redesigned on the basis of in-flight Seasat-A experience.

DISCUSSION

The altimeter is comprised of two major subsystems: an RF section and a signal processor section. The two primary outputs of the radar altimeter are the precision height from which the ocean geoid and surface topography are determined and the ocean wave-height estimate. In addition, receiver gain control settings are provided in the operate and calibrate modes for the determination of the ocean surface reflectivity. The signal processor is partitioned into functional units (see Fig. 1), each of which is defined by performance and interface specifications. Figure 2 is a photograph of the completed signal processor.

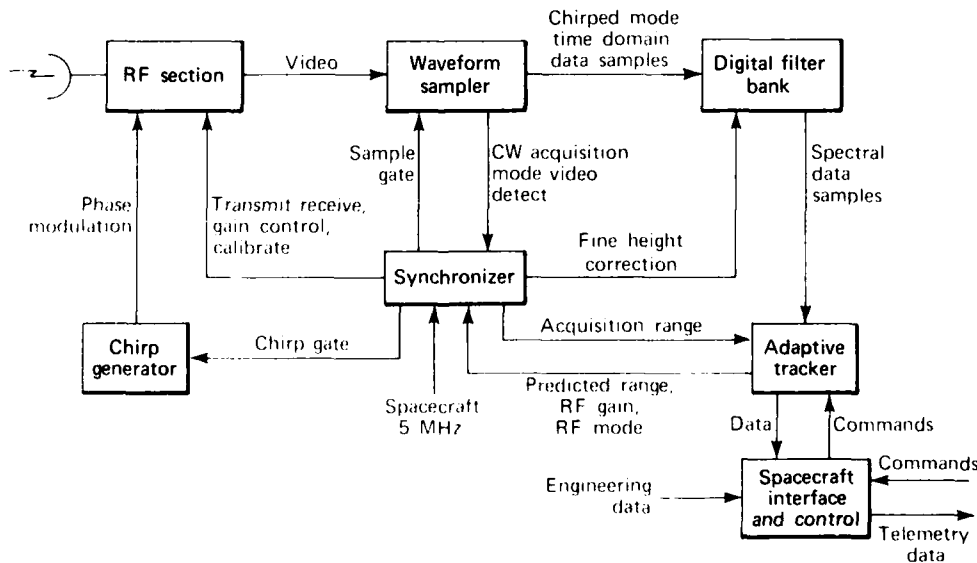


Figure 1 — The signal processor interface to the RF section and the spacecraft.

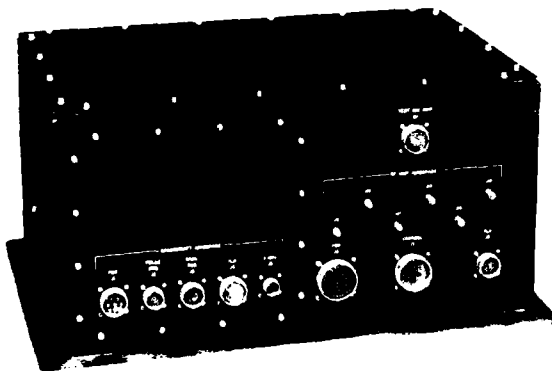


Figure 2 — The signal processor.

Waveform Sampler

The basic function of the waveform sampler is to digitize the in-phase and quadrature (I and Q) video returns from the receiver and to store the time domain samples for processing by the digital filter bank. During each radar pulse interval, two 5-bit analog-to-digital converters take 64 samples each at a rate of 625 kHz, which covers the 102.4 μ s receive gate window; the samples are stored temporarily in two 5×64 bit registers. At the end of the receive gate sampling/storing interval, the digital filter bank begins reading out the I and Q data samples in a repetitive, nondestructive manner until processing is complete. When the next receive gate interval begins, the new data samples are written over the previously stored data.

The waveform sampler performs a secondary function during the CW acquisition mode of operation. The incoming I and Q video is detected by a full-wave rectifier and difference amplifier combination; the outputs are compared to two thresholds, and returns exceeding those levels are reported to the synchronizer unit to determine acquisition range estimates.

Digital Filter Bank

The digital filter bank provides a spectral analysis of the video returns digitized by the waveform sampler. Because the radar pulse is frequency modulated, this spectral information provides range for tracking and data for the analysis of ocean surface characteristics. During the period between receive gate intervals (approximately 877 μ s), the digital filter performs a discrete Fourier transform of the 64 I and Q time domain samples into 63 power spectral samples. Sixty normal frequency terms are formed plus three special terms at band center. The filter resolution is approximately 10 kHz. Each of the 63 filter responses is determined by reading out the sampled data, multiply-

ing them by appropriate sine and cosine terms, and accumulating the results. Finally, the I and Q frequency terms are squared to form power values and are then added to give the measure of signal energy received at that particular frequency increment. As each filter value is computed, it is sent to the adaptive tracker for further analysis.

Fine height correction is also accomplished in the filter bank. Information supplied by the synchronizer is used to modulate the phasors in the multipliers, thus shifting the entire filter bank in frequency. The digital filter bank module (shown in Fig. 3) is an example of typical construction in the signal processor.

Adaptive Tracker Unit

The adaptive tracker unit is a microcomputer built around an 8085 microprocessor. It contains 8192 bytes of read-only program memory and 2048 bytes of read-write storage memory. Dual input storage buffers alternately accumulate radar return waveform sample data from the digital filter band for 50 pulse returns and hold the data for processing by the microprocessor. Height tracking, automatic gain control, and wave-height estimations are then performed at a rate of 20 inputs per second, based on the smoothed waveform samples.

Telemetry data formatting, interpretation of commands, and control of the altimeter mode sequencing between acquisition, track, and calibrate states are accomplished within the adaptive tracker unit. For that purpose, interfaces are established with the interface/control unit and the synchronizer unit.

Processing within the adaptive tracker unit is keyed to the radar transmit pulse that occurs every 980 μ s; that is the highest-priority normal interrupt to the microprocessor. The interrupt initiates the data transfers to and from the synchronizer unit and interface/control unit that must occur each radar trigger. In addition, a modulo 100 count is maintained of the

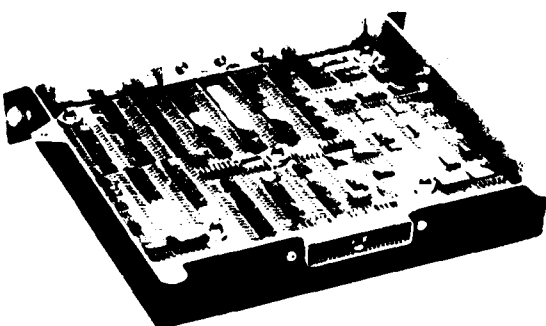


Figure 3 — The signal processor digital filter bank

transmit trigger interrupt that is used to key the next lower priority tasks. At pulse counts of and 80, the 20 inputs per-second processing based on the smoothed waveform samples commences and lasts for approximately 40 pulse intervals. During that time, only the higher priority radar pulse interrupt is honored. In the remaining time, command processing is allowed to proceed with the restriction that the maximum command interrupt rate is one per second.

Synchronizer

The synchronizer unit combines several related functions in a single unit. Timing waveforms are generated on the basis of a countdown from an 80-MHz oscillator locked to the spacecraft's 5-MHz reference. As the result of instructions from the adaptive tracker unit, control signals are passed to the K1 section; those signals set up the desired serial conditions and mode switching as a function of current acquisition track or calibration state. A precision digital timer either counts down coarse height as distance to successively more distant objects, including the retransmit of the digital range accumulator. That timing function is also used to maintain height precision. An timer also will appear at certain times in the height tracking loop. Finally, the synchronizer maintains a range count in the altimeter acquisition mode and reports the range measurement to the adaptive tracker unit.

Digital Chirp Generator

The digital chirp generator is designed to drive a single sideband modulator to produce a linear 40-MHz frequency sweep known as a chirp pulse. In a single sideband modulator, a carrier signal is split into I and Q components that are applied to two linear, bipolar modulators.

In the digital chirp generator, the modulating signals are generated digitally and applied through a pair of digital-to-analog converters to the single sideband modulator in the RF section. The desired parabolic phase progression modulation waveform is derived by accumulating the output of a counter at an 80-MHz clock rate. The resultant parabolic phase progression output is used to address sine and cosine read only memories. The outputs of those read only memories give the modulating values to be applied to digital-to-analog converters. The converter outputs drive the two linear bipolar modulators in the single-sideband modulator. The output of each modulator has an amplitude proportional to the modulating signal, including phase inversion for negative modulating signals. Adding the modulator outputs in phase gives the desired linear frequency sweep.

Spacecraft Interface and Control

Digital and some analog interfaces between the radar altimeter and the spacecraft are provided by the interface control unit. This function consists primarily of receiving commands for altimeter operation and sending out telemetry data from the altimeter. Analog input data from various altimeter subsystems, consisting mostly of temperatures, voltages, and currents, are processed and then multiplexed in turn to an 8-bit analog-to-digital converter. The digitized data words are further multiplexed with other status data and then sent to an accumulator buffer for transmission to the adaptive tracker. The tracker combines the data with waveform data, performs telemetry formatting, and then sends the data stream back through the interface control unit to the spacecraft. Conversely, commands received from the spacecraft are partially decoded and sent to the adaptive tracker for complete decoding and implementation.

STATUS

The Geosat-A altimeter signal processor has been integrated with the K1 section to form a functional module. All performance requirements of the signal processor have been verified. Thermal vacuum environmental testing of the altimeter using a return signal simulator is in progress and will be completed by 1 November 1983. Following integration with the spacecraft, launch into orbit is planned for late 1984.

ACKNOWLEDGMENTS

The authors would like to acknowledge the contribution of R. K. Burek in the design of the original Seasat A altimeter synchronizer, R. C. Moore in the design of the Seasat A altimeter interface control unit, and D. E. Rodriguez for completion of the Geosat-A flight digital chirp generator unit.

REFERENCES

1. J. M. Arkin, *Seasat A Radar Altimeter Design Description*, JHU/APL SDO 5232 (Nov 1978).
2. *Geosat A Technical Plan*, JHU/APL SDO 6002 (Dec 1982).

This work was supported by the Office of the Chief of Naval Operations, OP 211.

RF SECTION OF THE GEOSAT-A RADAR ALTIMETER

E. G. Weiermiller and J. Daniels

The Geosat-A mission was undertaken to satisfy the need for precise ocean wave-height and topographical information. Engineering and flight model RT units have been built, tested, and integrated into the engineering and flight models of the Geosat-A radar altimeter by API.

BACKGROUND

Over the past decade, API has participated in space programs that have significantly pushed the state of the art in precise spaceborne radar altimetry. Although Seasat A had a relatively short mission life, the quality of the altimetry data provided by its API-built radar altimeter caused great excitement among its scientific and military users. The Geosat-A mission was undertaken to satisfy the need for precise ocean wave-height and topographical information. This article describes the RF section of the radar altimeter for Geosat A, which is scheduled for launch in September 1984.

DISCUSSION

The conceptual design of the Geosat-A altimeter RF section is based upon that of Seasat A. The design approach of both was to use off-the-shelf components as much as possible to minimize cost.

Figure 1 is a functional block diagram of the RF section. The five units that comprise the RF section are the traveling wave tube (TWT) amplifier, the up converter/frequency multiplier (UCFM), the chirp generator, the microwave transmission unit (MTU), and the receiver unit. A 5 MHz crystal oscillator reference signal, supplied by the spacecraft, is the input to the UCFM. One output of the UCFM is used as the input carrier frequency for the chirp generator. ("Chirp" is the term used to denote a linear FM applied to radar pulses.) The chirp generator forms a chirped pulse with a carrier frequency of 250 MHz. That pulse is returned to the UCFM where it is up converted to a chirped transmission frequency of 13.5 GHz and a first local oscillator (LO) frequency of 13.0 GHz. Precise height information is obtained by operating on the frequency information that results when the chirped ocean return is mixed with a similarly chirped LO pulse.

The 13.5 GHz chirped pulse from the UCFM drives the TWT amplifier, the altimeter's RF power tube. The TWT amplifier output pulse is routed via the switching network of the MTU to the antenna of the radar altimeter where it is radiated to the ocean below.

The ocean surface return is transferred from the antenna to the MTU where the signal is amplified and the first frequency down conversion (to a 500 MHz IF) takes place. The return signal continues to the receiver

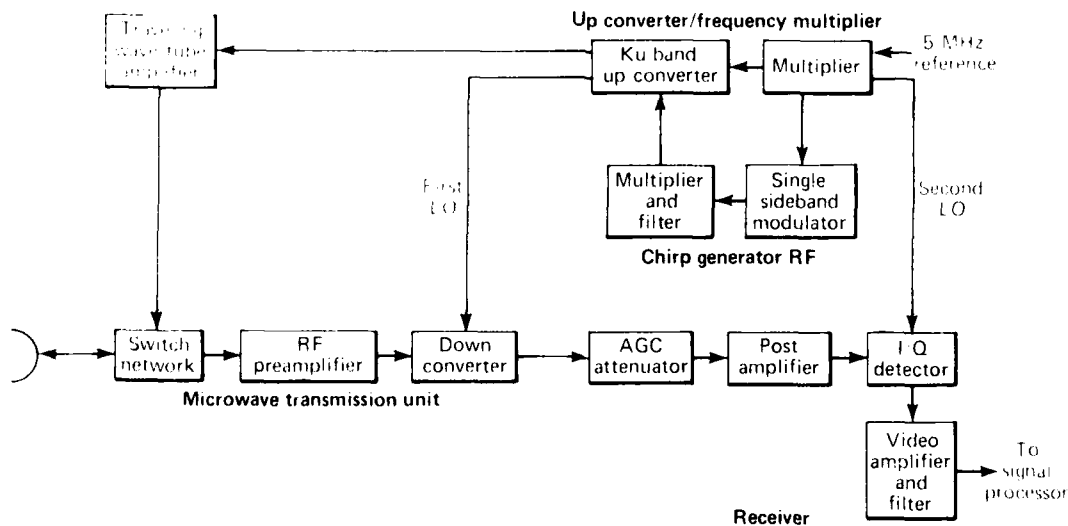


Figure 1 — The RF section of the Geosat-A radar altimeter.

unit where it is adjusted to a particular amplitude by an automatic gain control (AGC) and down converted again to extract two channels of video separated in phase by 90°. Those signals are then output to the signal processor section of the radar altimeter.

Although the initial plan called for an altimeter using the Seasat-A design, the 18 month mission design goal of Geosat-A was not compatible with the 2.5 kW TWT amplifier used as the power amplifier in the Seasat-A altimeter. A space qualified TWT amplifier having approximately 22 W of RF output power and easily able to meet the Geosat-A mission life goal was located.

A technique long used by radar designers to reduce transmitter power while maintaining maximum detection range was the primary way to compensate for the loss of RF power. The width of the transmitted pulse was increased so that the total amount of energy in the pulse (i.e., the product of pulse amplitude and pulse width) remained unchanged. A system design problem is normally associated with that technique. An increased pulse width usually results in a decrease in range resolution; however, because the Geosat-A altimeter makes its height measurement by operating on the chirp modulation rather than in the time domain, the resolution trade-off does not apply.

Several modifications to the Seasat-A RF design became necessary in order to accommodate the substantial increase in pulse width. They are discussed below.

TWT Amplifier

The Geosat-A TWT amplifier was procured under a subcontract from Watkins-Johnson. The unit provides approximately 22 W of RF output power at the 13.5 GHz transmission frequency.

Chirp Generator

The heart of the chirp generator, which was the unit most affected by the increase in pulse width, was a surface acoustic wave device supplied by Andersen Laboratories. A similar device capable of handling the compression ratio associated with the large ($\approx 100 \mu\text{s}$) Geosat-A pulse would have been beyond the state of the art; therefore, a completely different design approach was taken. The Geosat-A chirp generator, referred to as the digital chirp generator, was a joint effort by engineers for the digital and RF parts of the altimeter. The linear frequency was generated digitally and then, by means of RF techniques, a chirp pulse with the desired pulse width and carrier frequency was formed.

Microwave Transmission Unit

The MTU performs the necessary switching of transmit and receive signals, including isolating the receiving channel from TWT amplifier noise power while the altimeter is waiting for the ocean return. This new function was needed because the Geosat-A TWT amplifier, unlike its Seasat-A counterpart, cannot be switched off between pulses to cut out TWT amplifier noise.

The MTU, as noted earlier, also performs the initial functions of a receiver (i.e., signal amplification using a low-noise preamplifier and frequency down conversion to IF).

Other MTU functions include providing a channel to monitor the TWT amplifier output power and a way to calibrate the altimeter. The calibration is done by coupling the transmit signal through a channel known as the calibration path where it is attenuated and then injected into the receiver channel. The calibration path includes a programmable pin diode attenuator; by varying the loss in the known increments of the calibration path, changes in the operational signal path can be simulated and the system calibrated. The greatest challenge in building the MTU has been to isolate the calibration signal from leakage through the normal operational path and from RF interference (RFI) from parallel paths of unknown origin.

Several modifications have been made to the Geosat-A MTU to improve the calibration path isolation:

1. Separating the MTU switching assembly into three components to better isolate each portion from parallel path RFI,
2. Using an iridite (conductive) finish on the exterior surface of the waveguide components rather than the typical painted finish that might protect surface currents from attempts to break them up,
3. Adding a metal enclosure to isolate the MTU from potential external leakage,
4. Using RF absorbing material to attenuate the RFI.

RF absorbing material was used to line the enclosure and baseplate. It also was glued to sheet metal baffles placed between the channels to break up radiation within the box and was used as a wrapping for key power and control harnesses to attenuate any RFI on the wires.

Receiver Unit

The receiver unit consists of an AGC module, an in-phase/quadrature (I/Q) module, and matched

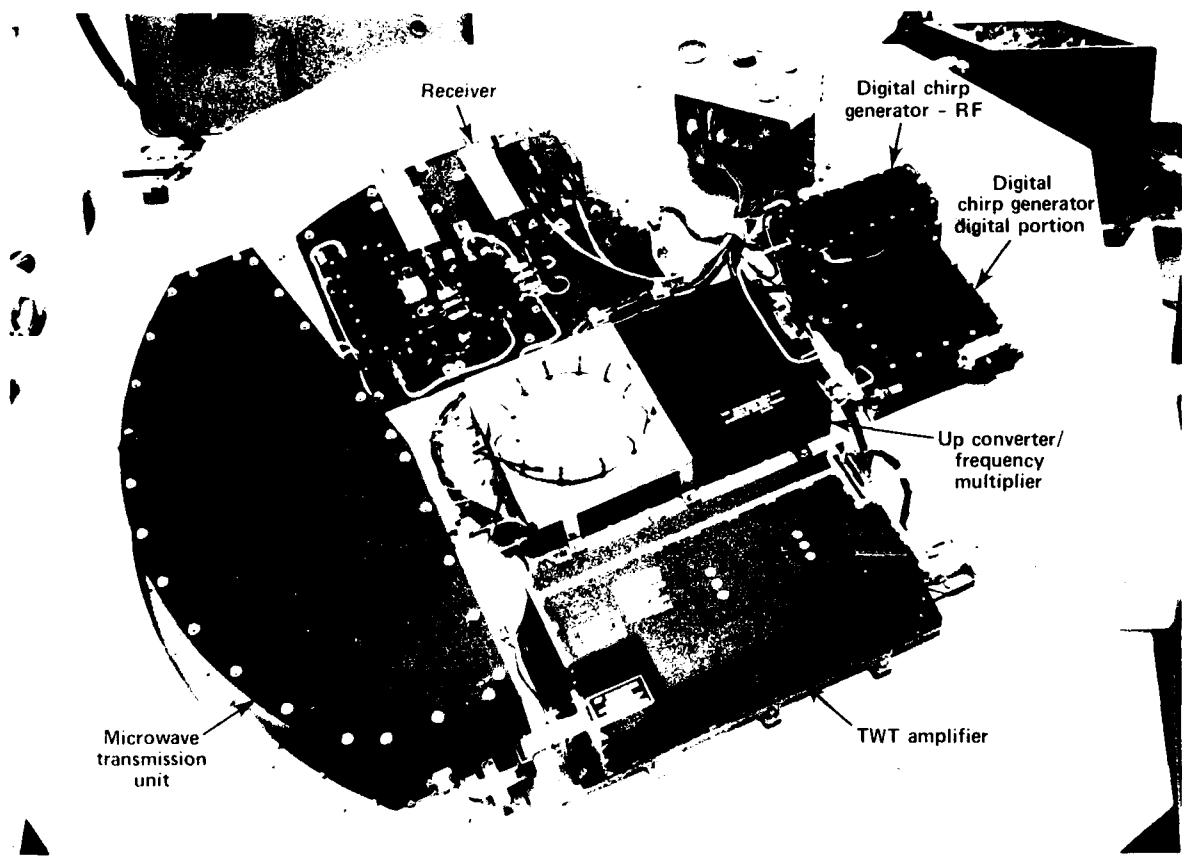


Figure 2 — The flight model RF deck.

phase-quadrature video channels. The AGC module ensures that a fixed signal amplitude is sent to the signal processor section. The I-Q module uses the 500 MHz LO signal from the UCFM to perform the second frequency down conversion. The down conversion produces two video signals that are in phase quadrature. The signals are filtered and amplified before being sent to the signal processor.

The AGC and I-Q modules have been designed using off-the-shelf microwave integrated circuit components rather than the discrete components used to build the Seasat-A receiver. Such components are readily available and mount directly to printed circuit boards, thereby significantly reducing module size and weight compared to those of a discrete component.

Up Converter-Frequency Multiplier

The UCFM uses the 5 MHz reference input to generate four output signals: a 125 MHz continuous signal that is used as a chirp generator input, the 13.5 GHz pulse (with or without chirp modulation) that drives the

TWT amplifier, the 13.0 GHz first LO signal used in the initial down conversion of the radar return in the MTU, and the 500 MHz LO signal for the second (I/Q) down conversion in the receiver. This unit was originally procured under subcontract from Zeta Laboratories for the Seasat-A Program. Only minor design modifications were needed for Geosat-A.

Testing and Integration

Engineering and flight model RF units have been built, tested, and integrated into the engineering and flight models of the Geosat-A radar altimeter. The flight model RF deck is shown in Fig. 2.

ACKNOWLEDGMENTS

The authors wish to acknowledge the efforts of F. A. Beck, J. P. Jones, J. L. MacArthur, P. C. Marth, J. J. Maynard, W. C. Powis, C. M. Russell, G. E. A. Thomann, U. J. Von Mehlem, and J. G. Wall.

This work was supported by the Office of Naval Research.

UPGRADE OF THE APL 60-FT DISH ANTENNA CONTROL SYSTEM

R. L. Konigsberg, V. F. Neradka, and T. M. Rankin

The drive and control system for the APL 60-ft parabolic dish antenna has been redesigned in order to meet pointing requirements for the reception of S-band frequency energy from the Geosat-A satellite following its launch in 1984. Using the Landsat-D satellite as a test target, dish pointing errors of less than 0.05° and peak RF pointing errors of less than 0.1° have been demonstrated. The system was used successfully to support the Husat satellite launch operations during July and August 1983.

BACKGROUND

The 60-ft parabolic dish antenna (Fig. 1) has probably been the most readily recognized facility of the Laboratory since its erection in 1962-1963 by Philco

Western Development Laboratories. The facility has supported reliably the development and operation of the Navy navigation satellites at 150 and 400 MHz. In the summer of 1982, it was proposed that the antenna be used to acquire data from the Geosat-A satellite, which will transmit data in the S-band frequency. The reliable reception of data from satellites of opportunity at that frequency proved to be impossible. A detailed engineering evaluation showed that a complete drive and control system redesign was necessary.

DISCUSSION

The task consisted of (a) redesigning and fabricating new control system electronics using modern technology, (b) completely rebuilding all hydraulic components, and (c) rebuilding all mechanical drive components (including the 2.5 ton gearboxes).

The newly designed and fabricated servo electronics were connected to a complete single-axis hybrid simulation of the antenna in the APL Inertial Laboratory using the actual antenna resolver for feedback from the servo rate table to simulate antenna axis rotation. By means of the simulation, the antenna servo rate loops and position control loops (which contain an imbedded microprocessor) were tested, debugged, and optimized before actual integration into the antenna.

The antenna's main bearings were found to be in excellent condition during an on-site investigation by their manufacturer, but the large gearboxes showed excessive wear. They were removed and shipped to their manufacturer for overhaul. All hydraulic components in the drive system were either overhauled and tested in the APL hydraulics laboratory or returned to the manufacturer for overhaul. The large hydraulic snubbers, which are required to preclude the possibility of a runaway antenna and are of particular concern, were completely rebuilt. To generate the equivalent of the maximum torque of 1,000,000 ft-lb that may be required of the snubbers in use, they were temporarily plumbed into the antenna's hydraulic supply and tested for proper rate control and snubbing action prior to reinstallation on the antenna.

Figure 2, a block diagram of the antenna control system, shows the dedicated HP 9836 pointing computer that computes at 1 Hz the predicted position com-



Figure 1 — The APL 60-ft dish antenna

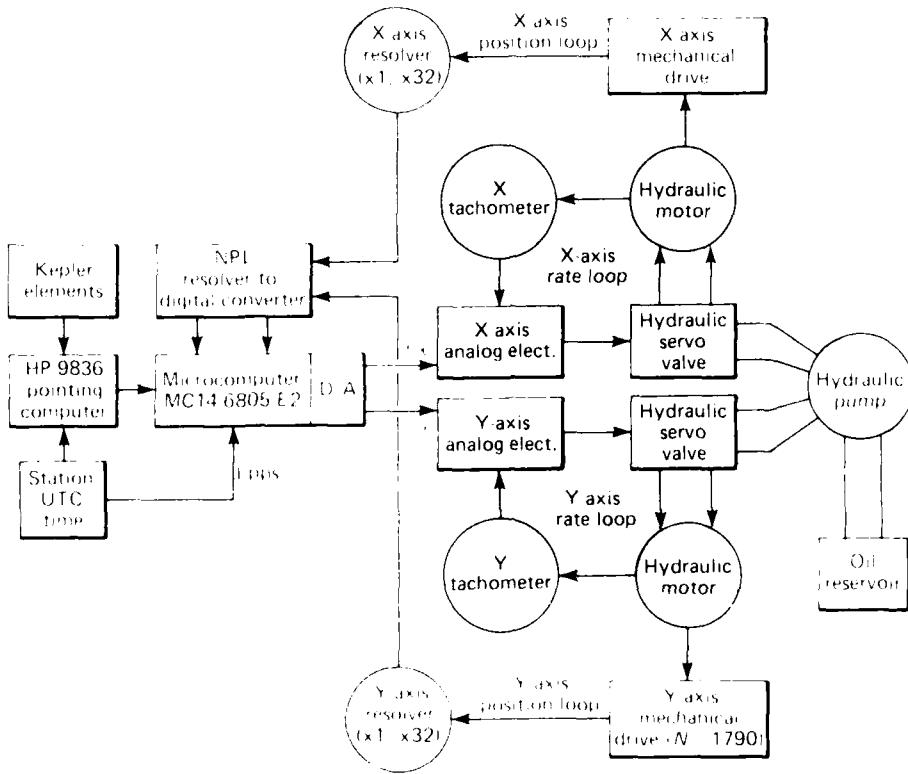


Figure 2 — The antenna control system

mands from the satellite Kepler elements and inputs 16-bit position commands to the microprocessor. The microprocessor linearly interpolates between discrete 1-s input position commands at a 32 Hz rate, comparing each interpolated command position with the actual antenna position that is obtained from the antenna shaft angle encoder. The resulting difference is output for each axis by a 16-bit digital-to-analog converter. Thus, the output represents the error signal needed to close independently each of the two position control loops. The microprocessor has its own accurate internal clock to generate the 32 Hz commands. It also synchronizes this internal clock to the station UTC 1-pps refer-

ence clock when it is commanded to "begin track" by the HP 9836.

To minimize pointing error while pointing dynamically at satellites, a type II servo loop has been implemented with an acceleration constant of 0.19 s^{-2} . The resulting maximum dynamic pointing error expected for Geosat-A is $<0.02^\circ$. Figure 3, a block diagram of the servo loops, shows the basic blocks of the design and the overall equivalent open-loop transfer function that defines the dynamic performance and the acceleration constant. To provide rapid repositioning and stowing of the antenna, mode switching is

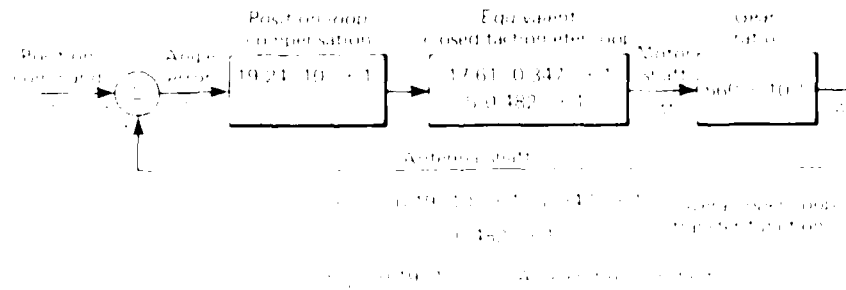


Figure 3 — The 60 ft antenna servo in type II mode

automatic if the error angle exceeds 0.9° . At that error level, the system switches from type II to the unconditionally stable type I system response. When the error drops to below 0.25° , the system reverts to the more accurate and responsive type II system. The electronics are also designed to be antenna-rate and acceleration limiting to preclude undue stresses on the drive system mechanical components, thereby extending the expected life and reliability of the facility.

The dynamic performance requirements of the servo electronics are not dictated by actual satellite line-of-sight dynamics but by the disturbances caused by wind-turbulence-induced torques. To study the effects of those disturbances and to serve as a guide during the development of new circuitry, a nonlinear, discrete computer simulation of the antenna was developed. The servo dynamics were designed with as broad a bandwidth as reasonable, while retaining adequate stability margins. Figure 4, which contains typical Bode plots of the measured antenna performance, shows phase and gain margins from the open-loop curves.

CONCLUSIONS

The complete pointing system was tested and evaluated using the Landsat-D satellite as an S-band

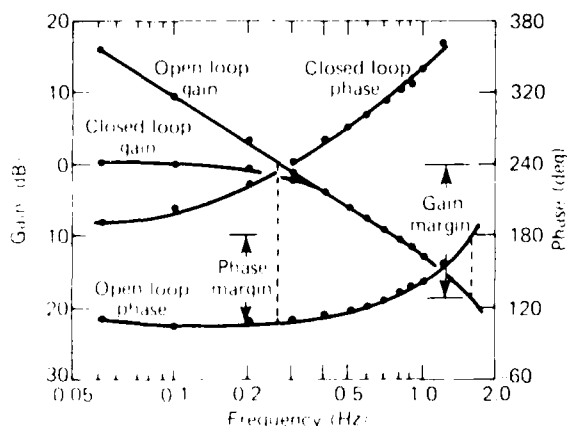


Figure 4 —Measured dynamic performance of the 60-ft dish antenna servo

target. The total RF boresight pointing errors were measured by scanning mechanically 0.25° at 1 Hz and observing the received RF automatic gain control signal. The manual closing of an RF track loop around the pointing system during the satellite passes enabled the measurement of the amount of manual correction needed to null track errors. Analysis of the data from about 30 satellite passes has shown that the dish servo and reflector are dynamically better than 0.05° and that the overall RF pointing error using satellite orbital predictions is less than 0.1° . This performance exceeds the requirements.

During the summer of 1983, the APL Satellite Tracking Facility entered a new era of reliability with automation by digital control. Beginning with the Geosat-A launch in 1984, the facility will track four passes a day until approximately 2200 passes have been accumulated. It is estimated that over the next two years the total use of the facility will exceed its use from its inception in 1963 through to the 1983 upgrade.

ACKNOWLEDGMENTS

This task required the cooperative effort of many APL organizations. The authors would like to acknowledge the work of R. H. Allen on the snubber, L. Wenrich on the hydraulics, R. Fry on the imbedded microprocessor, G. Bailey and M. Gantz on the pointing computer, E. C. Cope on the electronics fabrication system and integration support, and L. Fuhrman, E. Burnham, and C. E. Zimmerman on the disassembly and reassembly of the mechanical system. In particular, we thank L. Dubois (facility manager) whose expertise from 15 years at the station was invaluable in successfully completing the task.

This work was supported by Independent R&D

ALTERNATE FINE GUIDANCE SENSOR FOR THE SPACE TELESCOPE

M. D. Griffin, T. E. Strikwerda, and D. G. Grant

A preliminary system design and integration study of an alternate fine guidance sensor to control and stabilize the NASA Space Telescope has been completed. The Space Telescope must maintain a pointing stability, referenced to selected guide stars, of 0.007 arcsec (1σ). The recommended sensor consists of an electrostatically focused Digicon tube that images a desired guide star on a four-element silicon detector array operated in a photon counting mode. An algorithm for image quadrant intensity balancing is used to maintain the guide star position at the sensor boresight position, thus developing an error signal for Space Telescope pointing control. The performance of the system has been analyzed by means of a single-axis simulation of Space Telescope dynamics and has been compared with both the original system and with other possible control concepts.

BACKGROUND

The baseline fine guidance system (FGS) for the Space Telescope (ST) uses a Koesters prism interferometer to sense the wavefront tilt of light from a guide star relative to the ST boresight axis. The interferometer has a usable angular fine-lock range of, at most, ± 0.04 arcsec, outside of which the telescope pointing accuracy is uncertain to within several arc seconds. This characteristic, together with the possible existence of environmental and spacecraft-generated disturbance torques of sufficient magnitude to result in loss of fine lock, caused concern as to whether the baseline system could meet the ST pointing stability requirements. These and other issues led to the implementation of an Alternate Fine Guidance Sensor Program at API, sponsored by NASA's Marshall Space Flight Center, with W. G. Eastie of JHU's Homewood campus as the Principal Investigator. The three goals of the program were to develop a preliminary alternate sensor design that could meet the specifications with minimum program impact, to assess the cost and schedule requirements for integrating this sensor into the existing spacecraft, and to identify appropriate industrial teaming for the accomplishment of this work, should it be required.

DISCUSSION

Sensor Selection

Initial work at API centered around a study of the overall ST system to understand the environment in

which the alternate sensor was required to operate, in order to allow a credible recommendation to be made. The results are reported in Ref. 1. In parallel, the analysis of various candidate sensor concepts was undertaken, with the goal of identifying sensors most suited to the program requirements.

The emphasis during this study was on the requirements of a retrofit design. To be viable as a backup or an alternative, a sensor was sought that would satisfy the accepted ST science requirements while providing more flexible performance characteristics than the baseline approach. The "best" design was considered to be one that would have the least effect on the overall ST program, should conversion be required. The sensor should be conceptually and operationally simple, pose reasonable requirements for integration into the present spacecraft, and introduce minimum cost and schedule perturbations.

Six approaches were examined during the course of the study:

1. Software enhancements to the baseline system;
2. An optical splitter that would divide a star image into four separate beams, which then would be routed to the existing FGS photomultiplier tubes, generating signals to be used in a quadrant detection scheme;
3. Image dissector tubes, operated essentially as star trackers, but using ST optics instead of the normally smaller star-tracker imaging system;
4. Solid-state scanned arrays operated the same way as described for item 3;
5. A microchannel plate, operable either as an array sensor or in a quadrant anode configuration;
6. An electrostatically focused Digicon sensor operated as a quadrant detector but with the possibility of using a detector configuration having an outer "guard ring" for coarse control.

Our studies showed technically plausible ways in which each approach could be used in the system. However, on the basis of current information, the electrostatically focused quadrant Digicon (EFQD) marketed by the Electronic Vision Systems Division of Science Applications Inc. is the sensor that best fits the guidelines and constraints appropriate to a retrofit design.

Software interferometer enhancements offer substantially improved performance without hardware modification but can be undone by an unforeseen flaw in the basic interferometer design. Further, it is not clear that extensive software modifications and additions are to be preferred over hardware changes. Prismatic optical splitters offer potentially excellent performance and are conceptually simple both in design and system integration; however, test model splitters with acceptable characteristics have yet to be fabricated. Accordingly, proof of concept has not been demonstrated, and their true performance capabilities and their fabrication, mounting, and alignment requirements have not been determined. Solid-state scanned array sensors are attractive and may well be the sensor of preference for future pointing control applications, but they have not yet demonstrated the background of flight usage and qualification desirable in a retrofit or backup application. Microchannel plates are almost too sensitive for the SI application; awkwardly large image sizes are required to disperse the guide star image over a large enough area to stay within the count-rate limitations of current devices. Image dissectors have an extensive history of space applications and could be suitable but are substantially more difficult to integrate in a retrofit design than other choices.³

The electrostatically focused Digicon is a structurally and operationally simple device that can operate at 40 Hz (the existing, and difficult to alter, fundamental sampling rate within the SI control system) on 14.5 m⁻² guide stars (the desired dim-star limit) with noise equivalent angles in the 0.003 arc-s range. The Digicon operates by electrostatically accelerating electrons emitted from a photocathode, after which they impact on a silicon diode detector array, generating hole-electron pairs at the rate of one pair per 3.6 eV of photoelectron energy. Because an accelerating potential on the order of 16 kV is used, several thousand electrons are ultimately collected, amplified, and used in pulse generation and shaping circuitry to allow photon counting to be performed. Figure 1 shows the basic Digicon device together with a diode array appropriate for a guidance application similar to that for the SI.⁴

Work to date in the program shows the Digicon sensor to provide the best available match to the guide lines. Considerably more complex magnetically focused versions have been developed and space qualified for use on the SI in the Faint Object Spectrograph and the High Resolution Spectrograph. The use of inner/outer diode clustering (Fig. 1) allows a wide (5 arc-s) instantaneous field of view (IFOV) for acquisition, compared with the 3 arc-s IFOV in the baseline system, yet permits the use of a narrow (0.5 arc-s) IFOV for fine lock. This feature reduces sensitivity to background noise

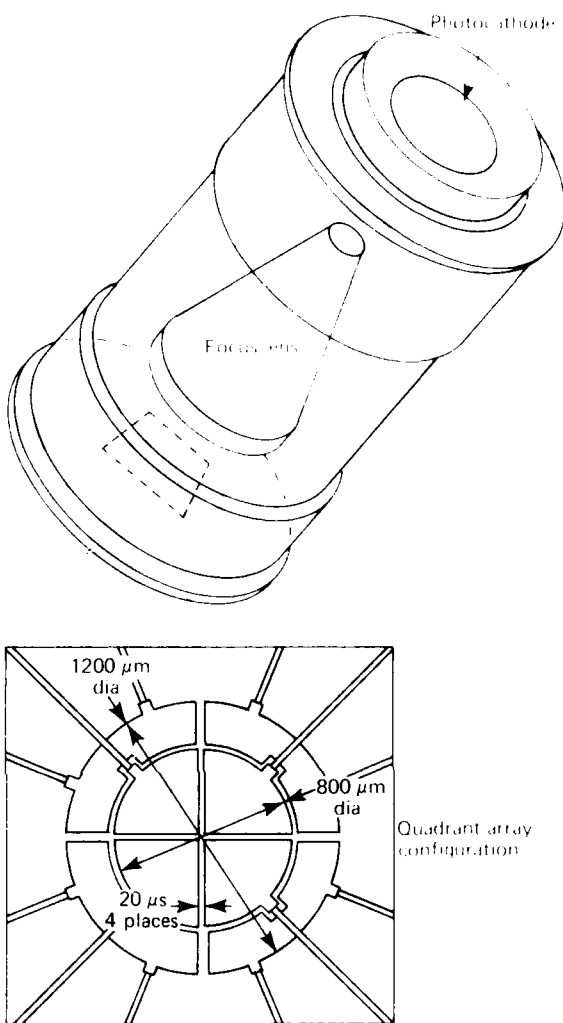


Figure 1 — The quadrant Digicon

and extraneous stars and has advantages for astronomy as well as for guidance.

Sensor Performance

All of the sensors considered in this study produce, or can be configured to produce, an error signal of the type shown by the dashed line in Fig. 2. Its important features are the essentially linear range about a region near the origin and a nonlinear transition to a limiting value of ± 1 far from the null position. This high signal limiting contrasts with the nominal Koesters interferometer characteristic (the solid line in Fig. 2), which returns to a low signal limit at large displacements. Both curves in Fig. 2 depict typical measured data for the two sensors shown.

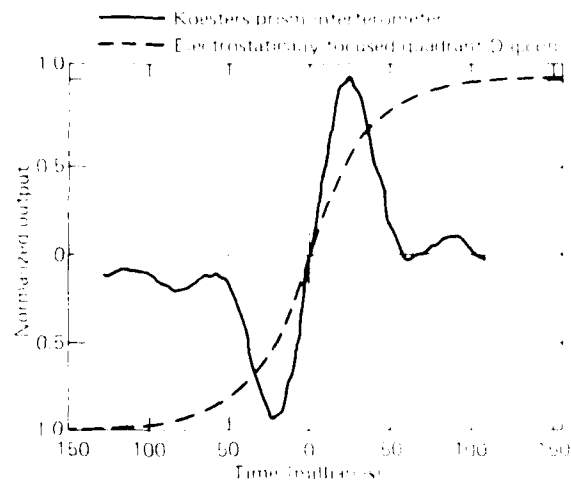


Figure 2 — Characteristic response of the KPI and EFOQD systems.

In the example in Fig. 2, the advantages of control system design are obvious; if the system is perturbed to, or is initially at, a position far from the desired null, appropriate directional information for error correction is still obtained. This characteristic allows a control scheme to be developed that is of a classic "bang-bang" form far from the origin and that provides a response proportional to the error near the origin. It allows good performance in fine lock while at the same time providing robust behavior in the presence of major disturbances.

Because the Koesters prism interferometer (KPI) has such a narrow useful range, a rather complex and very time-consuming guide star acquisition sequence is required. The sequence is modified for a sensor such as the Digicon, and portions of it (e.g., "coarse track") are deleted entirely, to be replaced by an API-designed "transition mode." The new scheme allows an extremely rapid guide-star acquisition sequence to be developed that is substantially more robust in the presence of effects such as photon noise and binary stars than is the baseline system. Figure 3 shows a typical acquisition sequence.

The control system performance in fine lock with the Digicon was assessed by means of a single axis simulation model of the SI, including the effects of EG8 and pointing control system dynamics, telescope flexible body modes, guide star quantum noise, motor whine/noise, rate gyro noise, and other effects. The model is derived from one originally developed at NASA Goddard Space Flight Center, and modified and adapted to meet the requirements of this study.

Various comparisons of the EFOQD sensor and the KPI were made. In the ideal case of noise limited

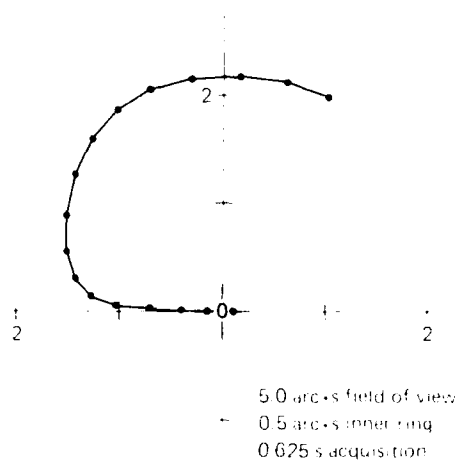


Figure 3 — Typical guide-star acquisition sequence.

operation, the simulation shows the two systems to be essentially equivalent, with a root mean square pointing jitter of 0.0042 arcsec for the EFOQD and 0.0045 arcsec for the KPI. (These results are intended for sensor comparisons only and should not be taken as an indication of a realizable overall SI pointing capability because many potential disturbances are not modeled in the simulation.) The EFOQD, as expected, provides substantially more robust control than the KPI in the presence of severe disturbances (e.g., thermal "creaking" of the structure). This is shown in Fig. 4, where response to a sudden boresight shift is plotted for both.

Sensor Design and Integration

System integration studies to establish the requirements for using the retrofit alternate sensor design in the baseline EG8 were undertaken as part of the program at API. The design involved the replacement of certain elements of the EG8 optical train (Figs. 5 and 6). Figure 7 shows one of the three EG8 assemblies in the baseline configuration; the encircled area shows the equipment to be removed and replaced by the alternate sensor. It is seen that the effects have been confined to a very small area of the SI. For reference, Fig. 8 shows the SI and indicates the location of the EG8 assemblies, which are designed to be orbit-replaceable units.

Many significant issues had to be addressed in this study to allow a credible recommendation to be made. Specific topic requirement attention included

1. Digicon space qualification.

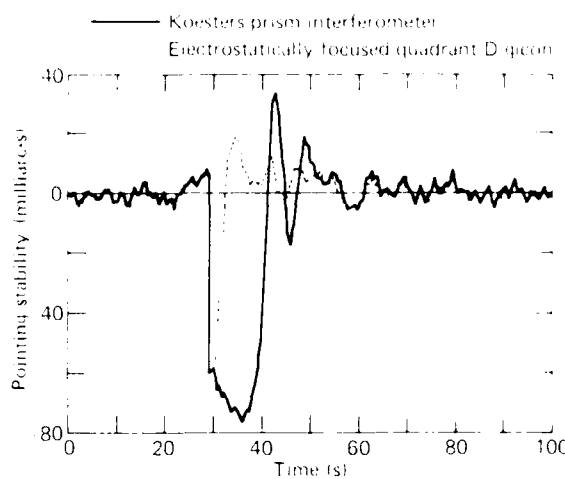


Figure 4 — The response of the KPI and EFQD sensors to a sudden boresight shift.

2. Magnetic field sensitivity and shielding requirements;
3. Availability of flight-qualified high-voltage power supplies;

4. Digicon count-rate limiting effects for bright guide stars;
5. Sensor lifetime and aging;
6. Design and fabrication of low-noise preamplifiers;
7. Cosmic-ray effects and radiation hardening;
8. Mass, volume, and mounting area constraints for an alternate sensor;
9. Power availability and requirements;
10. Thermal control requirements and system modifications;
11. Software/firmware modifications and interface requirements;
12. Imaging optics requirements and design.

In contrast to the interferometer, the alternate sensor design requires that a real star image be formed and thus necessitates the use of a re-imaging system ahead of the Digicon. The required analysis was provided by David Grey Associates under subcontract to API.⁷ Many of the sensor-related topics were addressed by the Digicon vendor, also under subcontract,⁸ while the system integration issues were examined by the API staff. All were favorably resolved,

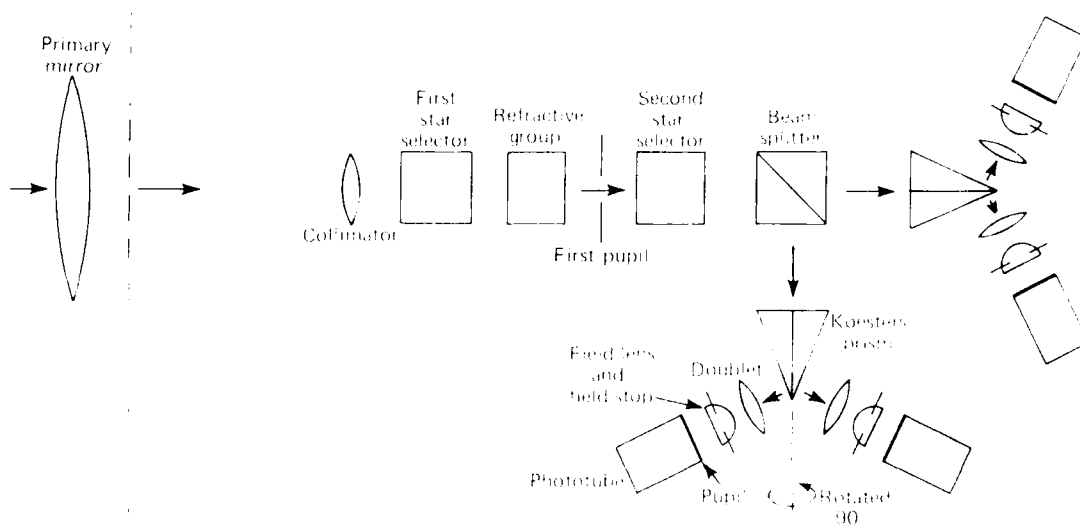


Figure 5 — Diagram of the KPI

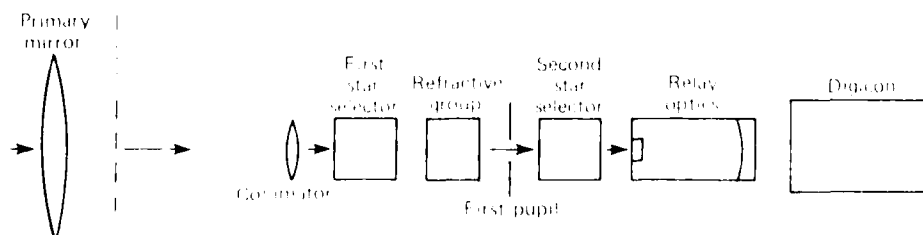


Figure 6 — Diagram of the alternate sensor

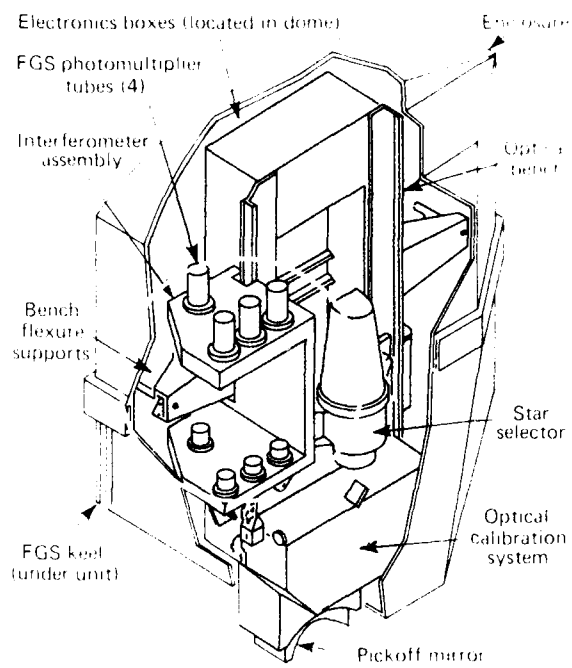


Figure 7 A fine guidance system assembly in the baseline configuration

with the result that high confidence exists in the viability of the Digicon based alternate fine guidance system, if no cue should be required.

ACKNOWLEDGMENTS

The work reported here is the product of many API staff members in addition to the principal authors. We take this opportunity to acknowledge the contributions of L. B. Coughlin, L. R. Dettmer, M. D. Eustis, R. L. Gold, G. A. Heyler, B. Hochheimer, B. E. Hottman, J. W. Hunt, D. Mehoke, F. L. Mobley, J. L. Mueller, A. J. Pue, J. C. Ray, W. E. Skellney, K. Strohbehn, R. M. Sullivan, C. A. Twigg, and C. A. Wingate. We also wish to acknowledge our Principal Investigator for this work, W. G. Fastie of JHU's Homewood campus.

REFERENCES

¹M. D. Griffin, L. L. Strickwerda, and D. G. Grant, *Space Telescope System Study Report*, JHU/APL SDO 6941 (Nov 1983)

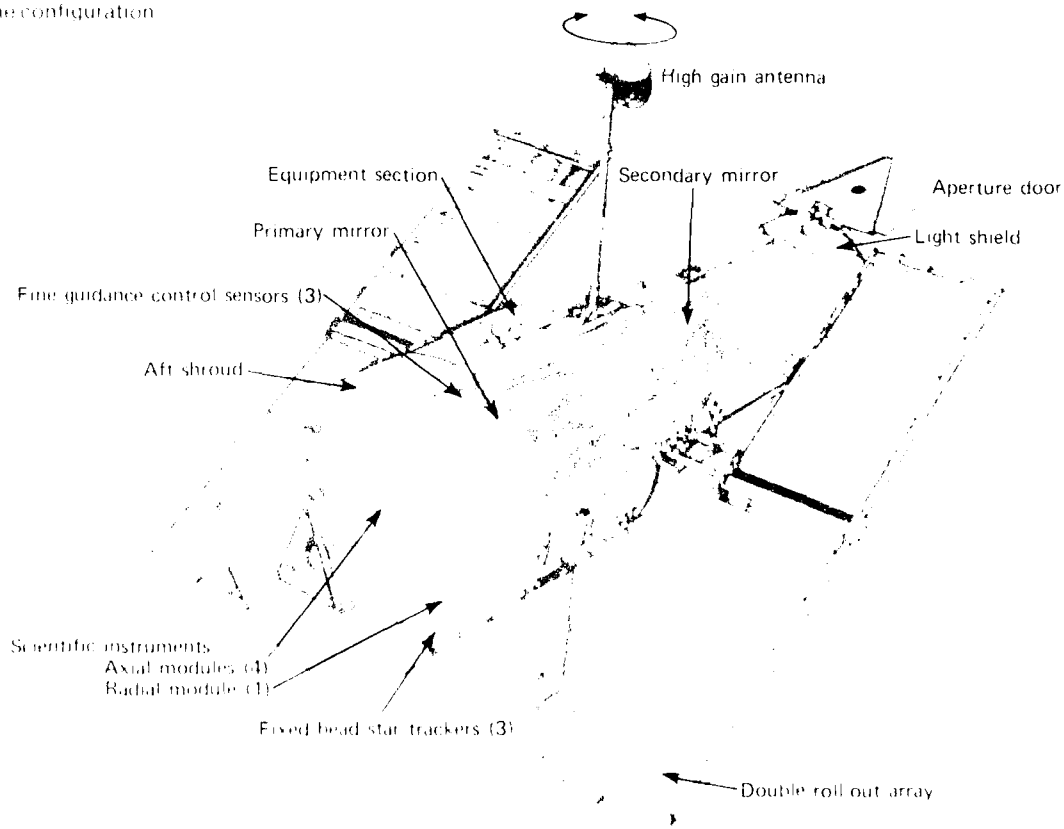


Figure 8 — The Space Telescope configuration

- M. D. Cuffman, T. E. Strikwerda, and D. G. Grant, *Space Telescope Alternate Fine Guidance Sensor Design Study*, JHU/APL SDO-7083 (Nov 1983).
- T. Wilcox, *Space Telescope Fine Guidance Sensor Study*, TEL, Ft. Wayne, Ind., Subcontract 601911 (2 Sep 1983).
- R. O. Omaviv, L. E. Acton, R. D. Smith, F. G. McCoy, D. G. Currie, and F. A. Beaver, "Performance of a Diagonal Photon Counting Autoencoder System," SPIE 8th Symp. on Photoelectric Image Devices, London (5-9 Sep 1983).
- A. T. Puc, *Description of the Space Telescope Three Axis Control System, and Some Sample Data Analyses*, JHU/APL SDO-7043 (Nov 1983).
- K. Strohschein and M. D. Foust, *Performance Evaluation of the Koesters Prism Interferometer and Alternate Sensors for the Fine Guidance System of Space Telescope*, JHU/APL SDO-7098 (Nov 1983).
- D. Grey, final report submitted to the Applied Physics Laboratory (Oct 1983).
- R. O. Omaviv, *Fine Guidance System Diagonal Study*, final report, SMC Electronic Vision Systems Division, San Diego (11 Oct 1983).

This work was supported by the NASA Marshall Space Flight Center.

NASA GROUND TERMINAL FAULT ISOLATION AND MONITORING SYSTEM

**D. E. Buchholz, A. J. Cote, Jr.,
and P. J. Grunberger**

NASA is replacing most of its Spaceflight Tracking and Data Network of ground stations with two Tracking and Data Relay Satellites operating at synchronous altitudes and a single ground station situated at White Sands, N. Mex. The Tracking and Data Relay Ground Segment (TDRS-GS) of the ground station provides the interfaces between the satellites and the network. The NASA Ground Terminal provides the interfaces among the TDRS-GS, NASA Communications (NASCOM), and the Network Control Center at the NASA Goddard Space Flight Center.

API was given the responsibility for designing a Fault Isolation and Monitoring System as part of the Ground Terminal to provide qualitative and quantitative assessments of the communication between the TDRS-GS and the Network Control Center. Monitoring takes place both before and after the interfaces to the NASCOM lines. API's effort included the development of all the software and the fabrication of some of the subsystems in the facility. The installation of the system was completed and the final software package was delivered in November 1982. The system is now in routine use.

DISCUSSION

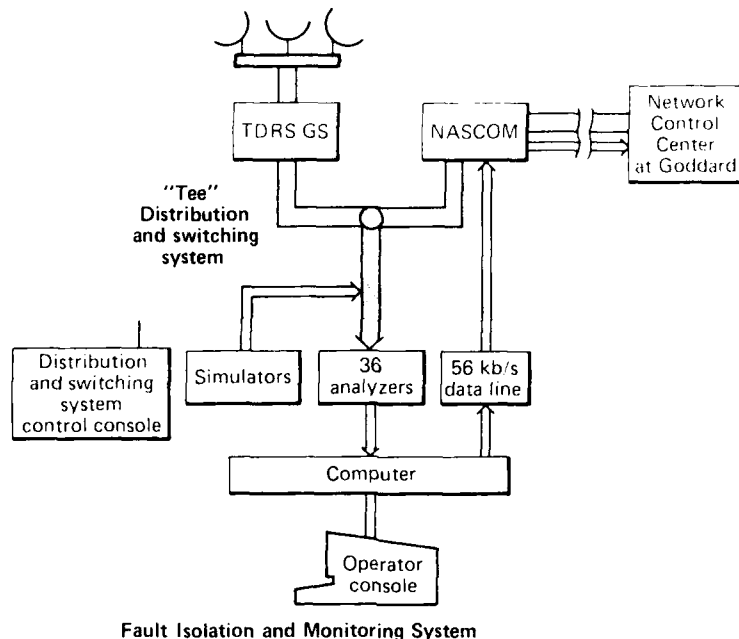
Figure 1 is an overview of the Fault Isolation and Monitoring System. All data to be analyzed enter through the distribution and switching system via a "tee" con-

nexion in the main data path between the Tracking and Data Relay Ground Segment (TDRS-GS) and the NASA Communications (NASCOM) data path. The monitored data are routed within the system to the frame analyzer hardware whose outputs are routed to the system computer. There, data are processed for transmission back to the Network Control Center. Data characteristics are observable at an operator console.

Operational Characteristics

Figure 2, an operational view of the system, conveys the data flow and identifies the major files and operational functions.

The system is assigned monitoring tasks by means of schedule messages that originate at the Network Control Center and are sent by the data line. These incoming messages are received automatically and placed into buffers. Receipt is noted in an activity log; the content is extracted, placed into an administrative message file, and printed at the operator's option. This reception process is automatic and includes an alert to the operator console indicating arrival of the message. A communications service available at the operator console permits access to the activity log, the alerts table, and the content of the administrative message file.



Fault Isolation and Monitoring System

Figure 1 — The Fault Isolation and Monitoring System.

Assignment messages identify the data links to be monitored, the time span of the monitoring, the data stream characteristics, and other information, as required. Initial analysis of the data stream is performed by the frame analyzers, each of which is connected to its assigned stream by the distribution and switching system. The connections between analyzers and streams are not fixed but are established by means of the control console as needed to support a particular mission's monitoring requirements.

Each frame analyzer is "set up" or initialized from the operator console to ensure compatibility with the data stream and to establish the range and character of the parameters to be monitored. Files of such setups can be established in advance of a mission and assigned individually or in groups to one or several analyzers, respectively. For example, the frame analyzer can be set to start and stop automatically at specific times to encompass a particular data stream support interval.

Frame analyzers produce packet reports that are processed and analyzed automatically to generate dynamic and pass summary reports. Dynamic reports, which convey the state of the stream at 5-s intervals, can be transmitted automatically back to the Network Control Center as they are received. The operator can examine both types of reports at his console as they are generated during the course of the mission.

A dynamic report contains nine items of information, including the state of the monitoring analyzer, a count of good frames received, a count of expected frames, and the bit error rate. A pass summary report has eight items, including the total of good frames received, the percentage of good frames, the times of initial acquisition of signal and last loss of signal, and the bit error rate.

Equipment Configuration

Figure 3 is a detailed view of the equipment configuration. The data streams are allocated to the analyzers by two types of switches that comprise the distribution and switching system. Type 1 handles signals with rates up to 12 megabits (Mb) per second while type 2 supports streams up to 85 Mb/s.

Similarly, there are two types of analyzers: 32 type 1 units (designed and built by APL) and four type 2 units (government-furnished equipment). Type 1 data can be simulated by means of a pulse code modulation (PCM) data generator while type 2 streams are synthesized by simulators built into the type 2 analyzers.

All the analyzers are interfaced through a data communications multiplexer to a minicomputer that hosts the operational software. The host computer has a normal complement of peripherals plus a high-speed data-

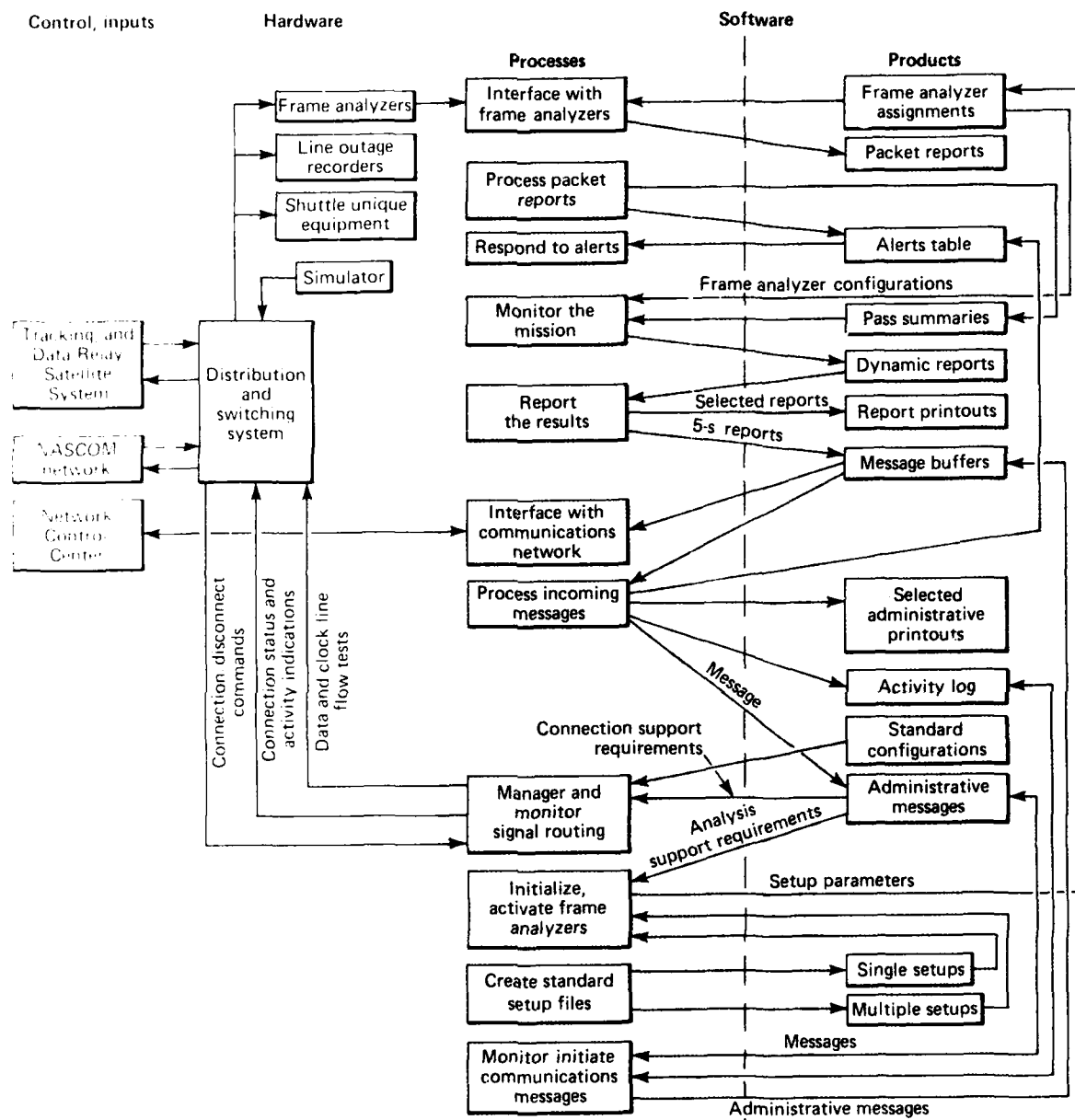


Figure 2 — Operational functions of the system.

set controller that provides the link to the Network Control Center data line.

Software Description

Figure 4 illustrates the role of the software and its interactions with the major hardware elements. Output products of a block on the main diagonal of the figure

are shown on a horizontal line connected to the block; inputs to a block are depicted along a vertical line.

There are four categories of software modules: analyzer, communications, service, and terminal. The concurrent execution of multiple tasks, regulated by task priority, is managed by the computer's operating system. The role of the modules in system operations (Fig. 2) is as follows.

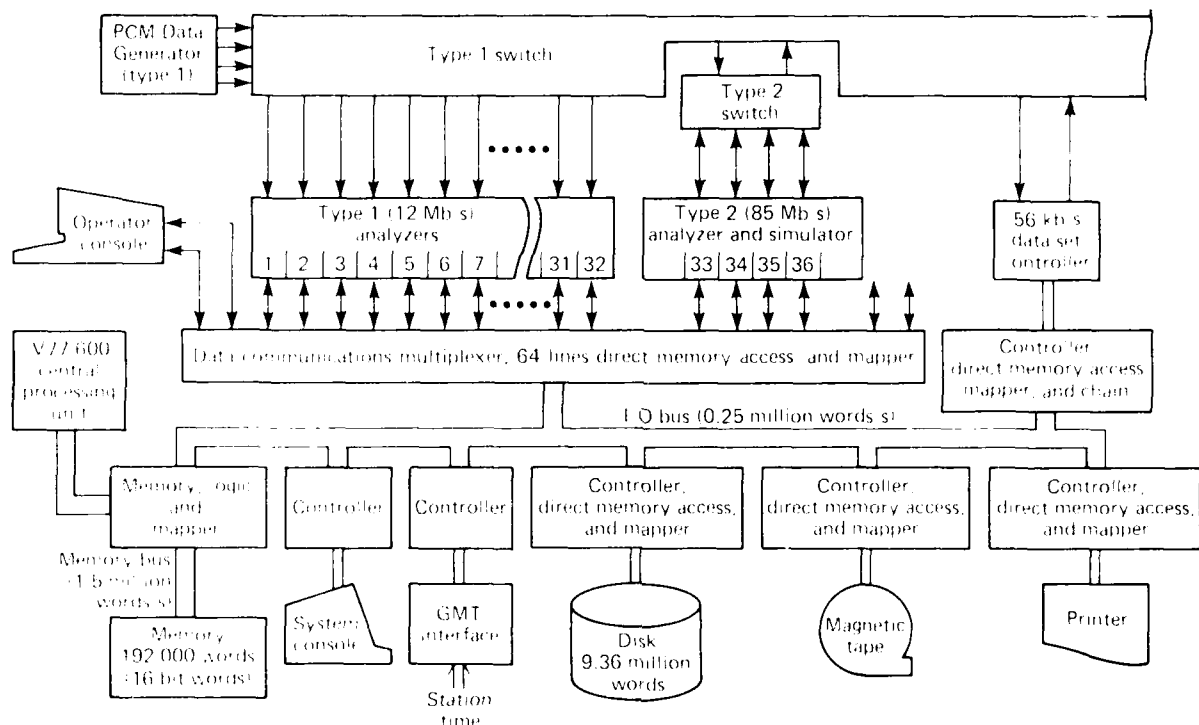


Figure 3 — Details of the equipment configuration.

Administrative messages arrive through the data-set controllers and are transferred to the message buffers. The message content is placed in a file, and acknowledgement and alert activities are initiated. The alert reaches the operator by means of a screen-update program. Within the service console, a separate program manages the keyboard, the screen, and transfers between the host and the console. On the host side of the interface, screen updates originate with one program while another supports the service being used by the operator. Such service support involves managing files and buffer interfaces with analyzer and communications software.

There are five available operator services, and each presents the operator with one or more screen image options. The images share a common field format, with fields for prompts, alerts, error messages, function key labels, and the main data field. An example is shown in Fig. 5, where the main field is split; the right side depends on a selection made by positioning the cursor on the left. Function key labels at the bottom of the screen indicate the current role of certain keys on the operator console. They are used to change the service, the frame within the current service, or the state of the system.

When an operator initializes a frame analyzer using such a service, the service program forwards the sup-

port request to the analyzer software. It then sends commands to the specific analyzer hardware unit that was requested. As the data streams are monitored, all active analyzers are reporting results by putting out periodic packet reports. Those reports are fielded by preposted read requests initiated by the analyzer software. They are subject to further processing to produce the statistics required for the dynamic and pass summary reports. This report composition software sends the reports to the screen and/or the message transmission software, as appropriate.

SUMMARY

The Fault Isolation and Monitoring System provides a measure of the quality of data received from the TDRS-GS. The use of software is a flexible way to allocate hardware resources among the various data streams and to manage the presentation and communication of the various data products.

ACKNOWLEDGMENT

Many individuals contributed to the development of the capabilities described here, including L. Azlin,

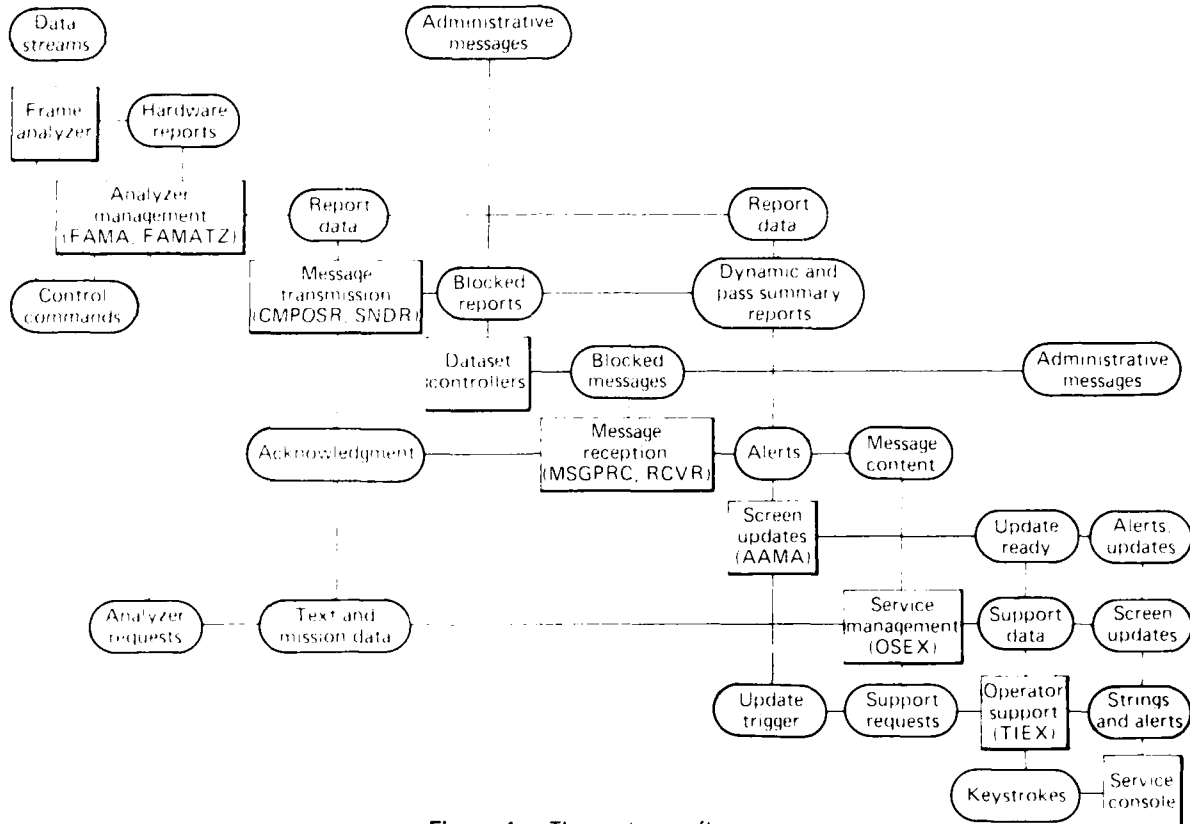


Figure 4 — The system software.

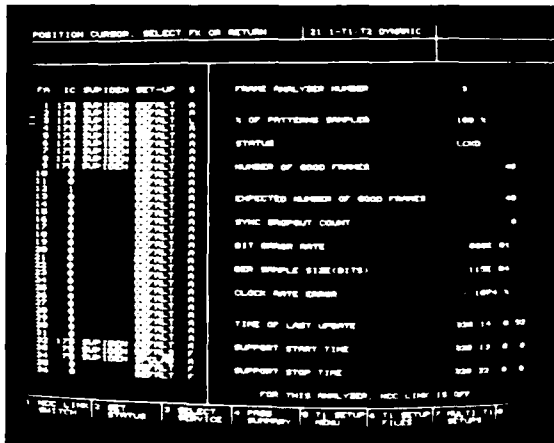


Figure 5 — An example of an operator display.

J. Boyd, C. Brown, P. J. Clark, N. V. Coon, D. B. Friedman, R. J. Heins, J. O. Jackson, E. F. Kiley, F. N. Lee, C. May, T. L. McGovern, R. Mylnarczyk, R. Pacheco, C. T. Pardoe, J. A. Perschy, J. Roche, C. Schroeder, A. Somers, R. T. Stellabuto, G. F. Sweitzer, G. T. Trotter, H. K. Utterback, R. L. Waddell, M. S. Waltrip, and H. D. Zink.

This work was supported by the NASA Goddard Space Flight Center.

REENTRY THERMAL-RESPONSE PREDICTIONS FOR THE GENERAL-PURPOSE HEAT SOURCE

P. T. Brenza and D. W. Conn

The thermal response of the General-Purpose Heat Source was determined for an off-normal orbital-decay trajectory that has been postulated for NASA's mission to Jupiter in 1986. The analysis considered uncertainty factors related to aerothermodynamic boundary conditions and the internal heat transfer characteristics of the structural configuration. The results will be applied within the framework of a statistical error analysis to assess the safety margin of the contractor's design. The design goal is to maintain the containment of the nuclear fuel during the off-normal reentry and the subsequent terrestrial impact.

BACKGROUND

For certain space applications, it is desirable to provide electrical power for the spacecraft by using the energy derived from the decay of radioisotopes. Two current missions that require such power are the Galileo flight to Jupiter and the Solar-Polar flight out of the plane of the ecliptic. To supply the power, contractors for the U.S. Department of Energy (DOE) have developed a new, more efficient Radioisotope Thermoelectric Generator that uses a new fuel module called the General-Purpose Heat Source (GPHS). These modules are designed to keep the radioisotope, plutonium 238, safely enclosed within an iridium clad during exposure to the environments of postulated launch accidents.

Under the aegis of the DOE Office of Special Nuclear Projects, radioactive fueled devices, including the GPHS, receive a thorough safety assessment. The Interagency Nuclear Safety Review Panel, composed of representatives from NASA, DoD, and DOE, review the safety analyses and, at the final review, provide a risk assessment of the mission as a prerequisite to obtaining Presidential approval for the launch. API serves in an advisory capacity to DOE regarding reentry technology. One of API's functions is to make independent predictions of reentry thermal responses for the fuel module.

DISCUSSION

General-Purpose Heat Source

Each Radioisotope Thermoelectric Generator contains a stack of 18 GPHS modules. Figure 1 shows the major components and indicates how they are installed

in the aeroshell. The overall dimensions of the module are 9.72 by 9.32 by 5.31 cm, its mass is 1.443 kg, and the four fuel pellets produce a total of 250 thermal watts of energy. The aeroshell, impact shells, and floating membranes are fabricated from a three-dimensional carbon-carbon composite. The insulators are fabricated from a carbon-bonded carbon-fiber (CBCF) material, and the clad is made of iridium. Each module is designed to reenter the earth's atmosphere independently and, upon impact, keep the radioisotope contained or immobilized.

Potential Reentry Failure Modes

The assessment of the reentry safety performance of a device such as the GPHS indicates that the failure modes that can be postulated to lead directly or indirectly to a fuel-containment breach are heat shield ablation burn through, heat shield stress failure, melt of the containment shell, and impact fracture of the containment shell. The latter mode has long been identified as the critical failure mode for GPHS and is the focal point of this article.

The critical component of the design from the standpoint of impact fracture is the iridium clad that contains the fuel. The ability of the clad to accomplish the design purpose depends on both its peak temperature during reentry and its temperature at the time of impact. The amount of time at which it is near peak temperature affects the grain structure of the material, while the impact temperature determines the degree of ductility. These factors relate to the ability of the iridium to absorb energy without fracturing in a dynamic loading environment.

Reentry Trajectory

Of the many possible reentry trajectories that result from postulated accident scenarios, orbital decay is the most probable; it also leads to one of the more critical temperature histories for the iridium clad. Therefore, the performance of the module during reentry along that trajectory is evaluated carefully at the safety reviews. In the initial portion of an orbital-decay reentry, aerodynamic heating generated during hypersonic-supersonic flight soaks into the interior of the module and increases the temperature of the clad. Later, flight in the subsonic regime causes the aeroshell to cool down and results in heat leakage from the clad, thus reducing the temperature. The temperature of the clad at impact has been the focus of an extensive sensitivity analysis with the objective of as-

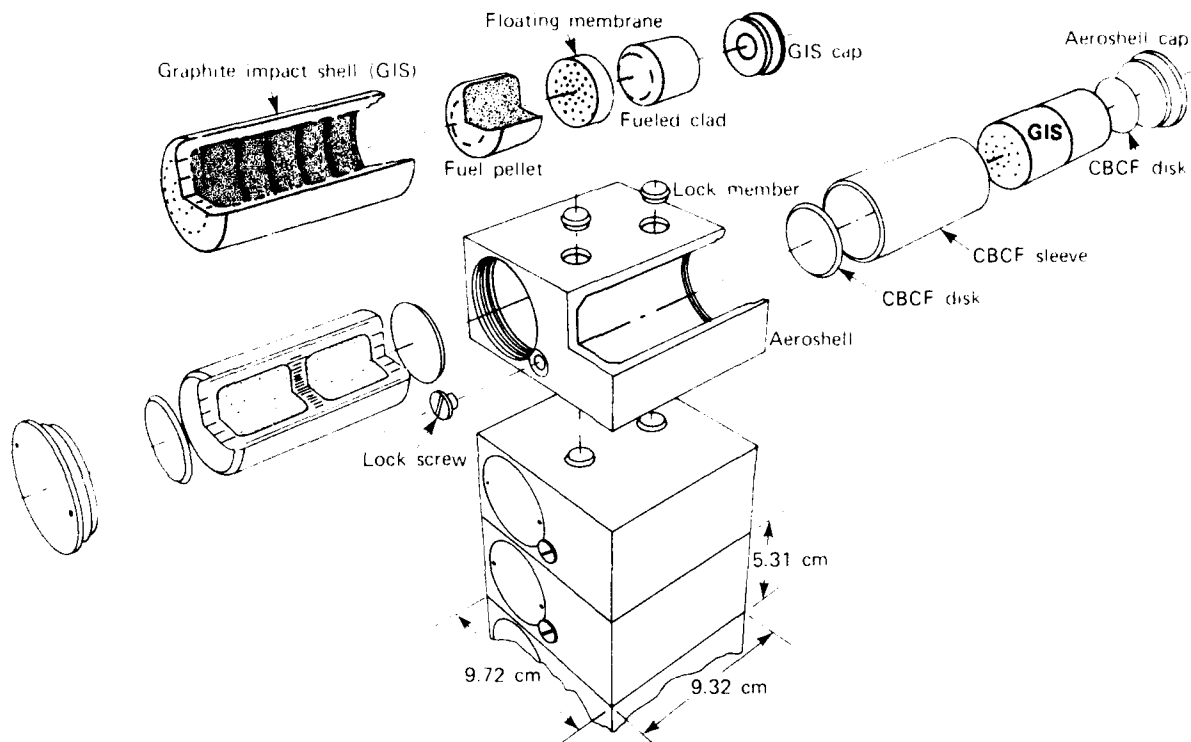


Figure 1 — The General-Purpose Heat Source

sessing uncertainties associated with the reentry environment and the GPHS design.

Thermal Response Sensitivity Analysis

The analysis involved two major steps. First, the thermal response of the GPHS was determined on the basis of aeroheating, material properties, and internal heat-transfer assumptions that were used by the design contractor. The results served as baseline values for the sensitivity analysis. Next, the sensitivity analysis was performed; the principal factors that affect the thermal response were varied individually to determine the significance of each.

The most exhaustive task in the analysis was the development of the thermal model, which is a computer representation of the transient heat-flow paths through the module and a description of the surface boundary conditions. Although the model takes advantage of the technique of using the geometrical symmetry of the configuration to minimize the grid size, approximately 850 nodes were needed to describe mathematically the thermal characteristics of a one eighth section of the module. To give an appreciation of the details included in the model, nearly two hours of IBM 3033 computer time are consumed for a single analysis (the evaluation of one in-

certainty factor based on the selected reentry trajectory that has a flight time of about 500 seconds).

To date, we have examined the significance of the uncertainty for 16 factors, including aerodynamic heating, thermal conductivity of the insulators, internal thermal contact between mating components, internal thermal radiation and gaseous conduction, and the effect of a stable versus a randomly tumbling module.

A typical result is shown in Fig. 2 for the case of a 50% uncertainty in the transient aerodynamic heating rates. The larger convective heat-transfer coefficients for the early period of the reentry when the module is traveling at hypersonic-supersonic velocities results in an increase of about 120° F in the peak temperature of the iridium clad. If the assumption is made that the uncertainty applies only to the latter portion of the reentry (the subsonic flight regime), the temperature of the clad at impact will be 60° F colder than the baseline value because the aerodynamic convection is cooling rather than heating the surfaces of the module.

Another result is shown in Fig. 3. That analysis assumes that the GPHS module reentered in a stable attitude so that the broadside was continually exposed to the severe windward convective heating rates. For the baseline analyses, the module was assumed to be tum-

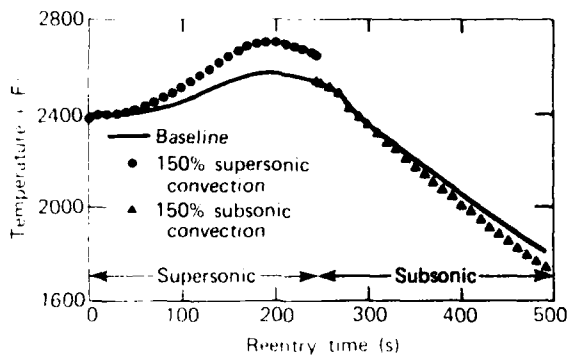


Figure 2 — Clad temperature, baseline versus 150% heat convection

bling randomly during the hypersonic-supersonic portion of the flight; thus, the severe convective heating rate was uniformly distributed over the total surface area. The temperature history of the surface that views the severe heating rates shows temperatures significantly higher than the baseline values. The higher temperatures caused the surface to act as an efficient radiator because radiative heat transfer is directly proportional to the fourth power of temperature. The net effect was that less heat soaked into the interior of the module during the hypersonic-supersonic portion of the flight, resulting in a colder temperature profile (peak temperature) for the clad. The temperature of the clad on impact, however, was nearly unchanged from the baseline value because the surface boundary conditions during the subsonic portion of flight were the same.

CONCLUSIONS

We have concluded that the sensitivity analyses that determine the thermal response of the GPHS to un-

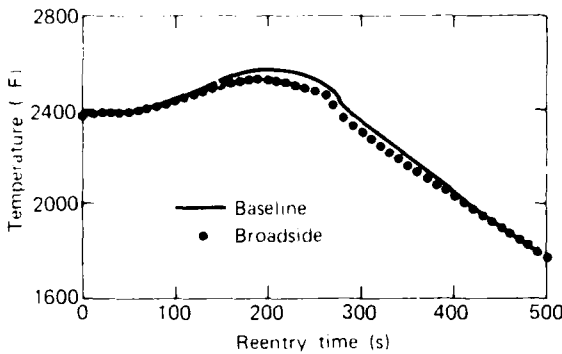


Figure 3 — Clad temperature, baseline versus broadside stable

certainty factors are a useful tool for the safety reviews. These analyses revealed the factors, such as convective heating rate, that are critical to the reentry thermal performance and revealed those that are not, such as the conductivity of the heat shield material. As a result of these conclusions and to ensure that the thermal response is predicted as accurately as possible, the values of the critical factors become the subject of closer scrutiny, first through more refined theoretical treatments and later, if necessary, through experimental verification. In addition, the completed package of results forms the framework for a statistical error analysis that can be used to assess the safety margin built into the GPHS.

This work was supported by the Department of Energy

COMPUTER TECHNOLOGY

INTRODUCTION

Computing technology at APL is an essential, integral element of all technical, systems, and administrative functions. The computer is so necessary to scientific achievement that the scope and magnitude of its contributions to space science, medicine, energy research, naval fleet defense, missile guidance, and other problems of national importance are often lost in the rigors of daily computer implementation activities. Yet the importance of the computer at APL with its myriad technologies and applications cannot be overemphasized. To this end, the Laboratory conducted a major review and assessment of computing capabilities and requirements for the future. Several areas that received particular attention include intelligent work stations, data networking requirements, central computing facility user groups, Class VI computing effort with the impending acquisition of a Cray 1M system, and technical planning, policy, and coordination of computer systems.

Extensive computational facilities maintained by the Laboratory for use by its scientists and engineers include a major digital computer; an integrated computer-aided-design/computer-aided-manufacturing (CAD/CAM) system; analog/hybrid computer laboratories; a computer-based image processing system; rapid real-time data reduction systems; five major stand-alone computer-aided-engineering workstations for electronic design; and hundreds of special-purpose computers, word processors, and computer-controlled data acquisition systems.

The central digital computer facility consists of an IBM 3033 multiprocessor with high-speed, large-scale, dual data processors. The 3033 uses a virtual memory operating system that accesses a 16 million byte main memory and up to 115 billion bytes in auxiliary direct access storage (disk and mass). The central computer serves a wide variety of tasks, including large-scale simulations, complex analyses, and data processing and reduction. The 3033 and its associated computers in the linked APL computer network provide extensive facilities for interactive real-time processing, image processing, large data-base transfers, advanced graphics processing, and resource sharing.

The Computervision CAD/CAM system has provided APL with a modern design, drafting, and manufacturing capability. It is a flexible system, providing three-dimensional design capability for mechanical, electrical, and electronic systems. Output from the system, in addition to the normal hard copies, includes photoplotted master masks and numerically controlled machine tool tapes. Resident system software, along with data links to larger computers, can provide design analyses including finite element modeling, logic simulation, and design rule checking. Stand-alone computer-aided-engineering stations, such as the Mentor Graphics System recently installed in the CAD/CAM center, are providing the Laboratory with the capability to do complex electronic circuit design, simulation, and test vector generation necessary for the fabrication of gate arrays, standard cell chips, and (ultimately) full custom integrated circuits.

API also supports two analog/hybrid computer laboratories: the Interactive Simulation Laboratory with EAI 680 analog computers and the Guidance Systems Evaluation Laboratory with the EAI Pacer 600 system. Analog and hybrid computations are essential to the solution of complex problems that require the simultaneous solution of a large number of differential equations. The hybrid laboratories provide simulations for large physical systems and are particularly useful in the missile and missile-guidance fields.

Because computers and computer applications at API are so interwoven with all Laboratory activities, it is impossible in a limited section to provide articles addressing all the yearly accomplishments in this field. The selected articles represent the generic type of activities that one may find in all parts of the Laboratory. They range from special-purpose processors, emulators, hardware, and data information facilities through standard modeling and simulation activities to specialized graphical outputs and even the solution of problems at the graphics level. This trend toward specialized computers—especially engineering workstations, novel methodologies, and emphasis on graphical display and interaction—is expected to continue.

IMPLEMENTATION OF A SAR PROCESSOR ON A VAX 11-780/EPS-164 SYSTEM

B. L. Raff, R. N. McDonough, and J. L. Kerr

A digital synthetic aperture radar processor has been developed within API for both satellite and air craft applications. The processor was implemented on a VAX 11-780 host computer with an EPS-164 attached processor, having been designed to maximize the use of the computational power, large memory capacity, and associated disks of the EPS-164. Care was taken to develop the source code in a sharable modules for synthetic aperture radars of different characteristics. The basic processing functions and their implementation on the EPS-164 are described briefly.

BACKGROUND

The digital production of images from synthetic aperture radar (SAR) signal data requires the implementation of a complex program on a high speed computer system having an extensive fast memory and bulk storage capacity. In the fall of 1982, the Laboratory undertook the development of such a capability for processing SAR data. There was available a dual-processor system that gave promise of meeting the objectives. It consists of a Digital Equipment Corp. VAX 11-780 computer with a Floating Point Systems EPS-164

attached processor. The EPS-164 is a high-speed, pipelined array processor with a large internal memory (1.7 million words of 64 bits each) and a disk storage system of 67 million words capacity. An extensive vector oriented math library and program development software are available. The system has the capability for overlapped processing in both computers, a feature that is particularly advantageous during tape and disk input-output operations.

DISCUSSION

Figure 1 shows a digitally processed Seasat scene near the Goldstone Tracking Station in the California Mojave Desert. The bright reflecting object is the SAR image of a 26 m antenna. The antenna is so bright relative to its surroundings that it is easy to trace its signature through the various phases of the processor. The figure was generated by performing a two-dimensional correlation of the SAR echo data with a reference function that is the theoretical SAR point-target response. The point-target response function is simply the radar-transmitted waveform along the range dimension and

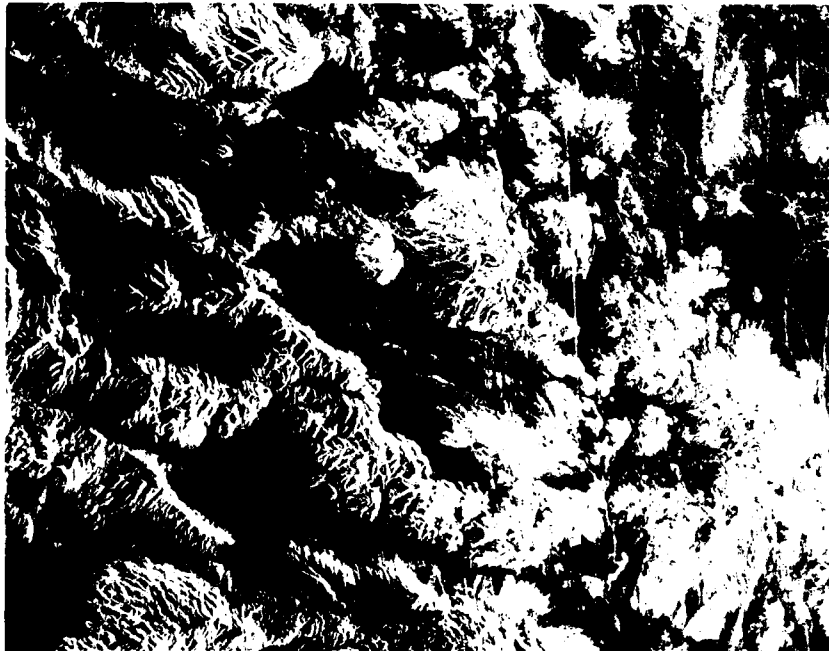


Figure 1 — SAR image showing the Goldstone antenna at upper center.

the point target phase history along the azimuth dimension.

Consider the correlation process in the range dimension, commonly referred to as "range compression." A radar pulse emitted at some transmitter location x is scattered by a point target on the earth's surface and received after a time delay that depends on the slant range r . In the common case of a transmitter pulse with a linearly swept frequency, the received waveform is

$$h(t, \nu) = \cos 2\pi [f_c(t - 2r/c) + (K/2)(t - 2r/c)] \quad (1)$$

where f_c is the carrier center frequency, K is the "chirp" constant, and c is the speed of light.

The result of range compression is illustrated in Fig. 2. The actual time waveform of the received reflection from the Goldstone antenna for one radar pulse is shown in Fig. 2a; the result of correlation with the transmitted waveform is shown in Fig. 2b. The correlation process is actually carried out by "fast" convolution, in which the inverse Fourier transform is taken of the product of the Fourier transforms of the reference function and the data. The antenna signature of Fig. 2a is thus compressed to the pulse of Fig. 2b. Note that the compressed range data for each pulse are really complex data - of the form $\exp(4\pi\nu^2/\Delta)$ - that exhibit the phase history of the target in terms of the slant range at each pulse. Ideally, the next step is to compress the data along the flight ("azimuth") direction. However, before this compression can be accomplished, it is necessary to adjust the data to account for a process called "range migration."

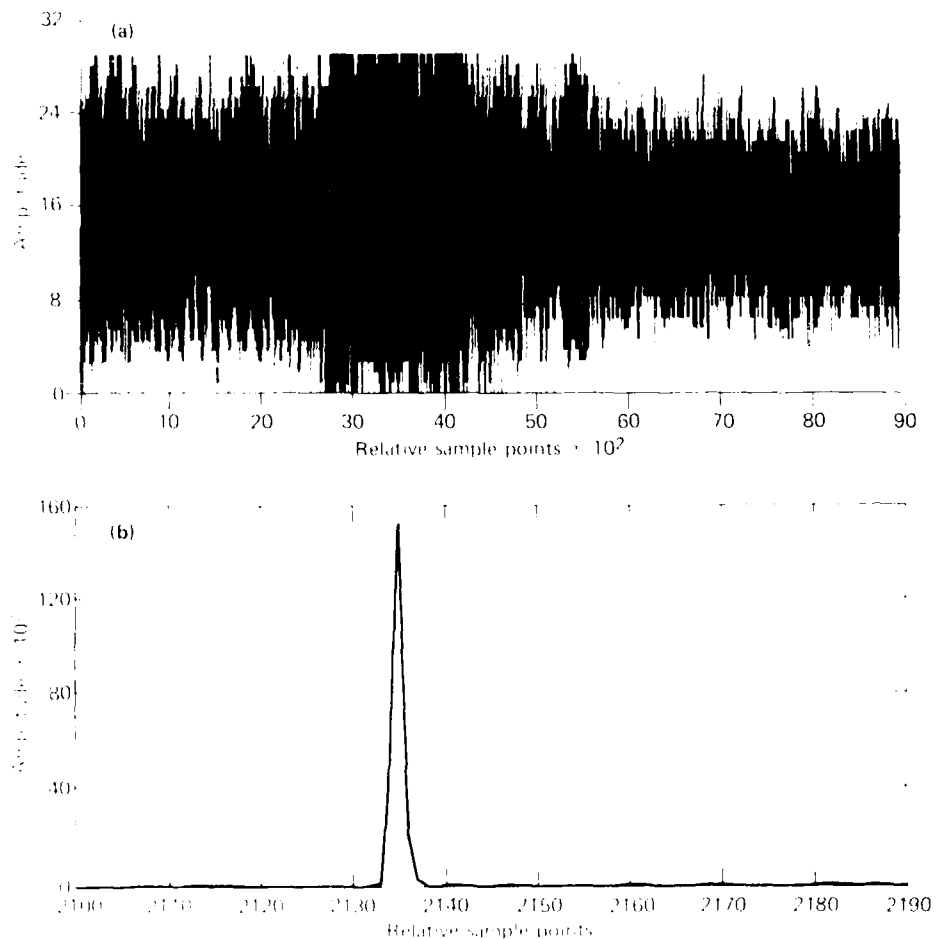


Figure 2 — The results of range compression: (a) Received reflection of the Goldstone antenna; (b) The Goldstone antenna target after range compression.

The slant range of a point target is approximately a quadratic function of the time τ along the flight path:

$$r - r_0 = (\lambda f_{Dop} / 2)(\tau - \tau_0) + (\lambda K / 4)(\tau - \tau_0)^2, \quad (2)$$

where r is range, τ is time, f_{Dop} is Doppler frequency (at the time the target is in the center of the radar beam), K is the rate of change of Doppler frequency with τ , and λ is radar wavelength. The linear term in Eq. 2 is called the "range walk," and the quadratic term is called the "range curvature." The total effect, range migration, represents movement of the point target response across range bins in the computer memory as τ varies. It is convenient to remove the range-walk term during the range compression process and to deal with the range-curvature term during the azimuth compression process. When both of these effects are compensated, data are more conveniently available in memory for correlation in the azimuth coordinate.

For machine implementation, data are transferred pulse by pulse to the array processor. For each range line (one pulse), the array processor performs the process of fast convolution and range-walk removal. The range-line data are stored in the array processor until 128 range lines have been accumulated. The block of 128 complex-valued, range-compressed lines is partitioned along the azimuth direction and written into 64 or more separate files on the four disks until 8192 range lines have been compressed and stored. At that point, each disk file contains 64 azimuth lines, each line consisting of 8192 data points in the τ coordinate. Dividing the range lines into sections and storing them in multiple disk files in effect performs a "corner turning," or matrix transposition, on the data. The size of each disk file, 8192 by 64 range cells, is governed by the memory available when one disk file is read in for azimuth compression. The number of range bins available at this stage of the processing is also convenient for performing the quadratic range correction.

After the corner turning has been performed, data are easily accessible along the time or azimuth coordinate, and the azimuth compression procedure can commence. Azimuth compression is completely analogous to range compression, as can be seen from the quadratic phase history corresponding to Eq. 2, and the fast convolution process is used again. However, it is first necessary to assemble the Fourier transform of the data along the azimuth direction. This assembly is done by removing the effect of the remaining range migration error on the spectra of azimuth lines. When appropriately corrected, the target energy appears only in one range bin. Azimuth compression then consists of multi-

plying the assembled data transform by a matched filter, thereby producing the final image response.

The generation of the azimuth compression filter requires knowledge of the azimuth chirp rate, K_A , the coefficient of the quadratic term in Eq. 2. Actually, K_A is often not known a priori to sufficient accuracy and must be estimated from the data. Currently, the so-called subaperture correlation method is used; it was found to work well even for oceanographic imagery.

Before the final image is assembled, the multilook process can be performed. With Seasat, which is typical of SAR designs, the synthetic aperture is longer than is required to generate the desired azimuth resolution. It is therefore possible to divide the synthetic aperture into several subapertures, or "looks," that can be compressed independently along azimuth, detected, and summed in order to reduce the SAR speckle noise in the final image. Figure 3 illustrates multilook processing. The overall azimuthal target spectrum has been processed independently by four compression filters, producing the four independent realizations shown of the image. Those realizations are simply aligned and summed to produce the result in Fig. 3b.

In the machine implementation of azimuth compression, as discussed above, the range-compressed data are resident in disk files organized in 64 by 8192 range cells. Each file is transferred into memory in turn, and a Fourier transform is performed on each azimuth line. Then the two-dimensional array is corrected for quadratic range migration by a shift and interpolation applied to each of the 8192 vectors of length 64. Finally, the data are multiplied independently by each of the four multilook azimuth filters, detected, and summed to assemble the final image.

Elapsed (wall clock) and computational (central processing unit) times were obtained for many components of the processing on both the VAX and the EPS 164 computers. The total elapsed time required to produce a four-look 100 by 100 km image from SAR data on six Seasat tapes for this initial version of the processor, running on an unloaded system, is 5.6 hours. Fast Fourier transform calculations, which overlap input-output processing at a few stages, are executed during 36% of the total processor time.

While 5.6 hours to generate a 100 by 100 km image compares favorably with published timings for similar systems, enhancements to the initial system are expected to improve the processing speed. Input-output processing time on the VAX could be reduced considerably by acquiring a large disk storage capability so that tape input and output could be avoided. Also being investigated is the possibility of attaching a smaller array processor to the EPS 164 for the sole purpose of com-

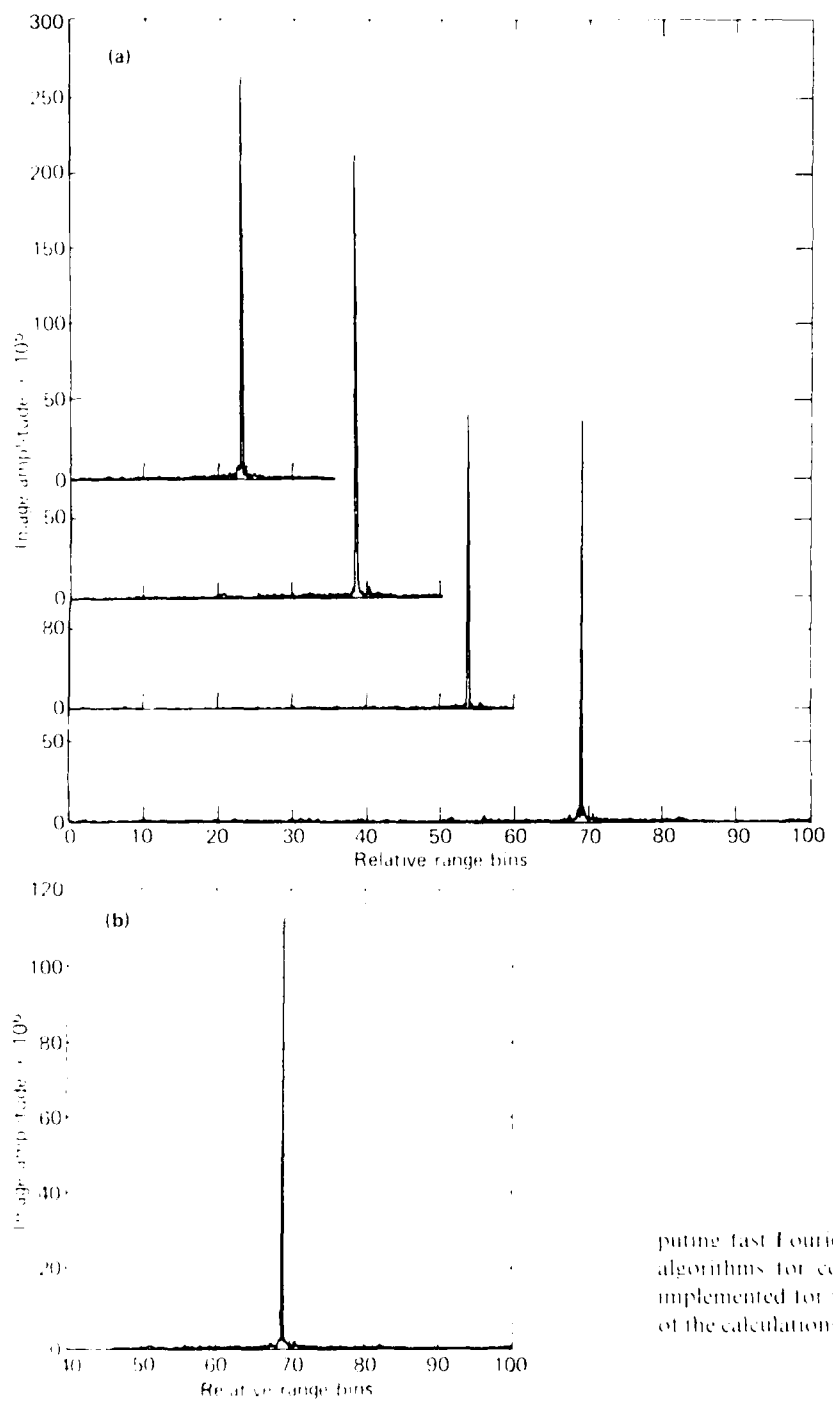


Figure 3 — Multiple-look processing of images produced by a 10-pulse multi-subfilter. (a) The Goldstone antenna target after multiple summation.

puting fast Fourier transforms. Finally, more efficient algorithms for computing fast Fourier transforms, if implemented for the EPS-164, could speed up that part of the calculations by as much as 50%.

This work was supported by the Defense Advanced Research Projects Agency.

SIDE-LOOK SONAR IMAGE EXPLOITATION

D. C. Doty and C. A. Twigg

Side-look sonar systems are powerful tools for collecting information. Systems now operational perform exclusively one-dimensional signal processing on the sonar data to form images. This paper describes an application of two-dimensional signal and image processing to side-look sonar data at or near real-time rates to improve geometric quality and image interpretability.

OVERVIEW

This paper presents the results of an application of two-dimensional signal and image processing techniques to side-look sonar (SLS) imagery. The project had four objectives:

1. Develop and demonstrate a capability to perform two-dimensional signal and image processing at or near real-time rates,
2. Develop and evaluate filters to enhance the use of SLS images for water column and bottom search operations,
3. Develop and evaluate an algorithm to correct SLS images for distortions caused by platform motions,
4. Demonstrate the use of the SEL-II sonar signal processing system as a research tool.

BACKGROUND

An SLS system uses acoustic energy to produce an image of the ocean bottom. A transducer illuminates the bottom with a narrow pulse of acoustic energy several times per second. Following each illumination, a transducer array receives the energy reflected from the bottom and forms the return into a narrow beam. The system electronics apply one-dimensional signal processing and assemble successive beams into an image on a hard-copy display.

The SEL-II signal processing system was developed at API to study the application of advanced signal processing techniques to SLS images and to act as a test bed for algorithms proposed for inclusion in the operational systems. The processing subsystem of SEL-II consists of a control unit, a control bus, two data buses, and an arbitrary number of processing modules connected to the buses. The control unit may route data between the processing modules in arbitrary combinations under software control. This architecture allows the system to be

expanded nearly indefinitely without hardware modification. Processing modules in the current system include sonar signal input, one-dimensional digital filters, video output, and a bidirectional interface to a minicomputer used in algorithm development and experimentation. Processing rates of four times real time have been demonstrated.

DISCUSSION

Enhancement Filters

We identified three classes of enhancement filtering algorithms to apply to the SLS images:

1. Segmentation algorithms to emphasize potential target characteristics such as lines, edges, and points;
2. Two-dimensional noise reduction techniques to enhance details by increasing the signal-to-noise ratio;
3. Contrast enhancement techniques to redistribute the image information in order to utilize fully the dynamic range of the display devices.

Each algorithm described below has been implemented in software to process operational data.

The segmentation filters were implemented as convolutions of the image with 3 by 3 masks. Each mask was chosen to emphasize one class of feature, but several masks could be applied simultaneously to a given image. This filter was most effective when used as an edge detector.

The two-dimensional noise-reduction techniques were the local (3 by 3 window) mean and the median. The local mean was implemented using the 3 by 3 convolution described above. These techniques proved to be most useful as preprocessors for the image segmentation and contrast enhancement algorithms, although they also provide great subjective improvement in the quality of the images.

Two contrast-enhancement techniques were implemented: histogram modification and homomorphic filtering. Histogram modification treats the image as a probability density function of intensity levels and remaps the existing levels into a distribution that fills the dynamic range of the display. Figure 1 shows the intensity distribution of an image before histogram modification; Fig. 2

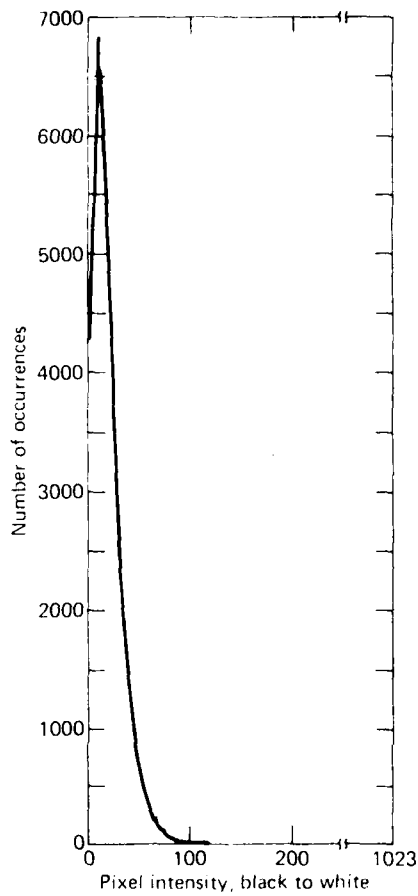


Figure 1—Histogram of an unprocessed SLS image. This graph shows the frequency of occurrence of pixel intensity versus intensity in a real SLS image before contrast processing. Notice that virtually all the image information is contained in the low-order 6 bits of the 10 bit dynamic range.

shows the result of the modification. Linear and hyperbolic redistributions of intensity were implemented. (The hyperbolic redistribution theoretically corrects for the response of the human eye.)

Homomorphic filtering models intensity as the product of illumination and reflectance. Taking the logarithm of the image transforms the product to a sum. We apply a conventional two-dimensional fast Fourier transform and frequency domain filtering to remove the illumination (which is primarily low frequency) and leave the reflectance (primarily high frequency). When the result is inverse fast Fourier transformed and exponentiated, the combination of noise reduction and uniform illumination makes the image much clearer. Figure 3 is a block diagram of this algorithm.

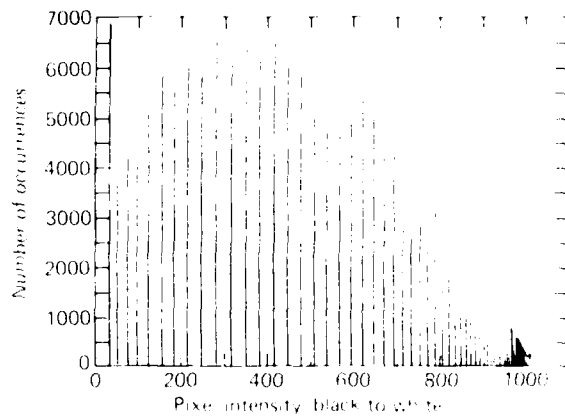


Figure 2—Histogram of the SLS image after contrast enhancement. Notice the quantization of the result, corresponding to the 6-bit quantization of the original. Although the frequency of the high-intensity pixels decreases, the closer spacing of the occupied levels keeps the distribution approximately constant over the full 10-bit dynamic range.

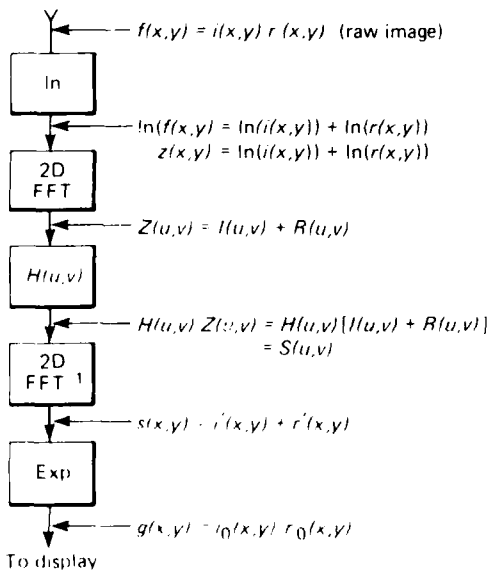


Figure 3—The homomorphic filtering process. Homomorphic filtering assumes a multiplicative model for illumination and reflectance. The two components are separated by taking the logarithm, transformed to the frequency domain, filtered with a high- or band-pass filter to reduce the low-frequency illumination and enhance the high-frequency reflectance, returned to the space domain, and exponentiated to regain the original dynamic range.

Platform Motion Compensation

The utility of the preceding two-dimensional filtering depends on having an image where neighboring lines of the image correspond to neighboring slices of the ocean floor. Because the SLS images are formed one line at a time, any maneuvering by the sonar platform can distort the image beyond recognition. Therefore, the images must be corrected for the distortions before enhancement algorithms can be applied.

We developed a correction algorithm using the navigation information available on typical platforms. To test the algorithm, we developed a simulation to take a known target (a rectangular grid) and "insonify" it from a "platform" with typical dynamics. The simulation was necessary because the SEL II system does not currently provide an interface between SLS and navigation data. Our experimentation showed that we could, given a hardware implementation and sufficient navigation data, correct for platform motion variations in real time. The corrected images could then be enhancement filtered as described above.

CONCLUSIONS

The following conclusions were reached:

1. Each filtering method was implemented in software in the minicomputer component of the SEL II system. With the exception of the homomorphic filtering with two 512 by 512 fast Fourier transforms, the algorithm performs at or near real time. Hardware implementation should be straightforward and should easily reach two to four times real-time rates. (The image segmentation, noise reduction, and motion compensation algorithms process one image line per second—slower than real time by

a factor of the pulse repetition frequency. The pulse repetition frequency for operational systems ranges between 1 and 14.)

2. Present systems are not fully exploiting the information available in the images. (a) Platform motion effects should be removed before any enhancement processing is applied. If the corrections are not made, the bottom features of interest may not be recognizable. In addition, the correction can make the operator aware of areas not insonified or of multiple insonifications, and it allows for real-time correction of the search pattern. (b) Application of the enhancement algorithms can significantly improve the interpretability of the images and can lead to the automatic or semiautomatic detection of targets.
3. The architecture of the SEL II system makes it ideal for experimentation in signal and image processing, either in software or hardware, and it can be used as a base for operational systems.

ACKNOWLEDGMENTS

We would like to acknowledge the efforts of R. H. Bauer, D. P. Crawford, R. F. Dove, R. A. Quinnell, and R. T. Stellabuto.

REFERENCES

- C. A. Twigg, D. C. Doty, and R. A. Quinnell, *Image Exploitation Effort, Final Report*, IIRU API-S3-E-084 (Jan 1983)
R. T. Stellabuto, *Documentation for Image Enhancement Routine*, AZNEH/ENCE, IIRU API-S3-E-081 (Jun 1983)

DEVELOPMENT OF POWERFUL SPACE-QUALIFIED COMPUTERS

B. W. Ballard, R. M. Henshaw, and T. Zaremba

API has designed, built, and tested prototypes for the two computers that will control and monitor the Hopkins Ultraviolet Telescope, a 1986 Space Shuttle experiment. These prototypes are the first members of a family of fast, reliable, language-based computers to be developed by API.

BACKGROUND

The Hopkins Ultraviolet Telescope (HUT) is a Space Shuttle experiment designed to obtain the far-ultraviolet spectra of astronomical objects as faint as seventeenth magnitude. Accurate real time computation of the wavelength of each photon sensed by the HUT detector requires greater processing power than is available in any space qualified microprocessor being produced commercially. In addition, the complex and changeable control and monitoring requirements of HUT dictate the use of a powerful and flexible computer system that can be programmed in a high-level

language. This article describes the design and development of a computer system to meet the data processing requirements of HUT. Fabrication and test of the flight computer systems based on the already completed prototype system will be completed in April 1984.

DISCUSSION

System Architecture

Figure 1 shows the interfaces that connect the HUT flight computer system to the other components of the telescope and to the Shuttle's experiment support equipment. Two independent processors, the spectrometer processor and the dedicated experiment processor, provide the computational power for HUT. The spectrometer processor receives data generated by the telescope's detector, computes the wavelength of each ultraviolet photon detected with a high-speed centroiding algorithm, and periodically forwards the accumu-

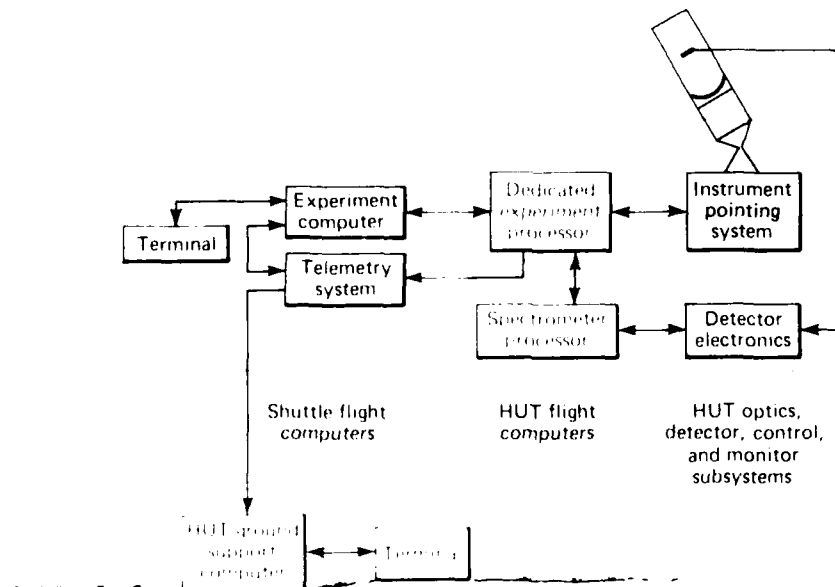


Figure 1 — The HUT configuration

lated spectral data to the dedicated experiment processor. The latter processor receives the data, handles telescope control and monitoring functions, interprets commands and generates displays in the Shuttle aft flight deck for HUT's astronaut-operator, acquires and analyzes star-field pictures to assist in telescope pointing, and transmits status, video, and spectral data to the ground by means of Shuttle's telemetry system. Tables 1 and 2 summarize those functions.

Table 1 — HUT computer functions, spectrometer processor

Function	Rate
Read data from ultraviolet detector	1024 6-bit analog-to-digital conversions per millisecond
Compute photon wavelength	Once per photon, up to 9000 per second
Send ultraviolet spectrum to dedicated experiment processor	2067 words every 2 s
Interpret five command types from dedicated experiment processor	Once per command

Table 2 — HUT computer functions, dedicated experiment processor

Function	Rate
Receive spectrum from spectrometer processor	2067 words every 2 s
Control 8 motors, 6 power supplies, 14 heaters	Occasional, as commanded
Monitor 60 analog, 56 discrete lines	Once every 2 s
Interpret 88 command types	Once per command
Generate one of four displays	Once every 2 s
Analyze TV picture, compute pointing errors	Once every 20 s
Transmit telemetry to ground station	97,656 bits/s continuous
Control observing sequence	Continuously during observation; average duration 20 min

Computer Architecture

The two processors have identical central processing unit and memory board designs, with additional boards to handle unique processor input output requirements. The spectrometer processor contains one board for the interfaces with the telescope detector and dedicated experiment processor, while the dedicated experiment processor has several boards for video memory, video control, equipment monitoring and control input output, and interfaces to Shuttle systems. Table 3 lists some of the hardware features of the processors.

The central processing unit is a 16-bit microprogrammed machine containing four Am2903 4-bit microprocessor slices, an Am2910 sequencer, an Am2902 carry look ahead unit, an Am2904 status and shift control unit, and an Am2925 programmable clock generator, all from Advanced Micro Devices, Inc. The microprogram consists of 512 64-bit words stored in programmable read-only memory, and the microinstruction execution time varies from 200 to 400 ns under microprogram control, with automatic wait states for slow peripherals.

Table 3 — HUT computer features

	Spectrometer Processor	Dedicated Experiment Processor
Size (in.)	Three 6 by 11.8 boards	Eight 6 by 11.8 boards
Power (W)	~30	~60
Central processing unit	16-bit microprogrammed	16-bit microprogrammed
Clock rate (MHz)	25	25
Microcycle rate (MHz)	2.3–8.0	2.5–8.0
Instruction rate	500,000 primitives/s	500,000 primitives/s
Microcode PROM	512 64-bit words	512 64-bit words
Interrupts	16 available, 4 used	16 available, 10 used
Main memory RAM	20,480 16-bit words	49,152 16-bit words, redundant main memory
		65,536 16-bit words, video memory
Main memory PROM	4096 16-bit words	4096 16-bit words
Type of memory access	Memory mapped	Memory mapped

The main memory is a 16-bit wide, word addressable design using 16-kilobit NMOS technology memory components. The memory access time is 240 ns, and the memory write cycle is 280 ns. The memory designs have been reviewed for sensitivity to transient and permanent faults caused by radiation. Various central processing unit and memory design changes have been incorporated to reduce that sensitivity.

Microcode

Instead of interpreting a conventional assembly language, the processors' microprograms implement primitives of the Forth high-level language directly. The measured execution speed is approximately 500,000 Forth primitives per second for a typical instruction mix. (A Forth primitive is anything from a simple arithmetic operation to a complex loop control or block move operation.) Forth, an interactive extensible language, has been used in a rapidly growing number of real-time minicomputer and microprocessor applications since its development in 1973.

Slightly over half the microcode space of the processors is used to implement processor initialization, interrupt service logic, the macroinstruction fetch-execute loop, and 66 Forth primitives. This microcode is the same in both processors, while the remainder of the microcode space is available for the migration of application software to microcode. The additional space in the spectrometer processor contains data collection and centroiding routines to calculate the wavelengths of individual photons. The dedicated experiment processor uses this space for video processing, character string manipulation, and operating system support routines. The processor-specific microcode routines are accessible to the programmer in the same way as standard Forth primitives are.

Software

The processors are programmed entirely in Forth since they have no assembly language in the normal sense. A small operating system (written in Forth) provides the interactive programming environment common to all Forth language implementations. That environment interprets Forth source code entered through the terminal or from mass storage devices, either executing it immediately or compiling it incrementally into memory for fast execution later. Thus, the programmer deals only with source code, bypassing the separate intermediate steps of compilation and linking.

The processor microcode contains extensions to the standard Forth language to support concurrent pro-

gramming. The extensions allow the definition of any number of independent Forth processes that compete for the processor on a priority basis. Hardware interrupts and software-initiated interprocess signals are represented as operations on counting semaphores. Any process may signal or await the signaling of any semaphore. The signal and wait semaphore operations cause the processor to be reassigned to the highest priority process not waiting for an unsignaled semaphore. Semaphore operations provide mechanisms for interprocess communications and for mutually exclusive access to shared resources.

These concurrency concepts have been used extensively in implementing the HUT applications software. The spectrometer processor software consists of seven independent processes, while the dedicated experiment processor software is implemented as 26 processes.

Project Status

API has built and tested engineering prototypes for both processors. The fabrication of flight versions qualified for the Shuttle orbital environment and designed for efficient heat dissipation will be completed by April 1984. The development of all microcode and of the spectrometer processor application software is complete; the dedicated experiment processor application software will be completed by May 1984. Integration with the rest of the telescope will begin in May, and the complete instrument will be delivered to the Kennedy Space Center in December 1984 for Shuttle integration. The first of three 10-day Shuttle flights is scheduled for March 1986.

API has started the design of a single-board implementation of the computer architecture embodied in HUT's processors for use in future applications. It will offer higher speed, use less power, accept memory integrated circuits of various technologies, be compatible with an industry standard bus, and execute the recently approved Forth-83 version of the Forth language.

ACKNOWLEDGMENTS

We wish to thank the HUT Principle Investigator Arthur E. Davidsen of the JHU Physics Department and HUT Program Manager Glen Fountain of API for their support and encouragement.

This work was supported by the National Aeronautics and Space Administration.

TEXT PROCESSING PROMPTERS FOR THE IBM 4341 VM/CMS SYSTEM

S. M. Schaa

Text processing software has been available for several years at APL's McClure Computing Center, but typically it has been difficult to learn and cumbersome to use. User interfaces have been developed at the Center to provide a very productive, easy-to-use environment for text processing on the IBM 4341 computer.

BACKGROUND

While computerized text processing has many well-recognized advantages over the "old fashioned" manual methods (ease of revision and spelling verification, for example), it also has some disadvantages. With manual typing, one only had to learn how to type; on a computerized system, an inexperienced text processor has a great deal to learn before even starting to process text. Most significantly, one must learn how to use a text editor for textual data entry, a text formatting control language for marking up text to be formatted, and the commands and options required to execute the text formatting program, i.e., to translate the marked-up text into formatted text suitable for printing.

Two excellent text processing tools are available on the VM/CMS system (an operating monitoring system for interactive computing on the IBM 4341): XEDIT, the VM/CMS full-screen editor used for textual data entry; and GML, the Generalized Markup Language, a text formatting language supported by the IBM Document Composition Facility (commonly known as SCRIPT).

Two user "prompters" (MEMO for internal memoranda and GDOC for larger general documents) have been developed at the Center to combine those tools into an easy-to-learn, easy-to-use text processing system. In this context, a prompter is a user interface that provides assistance and information to the user of a system while he is using it. With the MEMO and GDOC prompters, even someone with no experience using computerized text-formatting languages can, with very little effort, produce nice-looking, well-formatted documents. Before describing the prompters, a brief discussion of the tools on which they are based is in order.

The Generalized Markup Language

With many text formatting languages, the typist must use special control words to specify exactly how each text component (e.g., Paragraph, Heading, List, and Title

Page) should look when formatted. For an ordered list (like the following one), the typist might have to

1. Use the "space" control word to create blank lines before and after the list;
2. Use the "indent" control word to indent each item in the list (notice that the text of each list item is indented, or offset, to the right of the number);
3. Number each item explicitly, which makes revision difficult if additional list items are inserted;
4. Reset the indentation for the text that follows the list.

This is known as specific markup and is not only tedious to use but difficult to revise.

With GML, tags are used to tell the formatting program, SCRIPT, what the text is, not how it should look; SCRIPT already knows how it should look and takes care of all the details to format it properly. For the ordered list, only the following three GML tags are necessary: OI, to tag the beginning of the ordered list; LI, to tag each list item; and EOI, to tag the end of the order list. SCRIPT inserts the blank lines, indents where necessary, and numbers the list items.

Two sets of GML tags are available on the McClure Center's IBM 4341 computer:

1. General document tags. These tags were supplied by IBM with the SCRIPT text formatting program. They may be used to mark up large documents consisting of such components as Title Page, Abstract, Preface, Table of Contents, List of Figures, the main body of the document, Appendices, Glossary, and Index. There are many additional tags for text components found in the body of the document: Paragraphs, Headings, Lists, Figures, Footnotes, and so forth.
2. Memorandum tags. These tags were developed by the McClure Center to support the familiar internal memorandum style. They include: To, Via, From, Subject, List of References, List of Enclosures, Signature, and Distribution List, in addition to those used in the body of a general document.

Almost all of the GML tags have "names" that are both easy to learn and easy to remember, but, with

the MEMO and GDOC prompters, there is little need to learn or remember them. They are generated by program function (PF) keys—special programmable keys found on many terminal keyboards.

The VM/CMS Full-Screen Editor

The VM/CMS editor, XEDIT, and the EXEC2 command language give the program developer extensive capabilities to tailor the full-screen editing environment for a specific application. He can program new editor commands, known as XEDIT macros; assign commands to the PF keys, to be executed by a single keystroke; and reserve lines on the full-screen display to be used for constant (i.e., nonscrollable) text, such as a menu describing the functions of the PF keys. The McClure Center has taken advantage of these capabilities to develop the MEMO and GDOC prompters.

DISCUSSION

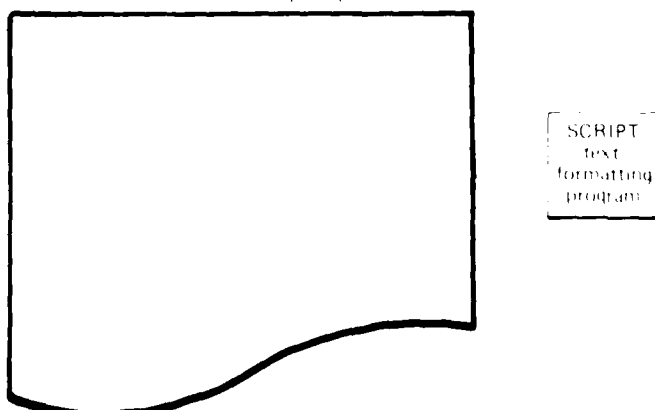
MEMO and GDOC are VM/CMS commands that create specially tailored text entry environments for the creation of memoranda and general documents, respectively. With them, the typist has the complete capabilities of the VM/CMS editor, but the PF keys have been programmed to correspond to GML tags. When one of those keys is pressed, a program is executed that causes the appropriate tag(s) to be inserted into the document, leaving the cursor in position for the typist to enter the corresponding text. Because there is a menu at the bottom of the editing screen describing the function of each PF key, there is no need for the typist to remember the names of the GML tags or the numbers of the keys to which they correspond.

The menu shown in Fig. 1 is the first one displayed at the bottom of the editing screen when a new memoran-

===== PF keys for APL Memo: Standard Header Tags =====		
1= HELP XEDIT	2= Reference	3= FILE Memo and Quit
4= To:	5= Reference List	6= Via:
7= From:	8= Enclosure:	9= Title Citation
10= Subject:	11= Enclosure List	12= Body of Memo

Figure 1 — The MEMO prompter's first text entry menu.

SCRIPT input file as entered by the typist
with the aid of the MEMO prompter



Formatted SCRIPT output file printed on
a letter quality system printer

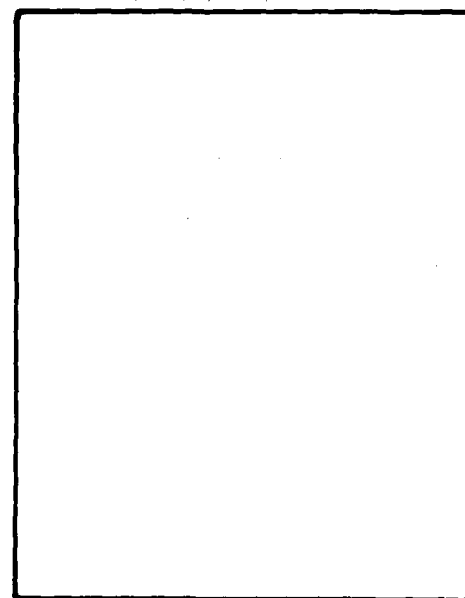


Figure 2 — A sample memorandum entered with the aid of the MEMO prompter, formatted with SCRIPT, and printed on a letter quality system printer

dum is being created via the MEMO prompter. As can be seen, the functions of most of the PF keys are self-explanatory. When a PF key is pressed, the corresponding GML tag is inserted automatically into the document, and the cursor is left in the appropriate position for the typist to enter the required text. After the tags and text of To, From, Subject, References, and/or Enclosures have been entered, PF12 is used to tag the beginning of the body of the memo. It causes a new menu to appear (because the tags on the first menu will not be needed again). Additional tags such as Signature, Distribution, Figures, Footnotes, and Paragraphs are assigned to PF keys on the second menu and also on a third menu that is accessed via PF12 on the second one.

The GDOC environment is functionally similar to the MEMO environment, but the PF keys are programmed to correspond to text components typically found in larger documents, e.g., Title Page, Table of Contents, and Preface.

Using the MEMO and GDOC prompters, it is easy to enter the text of a document. The typist can concentrate on typing rather than on formatting. Once the text has been typed, the document may be filed (i.e., stored

on a disk) and then formatted with the SCRIPT command. The output may be viewed on a terminal screen or sent directly to one of the system printers.

Figure 2 is an example of a memorandum created with the MEMO prompter, before and after processing with the SCRIPT formatting program. The GML tags, which begin with a colon and end with a period, were inserted by the prompter when the typist pressed the appropriate function keys. SCRIPT has been programmed to "know" what each tag means and to format the corresponding text accordingly.

REFERENCES

- Document Composition Facility - Introduction to the Generalized Markup Language Using the Starter Set*, International Business Machines Corp., SH20-9186 (Feb 1980).
- FM-SP System Product Editor Command and Macro Reference*, International Business Machines Corp., SC24-5221 (Sep 1983).
- S. M. Schadt, *New SCRIPT GML Tags Supporting the "API Memorandum" Format*, IHC API TCS 1-045-83R (Jun 1983).

This work was supported by NAVSEASYSOM.

THE COMPUTERVISION CADD 4 FINITE ELEMENT MODELING PACKAGE

D. F. Persons

Users of the MacNeal-Schwendler Corp., NASA Structural Analysis (MSC/NASTRAN) finite element analysis program at API now have software in house to generate interactively a finite-element model. The Computervision CADD 4 finite-element model building package was used to generate an MSC/NASTRAN input data deck for the structural analysis of the electronics module cover of the Hopkins Ultra violet Telescope. An interface program between MSC/NASTRAN and CADD 4 has been developed to enable the analyst to display the response of the model on*

the basis of endpoint displacement data recovered from the analysis.

BACKGROUND

Finite element models can be constructed 5 to 10 times more quickly with the use of finite-element model generators than when built manually. The use of computer-aided engineering on the electronics module cover of the Hopkins Ultraviolet Telescope provided a more

accurate analysis in less time than if it had been done without computer-aided engineering. The time saved using those techniques was spent optimizing the initial design; the result was a substantially stiffer structure.

The electronics module cover has an aluminum angle frame stiffened with a thin outer skin of aluminum sheet. Stiffening beads and hat-sectioned stiffeners provide support for various components attached to the outer skin. The finite-element model representing this structure had to be complex enough to represent the interaction of the many components and detailed enough to provide flexibility for the easy representation of changes in the design. The final MSC/NASTRAN model of the cover (Fig. 1) consisted of 236 gridpoints and 402 beam and shell elements. Building a finite-element model of this size by hand would have taken approximately three weeks. Using the Computervision modeler, 90% of the analysis input deck was generated in two days.

This article summarizes the strengths and weaknesses of the Computervision finite-element package that were found during the construction of the finite-element model of the electronics module cover. Also outlined are typical steps for model preparation and post-processing and the capabilities of the new CADD 4X package. A prospective user of the modeler could use this report to evaluate the feasibility of using the Computervision finite element package to meet his needs.

DISCUSSION

The Computervision CADD 4 and the upgraded CADD 4X finite element packages are actually subsets of the total Computervision graphics package—they are not stand-alone programs. The complete graphics capability is presented in order to aid the finite element modeler in defining the initial wire frame geometry. Use of the mass property calculation package will give the user areas, volumes, masses, and area and

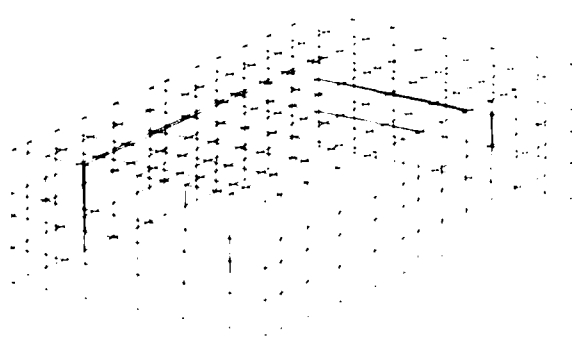


Figure 1 — The finite-element model of the 14-pinhole Ultraviolet Telescopic electronics module.

mass moments of inertia of the wire frame regions. However, the system can become intimidating because of the large number of commands available. Usually, it is better to have an experienced designer define the wire frame geometry, thus freeing the finite-element user to familiarize himself with only the finite-element package. Outlined below are the major features and capabilities of the finite-element package; useful capabilities that are not currently available are also indicated.

Graphics and Data Input

1. Finite-element package commands may be input by using the cursor to pick from a dynamic menu.
2. Graphics commands may be selected by digitizing a programmable function tablet.
3. Full-color display is available.
4. Infinitely variable dynamic rotations and translations are available by using the Image Control Unit functions.
5. Geometry data can be input by digitizing an existing drawing, by creating the geometry through the use of graphics commands, or by using an existing CADD 3 or CADD 4 data base.

Mesh Generation and Preparation of the Analysis Deck

1. The MSC/NASTRAN, ANSYS, SUPERB, STRUDL, and SAP5 finite-element analysis codes are supported.
2. Fifty-four element types are available.
3. The user may automatically generate a mesh of one- or two-dimensional finite elements by defining a boundary and specifying the number of elements required along each side of the boundary. An existing mesh may be rotated, translated, or mirrored to produce additional elements.
4. Individual elements can be inserted by the ordered picking of existing gridpoints with the cursor.
5. Specifications for loading, for the single point constraint set, and for material and element properties can be generated easily.
6. There is complete control over element order and element numbering.
7. There is little need to display element numbers because the cursor can be used to identify desired line, point, gridpoint, or element.
8. The user can shrink elements to check for continuity, merge coincident endpoints, and

a user-defined spherical tolerance, and with the CADDSS 4X system highlight selected sets of gridpoints and elements.

Post-Processing

The deformed shapes of the model can be displayed using MSC/NASTRAN gridpoint displacement results post-processed by means of an interface written by API.

Additional Features Available with the CADDSS 4X Upgraded Finite-Element Package

Stress results can be displayed by means of an element color fill procedure. (The interface between MSC/NASTRAN and the Computervision finite-element package has not yet been written.) In addition, elements with selected numbers, properties, or material descriptions and gridpoints with selected numbers, single-point constraint sets, or loads can be highlighted for model checking purposes.

Computervision Finite-Element Package Features Not Available but Needed

The finite element package lacks the capability to convert an existing finite element analysis program input deck into a CADDSS 4 data base for subsequent display or modification. This should be corrected. Also, the model checking features should be expanded to include the automatic orientation of element face normals by comparison to a user defined vector, a check of element aspect ratios (the ratio of length to width to height), an element interior angle check, and a two-dimensional shell element flatness check. (Both of these deficiencies can be remedied by stand-alone programs that have not yet been written.)

PROCEDURE

Outlined below are the general steps used to generate a finite element model using the Computervision finite element package. Also given is a summary of the procedure that must be followed to recover the analysis displacement data for display as a deformed shape on the Computervision graphics terminal.

Model Preparation

1. Obtain geometric data on the part to be analyzed from digitizer input, from the use of Computervision graphics commands, or from an existing data base.
2. Input the material and element properties

3. Generate the finite element mesh using automatic mesh generation methods combined, whenever possible, with the graphics modifier "near." Correct missing or oddly shaped elements by means of individual element generation methods.
4. Merge duplicate gridpoints. Reduce the computation time required by means of the "ip window" command to isolate the mesh boundaries.
5. Add loadings and constraints to the gridpoints. Complete the model check by using the element shrink option and, with CADDSS 4X, by highlighting selected entity sets.
6. Edit the model to correct problems found during the model check.
7. Write the MSC/NASTRAN (or another supported analysis code) bulk data card images to tape. Transfer the tape to the IBM 3033 for analysis.

Post-Processing

Reference 3 details the procedures used for the recovery, translation, and display of MSC/NASTRAN gridpoint displacement results. A brief summary of the procedure follows.

Add a series of MSC/NASTRAN direct matrix abstract programming language statements to the analysis deck before execution. These statements write the interior endpoint displacement table OUT61 to tape on the IBM 3033. After reviewing the analysis, execute the reformatting program to read the above tape and produce a Computervision readable file on the same tape. Transfer the tape to the Computervision system and convert the character set to Computervision format. Execute a program to complete the reformatting, and write the displacement data for each loadcase into a separate file. Read each loadcase file into the Computervision finite element package, and display the deformed shape overlying the original model.

With the installation of the CADDSS 4X system, a direct line will be available between the Computervision Designer System and the IBM 3033. This improvement will eliminate the need for handling tapes because the data file will be directly transferred. The previously mentioned programs must be modified to take advantage of the new capability.

ACKNOWLEDGMENTS

The author wishes to thank Daniel Pani who developed the procedure and programs to take advantage of the post-processing capability of the finite element

package. John Ecker, Gordon Heidelbach, Linda Marudas, William Roemer, and Steven Schachtner provided valuable assistance.

REFERENCES

1. K. Koenig, "Using FEV with Automatic Meshing," *Comput. Struct.*, 14 (May-Jun 1983).

²CADDY 4X Finite Element Modeling Reference Manual, Computervision Corp. P001-00723
D. Paul, *The Computerized Designer System and the IBM MSC/NASTRAN Interface*, IBM API TEC 83-055 (3 Nov 1983).

This work was supported by the National Aeronautics and Space Administration.

OCEAN SCIENCE AND TECHNOLOGY

INTRODUCTION

From striped bass to synthetic-aperture radar, the range of the Laboratory's work in matters that relate to the oceans is wide indeed. At the one extreme, we try to fathom processes that are at the core of the decline of the toothsome rockfish; at the other, we seek to exploit the capabilities of advanced radars to map the mesoscale features of the ocean's surface.

Between such contrasting pursuits lies a great diversity of effort here at API in the fields of ocean science and ocean technology. The common threads that run through such varied endeavors are, first, the search for understanding and, second, the application of that understanding to practical purposes — the same threads that have been woven into the very fabric of the Laboratory's work since its inception.

As might be expected, many of the projects in ocean science and technology (OST) contribute directly to the support of Navy programs. Both surface and subsurface ocean processes and properties are investigated, and the knowledge gained is put to use in a variety of programs, most notably those related to under-sea warfare. Currently the Laboratory supports several different Navy sponsors in more than a score of such projects.

Not so well known is that the Laboratory works in significant OST programs for a variety of sponsors other than the Navy; they include the following agencies:

Defense Advanced Research Projects Agency
National Oceanic and Atmospheric Administration
Public Service Electric and Gas Co. (of New Jersey)
State of Maryland
United States Army
United States Fish and Wildlife Service

A small sample of OST work done for Navy sponsors appears in this section. Most such efforts must go unremarked for reasons of security, but the accomplishments reported here, albeit for the military, illustrate the way in which the Laboratory applies its capabilities toward the solution of ocean-related problems of importance to several components of our society.

A NEW TECHNIQUE FOR THE ENCAPSULATION OF THERMISTORS

C. W. Anderson and G. J. Farruggia

A new technique was developed to encapsulate thermistors used on a towed oceanographic instrument array. The technique has significantly increased the serviceable life of the thermistor assemblies by reducing by an order of magnitude the frequency of leaks caused by water intrusion into the insulating encapsulation. It also has reduced the fabrication time by two-thirds and the production costs by one-half.

BACKGROUND

In 1975, development began on an oceanographic instrument system consisting of an array of thermistors mounted along an electrical mechanical cable. Measurements from the thermistors provide a vertical profile of the ocean's temperature as the array is towed behind a research ship. The combination of plastic low-drag fairings on the cable and the hydrofoil depresor allows the thermistor array to trail at a steep vertical angle. The fairing nose is used as the mounting location for the thermistor in order to expose it to maximum free flow.

The thermistor mounting should have the contour of the fairing nosepiece; it needs to be flexible so that it can be secured around the cable strength member, and it must provide mechanical and electrical integrity for the protection of the fragile glass-bead thermistor and electrical connections.

Originally, the mounting that encapsulated the thermistor was made of a single polyurethane compound because it appeared to meet the criteria for flexibility, strength, and electrical insulation. Thermistor assemblies had shown no degradation of insulation integrity when tested under hydrostatic pressure loading, but the units were not exposed to mechanical flexing. Under actual use, the mechanical flexing and hydrostatic pressure loading caused the bonds along the thermistor stem and wire feedthrough section to break down, resulting in seawater leakage and electrical shorting.

During early sea tests, the quantity of thermistors in the array (fewer than three dozen) was as large as could be maintained in the field, given the low reliability of individual sensors. By 1982, test schedules had become demanding to a degree that allowed little more than minor repairs in the field, resulting in some loss of data during test operations. Concurrently, the requirement for a larger thermistor array emerged. In addition

to the limiting factor of sensor reliability, the fabrication techniques then available militated against a large increase in the size of an array because of the high cost of each sensor assembly. It became clear that much-improved encapsulation techniques were needed in order to field a new, larger system in a reliable configuration at an affordable price.

In the spring of 1982, API's Electrical Fabrication Group, Electrical Design Group, and the Test Group of the Submarine Technology Division combined efforts to develop an inexpensive way to fabricate large quantities of thermistor assemblies that would remain mechanically and electrically sound throughout several oceanographic tests.

DISCUSSION

An investigation was started to determine the good and bad characteristics of the existing mounting design and encapsulating procedures. Its objectives were to prevent seawater leakage into the encapsulated assembly, simplify the encapsulation procedures, identify the material properties of available encapsulants when used in the ocean environment, and establish testing methods to evaluate various designs.

Those objectives were met systematically by procuring numerous encapsulation materials and by building and testing several prototype thermistor casting mold configurations. Mechanical fixtures were built for running dynamic, flexural, and shear tests under hydrostatic pressure in order to expose bonding delaminations and cracking weaknesses. The final design of the casting molds focused on eliminating tight assembly tolerances while maintaining high piece-to-piece uniformity. Graphic step-by-step fabrication procedures were documented for use by shop technicians to improve the quality of the finished assemblies.

The production of the thermistor fairing mounts begins by preparing the glass-bead thermistors and the electrical wires that extend from the thermistors to the electronics. The fragile thermistors are cleaned in boiling acetone and kept free of contamination, including fingerprints, throughout the remaining assembly steps.

Electrical wires designed specifically for the application are encapsulated in a thin outer jacket of

Conap EN-7 urethane (Fig. 1). The wire is twisted and shielded to reduce capacitive coupling and is covered with an inner polyvinyl chloride (PVC) and an outer polyurethane jacket. The PVC provides high electrical-insulation integrity, and the polyurethane provides a tough abrasion-resistant cover. Both materials adhere well to the encapsulant. Prepotting the wire provides an initial barrier against seawater intrusion and serves as a way to locate the device in the subsequent assembly.

The ends of the prepotted electrical wires that will be attached to the thermistor leads are trimmed, and the piece is placed in the nosepiece mount casting mold (Fig. 2). A single alignment check ensures proper wire placement. The molds are coated with a permanent nonstick surface of Istatt 33 Teflon and have Teflon inserts in certain critical areas. No spray-on release agents are applied because contamination by release agents has been shown to degrade encapsulant adherence properties.

The nosepiece mold is filled with Conap EN-7 urethane encapsulant that is prepared and cured according to specific instructions. Encapsulant leakage, called flashing, may show up near the casting-mold parting lines when the nosepiece is removed after curing. The flashing is easily trimmed off and occurs only in noncritical areas because the molds were built to very tight machining tolerances.

Large quantities of nosepiece mounts can be fabricated whenever there is an anticipated need because the thermistors are not placed in the mounts until all the complicated fabrication steps have been completed.

The Teflon block shown in Fig. 2 is used to form a small cavity in the nosepiece that will later hold the

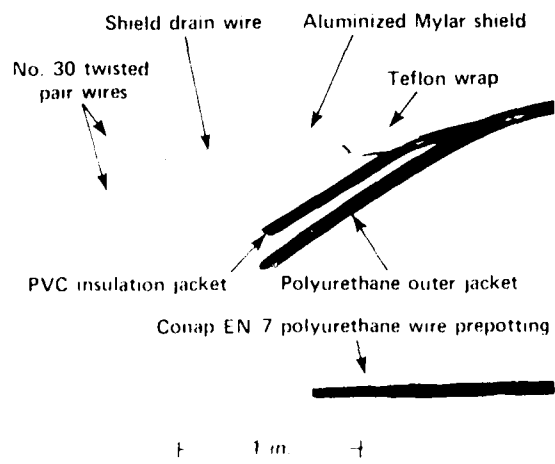


Figure 1 — The wire structure of the twisted pair and foil-shielded wire prior to the prepotting process.



Figure 2 — A partially assembled nosepiece mold.

thermistor and the encapsulant around the thermistor. Electrical conductors from the prepotted wires placed in the Teflon block are exposed in the cavity and are ready to be soldered to the thermistor leads.

Thermistor installation in the molded nosepiece takes place in a soldering fixture (Fig. 3). It gently holds and accurately locates the glass thermistor probe so that the technician's hands are free to solder the fine No. 40 gauge wires. The installation of the thermistor can be completed within several minutes.

The final assembly step consists of filling the cavity around the thermistor with Ecobond 24 epoxy, which forms a rigid structural foundation for a seal around the thermistor and electrical wire. Prior to en-

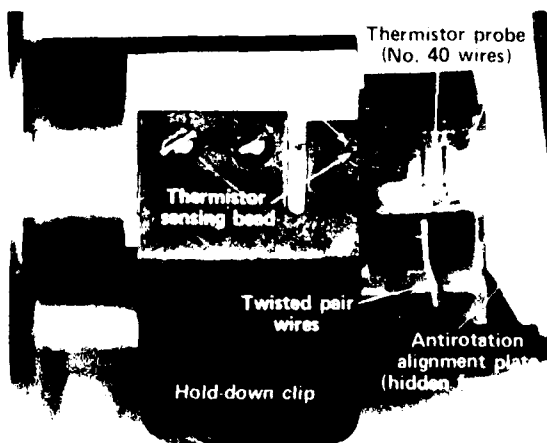


Figure 3 — The soldering fixture.

capsulation, a horseshoe-shaped mold is clamped against the nosepiece to complete the cavity walls and form the contour of the nosepiece's leading surface. No primers are required on the glass-bead or urethane surface to achieve bonding; this is an advantage because some primers absorb water and cause leaks after extended submersion. The urethane epoxy bond without primers has proven to be stronger than the urethane material.

Figure 4 shows the horseshoe-shaped thermistor potting mold, a completed thermistor nosepiece and a protective cover that clips over the nosepiece to prevent accidental breakage during succeeding calibration procedures and total system assembly.

RESULTS

The newly developed thermistor mounts look similar to those made prior to this work; however, they have little in common with the earlier versions. The choice of materials, the type of electrical conductor wires, the complexity of molds and fixtures, and the simplicity of assembly procedures are changed markedly.

Samples taken randomly from production were mechanically fatigue-tested by severely twisting the nosepiece mounts while under hydrostatic pressure (300 psi). No measurable degradation to the thermistor assemblies was found after tens of thousands of cycles. Similar tests on previously built units showed insulation loss after several hundred similar cycles.

The towed thermistor array built for a fall 1982 field test was used for four weeks of shipboard operation, including five days of continuous 24-hour towing. Field testing involved daily flexing and twisting of the thermistor nosepieces as the array was wound around the winch and over the towing sheave. All modes of failure, including insulation loss and mechanical glass breakage, affected less than 3% of the assemblies, a considerable improvement over prior experience. A second and independent thermistor system was built for a field test conducted in the spring of 1983. No encapsulation failures occurred after several weeks of field test use.

Thermistor fabrication time is now reduced by 65%, from over 10 hours per unit to 3½ hours. Additional savings are realized because few replacement units are needed for spares, and field repair is almost eliminated.

Although these techniques were developed specifically to encapsulate glass-bead thermistors, they are being used in several other areas and may eventually prove useful for encapsulating other types of oceanographic sensors.

REFERENCE

E. E. Mobley et al., "A New Thermistor Chain for Underwater Temperature Measurement," Oceans '76 Conf., Washington, D.C. (15 Sep 1976).

This work was supported by the Office of the Chief of Naval Operations, OP 213.

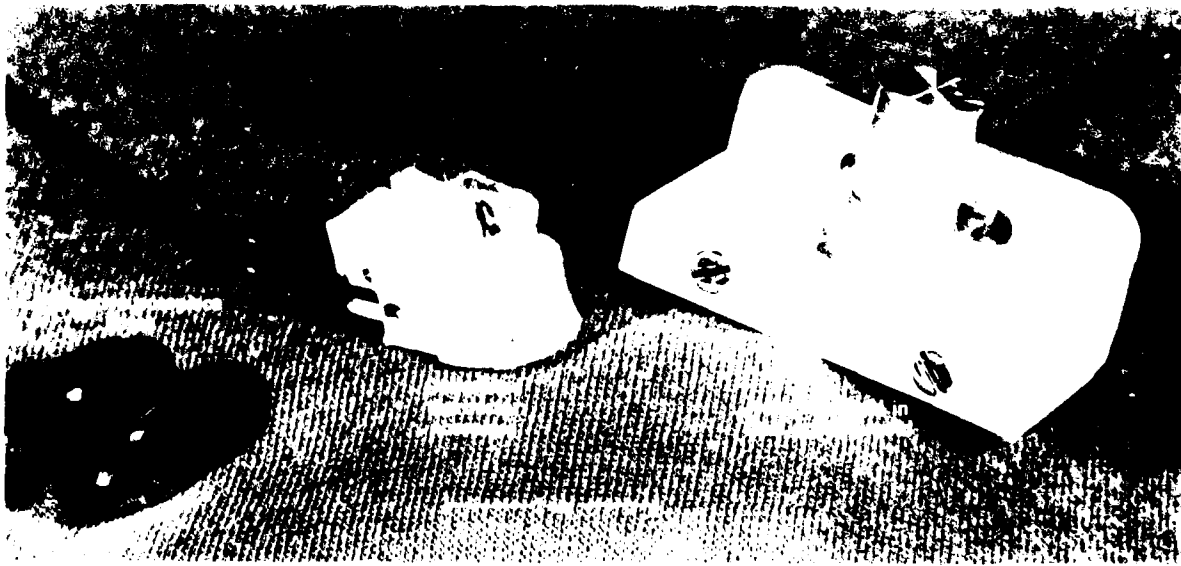


Figure 4 — The horseshoe-shaped thermistor potting mold, the completed thermistor nosepiece, and the protective cover.

MODEL FOR THE ASSESSMENT OF ANTISUBMARINE ACOUSTIC SURVEILLANCE SYSTEMS

J. L. Bowen and R. E. L. Johnson, Jr.

A computer model of the detection of a submarine by a field of passive acoustic sensors has been developed. A Monte Carlo model, it generates contact statistics based on the submarine signature (including its time varying components), the motion of the submarine relative to the individual sensors (including the associated effects on received signal levels), and the environment (including the rapidly changing background noise).

BACKGROUND

The problem was to assess the acoustic detectability of a submarine in a field of towed array sonars. The approach of developing a simulation model was adopted because many random and dynamic effects are involved in an encounter between a submarine and a field of sensors. Those effects, in the aggregate, would make the development of analytic expressions for the desired results extremely difficult. The results the model generates are quantitative estimates of surveillance performance in terms of operationally significant measures. For example, estimates of contact and loss rates as functions of sensor density in different operating environments, with the implied anisotropic and dynamic behavior, are particularly valuable performance measures. The model provides the distribution of such measures for various combinations of steady state and time dependent radiated signals. Accordingly, the results readily apply to the quantitative examination of such things as the effects of noise reduction as a countermeasure.

DISCUSSION

Overview

Figure 1 is a simplified diagram of the major functions in the model. The basic objective of the calculations is to find the signal excess (SE_t) at each acoustic receiver in each time interval. Signal excess is defined as the amount of signal to noise ratio in excess of a threshold value needed to discern the presence of a target, with the detection thresholds varying with the characteristics of the signal, e.g., stability and spectral

The various types of acoustic signals radiated by a submarine encompass differences in level, spectral

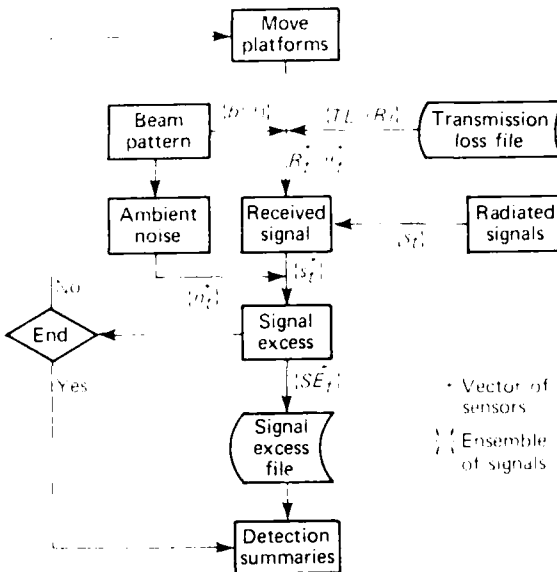


Figure 1 — Flow chart of model functions

content, frequency of occurrence, and duration. Towed-array receivers have azimuthally varying response functions that selectively enhance energy arriving from preferred directions. Signals are attenuated in water by an amount that is range- and frequency-dependent (transmission loss, $TL(R)$). The received signal level (s) varies with time because of changing target-receiver distances (R) and angles (θ) that are inherent in any surveillance encounter. Furthermore, all the signals are accompanied by frequency-dependent, time-varying noise (n) because the noise background contains important contributions from the sea surface and from shipping in the region, both random functions of time.

One can calculate a file of signal excess based on these dynamic factors, and the file can be manipulated to yield detection statistics of operational interest.

Model Structure and Specifications

The model developed to represent the necessary features of the problem is a time-step Monte Carlo simulation, coded in Fortran 77 and currently available on a VAX Model 11-780 computer. The model has about 3000 lines of code and requires some 430,000 bytes of storage, of which slightly more than half is needed for

transmission loss tables. It is divided into subroutines, distinct blocks of which perform each of the functions in Fig. 1. Wherever possible, specific parameters or data are provided externally through data files or program inputs. Table 1 identifies the major functional blocks and the types of data provided to each.

Table 1 — Functional modules and inputs

Module	Functions	Input Data
Main	Reads run parameter Performs detection calculation Generate output of results	Run parameter Detector threshold Output specification
Sensor	Develop received signal	Target signature Transmission loss
Ship motion	Compute ship position versus time	Ship motion parameters
Target motion	Compute target motion versus time	Distribution function in headwind and downwind change
Ambient noise	Supply ship noise Supply wind noise	Parameters characterizing ship noise field Transmission loss Mean and standard deviation of noise versus frequency and wind speed
Run	Read initial file input	

Fundamentally, the model allows the placement of some number of receivers at initially specified locations, and then it moves them. At present the receivers are towed arrays, and they are being moved back and forth along parallel track segments. The target submarine conducts a "random" patrol (at present) in the midst of the moving receivers while its detectability is evaluated. Target motion is constrained to remain within the field of sensors in a way that simulates unconstrained motion in a larger field.

Typical runs involve a target on patrol for 800 hours in a field of nine sensors; computations are performed every 6 min. One replication of such a run requires about 90 min of central processing unit time. Typically, more than one replication was found to be unnecessary because the temporal variations over one 800 h run are sufficient to establish reliable statistics.

Submodule Characteristics

The submodule realizations that constitute the model are based extensively on available data. A statistical characterization of submarine motion was devel-

oped, as were distributions of randomly timed intermittent acoustic emissions. Signal source levels are based on at-sea measurements. The model treats the signal spectrum as if it were composed of discrete bands of varying widths; each band is associated with properties necessary to infer detection thresholds (treated as model inputs) and to select the suitable transmission loss from data files representing specific environments.

The most complex and challenging submodule is the one that estimates ambient noise. As was noted earlier, the intrinsically time-varying constituents of noise result from shipping and wind. Those components are modeled separately and are then power summed.

Shipping noise is based on a time series generated by a model that allows for the movement of ships about a receiver, thus changing not only distances but also the bearings relative to the receiver array pattern. The total shipping noise at any time is the incoherent sum of contributions (beam formed as necessary) from individual ships. Shipping-noise time series are frequency dependent because the ship-radiated levels, the propagation to the receiver, and the array patterns are all frequency dependent. The shipping-noise time series are then processed by a derivative model that abstracts the temporal behavior of the mainlobe and sidelobe contributions separately; the former cause short duration peaks or spikes in the noise, while the latter make more slowly varying contributions.

The wind-noise variations are induced primarily by changes in wind speed. In the model, wind speeds are drawn randomly from regionally and seasonally specific distributions at time intervals selected from a second (exponential) distribution. They are then converted to wind-noise variations in time; the mean and standard deviation of an (assumed) Gaussian process are related deterministically to the wind speed, and random draws are made from that distribution. The procedure results in a rapid and small wind-noise variation superposed on a (typically) slower and larger variation induced deterministically by wind speed changes.

It should be noted that this complex model of ocean ambient noise follows physical evidence that is widely documented in the literature. It has been carefully compared with, and influenced by, extensive at-sea measurements made by laboratory personnel, particularly those made in 1980 and 1981.

Model Outputs

The principal results generated by the model, summarized in Table 2, were selected so as to permit broad analyses of a variety of factors relating to surveillance system effectiveness. Each output is computed for

Table 2 — Model outputs for each signature element.

Histograms
Number of ships holding contact
Time since last contact
Length of time contact was held
Length of time contact was lost
Summary statistics
Probability that target is in contact
Total number of detections
Mean and standard deviation of ranges of detection

the different signal elements in the submarine signature; these elements can be combined in different ways, including a combination incorporating all potentially detectable signals.

Analyses of the outputs from a particular run permit the identification of the most significant (i.e., most compromising) elements in the signature. Surveillance effectiveness can be estimated in terms of distributions of times in and out of contact, probabilities that at any random time the searchers are in contact with the target, and the distributions of times since

contact was last held. The effects of variations in numbers (density) of search platforms, target or search platform speeds, or levels of target-radiated noise can be established with successive runs of the model.

ACKNOWLEDGMENT

We are indebted to the following people who participated in development of the assessment mode. E. J. Moses, assisted by W. Knox, directed model implementation by ORI, Inc. The noise model was developed by J. R. Davies (ORI) and A. C. Biondo (API), while R. Doolittle (as a consultant to ORI) contributed significantly to the reconciliation of noise model results and field measurements.

This work was supported by the Department of the Navy.

BIOMEDICAL SCIENCE AND ENGINEERING

INTRODUCTION

The collaborative biomedical program between API and The Johns Hopkins University's School of Medicine began in 1965. The program brings together the expertise in medical and biological sciences found at the Medical School with those in the physical sciences, engineering, and mathematics found at API, in order to solve significant problems in biomedical science and health-care delivery. From the beginning, the collaboration has received strong support from the University's leadership and encouragement from the Navy, API's sponsor. The strength of the collaboration is evidenced by the joint appointments made within the two University divisions: 18 members of the API staff have appointments at the Medical School, and 16 members of the medical faculty have Principal Professional Staff appointments at API.

Currently, there are 30 active projects in ophthalmology, neurosensory research and instrumentation development, cardiovascular systems, patient monitoring, therapy and rehabilitation, clinical information systems, and clinical engineering. Thirty-six API physical scientists and engineers are working in collaboration with biomedical scientists and clinicians from 12 JHMI departments on those projects. Their research and development results are published in the peer-reviewed scientific and medical literature. Since the program's inception, over 390 papers have been published, and there are even more published abstracts and presentations at major scientific and medical meetings.

The articles appearing in this year's *API Selected Accomplishments* indicate the breadth of the collaborative biomedical effort. They describe efforts in ophthalmology, the magnetic detection of brain waves, artery repair, and the development of devices for specific medical problems.

RETINAL VASCULAR DEVELOPMENT IN KITTEN AND PUPPY EYES

R. W. Flower (API) and D. S. McLeod, G. A. Lutty,
B. Goldberg, and S. D. Wager (JHMD)

The full-term newborn kitten and puppy have eyes whose retinal vascularization is as incomplete as that of the eyes of premature born human infants. These animals therefore are used extensively as experimental models to study the pathogenesis of retinopathy of prematurity, a blinding retinal disorder occurring mainly in premature infants and associated with preterm birth or respiratory distress syndrome. Observations made during this study suggest some shared or common features in the pathogenesis of those disorders and lead to a more precise definition of the stages of vascular development after the neonatal period than previously existed. Moreover, the collected data add to the data describing the process of eye development.

BACKGROUND

It has long been accepted that the human retinal vasculature is proximately through the sixteenth week of gestation, the physiological requirement apparently being met by blood flow through the adjacent choroidal vasculature and the hyaloid arterial system. Ashton's histologic studies of fetal eyes have established that after the sixteenth week the avascular retina is invaded by a vanguard of mesenchymal cells from the stalk of the optic larynx at the optic nerve head. As this vanguard of cells moves centrifugally across the face of the retina toward the periphery, it lays down a network of primitive endothelial cells, probably that gradually differentiate to become arteries and capillaries on the inner surface. Normally, on full-term birth, the first arterioles and capillaries of the periphery of the retina reach the macula, the last part of the retina to reach that point.

Michaelson et al. (1974) reported that the first retinal vessels appear in the macula of the mouse embryo at day 11.5, and that they have reached the optic disc by day 13.5. They also found that the retina of the mouse is fully vascularized by day 16.5. In the dog, Ashton (1962) reported that the first retinal vessels appear at the twelfth week postpartum. More recently, Ashton (1974) described the first retinal vascularization in the mouse by two days of age, and in the dog by 10 days postpartum. In the cat, Ashton (1962) reported that the first retinal vessels appear at the twelfth week postpartum. More recently, Ashton (1974) described the first retinal vascularization in the cat by 10 days postpartum.

Flower (1978) described the vascularization of the retina in the day 54 dog by birth, the average gestation 60 to 65 days, three times an earlier report of retinal vascularization in the dog. He also reported that vessels were present at the entire retina by the twelfth postnatal day. It thus appears that while the human, cat, and dog retina may all vascularize similarly, there are significant differences in how far during the gestation vascularization is initiated and how rapidly it proceeds.

For many years, the parallelism in human and animal retinal development and the observation that the initial retinal vascularization of the animal occurs after exposure to the same air that of the premature human have justified the use of those animals as animal models for studying the pathogenesis of retinopathy of prematurity (ROP). The use of the animal model most often has consisted of comparing retinal vascular patterns of untreated to oxygen-exposed fetuses at about three to four weeks of age, that is, two to three weeks following a normal period of uterine oxygen exposure. For the most part, the visualization of the vascular patterns has been sufficient for the comparisons, and the same time honored technique of ink infusion used by Michaelson in 1954 is still widely used. However, as investigations into the mechanisms that initiate retinal vascular changes in ROP become more sophisticated, more refined methods must be developed in order to acquire more precise data concerning both the morphogenesis and the physiology of the retinal microvasculature during the perinatal period. Unfortunately, Michaelson's technique and variations of that involve injection of tracer substances subject the immature retinal vasculature to extremely compromised blood flow (low pH), and thermal pressure. All can produce artifacts that mask subtle vascularization changes, particularly in the macula, to detect the first retinal vessels.

This investigation was undertaken to develop a technique for preparing the isolated kitten and puppy retina that minimizes vascular disruption. This will facilitate the study of the development of the retina in the isolated animal, and the development of the retina in the intact animal. The second objective was to compare the early development of the newborn kitten and puppy retinal vasculature. Our study concern that difference in the puppies' blood vessels was stimulated by comparison of the observations of Michaelson and Ashton that the first retinal vascularization in the newborn puppy appears to resemble more

cover the calculation of the two main types of prematurity found in man than that of the newborns themselves.

METHODS AND RESULTS

An enzymatic electron microscopic technique that minimizes the geometric effect was developed. It makes possible for the first time to visualize the retinal nerve fiber layer in considerable detail while avoiding any damage and distortion of tissue substance. By means of this technique the process of normal retinal vascular development in the newborn kitten and puppy was observed and described in detail. To date, the technique has been used successfully on approximately 150 patients and in another data from a variety of physiologically states including retinal tissue eight monomeric eyes from three litter and 17 Beagle puppies from four litters that served as control and comparison. At various ages ranging from one day to several weeks, the animals were killed and their retinae were prepared for examination by our technique which is a modification of the standard photometric technique for the enzyme alkaline phosphatase (ALPase) of Wachstein and Meisel.¹ It was demonstrated that a significant similarity exists between the development of the animal eye and human eye than had been described previously.

Two thin-mounted retinae prepared by this method are shown in Fig. 1, where the relatively uniform ALPase activity of the colloidular glomerules evinced a low magnification. More pronounced activities found in arteries and arterioles, particularly where active areas of the capillary bed, somewhat less, although ALPase activity was more intense and varied.

The pattern characteristic of the retinal vascular development in the kitten and puppy is depicted by the sequence of developmental stages reported in Fig. 2. The micrographs are of 18 kittens ranging in postnatal age from 1 to 24 days. In the earliest stages, the vessels appear as a few fine threads of blood vessels roughly 0.09 mm toward the periphery of the eye. These are followed by a few small, 0.1 mm in diameter, vessels which will become the first true capillaries. As the vessels increase in size, they become more numerous and more complex.

At an early stage, the diameter of developing arterioles can be identified by the diffuse, often vacuous, narrow (Fig. 2b), the endocanal of the small vessels due to vascularization. The peripheral vessels consist of tubular as well as the irregularly branched, 0.1 mm in diameter, and the larger, dilated vessels of capillaries (Fig. 2c and 2d). Macrocavitation of the vascular system is evident at 17 and 18 days (Fig. 2e and 2f). The peripheral vessels are now large, 0.2 mm in diameter, and the central vessels are 0.3 mm in diameter (Fig. 2g and 2h). Macrocavitation of the vascular system is evident at 17 and 18 days (Fig. 2e and 2f). The peripheral vessels are now large, 0.2 mm in diameter, and the central vessels are 0.3 mm in diameter (Fig. 2g and 2h).



Figure 1—ALPase reaction of peripheral retinae in the puppy. (a) A low power of the peripheral retinae and the colloidular glomerules.

and a elliptical interface. Just beyond the leading edge of vascularization, the diameters of the segments are equal and they become tubular because they appear to have fusion.

At an early stage, the diameter of developing arterioles can be identified by the diffuse, often vacuous, narrow (Fig. 2b), the endocanal of the small vessels due to vascularization. The peripheral vessels consist of tubular as well as the irregularly branched, 0.1 mm in diameter, and the larger, dilated vessels of capillaries (Fig. 2c and 2d). Macrocavitation of the vascular system is evident at 17 and 18 days (Fig. 2e and 2f). The peripheral vessels are now large, 0.2 mm in diameter, and the central vessels are 0.3 mm in diameter (Fig. 2g and 2h). Macrocavitation of the vascular system is evident at 17 and 18 days (Fig. 2e and 2f). The peripheral vessels are now large, 0.2 mm in diameter, and the central vessels are 0.3 mm in diameter (Fig. 2g and 2h).

The peripheral vessels consist of tubular vessels, which are large, 0.2 mm in diameter, and the central vessels are 0.3 mm in diameter (Fig. 2g and 2h). Macrocavitation of the vascular system is evident at 17 and 18 days (Fig. 2e and 2f). The peripheral vessels are now large, 0.2 mm in diameter, and the central vessels are 0.3 mm in diameter (Fig. 2g and 2h).

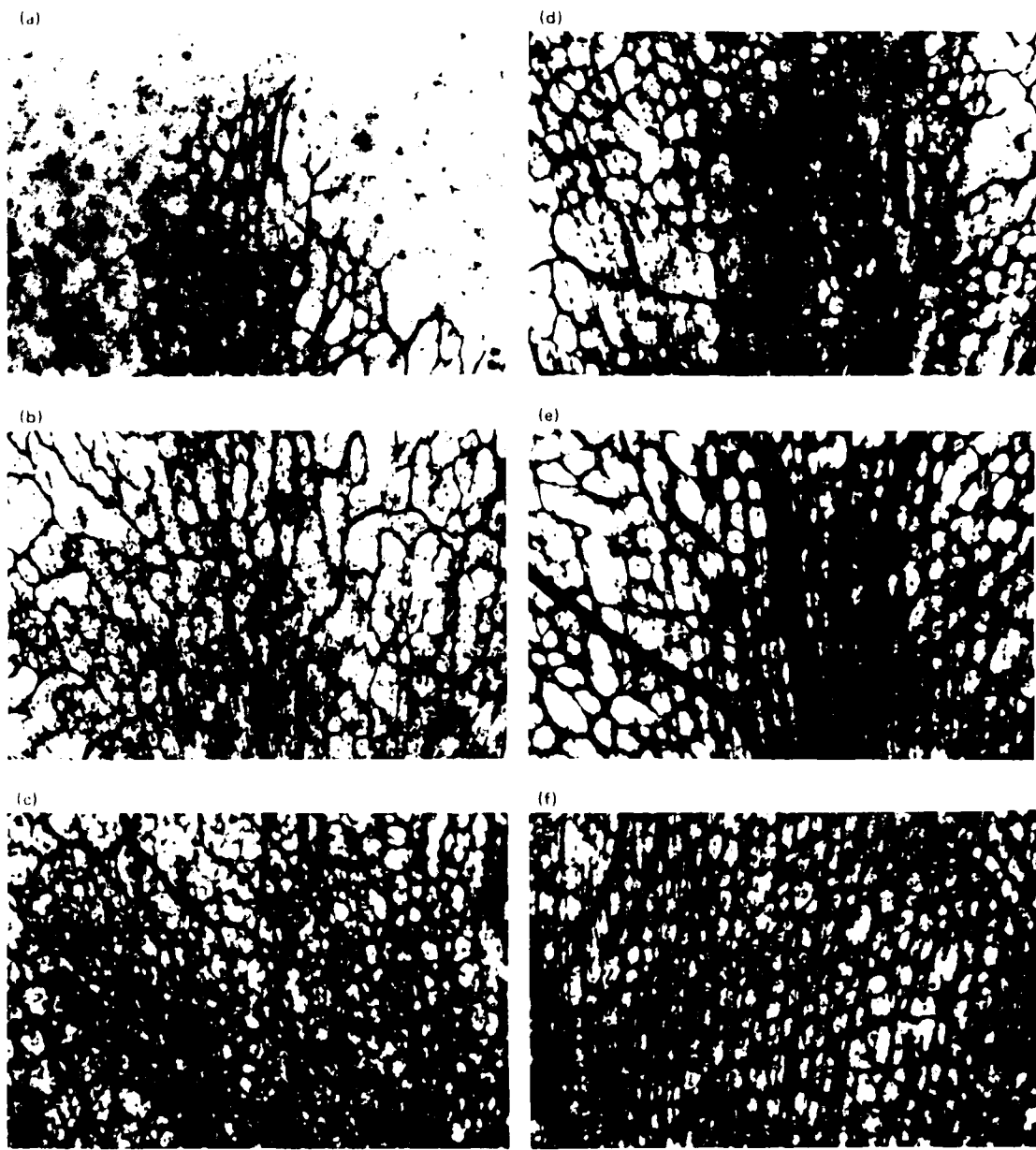


Figure 2. Capillary patterns in rat optic nerve fiber layer at different stages of development. (a) At 10 days postnatal, the first capillaries appear in the outer part of the nerve fiber layer. (b) At 20 days postnatal, the capillary network is more extensive. (c) At 30 days postnatal, the capillary network is well developed. (d) At 40 days postnatal, the capillary network is very dense. (e) At 50 days postnatal, the capillary network is fully developed. (f) At 60 days postnatal, the capillary network is fully developed and appears similar to that seen in adult rats.

charact are formed by coagulation of intravascular plasma and conglutinates of the components of the glomerular capillaries. The arteries of the optic nerve apparently evolve through a different process and are found to be incomplete just beneath the capillaries. The embryonic capillaries that penetrate capillaries throughout the reendothelial process undergo reduction

in number, size, and luminal diameter (compare Fig. 2 to 2*D*).

Finally, when a capillary bed of mature appearance is established in the nerve fiber layer, a second distinct layer of capillaries begins to develop in the inner and outer aspect of the outer nuclear layer (see Fig. 2*E*

This deep lying net appears to be an outgrowth of the original superficial one and begins to develop near the edge between the fourteenth and twenty-first days.

On the basis of observations of normal full term kittens and puppies during the first three postnatal weeks, we propose that retinal vascularization involves the steps discussed below.

Initiation of Vascularization

Spindle cells advance along fine lateral processes running through tunnels formed within and between the Müller cell processes just below the HM (fig. 3). (Müller cell processes appear to be the "skeletal matrix" to which the other retinal tissues are attached.) The endothelial cells form cords that then develop lumens, creating primordial vessels (fig. 2a). Vessel morphogenesis appears to involve endothelial mitosis and vessel sprout generation (fig. 4a) as well as primordial vessel formation resulting from differentiating hemangioblastic masses that anastomose with one another (fig. 4b). It is possible that the hemangioblastic masses may evidence the presence of mesenchymal precursors to capillized vessels. This would indeed make vascularization of the newborn animal retina—especially that of the puppy—comparable to that of man.

Arteries

Arterial vessel formation occurs along preferential pathways whose courses are probably genetically based; we speculate that a manifestation of that bias may be the pattern and characteristics of primary tunnel through the inner Müller cell processes. The most newly formed distal end segments of the advancing



Figure 3 — Transverse imprints of the optic nerve fiber layer between two adjacent retinal layers at 6000 \times magnification. W.P. of the optic nerve fiber layer, Müller cell processes, and primary blood vessels. Note the importance of the primary blood vessels in the development of the vascular plexus. (Prepared by the electron microscope technique of Dr. J. E. H. Smith, Department of Anatomy, University of Alberta, Canada.)



Figure 4 — (a) Sprouting of new blood vessels from the vascularized skeletal matrix of the optic nerve fiber layer. (b) Hemangioblastic masses appearing to be the precursors of primary blood vessels. (Prepared by the electron microscope technique of Dr. J. E. H. Smith, Department of Anatomy, University of Alberta, Canada.)

arteries lie just proximal to the lead in edge of primordial vessel formation. The ends are in the form of incompletely closed loops, and they lie below and are concurrent with the proximal portions of completely closed loops belonging to the primordial vascular bed.

Each newly formed segment of an artery lies just below the plane occupied by the respective supply artery of that area. How far a part of the retinal edge lies below the artery may vary toward the HM, apparently in proportion to the size of the artery, but it is not constant enough to be of practical value in tracing the course.

Embryonic Capillaries

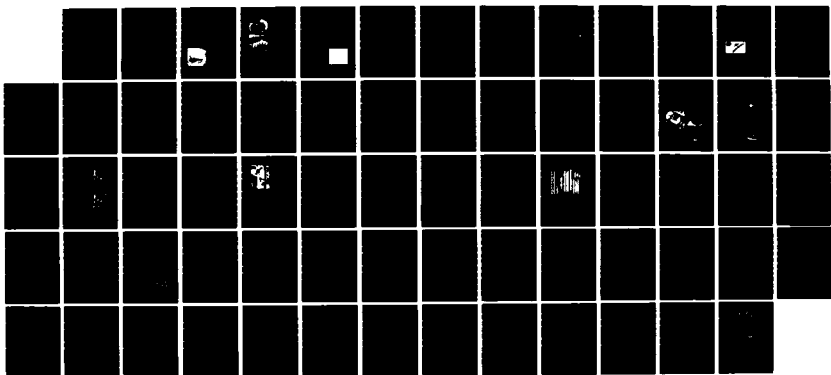
At approximately the time of initiation of formation of the Mullerian glial cell nuclei, the stroma of the retina appears to undergo differentiation. HM appears to become covered with a reticular layer of connective tissue. This accounts for the appearance of a very large number of capillaries characteristically distributed in the outer nuclear layer (figs. 2, and 20). These capillaries are the embryonic capillaries

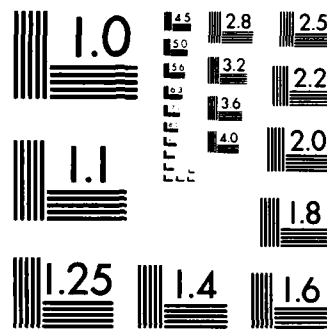
AD-A156 674 DEVELOPMENTS IN SCIENCE AND TECHNOLOGY(U) JOHNS HOPKINS 2/2
UNIV LAUREL MD APPLIED PHYSICS LAB 1983 JHU/APL/DST-11
N00024-83-C-5301

UNCLASSIFIED

F/G 5/2

NL





MICROCOPY RESOLUTION TEST CHART
NATIONAL BUREAU OF STANDARDS 1963 A

overlie arteries, capillary-free zones eventually form as the arterial vessel gradually moves into and occupies the capillary plane. We speculate that capillary atrophy may, in fact, be initiated by displacement of the capillaries.

Veins

Veins are formed by the coalescence of embryonic capillaries into lacunas, which then remodel into veins. The pattern of venous vessels appears to depend passively on the earlier developed pattern of arterial vessels, the shape and size of each vein being a consequence of the total blood flow and pressure it must accommodate.

REFERENCES

- ¹N. Ashton, "The Mode of Development of the Retinal Vessels in Man," in *The William MacKenzie Symp. on Ocular Circulation in Health and Disease*, J. S. Cant, ed., C. V. Mosby, St. Louis (1969).
- ²I. C. Michaelson, *Retinal Circulation in Man and Animals*, Charles C. Thomas, Springfield, Ill. (1954).
- ³G. D. Aguirre, L. F. Rubin, and S. I. Bistner, "Development of the Canine Eye," *Am. J. Vet. Res.* **33**, 2399 (1972).
- ⁴N. Ashton, B. Ward, and G. Serpell, "Effect of Oxygen on Developing Retinal Vessels with Particular Reference to the Problem of Retrobulbar Fibroplasia," *Br. J. Ophthalmol.* **38**, 397 (1954).
- ⁵M. Wachstein and E. Meisel, "Histochemistry of Hepatic Phosphatases at a Physiologic pH (with Special Reference to the Demonstration of Bile Canaliculi)," *Am. J. Clin. Pathol.* **27**, 13 (1957).

This work was supported by U.S. Public Health Service Grant EY-02482(NEI) and Independent R&D.

SEM STUDY OF THE HYALOID VASCULAR SYSTEM IN NEWBORN MICE EXPOSED TO OXYGEN

P. M. Bischoff and S. D. Wajer (JHMI)
and R. W. Flower (APL)

For a significant period during their development, the vitreous and lens of the eye are nourished by the hyaloid vascular system, a network of blood vessels that consists of the tunica vasculosa lentis (vessels that surround the immature lens) and the vasa hyaloidea propria (vessels that permeate the vitreous). As the eye matures, the hyaloid system gradually atrophies, and it disappears shortly after maturation of the eye. Several species of animals, including cats, dogs, and mice, normally are born full term with immature eyes, providing an opportunity to study the hyaloid system. It has been reported¹ that neovascularization occurs in the tunica vasculosa lentis of newborn mice reared in environments of high oxygen content, but our study produced evidence that indicates instead that oxygen exposure delays the normal atrophy of the hyaloid vessels, causing them to persist for an abnormally long time postnatally.

BACKGROUND

It has been suggested that the hyaloid vasculature of newborn mice undergoes vasoproliferation after oxygen exposure and therefore might be used as an experimental model of neovascularization. A scanning electron microscopic (SEM) technique that provides visualization of the entire hyaloid vascular system was used to study its response in mice exposed to elevated oxygen levels. Marked differences were found between the hyaloid regression in oxygen-exposed mice compared to control mice kept in air, but no evidence of neovascularization was found in any group. It was concluded that the dilated, persistent hyaloid vessels and accompanying exudates may have been misinterpreted previously as vasoproliferation in the histologic cross sections of the earlier studies, indicating that the new-

born mouse is not a proper model of neovascularization.

For a significant period during early development of the eye, the hyaloid vascular system constitutes the main blood supply for the developing lens and vitreous. As the eye matures, the metabolic needs of the lens and vitreous gradually decrease, and the retinal vasculature matures concomitantly with the atrophy of the hyaloid vasculature; yet both the retinal and hyaloid vascular systems share a common arterial supply at the optic nerve head. It has been long recognized that both of these vasculatures are affected by prolonged exposure to elevated oxygen levels.

The mouse eye is suitable for the study of the hyaloid vessels because these vessels are fully developed at full-term birth (Fig. 1). The retinal vessels, on the other hand, have only begun to form near the optic disc at birth; this vascular development is comparable to that in the human embryonic eye at about three to four months gestation. The changes seen in the newborn mouse during the first four weeks of life may reflect (at least approximately) human eye development between the fourth month of gestation and birth.

In early experiments, the hyaloid vessels of oxygen-exposed newborn mice were examined by histologic cross sections made of whole eyes. It was reported that a persistence and probable proliferation of the retrorenal hyaloid vessels occurred and that the retinal vessels were constricted.² Later studies using eyes injected with

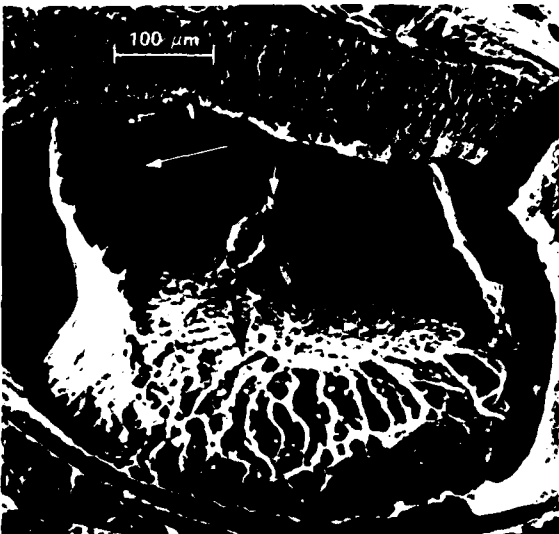


Figure 1 — Anatomy of the normal hyaloid vasculature from a 3-day-old mouse eye: hyaloid artery (short white arrow), hyaloid vessels nourishing the posterior lens (black arrow), and vitreal cavity (long white arrow) (bar gauge = 100 μm).

India ink suggested a "profuse proliferation of new vessels" in the hyaloid of newborn mice exposed to oxygen for 5 days and then returned to air for 5 days.³ Patz first suggested the SEM technique to study the oxygen effect on the mouse hyaloid and found a "second layer of vessels" overlying the persistent hyaloid. However, he was not able to distinguish between "abnormal persistence or possible proliferation" of those vessels. Using the same technique and procedure but examining mice in different age groups during and after oxygen exposure, we attempted to determine if the hyaloid vasculature in oxygen-reared mice truly develops neovascularization.

METHODS

One-day-old albino mouse litters and mothers were reared either in air as controls or in 70% oxygen/30% nitrogen as test animals. Test mice were raised in isolettes ventilated with the humidified gas for up to 14 days and then returned to room air. Mice from each group were killed on days 1, 3, 7, 10, 14, 21, and 28. Specimens were prepared using a standard biologic technique for SEM.

RESULTS

In contrast to the vasoconstriction response observed in the developing retinal vessels during continuous exposure to 70% oxygen/30% nitrogen, it is noteworthy that the hyaloid vessels remained patent. While there was little change in the vascular pattern during the first days of oxygen exposure, by the second week of continuous hyperoxia a vascular persistence of delayed vascular regression accompanied by increasing vascular distention occurred in the tunica vasculosa lentis (TVL); this occurred to an even greater extent in the vasa hyaloidea propria (VHP). These oxygen-induced changes were even more pronounced when the mice were returned to room air for one week following 6 to 14 days of oxygen exposure (Fig. 2a). In addition to vasodilation in both the TVL and the VHP, there often were exudates in the primary vitreous that partially or totally masked the posterior surface of the lens. After a second week in air, those vessels always became smaller and continued their regression. In no specimen examined was there ever a greater number of TVL vessels than was present in a normal newborn eye, and there was no indication of neovascular tuft formation.

Our interpretation of the data from this study leads us to the following conclusions with respect to the mouse eye as an experimental model:

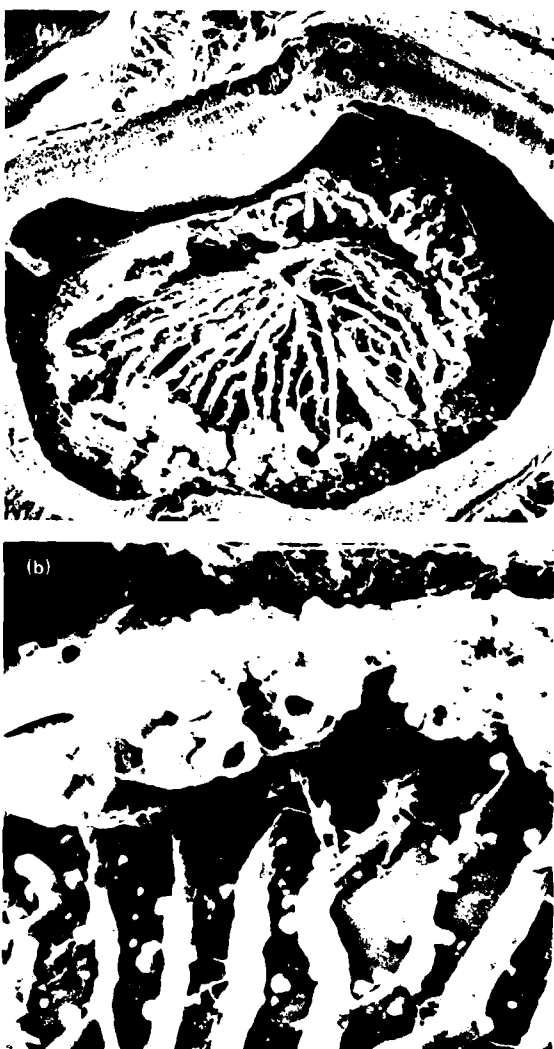


Figure 2 — Scanning electron micrographs of the eye from a 10-day-old mouse reared in oxygen for 6 days and then returned to room air for 3 days. (a) Note huge vascular distention in vitreal hyaloid vessels overlying the hyaloid vessels of the posterior lens ($\times 75$). (b) Higher magnification view. Note the open and distended overlying vessels embedded in exudates and cells ($\times 370$).

1. The mouse hyaloid vasculature appears not to be a model for the formation of intraocular neovascularization.
2. Oxygen exposure of newborn mice leads to pathologic persistence and distention in the TVL and also, to an even greater extent, in the VHP with subsequent bleeding and exudate deposition in the primary vitreous. Conceivably, pathologic changes of the vitreal branches of the hyaloid vasculature could play a role in some of the cases of advanced stages of retrorenal fibroplasia (a blinding retinal disease of premature infants associated with prolonged oxygen exposure).
3. The hyaloid vasculature is an appropriate model for studying the relationship between atrophic vessels (the hyaloid system) and a developing vasculature (the retinal circulation); these two systems are hydrostatically coupled to "active" vessels capable of responding to changes in the arterial pO_2 level. Such vascular combinations may exist in human diseases. Examples of the relationship might be found between extant preretinal vessels and the normal retinal vasculature in diabetic retinopathy following laser photocoagulation therapy or even in cases of regressing retrorenal fibroplasia.

REFERENCES

- 1 P. M. Bischoff, S. D. Wajer, and R. W. Flower, "Scanning Electron Microscopic Studies of the Hyaloid Vascular System in Newborn Mice Exposed to O_2 and CO_2 ," *Graefe's Arch. Clin. Exp. Ophthalmol.* **220**, 257-263 (1983).
- 2 A. Patz, A. Eastham, D. H. Higginbotham, and T. Kleh, "Oxygen Studies in Retrorenal Fibroplasia: II. The Production of the Microscopic Changes of Retrorenal Fibroplasia in Experimental Animals," *Am. J. Ophthalmol.* **36**, 1511-1522 (1953).
- 3 N. Ashton, "Some Aspects of the Comparative Pathology of Oxygen Toxicity in the Retina," *Br. J. Ophthalmol.* **94**, 715-743 (1982).

This work was supported by U.S. Public Health Service Grant EY-02482 and Independent R&D.

STROMAL DAMAGE IN RABBIT CORNEAS EXPOSED TO CO₂ LASER RADIATION

R. L. McCally, C. B. Bargeron, W. R. Green (JHMI), and R. A. Farrell

We have found that threshold damage of all types of corneal cells—stromal, epithelial, and endothelial—is correlated with their achieving similar peak temperature increases that have similar dependences on exposure duration. This suggests that all these cell types have the same thermal damage mechanism.

BACKGROUND

The cornea is the transparent front wall of the eye through which we see. From front to back, it consists of a tear layer (about 6 μm thick), a cellular layer five to six cells thick called the epithelium (about 40 μm thick), the collagenous connective tissue layer called the stroma (about 350 μm thick), and a single layer of cells called the endothelium (about 5 μm thick). Cells called keratocytes are interspersed within the stroma and occupy 3 to 5% of the stromal volume.

Because the cornea is about 80% water, it strongly absorbs infrared radiation. Indeed, 99% of the 10.6 μm radiation emitted by a CO₂ laser would be absorbed in the first 48 μm of penetration and would therefore raise the temperature of the cornea's epithelium. Thus, most investigations into the nature of CO₂ laser damage and the threshold conditions that cause it have concentrated on this cellular layer.^{1,3} However, heat conduction causes the spread of the thermal insult to deeper layers. In this regard, we recently have reported the threshold conditions for damaging the endothelium^{4,5} and have determined the temperature histories at the endothelium following such exposure.^{5,6}

During the course of those investigations, we noted that corneas that had been exposed above the threshold for epithelial damage, but below that for endothelial damage, developed characteristic bowl-shaped lesions in the stroma. Examinations 48 hours following such exposures showed that the edges of the lesion were sharply defined, and histology showed that the injured area was essentially devoid of cells. Furthermore, the keratocytes just outside the cell-free region were found to be normal. These observations suggested to us that the keratocyte damage depends sensitively on the thermal insult. Thus, we designed experiments to determine the conditions that produce minimal thermal damage to keratocytes in order to discover how their damage thresholds compare to those of the other corneal cells.⁷

RESULTS

A CO₂ laser operating in the TEM₀₀ mode, which has a Gaussian irradiance profile, was used to produce stromal damage.⁷ With the laser operating at 0.27 W, the 1/e radius of the beam was set at 0.94 mm and the peak irradiance was 9.7 W/cm². At 1.2 W, the 1/e radius of the beam was 1.2 mm, and the peak irradiance was 26 W/cm². The exposure durations for these two power levels were 2.5 and 0.4 s, respectively. Both exposures are about four times longer than that required to produce minimal epithelial damage at the respective power levels,^{1,3} and both produced similar damage to the cornea.

Figure 1 is a slit-lamp photograph taken 48 hours following an exposure of 26 W/cm² for 0.4 s. It shows the profile of the bowl-shaped lesion at its deepest point. Figure 2 is a composite light micrograph of another cornea exposed the same way as the one in Fig. 1. The sections were cut as nearly as possible to a plane passing through the center of the circular damage area. At its deepest point, the essentially cell-free lesion extends about halfway through the stroma. Higher magnification electron micrographs of this lesion (not presented) show that the few remaining cells are dead. They have small vacuoles and show a loss of normal



Figure 1 — Slit-lamp photograph of a laser lesion 48 hours after an exposure of 26 W/cm² for 0.4 s. The slit lamp was arranged so that the light was incident perpendicular to the surface of the cornea at the middle of the circular lesion. The bowl-shaped profile of the lesion at its deepest point is revealed.



Figure 2 — A montage of light micrographs of a stromal lesion 48 hours after an exposure of 26 W/cm^2 for 0.4 s. The essentially acellular lesion extends about halfway through the stroma. The lesion is bordered by normal keratocytes.

intracytoplasmic organelles. The electron micrographs also clearly reveal the sharpness of the demarcation between the damaged and undamaged stroma.

Figure 3 shows the profiles of the border of the bowl-shaped lesions that were obtained by carefully measuring enlarged slit-lamp photographs like the one in Fig. 1. The curves are the calculated profiles of surfaces having equal peak temperature increases. For the 9.7 W/cm^2 , 2.5 s exposure, the lesion border closely corresponds to the 47°C surface, whereas for the 26 W/cm^2 , 0.4 s exposure, the border is close to the 52°C surface.⁷

The calculations also reveal that the temperature history is nearly the same at any position on a given peak temperature isotherm.⁷ This is illustrated in Fig. 4, which shows the temperature histories at two positions on the isotherm corresponding to a peak temperature increase of 45°C . As expected, the temperature rise occurs later for the deeper position, but the shapes of the two curves are nearly identical.

DISCUSSION

The experiments show that the border of the stromal lesion produced by CO_2 laser radiation is sharply delineated, that it corresponds to a surface of equal temperature rise, and that the temperature rise depends (but not strongly) on exposure duration. The conditions on this border represent the threshold for keratocyte damage, which is at a slightly higher temperature for short-duration exposures than it is for longer ones.

Thermal damage of the epithelial and endothelial cellular layers has been correlated with their achieving peak temperature increases in the 30 to 50°C range.^{1,2} Epithelial damage resulting from exposure to various sequences of subthreshold pulses also is correlated with peak temperature increases in the same range, even though the temperature/time histories were varied widely in the experiments.³ Such experiments

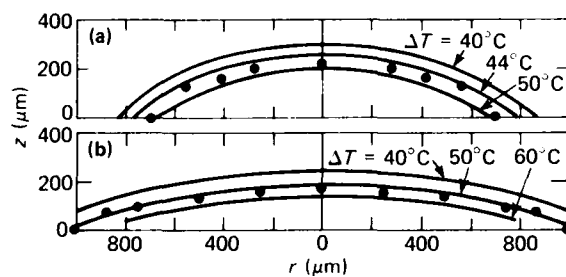


Figure 3 — Measured position of the border of the bowl-shaped lesion compared with calculated surfaces of equal peak temperature increases. The points are obtained from highly magnified slit-lamp photographs taken 48 hours after the exposure. In the figure, r is the radial position from the center of the beam and z is the depth beneath the anterior surface. (a) The exposure was 9.7 W/cm^2 for 2.5 s, and the $1/e$ radius of the beam was 0.94 mm. The points are from a single cornea. (b) The exposure was 26 W/cm^2 for 0.4 s, and the $1/e$ radius of the beam was 1.21 mm. The points are the average values from two corneas.

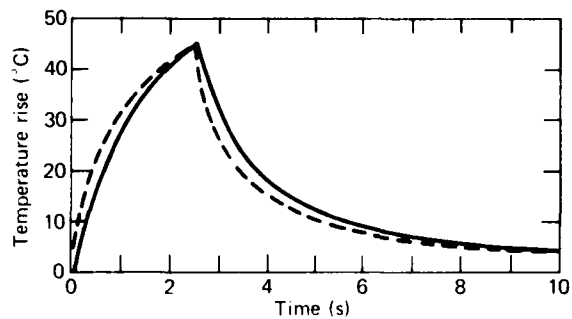


Figure 4 — Temperature histories at two positions on the surface having a 45°C temperature rise following a 9.7 W/cm^2 , 2.5 s exposure. The solid curve is on the beam axis at a depth of $243 \mu\text{m}$. The dashed curve is at a point $695 \mu\text{m}$ from the beam axis, $50 \mu\text{m}$ below the surface.

tend to support the use of the peak temperature increase to correlate threshold damage; however, the required temperature increase does appear to depend weakly on

exposure duration. For example, Egbert and Maher³ reported that epithelial damage thresholds were associated with peak temperature increases (above the ambient value of about 35°C) ranging from 50°C for a 100 ms exposure to 39°C for a 100 s exposure. We reported similar results for endothelial damage.^{4,5} For exposure durations between 1 and 5 s, damage occurred when the calculated endothelial temperature rose about 48°C above ambient, whereas for a 240 s exposure it occurred at only 32°C above ambient.

The temperature values on the damage border in the stroma, and their weak dependence on exposure duration, are similar to those required to damage the epithelial and endothelial cells. This suggests that all corneal cells have essentially the same thermal damage mechanism.

REFERENCES

- ¹N. A. Peppers, A. Vassiliadis, L. G. Dedrick, H. Chang, R. R. Peabody, H. Rose, and H. C. Zweng, "Cornea Damage Thresholds for CO₂ Laser Radiation," *Appl. Opt.* **8**, 377-381 (1969).
- ²A. S. Brownell and B. E. Stuck, "Ocular and Skin Hazards from CO₂ Laser Radiation," in *Proc. Ninth Army Science Conf.*, pp. 123-138 (1974).
- ³D. E. Egbert and E. F. Maher, *Corneal Damage Thresholds for Infrared Laser Exposure: Experimental Data, Model Predictions and Safety Standards*, USAF School of Aerospace Medicine, Brooks AFB, SAM-TR-77-29 (1977).
- ⁴C. B. Bergeron, R. A. Farrell, W. R. Green, and R. L. McCally, "Corneal Damage from Exposure to IR Radiation: Rabbit Endothelial Damage Thresholds," *Health Phys.* **40**, 855-862 (1981).
- ⁵C. B. Bergeron, R. L. McCally and R. A. Farrell, "Structural Corneal Alterations from Exposure to Infrared Radiation," in *Developments in Science and Technology, Fiscal Year 1980*, JHU/APL DST-8.
- ⁶C. B. Bergeron, R. L. McCally, and R. A. Farrell, "Calculated and Measured Endothelial Temperature Histories of Excised Rabbit Corneas Exposed to Infrared Radiation," *Exp. Eye Res.* **32**, 241-250 (1981).
- ⁷R. L. McCally, C. B. Bergeron, and R. A. Farrell, "Stromal Damage in Rabbit Corneas Exposed to CO₂ Laser Radiation," *Exp. Eye Res.* (in press).
- ⁸R. A. Farrell, C. B. Bergeron, W. R. Green, and R. L. McCally, "Collaborative Biomedical Research on Corneal Structure," *Johns Hopkins APL Tech. Dig.* **4**, 65-79 (1983).

This work was supported by the U.S. Army Medical R&D Command.

MOTION NOISE REDUCTION IN NEUROMAGNETIC MEASUREMENT SYSTEMS

H. W. Ko, J. S. Hansen, and D. A. Bowser

Sensor systems that measure minute magnetic signals from the brain are susceptible to noise contamination from sensor motion. This noise has been reduced by as much as 40 dB in noise power by adaptive filter signal processing. The processing technique also shows promise for the identification of other noise signals that might be misconstrued as part of the biological response.

BACKGROUND

Recent neurological investigations of responses evoked by visual and auditory stimulation and by epilepsy use a sensitive, noninvasive magnetic sensor called a SQUID (superconducting quantum interference device). Neuromagnetic signals are generally about 100 fT (1 fT = 10⁻¹⁵ gamma) in amplitude, which is about one

part in 10^8 of the earth's static magnetic field. In order to cancel the relatively uniform time-varying geomagnetic field, the SQUID is used in a configuration called a superconducting second-derivative gradiometer (SSDG). This sensor is housed in a dewar cryostat and is cooled to 4 K with liquid helium.

Because magnetic fields evoked by sensory stimulation of the human brain are orders of magnitude smaller than typical environmental and biological noise at low frequencies, some technique of noise reduction is required to extract the biological signals from the measured data. Previous noise cancellation efforts applied to similar data usually have consisted of signal averaging, which requires large amounts of data to achieve adequate noise reduction. That technique imposes a serious limitation on the investigation of evoked responses when the concentration of a human subject on a repetitive stimulus is required. Its use might allow a hazard to develop in the case of medical monitoring by wasting precious time determining changes in vital life functions.

This study has implemented alternative techniques of noise cancellation with the goal of reducing the amount of data required to characterize the evoked response.¹

DISCUSSION

Noise Sources

Several kinds of noise contribute to the output of the neuromagnetic SSDG. One is the inherent noise of the SQUID and its electronics. The noise floor for the device used in this study is about $50 \text{ fT} \cdot \text{Hz}^{-1}$ and, in general, is not reducible. Another type of noise is that caused by motion of the dewar and the magnetometer in the ambient magnetic gradient. Motions of the building, support structure, and dewar are easily measurable by linear accelerometers.

The third type is environmental magnetic noise caused by changes in the ambient magnetic gradient (e.g., operating motors, moving metallic objects). The largest environmental magnetic noise, normally removed by a notch filter, is that from local power lines at 50 to 60 Hz. In general, ambient gradient changes are proportional to ambient field changes and can be monitored by a triaxial fluxgate magnetometer. When they are attached to the dewar, fluxgates will also sense motion noise because they move with respect to the ambient magnetic vector. The fourth type is biologic noise. The gradiometer senses magnetic signals that originate with the subject but are not related to the evoked signal.

Experimental Apparatus and Data Acquisition

To support studies of magnetic background noise characterization and cancellation, data were taken by APL in an urban environment at the Human Neurophysiology Laboratory at the University of California, Los Angeles.² The biomagnetic sensor was an SSDG with a noise floor of about $50 \text{ fT} \cdot \text{Hz}^{-1}$. For the results presented in the next section, the gradiometer dewar was mounted by a triaxial fluxgate magnetometer with a noise floor of about $10^6 \text{ fT} \cdot \text{Hz}^{-1}$ to monitor environmental magnetic noise. The gradiometer dewar also supported three orthogonal linear accelerometers, each with a noise floor of about $1 \mu\text{g}$ (about 10^{-5} m/s^2). The accelerometers measured only dewar motion noise (see Fig. 1). The data were taken in time segments of 2 or 8 s. All seven sensors were bandpass filtered at 1 to 35 Hz with a 60-Hz notch filter. Data

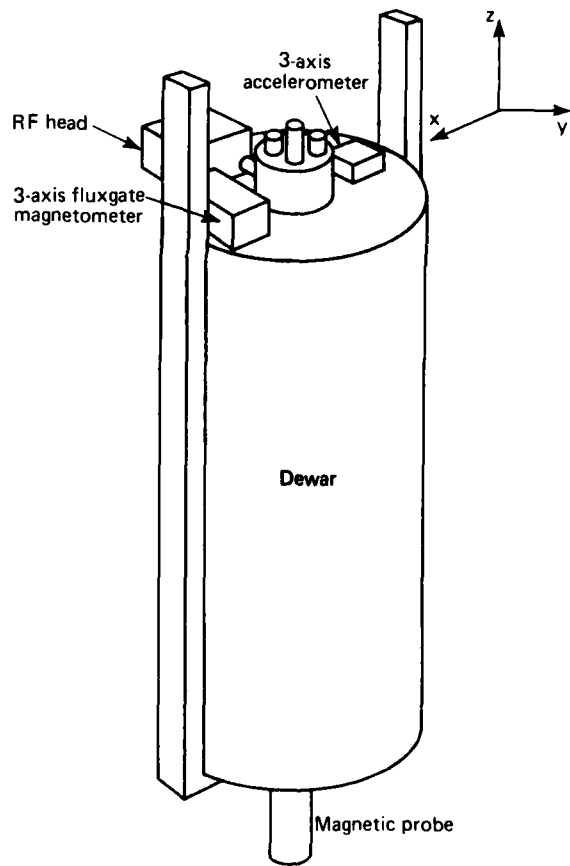


Figure 1 — The mounting locations of the motion monitoring sensors (triaxial linear accelerometers) and the ambient magnetic field sensors (triaxial fluxgate magnetometers).

were taken in real time and digitized on 12-bit analog-to-digital converters at 256 samples per second by a PDP 11/34 computer.

The multiple sensors capable of distinguishing different noise sources and the short duration of the biologically induced signal are amenable to adaptive digital filtering for noise cancellation. The adaptive filter parameters, and hence the frequency response of the filter, are allowed to change or adapt in time. Thus, if the noise is nonstationary, the filter also will vary, in an attempt to follow the changes and provide maximum noise reduction. The adaptation process itself adds "misadjustment" noise, which can be minimized by an appropriate filter, although it cannot be eliminated.

The adaptive filter, called the adaptive noise canceller (ANC), uses the algorithm developed by Widrow et al.³ Two parameters are chosen by the user: the length of the filter and the feedback constant. The filter length determines the number of samples required to specify the filter response and is also equal to the number of filter weights. The feedback constant determines the gain in the feedback loop that governs how quickly the filter weights are allowed to adapt. The choice of appropriate values for the two free parameters is based primarily on experience with the particular data of interest; in this analysis it was based on experience with parametric studies.

RESULTS

Although the mounting and laboratory location of the gradiometer were chosen so as to reduce motion and magnetic noise, the UCLA instrument was still sensitive to that contamination. Simultaneous measurements from the accelerometers allowed the identification and reduction of motion noise from the gradiometer. Similarly, simultaneous measurements from the fluxgate magnetometers allowed the identification and reduction of magnetic noise.

Figure 2a shows 2 s of simultaneous time-series data from the gradiometer and the two associated accelerometers. Only noise (no biologic response) is contained in these data. The obvious correlation between the x-accelerometer and the gradiometer time series suggests a large amount of motion noise at a nominal frequency of 4 Hz in the gradiometer data. The bottom time series of the figure shows the result of adaptively filtering the gradiometer data using the x- and y-accelerometers as reference sensors. The presence (and subsequent removal) of motion-induced magnetic noise in the gradiometer is evident both in the time-series data and in the power spectra of the filtered and unfiltered

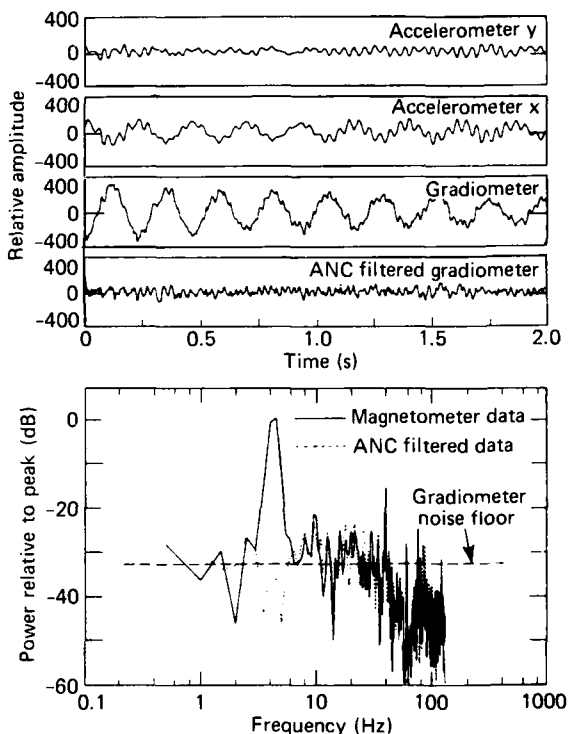


Figure 2 — (a) A demonstration in the time domain of the effectiveness of the adaptive noise canceller. **(b)** Spectra of the gradiometer output before (solid line) and after (dashed line) the application of the adaptive noise canceller.

gradiometer data (about 40 dB reduction in noise power) shown in Fig. 2b. Misadjustment noise, which shows up as increased power levels in the power spectra of the filtered data, is relatively minimal in this case, indicating that appropriate values for the feedback constant and filter length were chosen.

The results of this study show that noise can be reduced in real time and that small signals can be extracted from the ambient noise. The next step in the analysis is to apply the adaptive filter to data with an evoked response, in order to determine if noise can be reduced to such an extent that the number of averages required to study the evoked signal is reduced dramatically. If an appropriate biologic noise sensor is chosen, it is possible that one might obtain the evoked signal from a single response to a stimulus.

ACKNOWLEDGMENTS

The authors would like to thank M. H. Friedman of APL for his advice and support. Appreciation is noted for the collaboration of J. Beatty at UCLA and

D. Brenner of Rockwell International during the measurements.

REFERENCES

- ¹J. S. Hansen, D. A. Bowser, H. W. Ko, D. Brenner, F. Richer, and J. Beatty, "Adaptive Noise Cancellation in Neuromagnetic Measurement Systems," *Nuovo Cimento* **2D**, 203-213 (1983).
- ²D. Barth, W. Sutherling, J. Engel, and J. Beatty, "Neuromagnetic Localization of Epileptiform Spike Activity in the Human Brain," *Science* **218**, 891-894 (1982).
- ³B. Widrow, J. R. Glover, Jr., J. M. McCool, J. Kaunitz, C. S. Williams, R. H. Hearn, J. R. Zeidler, E. Doug, Jr., and R. C. Goodline, "Adaptive Noise Cancelling: Principles and Applications," *Proc. IEEE* **63**, 1692-1716 (1975).

This work was supported by Independent R&D.

SUTURELESS VASCULAR ANASTOMOSIS SYSTEM

J. J. Wozniak

The objective of this project is to develop a means of rejoining severed vessels (end-to-end anastomosis) without using sutures. Two essential elements in the concept, an instrument to evert the vessel and a biocompatible sleeve that contracts to bind the vessel together, are currently under development. Personnel from APL, the Johns Hopkins Medical Institutions, and the University of Maryland, representing talents in the disciplines of engineering, vascular surgery, and polymer science, are working on the project.

BACKGROUND

Severed blood vessels are frequently encountered in penetrating wounds inflicted during combat, civil violence, and accidents. When this type of injury is encountered near centers in which the required skills and facilities are available, the blood vessels can be rejoined with sutures during vascular surgery. Under combat or emergency conditions, the prerequisite skills, facilities, and time may not be available to prevent loss of limb or life.

At the present time, vascular anastomosis is accomplished using a curved needle. The sutures must be placed precisely, piercing the adventitia (fibrous sheath) from the outside and the intima (elastic tissue layer) from the inside in a number of locations for proper vessel approximation (tissue aligned and in good con-

tact). Either individual or continuous-running sutures are used.

Typically, for an artery with a 3 mm lumen, approximately 20 stitches are taken around the circumference using 6-0 (0.1 mm diameter) thread. Usually, an end-to-end anastomosis on a vessel of this size cannot be performed in less than 20 minutes.

The greatest success is achieved when the anastomosis is performed in cases where a good collateral blood supply is available or where loss of blood for moderate periods of time can be tolerated. If the intima is not approximated properly, vascular occlusion may occur, with disastrous results.

The application of sutures on intracranial vessels presents additional difficulties. Differences in the structure of cerebral arteries compared to that of extra-cerebral vessels with less adventitia and reduced media, the presence of many perforating branches that preclude rotation, and the limited time of vessel occlusion hamper the application of sutures to these vessels.

The sutureless concept attempts to avoid some of these problems while providing the benefits of a high patency rate, the virtual absence of post-operative bleeding, and a faster procedure. Additionally, the skill required for this technique should be less than that required for suturing. Therefore, the work can be done at locations other than centers that specialize in vascular surgery.

DISCUSSION

Figure 1 shows the steps involved in the sutureless anastomosis technique. Figure 1a shows the severed vessel, which characteristically constricts and retracts because of the smooth muscular structure (media) within the vessel wall. Temporary clips are applied to the transectional vessel, and the lumen is irrigated with heparinized saline. The vessel diameter is sized, and ferrules are selected that approximately match the outside diameter of the vessel.

The ends of the vessel (Fig. 1b) are then everted over the ferrules. This process opens the vessel fully for flow and ensures continuous intima contact, which is vital for preventing thrombosis when the anastomosis is completed.

In the next step, the outer sleeve, fabricated from a heat-shrinkable biocompatible thermoplastic, is placed on one section of the vessel. The two sections of the vessel are brought together, and the sleeve is cen-

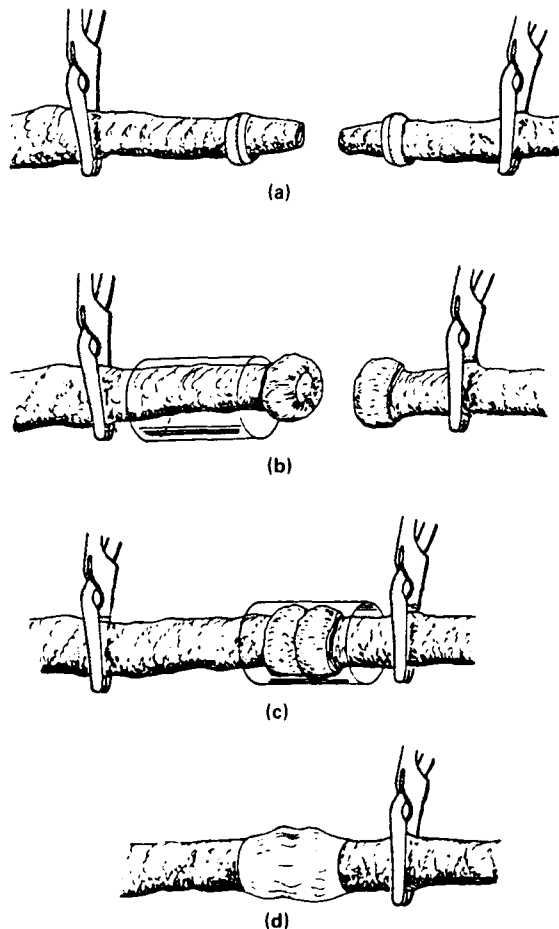


Figure 1 — Sutureless vascular anastomosis.

tered over the junction (Fig. 1c). The sleeve is heated with an instrument that provides a controlled warm air-stream or jet of warm saline. Heat causes the sleeve to contract and assume the local contour of the everted vessel (Fig. 1d). The sleeve also contracts 5 to 15% in length, ensuring good contact of the vascular intima.

In the completion sequence, the proximal clip is removed (Fig. 1d), and a hypodermic needle is inserted into the vessel lumen to relieve entrapped air. When a steady flow of blood through the hypodermic needle is achieved, the needle and distal clip are removed.

Vascular Everting Instrument

The proposed anastomosis procedure requires an efficient way to evert the ends of the severed vessel over the ferrule. For this purpose, an everting instrument has been designed, fabricated, and tested.

The everting instrument must cause minimal damage and displacement of endothelial cells lining the lumen and must be flexible so that it can evert vessels of different sizes. Three devices were developed for bench studies. The most successful of the three uses an iris-diaphragm mechanism to expand the leading edge of the lumen and a balloon, inflated within the lumen, to accomplish the everting action. With this apparatus, excised pig carotid arteries were successfully everted over thin-wall cylindrical ferrules. On the basis of this success, a prototype clinical configuration of the everter (Fig. 2) has been designed, built, and successfully tested *in vitro*.

Heat-Shrinkable Sleeve Development

The second essential element in the sutureless vascular anastomosis concept is the sleeve that contracts to bind the everted vascular sections together. Work began in this area with a literature study centered on identifying semicrystalline polymers that could undergo crosslinking (especially by ionizing radiation) and thereby attain elastic memory properties. Other requirements include biocompatibility, low-melting temperature, and reasonable crystallinity.

Polyethylene oxide (PEO) was the first polymer selected for fabrication trials on the basis of preliminary radiation-chemistry experiments and the knowledge that the material is highly biocompatible. PEO was successfully processed into a low-temperature, heat-shrinkable sleeve, but the sleeve swelled in water and therefore was unsuitable for the application. Coating the PEO sleeve with elastomeric materials and grafting a monomer to the surface of the PEO were the two approaches taken in attempting to waterproof the sleeve.

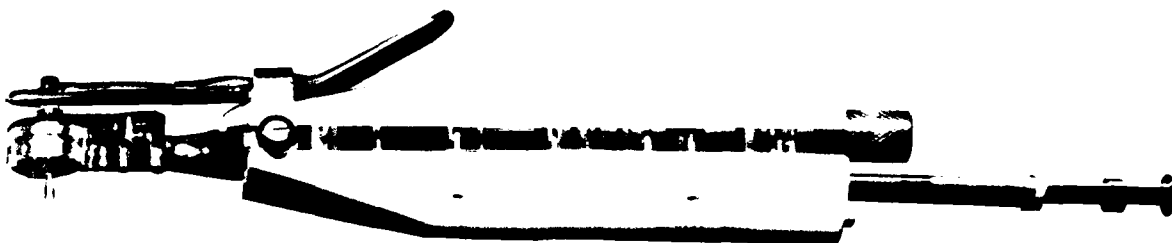


Figure 2 — The prototype clinical vascular evertting instrument.

Four different coating/graft attempts were made, but none provided the required degree of protection.

Recent efforts to develop the sleeve have centered on another polymer, synthetic trans-1,4-polyisoprene. A reinforced form of this material has found use as a low-temperature (130°F), moldable, orthopedic material.

An in vitro trial using a sleeve fabricated from trans-1,4-polyisoprene to anastomose a freshly excised pig carotid artery proved highly successful. Figure 3 shows the ferrules, sleeve, and anastomosed artery. Visually, the lumen remained patent throughout the artery, and the anastomosis remained intact when tension was applied. Unlike PEO, trans-1,4-polyisoprene is unaffected by water.

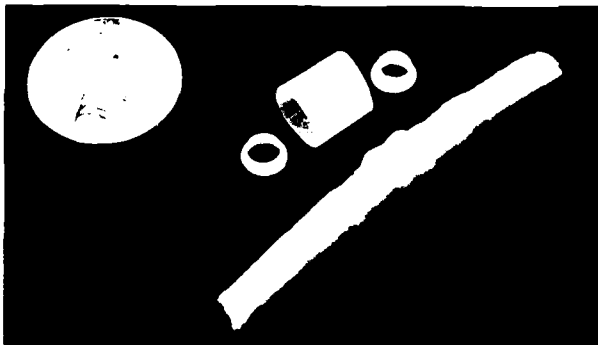


Figure 3 — Sutureless anastomosis applied to a pig carotid artery.

FUTURE PLANS

During the next year, the remaining components (biocompatible ferrules and sleeve-heating apparatus) needed for in vivo trials of the anastomosis concept will be developed. In a concurrent effort, a primary acute toxicity screening test will be performed on synthetic trans-1,4-polyisoprene to assess its biocompatibility. If it proves to be biocompatible, in vivo animal experimentation of the sutureless anastomosis concept will be initiated.

ACKNOWLEDGMENT

The author would like to acknowledge the many contributions made by Eugene Walters in supporting the implementation of the sutureless anastomosis concept.

This work was supported by the Naval Medical R&D Command.

A SYSTEM TO INHIBIT SELF-INJURIOUS BEHAVIOR

A. L. Newman

APL has designed and developed a system to inhibit self-injurious behavior (such as head banging) in severely retarded and autistic patients. Most of the functions of the device are controlled by an integrated circuit designed at APL. A working prototype of the chip has been fabricated and tested.

BACKGROUND

Self-injurious behavior (SIB) is a hidden problem. Most people have never heard of it, and yet as many as 150,000 mentally handicapped patients compulsively beat and abuse themselves. Starting in the crib, a child may eventually beat himself so severely as to threaten blindness, brain hemorrhage, and death. SIB is a horrifying, life-threatening problem of psychopathology with no known cure. To address the problem, APL is working under the sponsorship of the American Foundation for Autistic Children to develop a system to inhibit SIB.

There is a great need for successful, less expensive SIB therapy. Current SIB patient care is very expensive, labor intensive, and time consuming. It is also emotionally demanding. Physical restraints for immobilizing hands, arms, or legs and protective shielding and padding are often used; this protects the patient but neither eliminates the behavior nor permits rudimentary education and social interaction.

Behavioral conditioning is a form of therapy that has been used with some success in the treatment of SIB. In this paradigm, an aversive stimulus is delivered to the patient in close temporal association with the undesired SIB. The patient responds by decreasing the frequency of the undesired behavior. Ideally, the inhibiting stimulus should be delivered automatically and consistently.

The initial application of behavioral conditioning as SIB therapy used a therapist to close the loop in a simple biofeedback system by administering a stimulus at the onset of SIB. Aversive stimuli tested for their ability to decrease SIB included loud noises, hair pulling, slapping, noxious odors, and aromatic ammonia, but none has been as effective as electric shock. Lovaas and Simmons concluded: "First, the use of shock, given contingent upon self-destructive behavior, brings about an immediate cessation of that behavior. Second, the effect of shock appears specific to the situations in which it is administered."¹ Investigators have found

an almost immediate or, at least, quick cessation of SIB when the child was shocked with a hand-held "shock stick" by his therapist or attendant. The shock used as an aversive stimulus for SIB is described by J. Carr as an "electric shock of sufficient strength to give an unpleasant, though very brief, sensation, but not to cause injury."² However, the behavior returned when the attendant who had delivered the stimulus or the child left the therapy room. Suppression of SIB was only effective in that room, not elsewhere.

It is thus clear from the literature that therapist-administered shock is not the optimal therapy. The shock becomes psychologically paired with the therapist and the environment, and there are variable delays between head banging and shock. In such a situation, the inhibiting stimulus cannot reliably be delivered automatically and consistently.

A further advance in behavioral conditioning of SIB was made when the American Foundation for Autistic Children (AFAC) developed a device that sensed "abnormal" accelerations of the head and delivered a shock to the arm. Such a device obviates the need for the therapist to observe the SIB and eliminates human delay in delivery of the aversive stimulus. It ensures that the stimulus will be paired automatically with a specific behavior (head banging) and also will be delivered consistently.

The AFAC device consists of a helmet on the head connected by wires to an arm electrode. The helmet contains an accelerometer and also protects the head. The accelerometer switches a power circuit on the patient's back that is connected by wires to the electrode assembly on the arm. Several of these devices were built and have been found to inhibit SIB successfully. In fact, patients feel so safe and secure with the device that they struggle to keep it on when one tries to remove it. With these successes, AFAC came to APL with the idea of further developing, through the application of state-of-the-art technology, a Self-Injurious Behavior Inhibiting System (SIBIS).

DISCUSSION

The basic configuration of SIBIS is shown in Fig. 1. When the sensor module, contained in a headband, detects abnormal accelerations (2 g or more) resulting from head banging, it transmits a digitally coded signal to the stimulus module on the arm. On re-

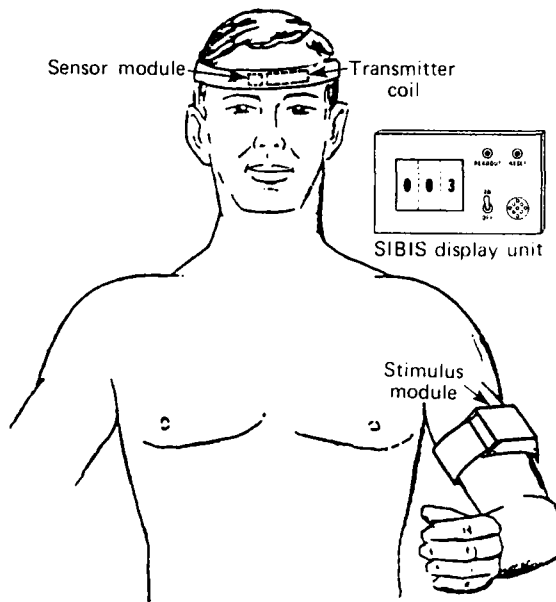


Figure 1 — Configuration of the SIBIS device as worn by an individual.

ceiving this signal, the stimulus module checks the signal code with a stored identification code and delivers a shock and sounds a buzzer if the codes match. The sensor module electronically counts each transmission, and the stimulus module counts each shock. An equal number of counts in each module, as shown on the display unit, verifies proper system function.

The design goals for SIBIS were as follows:

- Miniaturize the device
- Develop a wireless communications link
- Provide for data recording and display
- Keep the device inexpensive

We have accomplished these goals through extensive use of microelectronics and now have a working unit that proves our design. At the heart of SIBIS is a custom-made, large-scale integrated circuit called a gate array; that contains the bulk of the communications and control circuitry (see Fig. 2). Instead of designing two integrated circuits, one for the sensor module and one for the stimulus module, we designed one with all the circuitry for both sensor and stimulus functions. The chip's identity is one-bit programmable; i.e., the

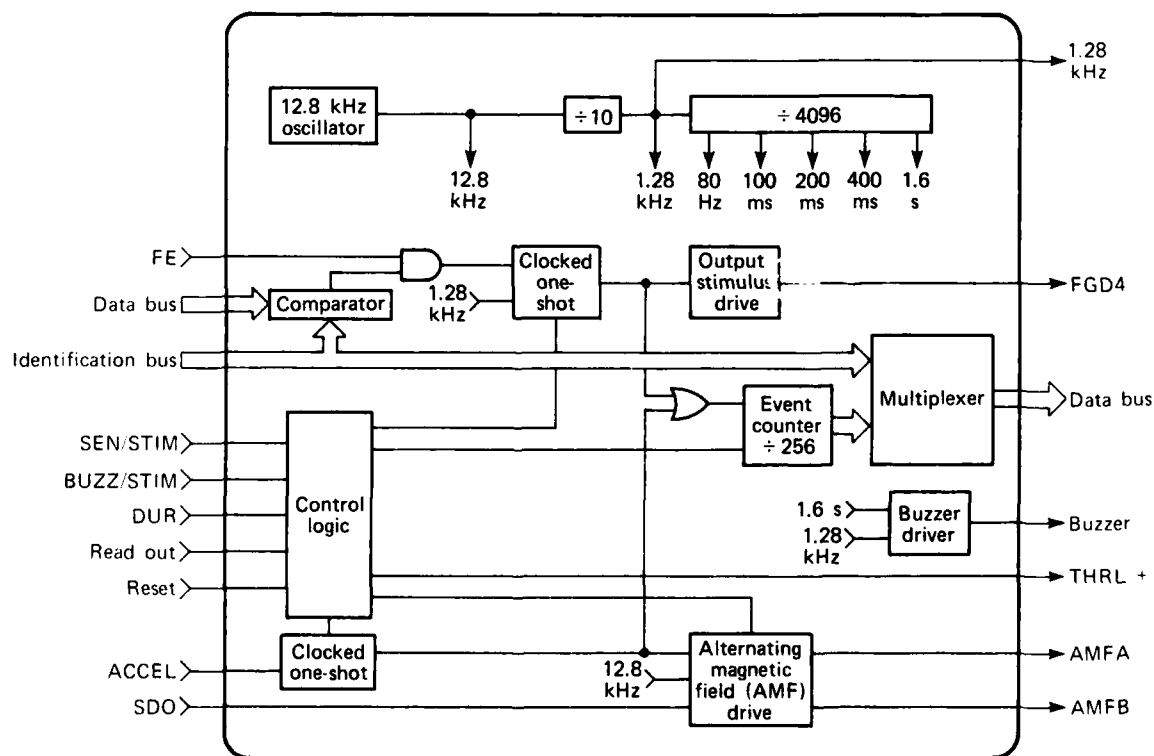


Figure 2 — Simplified diagram of the SIBIS gate array.

logic state of input SEN/STIM determines whether the chip has a sensor function or a stimulus function (Fig. 2). This approach not only minimizes development costs, but also simplifies the whole manufacturing process.

Hybrids are microminiature, multilayer printed circuit boards. Two were designed, one for the sensor module and one for the stimulus module. They contain the gate array as well as the discrete components (resistors, capacitors, etc.) and circuitry for supporting it and defining its function.

The gate array has circuitry for a low-power, crystal-controlled clock (12.8 kHz oscillator) and an associated divide-by-4096 counter for producing the different clock frequencies that are required by various parts of the circuit.

In the sensor mode, a digital one-shot is clocked by an accelerometer switch (input signal ACCEL, Fig. 2). This enables the alternating magnetic field drive circuitry on the chip that, concurrently, is digitally coded by the modulating input signal SDO. The different parts of the original AFAC device are connected by wires, an approach that is unwieldy and unreliable. In SIBIS, the coded alternating magnetic field serves as the communication link, and connecting wires are avoided. The code, different for each patient, prevents a patient from receiving inappropriate shocks because of another patient's SIB. It also keeps SIBIS immune to electromagnetic interference, both natural and man-made. A digital comparator on the chip is used in the stimulus mode for comparing the received coded signal on the data bus with that stored on the identification bus (Fig. 2). When there is a match, a clocked one-shot enables the output stimulus drive to start, via signal FGD4, the shock-producing circuitry contained elsewhere in the module.

In a series of experiments, we found that the subjective intensity of pain from shock is a function of shock duration. We allowed a choice of only two shock durations: 100 and 200 ms. Each shock was accompanied by a buzzer sound. The buzzer can be programmed by means of the signal BUZZ/STIM to occur

without a shock. A goal of SIBIS is to develop a psychological pairing of the shock with the tone so that the tone itself becomes aversive. The circuitry providing the limited choice (100 ms, 200 ms, or no shock) is "locked" on the silicon of the gate array in order to prevent abuse of SIBIS. Shock duration is programmed through the input DUR. The device cannot produce a more painful shock than the one lasting 200 ms.

An event/counter register in the gate array records the number of SIB events that have occurred. Data from this register are read out on a display unit, and it is then reset to zero (Fig. 1). This data logging provision will be important for the clinical evaluation of SIBIS as well as for the ongoing monitoring of a patient's progress.

We expect to have a working prototype of SIBIS by the fall of 1984. The packaging of each module has been kept simple because the electronic complexity of SIBIS has been limited to the gate array and the two hybrids in which it is placed. The manufacturer of SIBIS simply orders the hybrids as part numbers from the hybrid manufacturer. The final electronics assembly and packaging is simple and inexpensive, for yielding a marketable device that we hope will help thousands of patients.

ACKNOWLEDGMENTS

The author would like to acknowledge funding and support for SIBIS from the following organizations: American Foundation for Autistic Children; APL Development Fund; C. R. Bard Corp.; Oxford Medilog, Inc.; and Public Welfare Foundation. The important contributions of Robert E. Fischell, Kim Fowler, W. R. Powell, J. Patrick Reilly, and Henry Riblet are also acknowledged.

REFERENCES

- ¹O. I. Lovaas, and J. O. Simmons, "Manipulation of Self-Destruction in Three Retarded Children," *J. Appl. Behav. Anal.* **2**, 143-157 (1969).
- ²J. Carr, "The Severely Retarded Autistic Child," in L. Wing, *Early Childhood Autism* (2nd Ed.), Pergamon Press, pp. 253-258 (1976).

ENERGY, ENGINEERING, AND CIVILIAN TECHNOLOGY

INTRODUCTION

Included in APL's tasks are specialized investigations in which advanced scientific and engineering technologies are applied to designated civilian and defense-related needs. This section includes selected articles in those categories.

During the past six years, the Laboratory conducted programs for both the State of Maryland and the Federal Government associated with the generation, storage, environmental impact, and efficient use of energy. The work has been extended this year to include an assessment of the potential use of geothermal energy at Naval facilities on the East Coast. Other special engineering investigations conducted for the Navy include the design, fabrication, and successful use of a compact data recording system for special field operations.

The APL Transportation Program, active in urban transit technology since 1969, has developed and evaluated concepts for the rapid transit of the public in vehicles on automated guideways. A computer simulation has been developed and used this year to investigate the performance, control, and network management of such systems.

The development of prototype electronic systems at the Laboratory for stringent applications requires the use of highly reliable, miniaturized circuit assemblies and associated packaging. This necessitated in-house qualification of the pertinent assemblies. Related articles include epoxy characterization and qualification and the shear testing of ball bonds. Also, in-house computer-aided design tools have been developed for the design of custom very-large-scale integrated circuits.

GEOTHERMAL ENERGY ASSESSMENT AT EAST COAST NAVAL FACILITIES

R. W. Newman

Atlantic coast Naval facility sites have been evaluated to determine their potential to benefit from the installation and use of geothermal wells in order to reduce energy costs for hot water and steam heating. Of the 130 sites reviewed, six were selected for detailed investigation and two (the Jacksonville and Norfolk Naval Air Rework Facilities) have been recommended to the Navy as promising candidates.

BACKGROUND

The Arab oil embargo of 1973 underscored the nation's vulnerability to a sudden interruption of its oil supply and indicated the need for ensuring that such interruptions do not jeopardize the integrity of our military capability. Consequently, the Navy began a program to assess the feasibility of replacing some of the petroleum used at its bases throughout the world with geothermal energy.

Because of our past experience in geothermal energy¹ and our large data base associated with geothermal activity, the Navy has asked APL to review the Naval and Marine facilities along the Atlantic coastal plain as possible sites for the use of geothermal energy. A survey of the facilities showed that the most promising facilities are in Norfolk, Va., south-central Florida, and Charleston, S.C.^{2,3}. The following facilities were visited in those regions:

1. Norfolk Naval Air Rework Facility (NARF);
2. Jacksonville NARF, Cecil Field Naval Air Station, and Orlando Training Center;
3. Charleston Naval Shipyard and Charleston Polaris Missile Facility Atlantic.

The Norfolk and Jacksonville NARF's appear to be the best suited for geothermal energy use. Consequently, economic analyses have been performed on proposed geothermal systems at those two facilities.

DISCUSSION

Proposed Geothermal System at Norfolk NARF

The Norfolk NARF is located in a region of above-average temperature gradient. An extrapolation of the gradient results in a temperature of 107°F at the

top of the solid rock basement at 2700 ft. Currently, Norfolk's primary energy source is steam supplied by four power stations. Most of the steam is supplied by power station 1, which uses No. 6 fuel oil at a cost of \$6.36 per 10⁶ Btu. As a result of our study, a geothermal system has been proposed that uses 107°F geothermal well water to preheat make-up water for the power plant (Fig. 1).

An electrical pump brings geothermal well water up from a drawdown depth of 400 ft; the water goes through a water-to-water heat exchanger and transfers its heat to the incoming feed water. A 5°F temperature difference across the exchanger surface is a reasonable trade-off between heat exchanger costs and the amount of energy extracted from the geothermal water.⁴ The spent geothermal water is reinjected at 2000 ft, which is just below the potable water table. With this system, geothermal energy could provide 3.4% of Norfolk's yearly energy needs (equivalent to \$918,000 worth of fuel oil per year). However, an average geothermal water flow rate of 690 gal/min would be required. It is unlikely that this flow rate could be supplied by a single well, but five wells producing at a reasonable flow rate of 150 gal/min could supply the necessary energy.

As an initial step in the development of geothermal energy at east coast Naval facilities, a single well system has been proposed that would provide geothermal water at an average flow rate of 150 gal/min. Because of the relatively high inlet temperature of the make-up water in the summer, over 90% of the geothermal energy is provided during the colder months from October through May. Consequently, the limited water supply is better utilized in the winter months. With a weighted flow, that single well could replace \$229,000 worth of fuel oil per year.

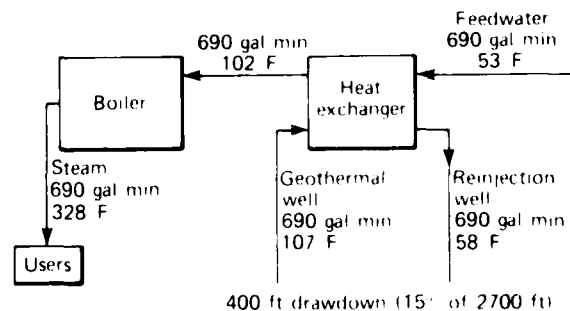


Figure 1 — Geothermal system to preheat feedwater at Norfolk NARF

A net-present-value economic analysis has been made of the income from this well, using the conditions presented in Table 1 and assuming that fuel costs and operating expenses increase at the inflation rate. The resulting net present value is \$2,600,000, which means that the net income, over the 20-year life of the well, is equivalent to having \$2,600,000 today. In other words, one would be willing to spend up to \$2,600,000 today to obtain the energy savings of a geothermal well over the next 20 years.

Table 1 — Estimated geothermal system characteristics for Norfolk NARF.

Water flow rate (gal/min)	150
Drawdown depth (ft)	400 (15% of well depth)
Water temperature (°F)	107
Cost of money (%)	10
Inflation rate (%)	5
Cost of fuel (million Btu)	\$6.36
Cost of electricity (million Btu)	\$11.80
Annual operating and maintenance costs	\$20,000

Geothermal System Costs

Estimates have been made of the capital costs of a geothermal system. They have been divided into four categories:

1. Production well depth-independent drilling costs,
2. Production well depth-dependent drilling costs,
3. Rejection well costs,
4. Heat exchanger and associated piping costs.

These costs are summarized in Table 2 for wells with production rates ranging from 100 to 200 gal/min. Well costs are based on drilling costs for geothermal test holes drilled on the east coast. Heat exchanger and pip-

ing costs are based on estimated current costs. At 150 gal/min, the system cost is \$929,000 and the net present value is \$2,600,000. In Fig. 2, values of system cost and corresponding net present value have been plotted as functions of average well flow rate and water temperature. They show that even at flow rates as low as 60 gal/min, a geothermal system is still economical. In addition, geothermal water temperatures as low as 80°F may still be practical if flow rates greater than 110 gal/min can be attained. The results indicate that a geothermal system at Norfolk is very promising and should be investigated further.

Proposed Geothermal System at Jacksonville NARF

A similar analysis was performed on a proposed geothermal system at the Jacksonville NARF. The major differences between the two sites are:

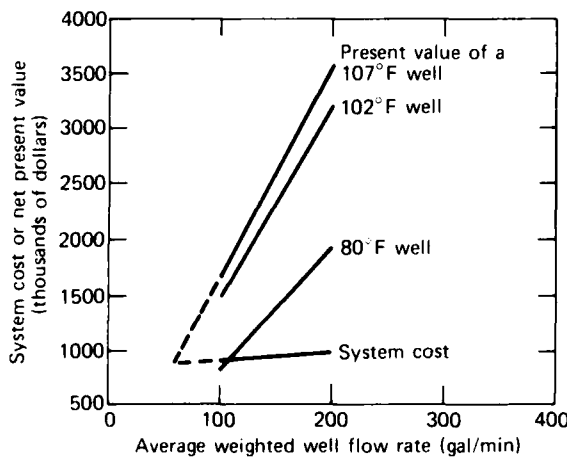


Figure 2 — System cost and net present value as functions of the average weighted well flow rate at Norfolk NARF

Table 2 — Geothermal systems costs and net present value

	100 gal/min	150 gal/min	200 gal/min
Production well (depth independent)	\$350,000	\$355,000	\$360,000
Production well (depth dependent)	285,000	285,000	285,000
Rejection well (3000 ft)	207,000	207,000	207,000
Heat exchangers and piping	60,000	82,000	120,000
Total cost	\$902,000	\$929,000	\$972,000
Net present value	\$1,650,000	\$2,600,000	\$3,560,000

1. The well at Jacksonville is deeper (4900 ft compared with 2700 ft) and has hotter water (124°F compared with 107°F).
2. Jacksonville uses gas to fire its boilers and currently gas is cheaper than oil (\$3.11 per 10^6 Btu compared with \$6.36 per 10^6 Btu).

The analytical results (Fig. 3) show that at a flow rate of 150 gal/min, the geothermal system cost is \$1,200,000 and its future energy savings have a net present value of only \$817,000. Flow rates over 200 gal/min are needed to make the system economically viable. Consequently, a geothermal system at the Jacksonville NARF is not as economically attractive as one at Norfolk.

We conclude from our analyses that geothermal systems at both Jacksonville and Norfolk are economically viable. The Navy is using these results to determine how best to develop geothermal energy at their east coast facilities.

REFERENCES

- ¹W. Toth et al., *Geothermal Energy Development in the Eastern United States, Final Report*, JHU/APL QM-81-130 (Oct 1981).
- ²R. W. Newman, *Evaluation of Three East Coast Naval Facilities as Potential Geothermal Users*, JHU/APL BBE/EM-5136 (Sep 1983).
- ³R. W. Newman, *Potential Geothermal Energy Use at East Coast Naval Facilities*, Naval Weapons Center, China Lake, NWC TP 6423 (Apr 1983).

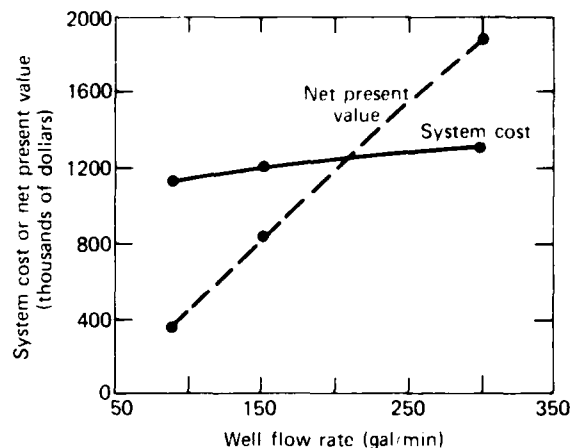


Figure 3 — System cost and net present value as functions of the average weighted well flow rate at Jacksonville NARF.

⁴R. W. Newman, *Potential Geothermal Energy Use at East Coast Naval Facilities*, JHU/APL BBE/EM-5093 (11 Oct 1982).

⁵R. W. Newman, *Heat Exchanger Costs*, JHU/APL QM-78-164 (1 Aug 1978).

This work was supported by the Naval Weapons Center, China Lake.

TAPE-X DATA RECORDING SYSTEM

R. A. Quinnell, R. L. Nelson, and C. A. Twigg

Tape-X is a digital data recording system based on a consumer-grade video cassette recorder. It was devised for an application where conventional data recorders had repeatedly proven unable to meet the system constraints. Taking advantage of the high bandwidth and long recording times on a video cassette recorder, Tape-X met system requirements in a compact, easy-to-use unit. It was used successfully to acquire the first field data ever collected in its intended application.

BACKGROUND

Post mission processing of data collected on Navy electronic systems in their operational environment provides valuable insights into the performance of those systems. As part of its continuing evaluation of system performance for the Navy, APL required data from an uninstrumented signal processing system. Attempts to collect the data using conventional data recorders were unsuccessful owing to the bulk and delicacy of such units and the difficulties in their use by untrained operators.

In response to the need for the data, APL devised the Tape-X system. In order to take advantage of the spare video cassette recorders (VCR's) in the system, Tape-X was designed to interface with an unmodified, consumer-grade VCR. The high bandwidth, long recording time, and ease of operation of the units made them well suited to satisfy the system constraints.

DISCUSSION

The performance of complex systems can be studied with the aid of an accurate estimate of their expected behavior. To provide this estimate, the system inputs must be known or modeled. Recording the actual system inputs in field operations provides the basis for

the best estimates. Tape-X was devised to record the inputs to a large signal processing system.

Data collection consists of data recording and data recovery. The data-recording portion of the Tape-X system is diagrammed in Fig. 1. Selected data from the input data stream are held in a first-in/first-out (FIFO) buffer and then are converted to a serial bit stream that is combined with a video sync waveform. The resultant waveform is similar to a standard composite video signal, although if displayed on a television monitor it would appear as snow. The waveform is recorded on an unmodified, commercial-grade VCR.

The format of the data recording is shown in Fig. 2. During the portion of the composite video signal that corresponds to the visible image on a monitor, data are encoded as white and black streaks in each scan line. The format consists of two blocks of 50 bits, each block being divided into five words. The first word of each block is a valid data indicator and synchronizing word that designates whether or not the remaining four words in the block are meaningful. A total of 80 bits of input data can be recorded on each scan line.

The average data rate available using this format is 1.2 million bits per second. The instantaneous data rate varies because data are not added to the composite video during the vertical retrace interval. In addition, data are not added during the scan lines just prior to the beginning of the vertical retrace interval. The gap is left in order to avoid the data distortion caused by the VCR, which switches its recording heads for alternate television fields. The FIFO buffers hold the incoming data during those intervals.

Recording the data is only half the job. The data-recovery portion of the Tape-X system is diagrammed in Fig. 3. The recorded data are detected and synchronized to a high-speed clock. Transitions in the

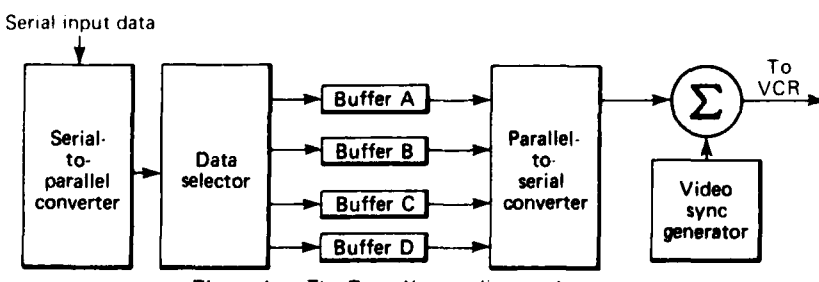


Figure 1 — The Tape-X recording system.

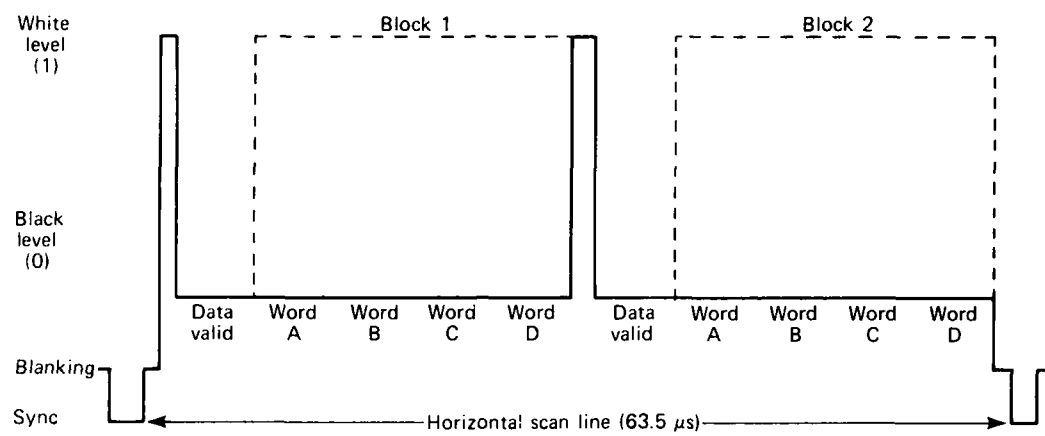


Figure 2 — The format used for Tape-X data recording.

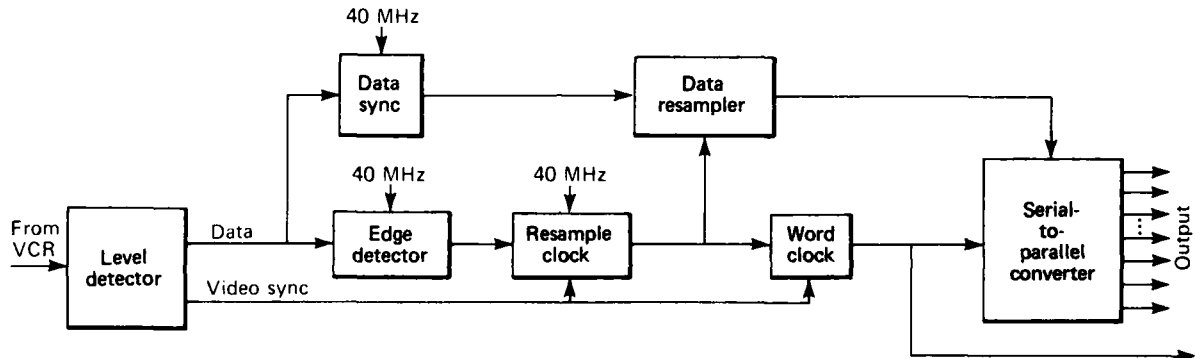


Figure 3 — The format used for Tape-X data recovery.

data are used to synchronize a data resampler, and the resampled data are shifted into a parallel output register. A word clock counter provides a signal whenever a full data word is available.

The data-recovery portion of the system is the most critical. The choice of data format is critical to its success. Bandwidth limitations of the VCR require that simple binary coding of the data be used in the recording. The resampling clock depends on data transitions to determine the beginning of a data bit interval. Those two factors lead to the use of the valid data word. The valid data indicator distinguishes between no data and zeros, since both result in an all-black line. The valid data indicator also provides a guarantee that at least one transition will occur for each 50 bits of data. Experiments with the VCR have shown that this transition density is sufficient to maintain synchronization of the resampling clock.

Data integrity is an important factor with all data-recording systems. The Tape-X system does not use special formatting to correct for data dropouts or

errors in the recording medium. The nature of the data being recorded in the design application is highly redundant. Because of the immense quantity of data recorded, error rates as high as 10^{-4} have little effect on the usefulness of the collected data. Field tests of the Tape-X system have resulted in very acceptable data integrity. The true bit error rate of the system has never been measured.

The system has been used successfully to collect some 36 hours of data from the field. Those data, the first ever collected on the system, are being used to evaluate the system's design and performance. In addition, the Tape-X data have allowed for post-exercise experiments in processing the data by means of direct comparison with field processing results. These new capabilities are yielding significant results in the evaluation of the system.

A NETWORK MANAGEMENT SIMULATION OF AGRT SYSTEMS UNDER VEHICLE-FOLLOWER CONTROL

H. Y. Chiu, D. L. Kershner, and P. J. McEvaddy

A computer simulation was developed to provide the first capability for efficiently evaluating station operations, vehicle management techniques, and vehicle-follower longitudinal control algorithms in a full Automated Guideway Rapid Transit (AGRT) network context. The simulation was then exercised to investigate the performance characteristics of vehicle control, network management, and station models and their interactions.

BACKGROUND

The use of AGRT has been proposed to alleviate many problems associated with conventional transportation modes in urban areas. The concept requires the deployment of remotely controlled vehicles carrying 10 to 50 passengers in a dedicated guideway network. Many strategies have been developed to handle the simultaneous longitudinal control of possibly hundreds of such vehicles. One generic control approach is vehicle following (VF), in which vehicle spacings and velocities are determined only by status information on the immediately preceding vehicle. VF has been examined extensively at the individual vehicle interaction level.¹ This article describes the development of a network management simulation (NMS) to provide the first capability to evaluate the operation of a VF control system in a full AGRT environment.²

With NMS, the network-level behavior of the VF approach to longitudinal control in AGRT systems can be examined in great detail. A typical AGRT system was constructed for an initial application of the NMS. The following study objectives were established:

1. Assess the practical link flow capacities as a function of system demand.
2. Determine the interactive effects of VF with station operations.
3. Ascertain the energy consumption and power demand characteristics of VF.

DISCUSSION

Simulation Design

A key simulation requirement was the ability to retain the dynamics of vehicle-to-vehicle interactions that are fundamental to VF control. A continuous, or

time-step, modeling approach was selected to simulate the movement of individual vehicles through the network as controlled by VF logic previously developed at APL.¹ The simulation of off-line vehicle movements (i.e., on station ramps and through the docking area) was accomplished by using a discrete-event modeling approach for shifting vehicles from one location to the next within a station because it required substantially less computation than continuous modeling and still preserved a level of fidelity sufficient for the purposes of the study.

To keep the computational burden from becoming excessive and to direct the focus of study toward the management performance of vehicle-related operations, the modeling of the passenger side of system operations was omitted. Although passenger arrivals and associated trip demands represent the "driver" in most network simulations, a fixed route type of service structure (based on the anticipated demand) was assumed and was used as a way to maintain the flow of vehicles through the network. This form of service has been used in many studies for peak period operations and, because of station operation complexities, may be the preferable mode of operation for initial AGRT deployments.

The resulting simulation product, shown schematically in Fig. 1, is a combined, continuous, discrete-event simulation incorporating VF logic to control mainline vehicle motion and using predetermined service route frequencies (i.e., vehicles per hour per route) to drive the vehicle flow in lieu of system passengers. An event-scheduling approach characteristic of discrete-event type simulations was used for primary control of the sequence of execution. Vehicle mainline operations, simulated using a continuous, or time-step, approach, were integrated into this event-based process by simply scheduling the state-update events at regular intervals that equaled the selected time-step interval. As indicated in Fig. 1, the types of events that were scheduled included station-related events for vehicles in the discrete-event mode, state-update events for vehicles in continuous mode, and state-related events to transfer vehicles from one mode to the other and to actuate logic for merge-control and network-path selection.

Network Configuration

The initial network configuration is shown in Fig. 2. It consisted of approximately 8 lane-miles of

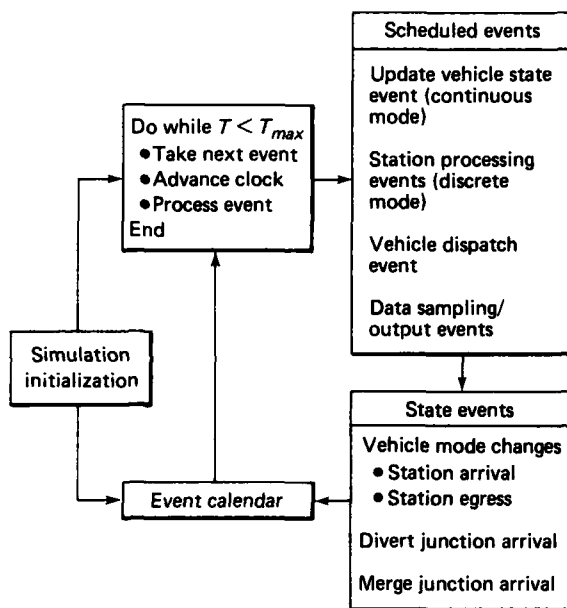


Figure 1 — Network simulation control structure.

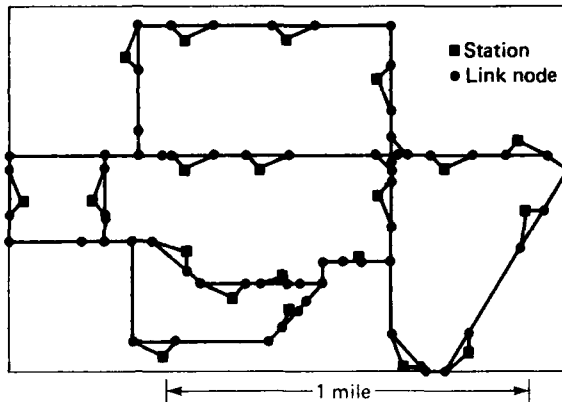


Figure 2 — Test network for traffic management simulation.

unidirectional guideway connecting 20 off-line stations. The network was representative of an activity center circulation system that might be typical of initial AGRT deployments. This configuration was chosen because it had many of the characteristics and complexities of larger networks (e.g., alternate paths, full intersections, multiple service routes) but was still amenable to simulation at a reasonable cost because of its limited size.

The configuration of the NMS included 90 links with line speeds ranging from 7 to 15 m/s. The links immediately upstream of merge junctions represented parallel data regions within which vehicles maneuver in

order to resolve merge conflicts. All stations were assumed to be single-channel, serial-berth configurations with an entrance, a dock, and exit queues.

Simulation Results

Several runs were made with the NMS with system vehicle fleet sizes. The duration of all runs was set to one hour of simulation time. Some of the following observations were made:

1. With vehicle flows close to theoretical system capacity, the NMS did not show any dynamic vehicle string instabilities, such as "bunching," that were due to vehicle-follower controls.
2. For heavily congested network segments, a constant-safety-factor spacing policy gave better system performance than a comparable constant-headway spacing policy.
3. A vehicle management reservation strategy significantly reduced station entry rejections of mainline vehicles without degrading other system performance measures.
4. The energy consumption per vehicle-mile traveled was found to vary by as much as 3%, depending on the spacing policy used.

The NMS was written in Fortran and executed on the Laboratory's IBM 3033 computer system. For the assumed network configuration, the NMS provided ratios of simulation times to computer processing unit times that ranged from 60 to 90. The efficiency of these ratios makes the NMS a potentially powerful tool for performing sensitivity studies of previously unaccessible network performance measures.

REFERENCES

1. A. J. Pue, *Control Law Implementation for Short Headway Vehicle-Follower AGT System*, JHU/APL TPR 045 (Oct 1979).
2. H. Y. Chiu, D. L. Kershner, and P. J. McEvaddy, *A Network Management Simulation (NMS) of Automated Guideway Rapid Transit (AGRT) Systems Under Vehicle-Follower Control*, JHU/APL TPR 048 (to be published).

This work was supported by the Urban Mass Transportation Administration.

EPOXY CHARACTERIZATION AND QUALIFICATION STUDIES

H. K. Charles, Jr., E. S. Dettmer, J. A. Weiner, and R. C. Benson

An extensive epoxy analysis, characterization, and testing program has been performed at APL. New epoxies have been qualified for use in high-reliability microcircuit environments. Advanced materials testing and surface analytical techniques to determine the electrical, mechanical, and chemical properties of epoxies have been used to certify an adhesive type of epoxy and also to develop optimum processing parameters and methods for lot-to-lot quality assurance. The new adhesives have been used in several ongoing programs.

BACKGROUND

Epoxies have played an extensive role in the attachment and packaging of microelectronic circuits. Epoxies (and other organic adhesives) provide the

microcircuit-designer/development-engineer with many advantages including lower temperature processing (less stress on chips and other packaging materials), ease of use (screen printable, amenable to automated assembly), rapid assembly processing (fewer complex and high-temperature processing steps), rapid rework methodologies, and ultimately lower costs. Historically, organic adhesives have caused many reliability problems, both at APL and throughout the electronics industry. Epoxy problems can be divided into three principal areas: (a) mechanical strength, thermal expansion, and adhesion problems; (b) electrical conductivity (resistivity) instabilities; and (c) chemical interactions (aluminum-gold intermetallic growth, aluminum corrosion moisture retention, etc.). Some examples of epoxy-related problems are illustrated in Fig. 1.

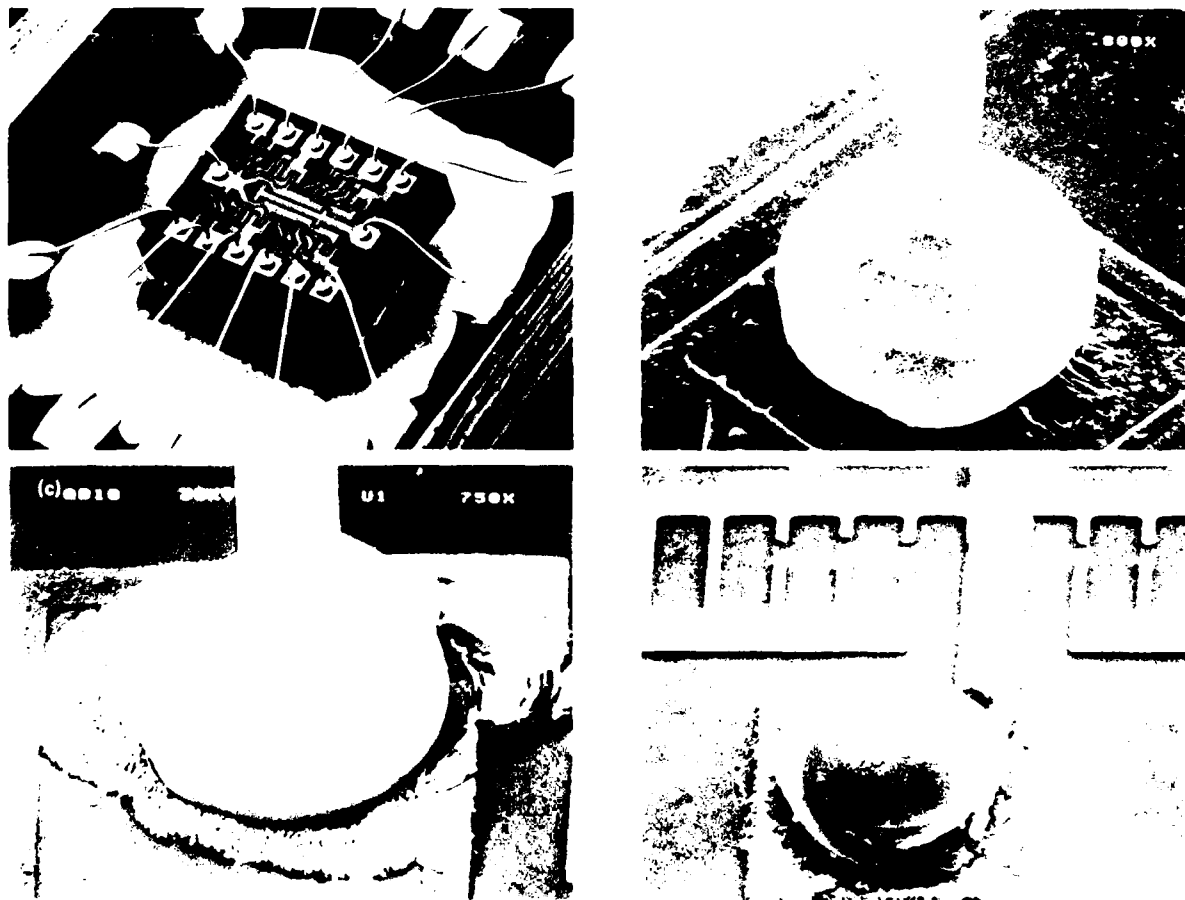


Figure 1 — Historical epoxy problems: (a) lifted die, (b) sheared wirebond, (c) Al-Au intermetallic, (d) Al corrosion.

In order to make use of the inherent advantages of epoxy die and substrate attachment, the API Microelectronics Group needed to qualify several new epoxy adhesives that were more flexible and performed better than the existing qualified epoxy. Particular emphasis was placed on a nonconducting epoxy with superior adhesion to gold and on a low-resistance high-stability conductive adhesive. Because epoxy failures (such as loss of adhesion and advanced intermetallic growth) had been associated with several important Laboratory programs, it was necessary to conduct an extensive development and analysis program prior to the introduction of the new epoxies into the microcircuit production line.¹ The program was divided into three major areas: bulk epoxy testing (mechanical, electrical, and chemical), controlled hybrid construction and process development, and the establishment of reliability and quality assurance criteria and equipment.

DISCUSSION

Bulk Epoxy Testing/Analysis

Mechanical testing has been performed using both shear and tensile test methods on bulk epoxy samples and on silicon dies attached to representative substrate materials. Shear test results for a typical epoxy sample set are shown in Fig. 2. The top histogram was produced just after curing while the bottom data were collected after thermal stressing at 150°C for 1000 hours. Although both distributions show that the epoxy is strong and quite suitable for die attachment (NASA² indicates that the minimum shear strength for epoxies should be greater than 7 MN/m², or 8 N for our sample

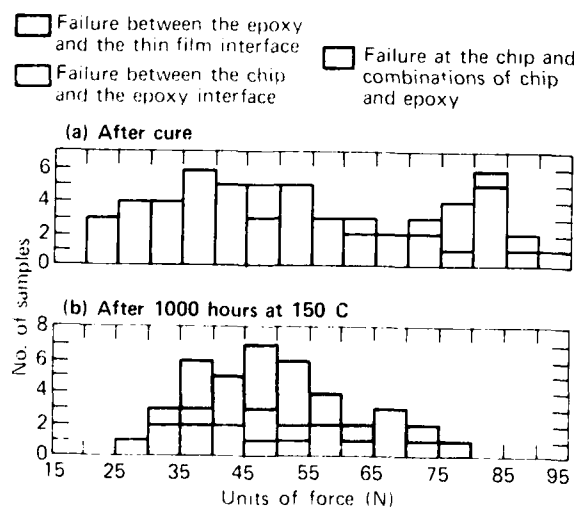


Figure 2 — Die shear strength of Ablebond 36-2 conductive epoxy

geometry), there is a distinct change in the failure mode with thermal aging. Following epoxy curing, the shear failure mode occurred in the bulk epoxy or else the silicon die fractured as is shown in Fig. 3a. Post-thermal-annealing failures were localized at the interfaces (Figs. 3b and 3c), indicating a loss of adhesion even though



Figure 3 — Die shear failure modes: (a) bulk failure, chip and chip epoxy combinations; (b) epoxy/die interface separation; (c) epoxy/substrate interface separation.

the shear strengths are still high. A tensile test that stresses the interface strength in the normal direction (perpendicular to the plane of the substrate and/or die) appears to be a more sensitive response parameter, especially after thermal annealing. All subsequent test sequences used a combination of shear and tensile force loadings. The tensile tests were conducted with special test buttons (about 60 mm²) with a surface plating representative of the particular substrate metallization system of interest (e.g., gold, aluminum). Full mechanical test flow sequences are presented schematically in Fig. 4.

The bulk resistivity of conductive epoxy was measured using a deposited four-point-probe technique. The results for two candidate epoxies are shown in Fig. 5. In the case of Ablebond 36-2, the experimen-

tal points agree quite favorably with the values obtained in a previous NASA study.² Stability measurements have been made under various conditions of thermal and electrical stress, as is shown in Fig. 4. Typical voltage versus current curves for test samples with ten epoxy joints in series are shown in Fig. 6. The curves are linear (implying constant resistance) for the three temperatures indicated and for all currents less than 2 A (900 A/cm²).

Advanced materials analysis techniques such as residual gas analysis, the scanning Auger microprobe, differential scanning calorimetry, and secondary ion mass spectrometry have been used to determine the compositional and behavioral properties of candidate epoxy materials both during and after curing as well as for an analysis of residual deposits (from the curing

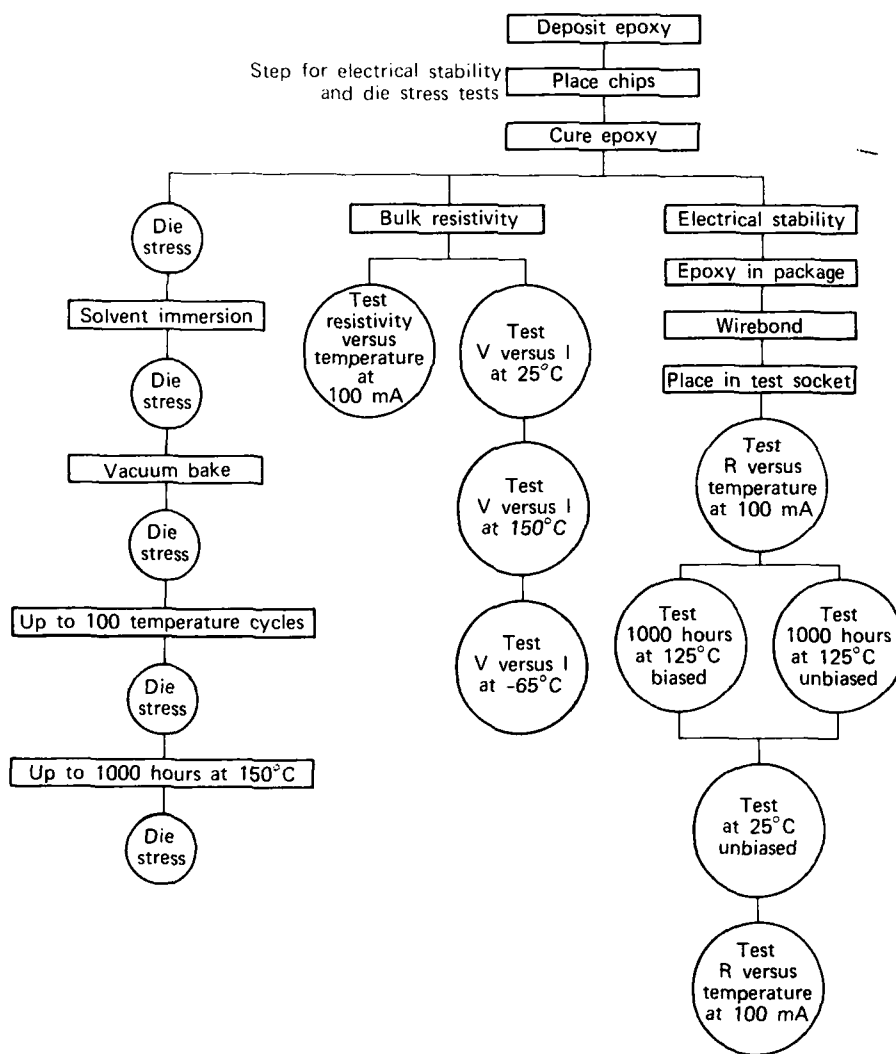


Figure 4 — Mechanical and electrical test flow sequences.

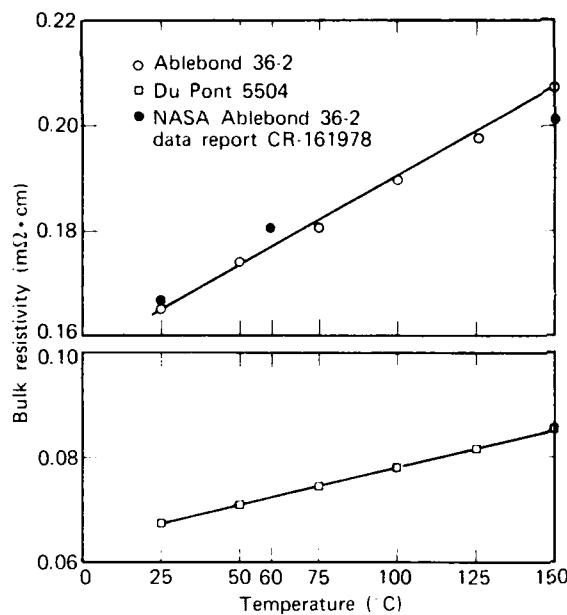


Figure 5 — Bulk resistivity versus temperature characteristics of conductive epoxies.

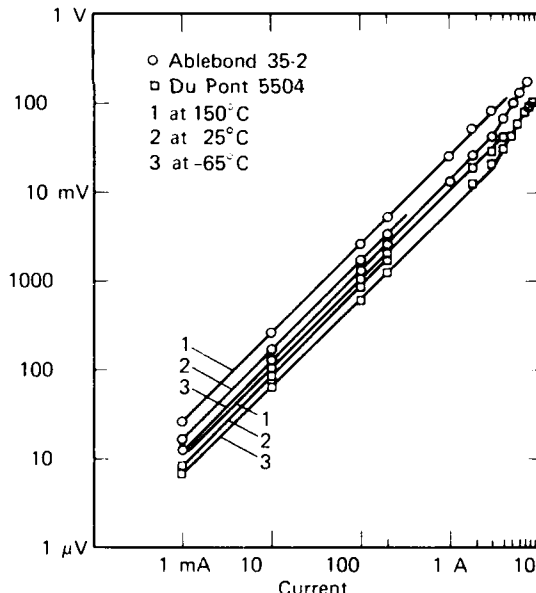


Figure 6 — Voltage versus current characteristics of conductive epoxies.

process) on adjacent substrate material.³ An example of a residual gas analysis is shown in Fig. 7. It was used to determine proper cure cycles, and it can be seen that the longer cure (twice the manufacturer's recommended time) produced less gaseous products during subsequent post-cure heating. Both the mechanical and

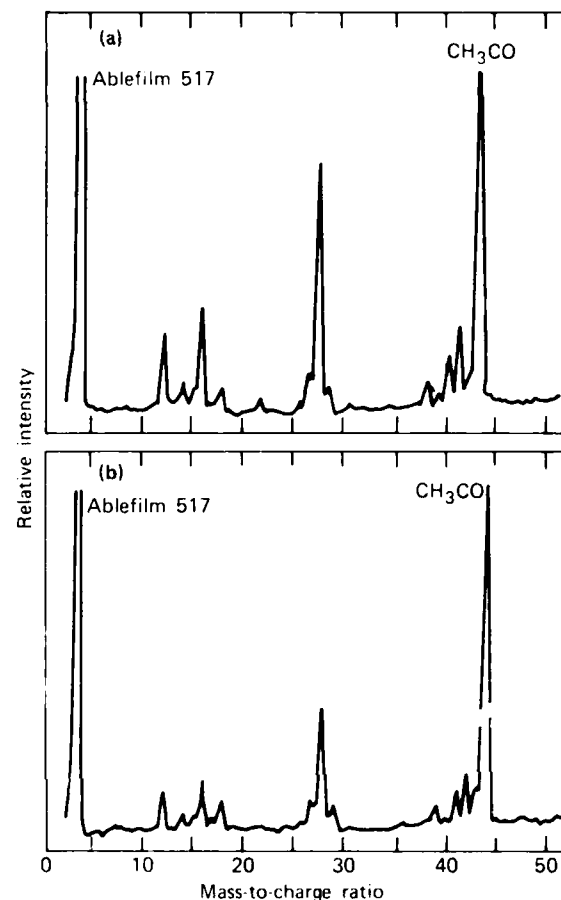


Figure 7 — Volatile species from cured epoxy after extended heating at 125°C (residual gas analysis spectra). (a) Short cure (2 h in nitrogen at 150°C); (b) long cure (4 h in nitrogen, 4 h in vacuum at 150°C).

the electrical properties of samples that were cured longer are equal to or exceed (in the case of shear strength) those of samples using the manufacturer's recommended time.

Secondary ion mass spectrometry and the scanning Auger microprobe have been used to analyze not only the bulk material but also the residual substrate deposits from the epoxy during curing. A typical Auger spectrum for a representative metallization is shown in Fig. 8. Carbon and fluorine signals appear in the vicinity of the cured epoxy and are absent on the control. Differential scanning calorimetry has been used to determine the glass transition temperature and the percentage of cure.³ Such information, when correlated with the residual gas analysis spectra and the Auger and secondary ion mass spectrometry results, can provide a comprehensive picture of the material characteristics and behavior.

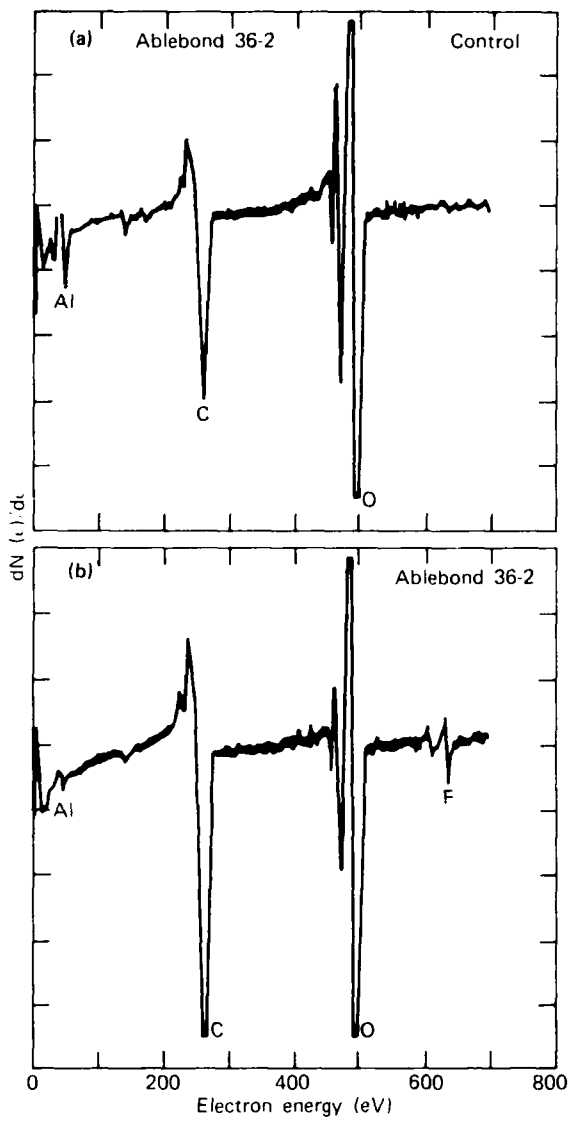


Figure 8 — Auger electron spectroscopy spectrum of substrate (aluminum on silicon) exposed to outgassing from Ablebond 36-2 epoxy during cure at 150°C (1 h in vacuum, 1 h in nitrogen). (a) Control. (b) exposed sample.

Hybrid Fabrication

Fabrication of representative hybrid test samples forms an integral part of the epoxy qualification program. A typical multifabrication technology hybrid (i.e., one that uses three forms of die attachment—eutectic (AuSi), solder (PbSn), and epoxy—is shown in Fig. 9a. The use of conductive epoxy would allow this hybrid to be assembled in a much faster manner with a higher initial yield (the matched transistor pair was par-

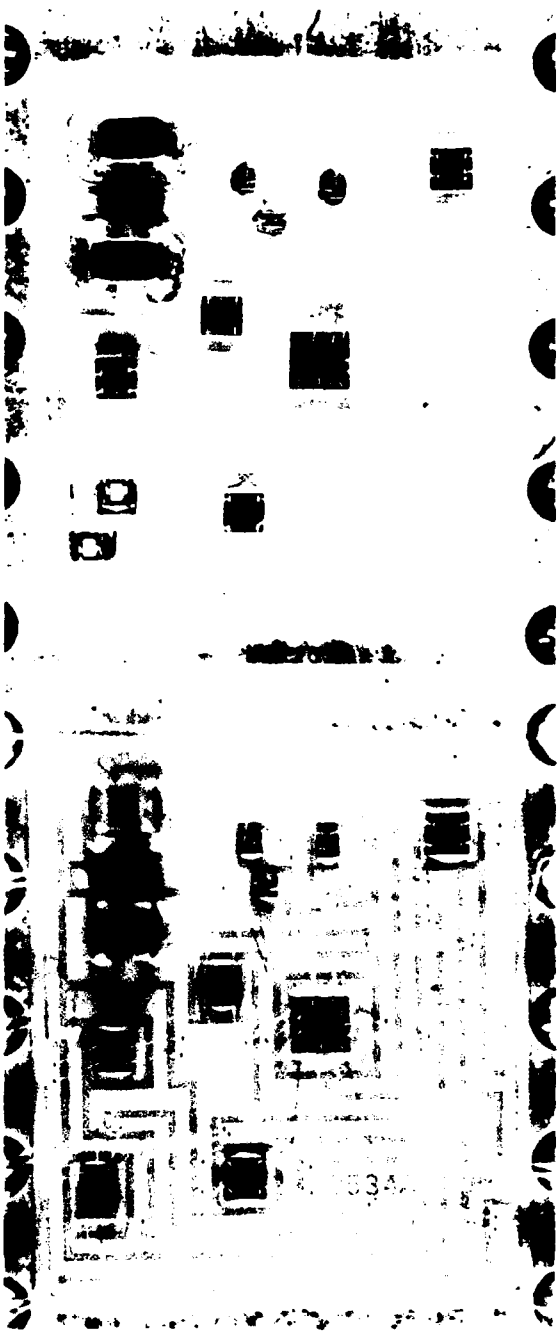


Figure 9 — Hybrid test samples (Model 0534 Peak Detector). (a) Multifabrication attachment system (standard process). (b) all-epoxy system (new process).

ticularly susceptible to the high temperatures encountered during eutectic die attachment). An all-epoxy version of this hybrid is shown in Fig. 9b. Full hybrid qualification has been performed on these hybrid samples and has shown that this method results in a better yield

than the multifabrication technology method. Detailed destructive physical analysis, long-term materials testing, and reliability studies are under way.

Reliability and Quality Assurance Considerations

An extensive qualification testing program to introduce new epoxies into the hybrid manufacturing line consisted of three distinct, but salient, phases: (a) mechanical and electrical property determination; (b) fabrication, screening, and analysis of representative hybrid lots; and (c) the application of advanced chemical and surface analysis methods to the bulk epoxy and to representative hybrid surfaces. Several interesting observations were made:

1. Although shear strengths remain relatively strong following long-term (1000 hours) thermal exposure and hybrid processing, it appears that changes occur either in the epoxy itself or at the interfaces. The changes shift the dominant mode of failure from bulk shear to interfacial separation, which suggests that a technique for die tensile testing may be a better measure of epoxy strength than the common shear test (especially considering the typical hybrid qualification test using constant acceleration).
2. Most electrical stability tests involve monitoring the room temperature resistivity after exposure to thermal and electrical stresses. It appears that the entire resistivity-versus-temperature curve should be monitored to detect end-point (intercept) changes and changes in slope.
3. Although the basic electrical and mechanical properties of an epoxy may appear to be acceptable, certain problems may occur in their actual use, such as handling, dispensing, and bleed-out during curing. Therefore, empirical hybrid fabrication must be included in any epoxy qualification program.
4. Advanced methods of materials analysis must be used to investigate both bulk impurities and, more importantly, adsorbed impurities on surrounding surfaces deposited during curing and subsequent hybrid processing. Such analyses should include differential scanning calorimetry, residual gas analysis, Auger electron spectroscopy, and secondary ion mass spectrometry.

The results of the program indicate that extensive complex testing and analysis are necessary to qualify an epoxy for high-reliability applications. Once they are qualified, certain basic tests can be performed routinely on incoming lots and, after specified time

periods, on lots in inventory to ensure lot-to-lot integrity and viability. The tests should include:

1. Viscosity measurement on conductive epoxies to provide for optimum screen printability, especially with epoxies whose solvents evaporate in air;
2. Bulk electrical resistivity with temperature (for conductive epoxies);
3. Mechanical die shear and tensile strength measurements (both conductive and nonconductive epoxies) to check the basic strengths and to monitor changes in surface adhesion properties;
4. Measurement of glass transition temperature and an analysis of residual gas when curing volatile species.

If results are nonstandard, either the lot should be rejected or the full new epoxy qualification plan should be repeated.

ACKNOWLEDGMENT

The authors greatly appreciate the efforts of the following individuals: G. W. Edwards for substrate preparation and epoxy curing; N. C. Kauffman, S. A. Brigman, K. J. Mach, and D. E. Talkin for epoxy application; D. P. Glock for all die shearing; J. M. McLean, H. S. Allwine, S. J. Mobley, and B. G. Carkhuff for electronic testing; D. O. Cowan for use of the DSC equipment; T. E. Phillips, W. A. Bryden, and M. Lee for DSC measurements; C. B. Bargeron and B. H. Nall for Auger spectroscopy; and F. G. Satkiewicz for SIMS analysis.

REFERENCES

1. H. K. Charles, Jr., B. M. Romenesko, G. D. Wagner, R. C. Benson, and O. M. Uy, "The Influence of Contamination on Aluminum-Gold Intermetallics," in *Proc. 1982 International Reliability Physics Symp.*, San Diego, p. 128 (30 Mar-1 Apr 1982).
2. J. J. Licari, B. L. Weingand, and C. A. Soylek, *Development of Qualification Standards for Adhesives Used in Hybrid Microcircuits*, NASA Contractor Final Report, George C. Marshall Space Flight Center, NASA CR-161978 (1981).
3. F. S. Dettmer, H. K. Charles, Jr., R. C. Benson, B. H. Nall, F. G. Satkiewicz, C. B. Bargeron, and T. E. Phillips, "Epoxy Characterization Using Mechanical, Electrical, and Surface Analysis Techniques," *Int. J. Hybrid Microelectron.* **6**, 283 (1983).

This work was supported by Independent R&D.

BALL-BOND SHEAR TESTING

H. K. Charles, Jr., G. V. Clatterbaugh, J. A. Weiner,
and G. D. Wagner

A comprehensive program to test ball-bond shearing has been conducted. It has led to the systematic modeling of the thermosonic ball-bonding process, the optimization of bonding machine parameters, and the production of highly reliable wire bonds for microcircuit applications. The ball-bond shear test has been used as a qualification tool for investigating the effects of thermal processing, contamination, and material morphology on the bonding interface. Over 13,000 thermosonic ball bonds have been sheared in 300 experimental test sequences.

BACKGROUND

The destructive wire-bond pull test is the universally accepted technique¹ for evaluating and controlling the quality (strength) of microelectronic wire bonds, for setting bonding machine parameters, and for certifying wire-bond line performance. Although that technique has been shown to be adequate for the evaluation and control of aluminum wedge bonds,² it is quite apparent that, because of its large interfacial weld areas (nominally six to ten times the cross-sectional area of the wire), it provides little information on the strength and hence the relative quality of the ball-bond/bonding-pad interfaces. Even in poorly made ball bonds the wire will break in pull testing¹ before the ball lifts. Only in the case of catastrophic failures, such as low-temperature impurity-driven intermetallic growth,³ will the destructive wire-bond pull test yield information other than the relative breaking strength of the wire. Thus, a new test that stresses the ball-bond/bonding-pad interface is needed as a complement⁴ to the traditional wire-bond pull test to ensure complete wire-bond viability in the various microelectronic packages and systems available today.

The ball-bond shear test⁵ (Fig. 1) can provide this interfacial stress. The test involves bringing a mechanical shearing ram up to the outside of a bonded ball, applying a force to the ball (parallel to the plane of the bonding-pad metallization) of sufficient magnitude to push the ball off the pad and/or substrate metallization, and recording the value of that force.

DISCUSSION

Equipment

The ball-bond shear data were obtained using a Dage-Precima MCT-20 Microtester, a semiautomatic

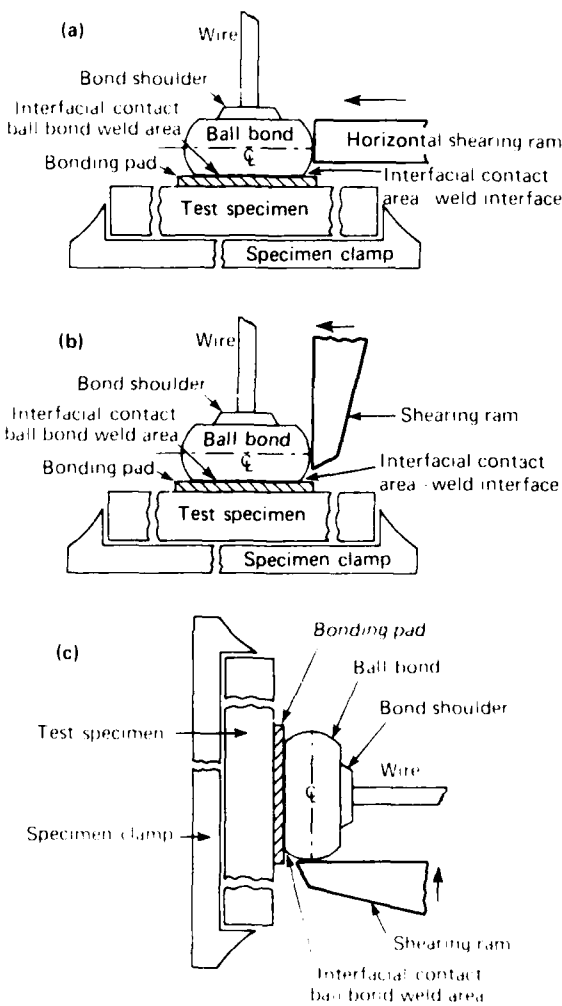


Figure 1 — Schematic diagrams of the ball-bond shear tests. (a) Horizontal sample and horizontal ram, (b) horizontal sample and vertical ram, and (c) vertical sample and vertical ram.

microprocessor-controlled unit in which the ram must be positioned manually. Using the micrometer-controlled universal sample holder (Fig. 2), the shearing ram can easily be positioned to tolerances better than $\pm 5.0 \mu\text{m}$ (0.2 mil) in the x and y directions and $2.5 \mu\text{m}$ (0.1 mil) in the z (above substrate) direction. Once positioned, the unit automatically performs the testing operation, it digitally displays the maximum value of shear force as measured by the built-in strain gauge (0 to 200 grams force, $\text{e} \cdot 1$ range).



Figure 2 — Close-up view of shearing ram and test substrate on the Dage-Precima MCT-20 Microtester.

The MCT-20 Microtester is also equipped to perform nondestructive ball shear testing (in complete analogy to the nondestructive wire-bond pull test⁶). In the nondestructive case, the shearing ram loads the ball bond with a predetermined load specified by the operator. When that load has been reached, the ram automatically returns to its starting position. The display indicates the preset load unless the ball sheared before the specified limit was reached; then the display indicates the failure load.

A flat chisel-shaped tool (Fig. 2) with a shearing edge dimension of 0.152 mm (6 mils) has been most effective for shearing ball bonds made with 25.4 μm (1 mil) diameter gold wire. The travel rate of the shearing ram on the MCT-20 is adjustable from 0.25 to 6.0 mm/s; experiments have shown that ball shear distributions are essentially independent of shearing rate in this range. Most of the 13,000 ball shears conducted to date were at a rate of 1.0 mm/s.

Baseline Data and Experimental Design

Using the shearing equipment and the general procedures outlined above, gold thermosonic ball-bond shear data have been collected on a variety of circuits and material sample configurations, including gold metallization on alumina (polycrystalline Al_2O_3 ,

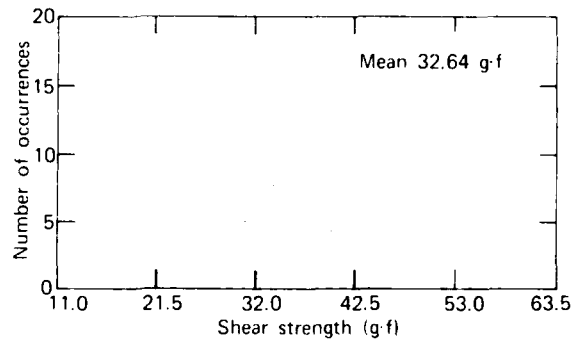


Figure 3 — Histogram of wire-bond shear strengths of gold thermosonic ball bonds to aluminum metallization on silicon.

99.6% pure) and aluminum metallization on silicon. Figure 3 is a typical histogram for the shear strength of gold ball bonds on aluminum metallization with silicon (*n/p* type, (100) orientation) as the substrate material.

Care was taken to clean all substrate metallizations with oxygen plasma or ultraviolet light (UV)-ozone before bonding. The bonding machine parameters were optimized using the standard wire-bond pull test. It was quite clear from preliminary experiments that this set of bonding parameters — although producing good wire bonds (by visual inspection and pull test criteria) and adequate shear strengths — did not optimize the ball-bonding process. With the ball shear test providing a direct measure of the ball-bond/bonding-pad interface strength, it was possible to construct experiments whose results provided specific guidelines for ball-bond optimization. In those experiments, the effect of bonding parameters on gold-to-aluminum ball shear were investigated using a fractional factorial design.⁷

A complete 2^3 factorial design table including second- and third-order interactions is shown in Table 1. (In the table, P is the first bond power in millivolts, T is the substrate temperature in degrees centigrade and D is the first bond dwell in milliseconds.) The responses denoted as S_i ($i = 1$ to 8) are the mean strengths for

Table 1 — Experimental design and observed responses for linear ball shear model.

1st Order			2nd Order			3rd Order	
P	T	D	$P \times T$	$P \times D$	$T \times D$	$P \times T \times D$	Response
1	1	1	+1	+1	1	-1	S_1
1	1	-1	+1	-1	-1	+1	S_2
1	-1	1	-1	+1	-1	+1	S_3
1	-1	-1	-1	-1	+1	-1	S_4
+1	1	1	1	-1	-1	1	S_5
+1	1	-1	1	-1	-1	1	S_6
+1	-1	1	-1	1	-1	1	S_7
+1	-1	-1	-1	1	+1	-1	S_8

each experimental treatment. The calculation of any effect is simply the sum of the products of each level and the corresponding response, all divided by 2^{k-1} where k in this case equals 3. For example, the effect of first bond power is

$$P = (-S_1 - S_2 - S_3 - S_4 + S_5 + S_6 + S_7 + S_8)/4.$$

Experimental results on aluminum metallizations of various thicknesses (1, 2, 3, and 6 μm) indicate that increasing the first bond power by 30 mV (i.e., -1 to +1) has a significant effect (except for the 6 μm film) on increasing the bond shear strength. The mean shear strength as a function of dwell time is plotted in Fig. 4 for various substrate temperatures and power settings. For the 100°C substrate temperature, the mean shear strength is a linear function of dwell time over the range from 26 to 50 ms with a slope of +0.25 g·f/ms. At 150°C, the linear relationship breaks down and the shear strength increases rapidly with dwell time up to approximately 40 ms.

Ball Shear Model

A linear model for the mean ball-bond shear strength in terms of the bonding machine parameters (P , T , and D) was constructed using a 2^3 factorial experimental design with replicated center points, as shown in Table 2. The resultant linear model for the shear strength(S) takes the form

$$S = B_0 + B_1 P + B_2 T + B_3 D,$$

● $P = 260 \text{ mV}$ $T = 100^\circ\text{C}$ ▲ $P = 260 \text{ mV}$ $T = 150^\circ\text{C}$
 ■ $P = 290 \text{ mV}$ $T = 100^\circ\text{C}$ ● $P = 290 \text{ mV}$ $T = 150^\circ\text{C}$

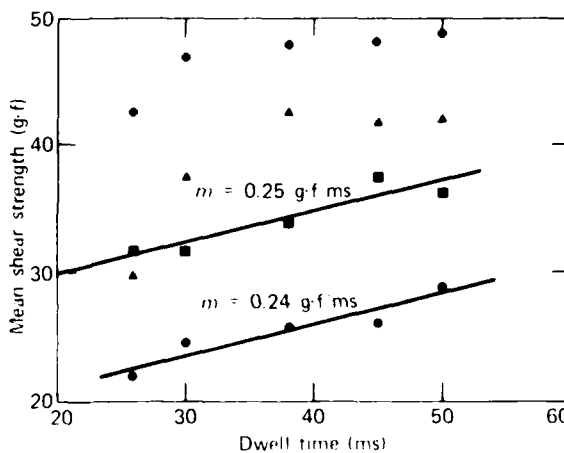


Figure 4 — Effect of dwell time on mean wire-bond shear strengths for various first bond power and pedestal temperature settings.

Table 2 — A complete 2^3 factorial design interaction table (unreplicated).

P^*	$T^†$	$D^‡$	Shear strength (g·f)
-1	-1	-1	24.7
-1	-1	+1	26.2
-1	+1	-1	37.8
-1	+1	+1	42.0
+1	-1	-1	31.8
+1	-1	+1	37.9
+1	+1	-1	47.0
+1	+1	+1	48.4
0	0	0	37.6
0	0	0	36.9
0	0	0	37.4
0	0	0	35.1

* $P (+1 = 290 \text{ mV}, 0 = 275 \text{ mV}, -1 = 260 \text{ mV})$

† $T (+1 = 150^\circ\text{C}, 0 = 125^\circ\text{C}, -1 = 100^\circ\text{C})$

‡ $D (+1 = 45 \text{ ms}, 0 = 38 \text{ ms}, -1 = 30 \text{ ms})$

where the coefficients for the responses shown in Table 2 are $B_0 = -104.3$, $B_1 = 0.29$, $B_2 = 0.27$, and $B_3 = 0.22$. The equation simplifies the understanding of how the bonding parameters influence bond strength, eliminating the need for the usual complex three-dimensional graphical plots. In addition, the linear factorial design provides an efficient way to generate new models should different substrates and/or substrate metallizations be required. The linear equation's "goodness of fit" to the experimental data was found to be within 95% for the range of bonding parameters considered. Figure 5 is a histogram of gold-to-aluminum ball shear data for optimized bonding parameters derived from the ball shear equation.

Parameteric Test Results

The influence of the thickness of the aluminum metallization on the strength of the gold-to-aluminum wire bonds was investigated using ball shear as a response parameter. The test results clearly indicate a linear reduction in the net shear strength as a function of film thickness for constant bonding parameters with a slope of approximately $1.9 \text{ g·f}/\mu\text{m}$ thickness of aluminum. In addition to metallization thickness, the effects of substrate surface roughness (morphology) and material were investigated. Silicon, alumina, and single-crystal sapphire (Al_2O_3) were used for the comparative analyses. The results were considered for several metallization thicknesses and a range of bonding parameters. The only significant as-bonded effect noted was the influence of film thickness (associated with a particular substrate morphology). That effect consisted of an increased mean shear strength for the rougher alumina as the metal film thickness increased while for the smoother silicon and sapphire the mean shear strength decreased.

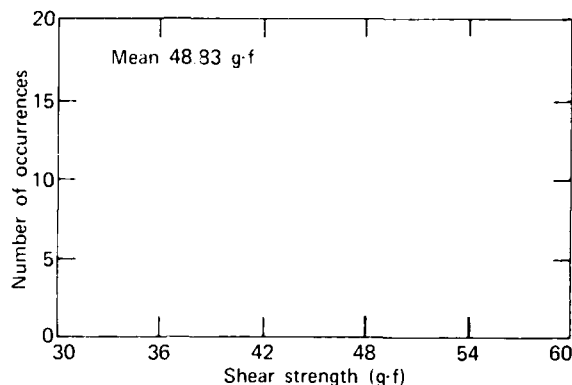


Figure 5 — Histogram of wire-bond shear strengths of gold thermosonic ball bonds to aluminum metallization (on silicon) after optimization with the ball shear equation.

Contamination and cleaning methods have been studied using ball shear as the parametric response parameter. Four different cleaning methods (hydrocarbon solvent, acid, UV-ozone, and oxygen plasma) were used to remove two types of contamination: photoresist and epoxy gaseous products. Typical test data have been published previously.³ Solvent cleaning was found to be the least effective way to restore ball shear strength to the levels of uncontaminated materials. The solvent treatment had little effect on cleaning either epoxy residues or photoresist; the shear strength differed little between the cleaned and the uncleansed surfaces. In fact, in most cases, the sample mean was actually lower after cleaning.

Cleaning both contaminants with a sulfuric acid/potassium persulfate solution did restore the mean shear strength to the level of bonds made on uncontaminated substrates. The method performed equally well on both aluminum and gold metallized substrates. Unfortunately, this type of cleaning process is incompatible with many organic materials used in microcircuit assembly, including epoxy resins. Oxygen plasma cleaning was also found to be acceptable for restoring shear strengths for both contaminants and substrate types. The UV-ozone cleaning yielded the most significant improvement in bond shear strength for both contaminants on gold metallization. For aluminum on silicon

samples, the sheer strength was not restored to uncontaminated levels, but there was some improvement.

Thermal wire-bond stressing experiments at elevated temperatures (125, 200, 250, and 300°C) were conducted to evaluate bonding mechanisms and aluminum-gold intermetallic growth. Activation energies were determined using parabolic intermetallic growth laws. During the initial growth phases, a combined activation energy of 13 kcal/mole was calculated on the basis of ball shear test responses.

ACKNOWLEDGMENT

The authors gratefully acknowledge the efforts of W. L. Smith, N. C. Kauffman, and K. J. Mach in wire bonding; D. P. Glock and D. F. Talkin in ball shearing; D. O. Shapiro in SEM microphotography; M. S. Mandella in general photography; and G. S. Mitchell, R. N. Neuwiller, and M. B. Bender in substrate fabrication.

REFERENCES

- H. K. Charles, Jr., B. M. Romenesko, O. M. Uy, A. G. Bush, and R. von Briesen, "Hybrid Wire Bonding Testing - Variables Influencing Bond Strength and Reliability," *Int. J. Hybrid Microelectron.*, **5**, 260 (1982).
- G. G. Harman and C. A. Cannon, "The Microelectronic Wire Bond Pull Test - How to Use It, How to Abuse It," *IEEE Trans. Components, Hybrids, Manuf. CHMT-1*, 203 (1978).
- H. K. Charles, Jr., B. M. Romenesko, G. D. Wagner, R. C. Benson, and O. M. Uy, "The Influence of Contamination on Aluminum-Gold Intermetallics," in *Proc. 20th IEEE International Reliability Physics Symp.*, p. 128 (Apr 1982).
- H. K. Charles, Jr., and G. V. Clatterbaugh, "Ball Bond Shearing - A Complement to the Wire Bond Pull Test," *Int. J. Hybrid Microelectron.*, **6**, 127 (1983).
- G. G. Harman, "The Microelectronic Ball Bond Shear Test - A Critical Review and Comprehensive Guide to Its Use," *Int. J. Hybrid Microelectron.*, **6**, 127 (1983).
- G. G. Harman, "A Metallurgical Basis for the Non-Destructive Wire Bond Pull Test," in *Proc. 12th IEEE Reliability Physics Symp.*, p. 205 (Apr 1974).
- I. Guttman, S. S. Wilks, and J. S. Hunter, *Introductory Engineering Statistics*, John Wiley and Sons, New York, p. 403 (1971).
- J. A. Weiner, G. V. Clatterbaugh, H. K. Charles, Jr., and B. M. Romenesko, "Gold Ball Bond Shear Strength: Effects of Cleaning, Metallization and Bonding Parameters," in *Proc. 33rd Electronic Components Conf.*, Orlando, Fla., p. 208 (16-18 May 1983).

This work was supported by Independent R&D.

CUSTOM LARGE-SCALE INTEGRATED CIRCUIT

R. C. Moore and R. E. Jenkins

A custom large-scale integrated circuit design capability has been established at APL. A fully integrated set of user-friendly software tools has been placed on two of the Laboratory's computer systems to enable design engineers to create and simulate custom integrated circuit designs. The facility has been used to create a complex NMOS design that has been successfully fabricated by a silicon foundry.

BACKGROUND

Out of the current technological advances in very large scale integration (VLSI) has emerged a potential for the cost-effective, full custom design of high-density integrated circuits in small lots. The availability of sophisticated computer-aided design (CAD) tools and the existence of competing silicon foundries offer government laboratories without in-house LSI fabrication facilities a unique opportunity to explore this potential. The possibility now exists for solving problems in innovative systems applications that cannot be accomplished with off-the-shelf components or gate arrays. APL has reduced this possibility to practice by designing a custom integrated circuit and having it fabricated.

DISCUSSION

The overall goal of this effort was to establish a capability for applying LSI technology to spaceborne systems. The effort was limited to design considerations; testing of complex LSI circuits is beyond the present capabilities of the Laboratory. However, certain built-in-test functions were included in the design to facilitate manual testing of the finished chips.

The heart of the design facility is an integrated collection of CAD tools running on a VAX-11 780 computer:

1. A hierarchical interactive color graphics editor (called CAESAR) by means of which cell libraries are built at the mask layout level;
2. A conversion or translation program that converts CAESAR data-base formats into Caltech intermediate form (CIF);
3. A circuit extractor that creates a device file and net list, including estimates of parasitic capacitances, from the CIF file;
4. Two logic-level functional simulators: one simulates enhancement mode transistors as if they were switches, the other performs simplified estimations of system timing as well;
5. A conversion program that translates the output of the circuit extractor into a format compatible with the circuit simulator;
6. A detailed circuit simulator that simulates actual node voltages and currents by modeling transistor parameters;
7. A design rule checker that checks the mask-level layout for design rule violations, e.g., the polysilicon too close to diffusion, the transistor gate not extending far enough beyond the source/drain region, improper overlapping of the ion implant, or buried contact with corresponding structures;
8. A Versatec plotter package that permits hard-copy checkplots to be created directly from the CIF files.

All of these tools are made compatible by maintaining files in particular predefined formats. File directory maintenance is performed by the UNIX operating system, under which all these CAD tools run. Several other CAD tools are available to supplement them, including an automatic, programmable, logic array generator.

The goal in the design was to include on the chip all the major portions of the carrier tracking logic for the digital phase-locked loop of a global positioning system navigation receiver. The most recent designs for global positioning system receivers use microprocessors to control the carrier- and code-tracking logic. The microprocessor performs arithmetic associated with scaling, integrating, and filtering the detected phase error signal. The microprocessor then controls a digitally controlled oscillator (DCO) that is usually a form of binary rate multiplier (BRM).

The minimum required hardware functions for carrier tracking in this type of design are two identical phase error detectors/integrators (one for each quadrature component, I and Q, of the local DCO), a BRM to function as the DCO, and some logic at the output of the BRM to produce the two quadrature phases of the local signal at baseband frequency.

To reduce the overall scope of the chip project to a realistic level, it was decided not to implement a complete stand-alone carrier tracking loop but to include the major pieces with sufficient input/output capability to test functionality and to include the chip in a breadboard version of a carrier tracking loop if that later proved desirable for demonstration purposes. Included were an 18-bit BRM designed to operate at a clock frequency of 2.5 MHz and a phase error detector/integrator designed to operate at a sampling frequency of 10 MHz. Figure

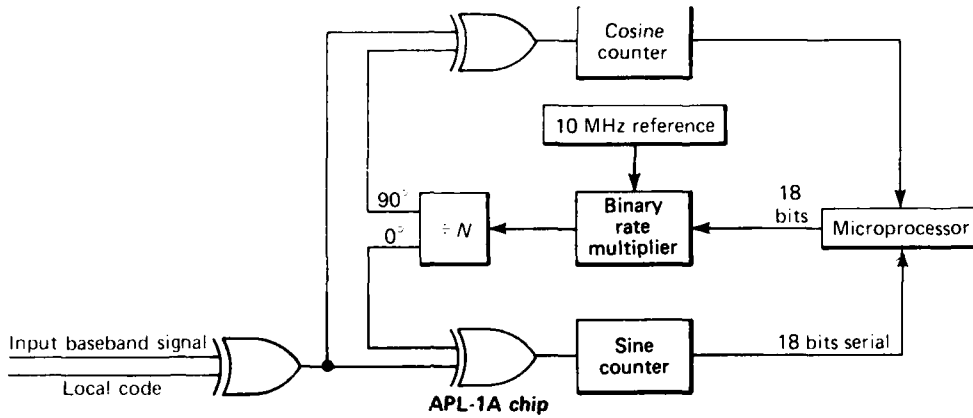


Figure 1 — The microprocessor-controlled carrier tracking loop.

1 is a block diagram of a microprocessor-controlled carrier tracking loop. The tinted area indicates the region included on the chip.

Two copies of the phase error detector (sine and cosine) would be required in an operational receiver; however, only one was included on the chip. This permitted the scope of the project to be expanded to include two other functions: a control unit switch and an arithmetic multiplier. The control unit switch is designed to control the switching of a computer terminal between two terminal control units. The arithmetic multiplier is an expandable, parallel two's complement design with wide application in signal processing. Figure 2 shows the completed chip.

The major function cells that were generated in the design are:

1. A toggle flip-flop used as high-order bits in phase integrator counters and in several divider circuits;
2. A D-type flip-flop widely used in various control circuits and in the control unit switch project;
3. A generator of two-phase, nonoverlapping clocks with super buffer line drivers;
4. An inverted exclusive-OR with 20 MHz response, used as a phase comparator;
5. A high-speed OP/NO-OP counter used as a lowest-order bit in phase integrator counters and in divider chains;
6. A binary full adder to compute the effective up/down count in the phase integrator;
7. A parallel-load, serial-shift register element to sample and shift out the phase integrator results;
8. A clock synchronizing cell with a super buffer line driver, used in control sections to syn-

chronize control signals with desired clock phases;

9. A 2-bit counter module with a synchronous carry chain, used in the BRM (the BRM counter is formed by nine of these modules);
10. An output logic module for the BRM that uses the positive derivative of BRM counter outputs to produce a BRM output that is rate controlled.

In addition to these cells, various others were produced for use in isolated places throughout the chip. Various test cells also were included; they will allow different types of devices to be tested by the probing of unpackaged chips.

Processed wafers, each containing about 165 dice, were received from the silicon foundry seven weeks after the purchase contract was issued. Probe testing of the wafers and subsequent testing of the packaged parts verified that the circuits work exactly as predicted by the computer design models. Pulses as short in duration as 20 ns were modeled accurately by the circuit simulator. The BRM easily ran at 2.5 MHz, and the phase error integrator ran at clock speeds up to 20 MHz. The completed circuits met all of their specifications with some margin on speed.

The chip was 0.197 by 0.219 in. and contained approximately 8000 transistors. Foundries can produce chips as large as 0.42 by 0.42 in. Therefore, using the existing CAD tools and design rules, one could design and fabricate a circuit that would contain 30,000 transistors. This is just a factor of two away from VLSI. These CAD tools are adequate for designs well beyond this level of integration, and their establishment puts the Laboratory in a position to exploit future improvements in foundry technology for custom VLSI design.

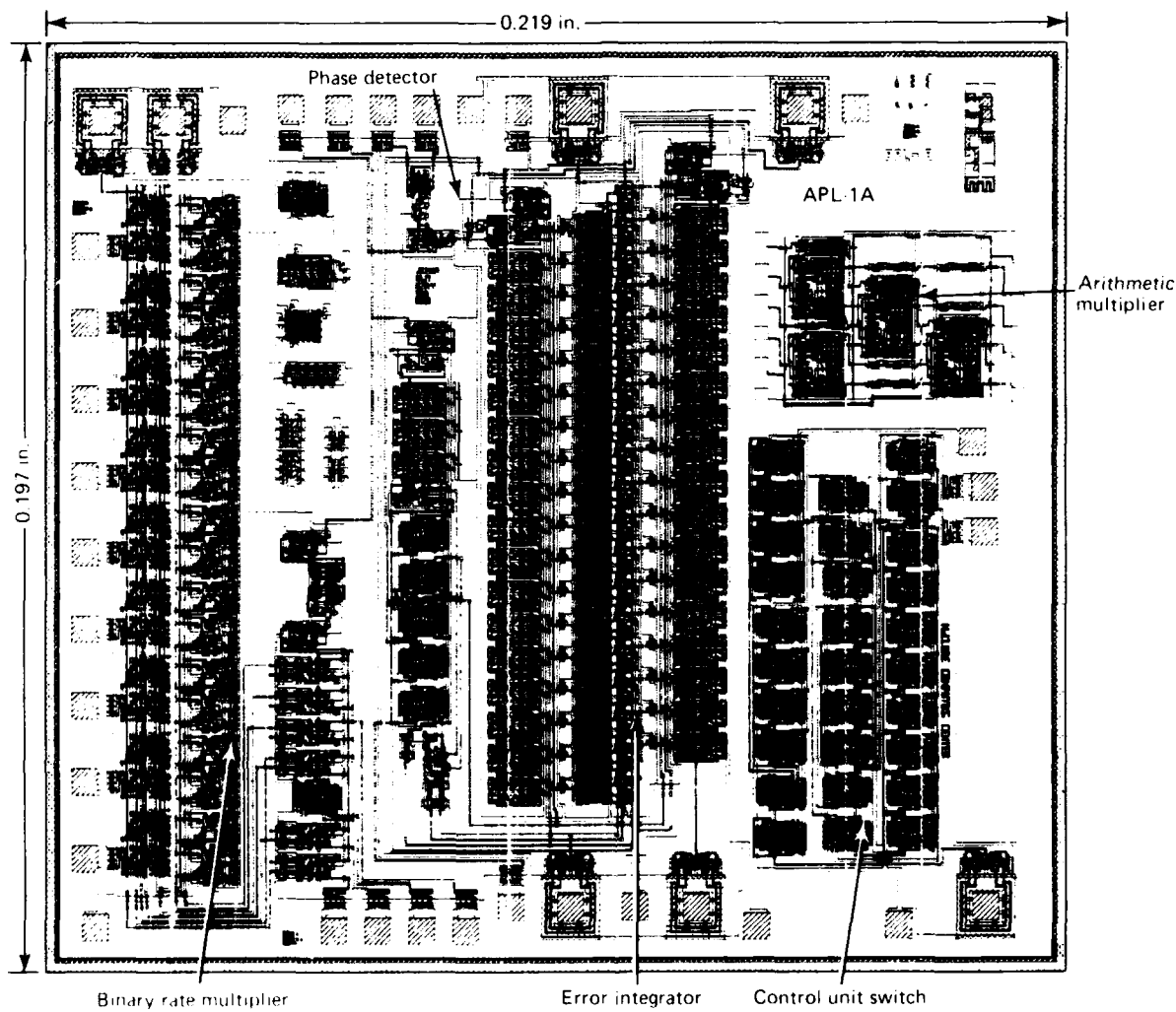


Figure 2 — The completed integrated circuit chip.

CONCLUSION

An integrated circuit design capability has been established at APL and has been proven by the creation of a working chip. Future expansion of the facility to in-

clude CMOS technology will enhance its usefulness to the Laboratory.

This work was supported by Independent R&D.

FUNDAMENTAL RESEARCH

INTRODUCTION

Fundamental research has been firmly established at APL for many years as one of the Laboratory's principal missions. Those missions include the application of advanced science and technology to the enhancement of the security of the United States and the pursuit of basic research to which the Laboratory's facilities can make an especially favorable contribution. The incorporation of basic research into APL's mission recognizes that such research will play a vital role in future technological achievements and that it is needed to avoid institutional obsolescence.

Much of the basic research conducted at APL is done in the Research Center, which was formally established in 1947. Its objectives are "to carry on basic research supporting present and potential mission areas of the Laboratory, to establish the Laboratory as a contributor to basic science, to provide research techniques and technical consulting for solving problems critical to Laboratory programs, and to serve as an entry for new talent and scientific information into the Laboratory." Since its inception, the Research Center has spawned new programs that are now carried out in other units of the Laboratory. Most notable are the Space Department and the Biomedical Research Program.

Today, the Milton S. Eisenhower Research Center is comprised of 52 staff members organized into four groups. Research is reported in the professional scientific literature; typically, 60 papers are published each year. The articles in this section describe some recent accomplishments in fundamental research by staff members of the Research Center.

PHOTOELECTROLYSIS OF WATER BY MODIFIED TRANSITION METAL OXIDES

T. E. Phillips, J. C. Murphy, K. Moorjani,
and T. O. Poehler

We have shown that the alloying of $FeTiO_3$ into the n-type Fe_2O_3 lattice significantly improves the photoelectrochemical spectral response of the semiconductor, making it a potentially attractive candidate for solar energy conversion applications.

BACKGROUND

Recognizing the difficulties generally associated with the currently established energy sources (such as reliability of supply, quantity, and pollution and safety problems), it is slowly becoming evident that alternative energy sources must be given serious consideration. Of all the other sources available, solar energy will most likely be the principal candidate.

Solar energy conversion by means of solid-state photovoltaic cells is a well established process and will play a major role in the use of solar energy in the years to come. Another less well known approach to solar energy conversion known as photoelectrochemistry is

beginning to show promise and may also play an equally important role in the future.

The basis of a photoelectrochemical cell lies within the Schottky barrier that is formed when a semiconductor is immersed in a liquid electrolyte (Fig. 1). The solution serves as a substitute for the metal electrode in a conventional Schottky junction. In fact, much of the interest in photoelectrochemical systems stems from the fact that with the replacement of the metal electrode by the solution, the barrier interface is now readily accessible for investigation and the "metal" electrode can be neatly and conveniently altered simply by varying the chemical composition of the solution. Also, with the interface so exposed, it is possible to perform productive chemical reactions right at the interface — notably the photoelectrolytic decomposition of H_2O to O_2 and H_2 .

Much of the work^{1,2} in this field has concentrated on the semiconductor side of the Schottky junction, searching for a material with a bandgap of about 1.3 to

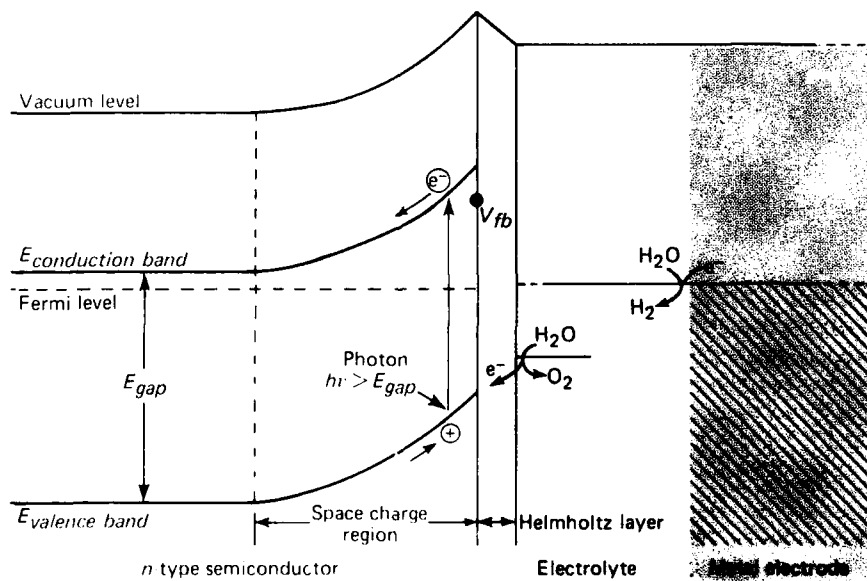


Figure 1 — Energy level diagram for an n-type semiconductor/electrolyte junction showing the relationships between the electrolyte redox couples O_2/H_2O and H_2O/O_2 , flatband potential, space charge region, bandgap, conduction and valence bands, and Fermi level. Also depicted is a simplified picture of an electron-hole pair being generated by the absorption of a photon ($h\nu > E_{gap}$), with the electron being accelerated into the semiconductor bulk, and the hole reacting with the solution.

1.8 eV in order to use the solar flux energy profile efficiently. The ideal material must be stable toward decomposition by the photogenerated minority carrier (a hole in the case of an *n*-type semiconductor), and its flatband potential (V_{FB} , almost equal to the energy of the conduction band) must be negative of the H_2/H_2O reduction-oxidation potential in order to photoelectrolyze H_2O .

No single known semiconducting material has all of these properties, although a family of semiconductors derived from transition metal oxides is not far from being ideal. Transition metal oxides are inherently stable toward decomposition, have fair-to-good efficiencies, and have reasonable V_{FB} 's. Their major drawback is a bandgap that is typically 2.2 to 3.8 eV – too high for solar energy conversion applications. Our approach has been to try to reduce the bandgap through chemical modifications while retaining the other positive features of the semiconductor material.⁷

DISCUSSION

Specifically, we are investigating a naturally occurring alloy system of Fe_2O_3 and $FeTiO_3$ (hematite and ilmenite) that forms a solid solution over the whole composition range.

In the hematite-ilmenite mineral series [$xFeTiO_3 \cdot (1-x)Fe_2O_3$], Mossbauer measurements⁸ indicate that for $x < 0.6$, there is a considerable amount of charge transfer from Fe^{+2} in the titanate to Fe^{+3} in the hematite. For many minerals where the crystal field interactions of the participating ions are different, the energy of this charge transfer reaction is often found in the visible region of the spectrum.⁹ It is important to examine the effects of those interactions ($Fe^{+2} \rightarrow Fe^{+3}$, $Fe^{+2} \rightarrow Ti^{+4}$, and $Ti^{+4} \rightarrow Ti^{+3}$) when introduced into the Fe_2O_3 photoelectrochemical system.

We also wanted to evaluate the stabilization of the Fe_2O_3 semiconducting properties by the introduction of Fe^{+2} ions contained within a nearly identical crystal lattice ($FeTiO_3$), as opposed to the usual addition by means of a structurally incompatible Fe_2O_3 spinel structure. Finally, changes in the other photoelectrochemical parameters of interest such as quantum efficiency and flatband potential in the alloy system were investigated.

The $xFeTiO_3 \cdot (1-x)Fe_2O_3$ samples were prepared in the form of thin films on glass substrates by RF reactive sputtering (known as RE oxides) and by thermal oxidation (known as thermal oxides). The films were characterized by X-ray diffraction measurements for information on structure and composition, secondary ion mass spectroscopy for elemental composition, and dif-

ferential capacitance measurements for flatband determinations. The results of the measurements will not be discussed explicitly; rather we will concentrate on visible absorbance, photoconductivity, and photoelectrochemical measurements and on the variations observed as a function of the $FeTiO_3$ concentration.

The absorptivity spectra of the RE oxides are presented in Fig. 2. If we take the 0% curve (Fe_2O_3) as a point of reference, the addition of 8.8 to 10.6% $FeTiO_3$ causes the absorptivity to increase somewhat in the 500 to 600 nm region. As the $FeTiO_3$ concentration increases beyond 10.6%, the absorptivity begins to drop as the edge appears to be blue shifted. This is to be expected because $FeTiO_3$ has a bandgap energy (E_{gap}) of 2.58 eV, and the film's spectral response should at some point reflect the fact that the $FeTiO_3$ content is increasing.

When these data are presented in the form $(\alpha h\nu)^{1/2}$ versus $h\nu$, where α is the absorption coefficient and $h\nu$ is the photon energy, the linear relationship indicates that the bandgap transitions are indirect. There is also some suggestion that the E_{gap} may have been lowered to 1.9 to 1.8 eV for the 8 to 11% films from the 2.0 value seen for Fe_2O_3 .

The photoconductivity of the RE oxides is shown in Fig. 3. Although it is not possible to overlay the photoconductivity response with the absorption spectra in an absolute sense because of variable electrode placement and excitation beam area, the photometric responses are qualitatively similar, with the concentration-dependent red shift being even more predominant in the photoconductivity spectra.

Because of the uncertainty in the absolute photocurrent yield (electrons per incident photon), it is not possible to calculate the absorptivity of the materials

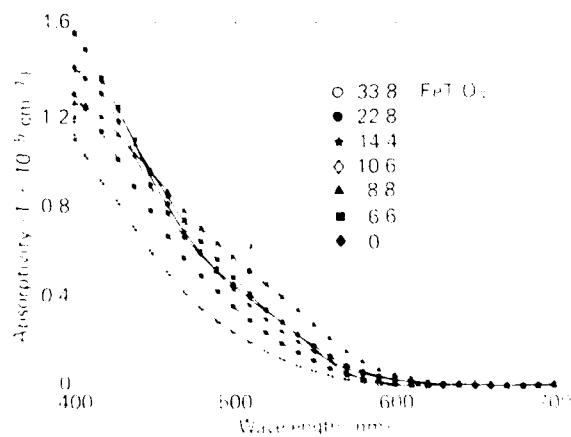


Figure 2 — Visible absorptivity spectrum for the $xFeTiO_3 \cdot (1-x)Fe_2O_3$ thin film.

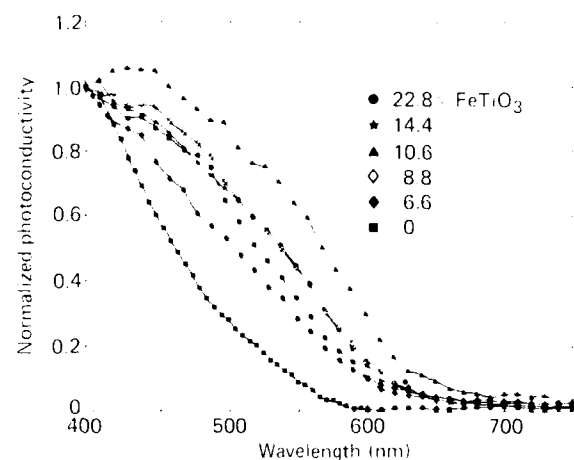


Figure 3 — Normalized photoconductivity as a function of wavelength for the RF oxides. Values were normalized to the value at 400 nm.

from the photocurrent. On the other hand, it is possible to calculate a relative photoconductivity spectrum from the absorptivity spectrum, assuming a constant quantum yield throughout the wavelength region of interest.

When this is done for the data in Figs. 2 and 3, the measured photoconductivity of the 0% film is less than the photoconductivity calculated from the absorptivity spectra. This indicates that not all the absorption events occurring in the film are resulting in the formation of free carriers in the conduction band. As the concentration of FeTiO_3 increases, the calculated photoconductivity curve begins to approach the measured photoconductivity spectrum, indicating that more of the photon absorption events are resulting in free-carrier formation.

Photoelectrolysis measurements were performed on both RF oxides and thermal oxides. Figure 4 depicts the photocurrent spectrum for the series of RF oxides at an applied potential of 0.0 V (versus saturated calomel electrode (SCE)). Taking the 0% curve as a point of reference, the relative photoresponse in the 450 to 600 nm region is enhanced for the lower FeTiO_3 content samples (8.8 to 14.4%). As the concentration increases above 14.4%, the response in this wavelength region begins to fall back to the 0% reference curve. Note also that the addition of Ti extends the photoresponse of the oxides beyond the 620 nm (2.0 eV) bandedge of Fe_2O_3 , as if the bandgap had been lowered. Attempts to determine the bandgap and nature of the transition by plotting $(\eta \cdot h\nu)^{-1}$ versus energy, where η is the quantum efficiency and n is a constant that depends on the type of transition, were inconclusive. It appears that the activity beyond the 620 nm bandedge probably results

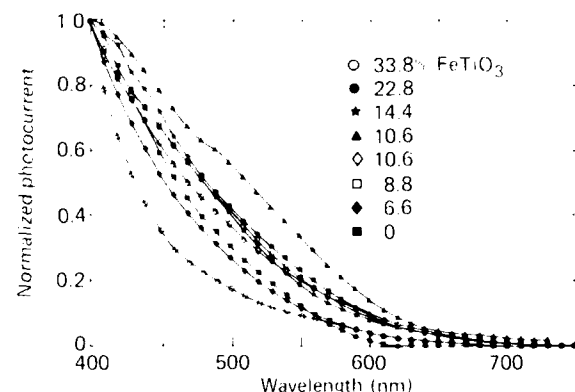


Figure 4 — Relative photocurrent as a function of excitation wavelength for the RF oxides. Each curve has been normalized to 400 nm and has been corrected for variations in the excitation intensity. The solution is 1 molar NaOH. The potential applied to each sample was 0.0 V (versus SCE).

from impurity states in the gap. All of the curves, except the 33.8% one, represent anodic photocurrents from an *n*-type semiconductor. The 33.8% curve, on the other hand, represents a cathodic photocurrent that one would expect from a *p*-type semiconductor.

Figure 5 shows the wavelength dependence of the photocurrent for the similar series of thermal oxides. Note the same general trend of enhanced photoactivity in the 425 to 600 nm region for the (8.8 to 10.6%) FeTiO_3 samples. As the FeTiO_3 is increased to 22.8%, the photoactivity curve returns approximately to the reference 0% curve. Unlike the RF oxides, the thermal oxides appear to have little or no photoactivity beyond 650 nm. This may be a consequence of the somewhat less energetic conditions under which they were produced compared to the RF oxides. The less strenuous conditions presumably produced fewer states in the gap and thereby reduced the tailing beyond the bandedge.

The photoconversion (quantum) efficiency, defined as electrons generated per incident photon, was determined for the RF oxides and the thermal oxides. The efficiency was determined at 450 nm and an applied potential of 0.5 V. Within the RF oxide samples, the efficiencies varied from 0.1 to 1.3%, with most of the samples lying in the vicinity of 0.4%. The conversion efficiency of the 0% sample was 0.35%. On the other hand, the thermal oxides, including the 0% sample, had efficiencies that varied from 3 to 4%. One 33% sample exhibited an impressive 11% conversion efficiency, suggesting that reasonable quantum efficiencies may be obtainable.

Preliminary stability measurements have been made on 0 and 10.6% RF oxides. A small amount of

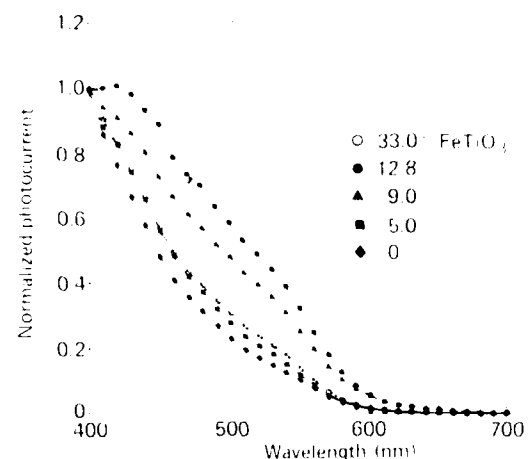


Figure 5 — Relative photocurrent as a function of excitation wavelength for the thermal oxides. Each curve has been normalized to 400 nm and has been corrected for variations in the excitation intensity. The solution is 1 molar NaOH. The potential applied to each sample was 0.0 V (versus SCE).

dissolution was observed in the 0% FeTiO_3 sample after 67 hours, but no decomposition was seen in the 10.6% FeTiO_3 sample after it was in solution for 96 hours and had passed 13.9 C of charge. The illumination source in both measurements was a 100 W mercury lamp.

CONCLUSION

We have examined a series of Fe_2O_3 thin films made by two different techniques containing various amounts of FeTiO_3 . There is a definite modification of the Fe_2O_3 thin films' properties upon the addition of FeTiO_3 . This can be seen in the consistent behavior of all the composition-dependent measurements, visible absorbance measurements, spectral response of the photoconductivity, and photoelectrolytic response. Although not presented here, similar trends in behavior were observed in the flatband potential and in the bias voltage dependence of the photoelectrolysis current. All of the measurements indicate the occurrence of dramatic changes in a narrow composition region ranging from approximately 2.5 to 14.4%.

From the standpoint of photoelectrolytic applications, the observed modifications are in the direction of improved performance and applicability. Specifically,

although the bandgap does not appear to change significantly, the enhanced absorbance and the resulting increase in photoactivity in the important region immediately above the Fe_2O_3 bandgap increases the collection efficiency of the solar flux there. Therefore, the effect is almost the same as if the bandgap had been lowered.

Secondly, and just as important, the modifications of spectral response were made without sacrificing any conversion efficiencies. In fact, there is a suggestion that the efficiency may actually be improved. Finally, a point not previously emphasized, at the very high concentration of FeTiO_3 , the thin films begin to exhibit *p*-type behavior. This is quite interesting because it is well known that *p-n* photoelectrolytic systems are much better photoconversion devices because the combination of the two electrodes reduces the bandgap and flatband potential requirements of the individual ones. The possibility of making *p-n* junctions simply by modifying the Ti concentration of an Fe-Ti oxide system has some very interesting and useful ramifications, which will be pursued.

ACKNOWLEDGMENT

We would like to acknowledge F. G. Satkiewicz for the secondary ion mass spectroscopic determination of the films' thicknesses and elemental compositions.

REFERENCES

- M. S. Wrighton, "Photochemistry," *Chem. Eng. News* (Sep 1979); A. J. Nozik, *Ann. Rev. Phys. Chem.* **29**, 189 (1978); A. J. Bard, *Science* **207**, 13 (1980).
- H. Tributsch, "Layer Type Transition Metal Dichalcogenides," *Ber. Buns-Gesell. Physik. Chemie* **81**, 361 (1977); "Hole Reactions from d-Energy Bands of Layer Type Transition Metal Dichalcogenides," *J. Electrochem. Soc.* **125**, 1086 (1978).
- T. E. Phillips, K. Moorjani, J. C. Murphy, and L. O. Poehler, " TiO_2-VO_3 Alloys - Reduced Bandgap Effects in the Photoelectrolysis of Water," *J. Electrochem. Soc.* **129**, 1210 (1982).
- B. Warner, P. Shive, J. Allen, and C. Terry, "A Study of the Hematite-Ilmenite Series by the Mossbauer Effect," *J. Geophys. Geoelectr.* **24**, 353 (1972).
- R. G. Burns, D. A. Nolet, K. M. Parkin, C. A. McCammon, and K. B. Schwartz, in *Mixed Valence Compounds*, D. B. Brown, ed., D. Reidel, p. 295 (1980).

This work was supported by NAVSEA SYSCOM and the Office of Naval Research.

NONDESTRUCTIVE TESTING AND EVALUATION OF METALS AND CERAMICS USING PHOTOTHERMAL IMAGING

L. C. Aamodt and J. C. Murphy

A method has been developed for evaluating nondestructively the integrity of materials by means of optical-beam deflection photothermal techniques. The method is noncontacting, can be used in hostile environments, does not require special sample preparation, and can often be used in situ. It can locate surface and near-surface cracks, discontinuities, voids, and abrupt changes in optical and thermal properties.

BACKGROUND

Many recently introduced materials such as composites, high-performance ceramic and polymer materials, new metal alloys, and thin-film compounds are important in electronic fabrication or as structural components. There is a need for better characterization of their thermal, optical, and structural properties and a need for more information about their latent defects. Photothermal imaging is well suited for this type of study. It is especially useful in examining thin films where it can measure film thickness and detect film disbonding. This method of imaging is presently being used only in a laboratory environment, but it has the promise of being adaptable to industrial applications because it requires no physical contact with the specimen, is relatively insensitive to its environment, can be used with larger specimens than most other thermal nondestructive evaluation methods, and involves relatively simple instrumentation.

DISCUSSION

The Basic Photothermal Technique

Heat flow in a specimen is determined by the type and location of its heat sources, by its shape and by its thermal properties and thermal environment. In general, the surface temperature of a heated body is a complicated function of all of those parameters, and the temperature at each surface point is affected by heat flowing to that point from all other points in the sample volume. However, when a modulated heat source is used, the time-varying component of heat flow attenuates rapidly as heat diffuses away from its source. Consequently, the modulated component of the temperature at each point in the sample depends predominantly

on thermal, optical, and geometric properties within a thermal diffusion length of that point. Because this length is a function of the modulation frequency, the localized region of interest can be changed experimentally within certain limits.

When a point source (usually an amplitude-modulated laser beam) is used to heat a sample harmonically, only the sample volume near the heated area contributes significantly to the modulated temperature. Consequently, the thermal map obtained by scanning the laser beam over the sample surface reveals the thermal and optical heterogeneity of the sample surface and the near-surface volume.

When a specimen contains structural defects such as cracks, fissures, voids, etc. or has structural variations such as grain boundaries or spatial amorphous-crystalline transitions, and the dimensions of these features are comparable to a thermal diffusion length, they disrupt the modulated heat flow in the specimen, causing nonuniformities in the surface temperature. To illustrate this point, Fig. 1 shows a thermal map of a 6061-aluminum surface. The thermal variations in the figure were produced by a series of subsurface cracks that extend beyond the visible tip of a small surface crack approximately 5 μm wide.



Figure 1 — A photothermal scan of a 6061 aluminum sample showing a series of subsurface cracks extending beyond the visible tip of a surface crack with a width of approximately 5 μm .

Optical-Beam-Deflection Imaging

The detection of the modulated thermal pattern on the sample surface can be accomplished by various means, each having its own advantages and limitations. The photothermal method developed at API uses the "mirage effect."¹⁻³ A "pump" laser heats a localized area on the sample, which, in turn, heats the gas that is in thermal contact with the heated surface. A "probe" laser beam directed parallel to the sample surface passes through the heated gas and is deflected by thermally dependent changes in the index of refraction of the gas. The deflection is measured by a position-sensitive light detector. This very sensitive method allows the measurement of temperature changes as small as 10^{-4} K.

A variant of that method ("reflective" optical-beam-deflection (OBD) detections) has also been developed at API.⁴ It differs from the "skimming" OBD detection technique described above in that the probe beam strikes the sample surface and is reflected prior to its being detected. In this case, the photothermal signal depends both on changes in the refractive index of the gas and on thermal expansion of the specimen.

OBD detection has certain advantages over other thermal detection methods. It is not restricted to small samples as photoacoustic detection is, it does not require physical contact with the sample as piezoelectric detection does, and it does not require a large ambient temperature as radiation detection does. The most significant advantage of the OBD method is its localized, vector mode of detection.⁴ Two deflection components exist, one normal to the sample surface (which is proportional to the average temperature along the projection of the probe beam path on the sample surface) and the other parallel to the sample surface (which is proportional to the transverse slope of the surface temperature averaged along the projection). Most other thermal imaging techniques average the surface temperature over the entire sample and thus obtain localization only through the use of localized excitation.

When localized detection as well as localized excitation are used, the topography of the temperature profile can be studied in the vicinity of a heated point; this aids in establishing the local geometry of a defect or a structural anomaly that is not possible with photoacoustic or piezoelectric detection.

Thermal and Optical Properties

If the only purpose of a thermal scan is to accept or reject a specimen such as an electronic component, a comparison of its thermal scan with that of a defect-

free sample may be sufficient. However, when more detailed information is wanted, features in the thermal scan must be related to changes in the thermal, optical, and geometric properties of the sample material. Some information that might be wanted is the location of incipient defects in the sample or an indication of what change in sample properties is a precursor of defect formation. Other items of interest might be the changes in physical properties caused by aging or changes caused by exposure of the sample to a particular benign or hostile environment. Still more basic would be a study of fundamental processes that change the thermal and optical properties of a material.

Basic to the use of photothermal imaging as an analytical tool is the ability to interpret thermal scans in terms of changes in the thermal properties of the sample material and, operationally, to know the effect of experimental parameters (such as the modulation frequency, the laser beam radii, the relative position of the pump and probe beams, and the distribution of energy in the cross section of the laser beams) on the photothermal signal.

Those relationships usually are complicated, but a detailed analysis⁵ of the OBD method shows that they are simpler under certain experimental conditions and for certain values of a sample's physical parameters. The results obtained from the analysis provide some useful rules of thumb for interpreting experimental data.

The results obtained in Ref. 7 show that the sensitivity of the photothermal signal to small changes in the optical absorption coefficient, β , the thermal conductivity, κ , and the thermal capacity, C , depends uniquely on two ratios, R/μ and δ/R , where R is the laser pump beam radius, δ is the thermal diffusion length, and μ is the thermal absorption length. μ and δ are related to β , κ , and C through the relationships, $\mu = 1/\beta$ and $\delta = (2\kappa/\omega C)^{1/2}$, where ω is the angular modulation frequency. A convenient way of showing this relationship is through topographical maps such as Figs. 2 and 3, which show contours of equal photothermal saturation and thermal character, respectively.

Photothermal saturation, σ , measures the photothermal signal's sensitivity to changes in optical absorption. When the photothermal signal is 100% saturated ($\sigma = 100\%$), it is insensitive to any changes in β , whereas when it is completely unsaturated ($\sigma = 0\%$), it is linearly proportional to changes in β .

Thermal character (TC) measures the sensitivity of the photothermal signal to changes in thermal parameters. When $TC = 1$, the signal depends exclusively on κ ; when $TC = 0$, it depends exclusively on C ; and when $TC = 1/2$, it depends only on κ and C through the

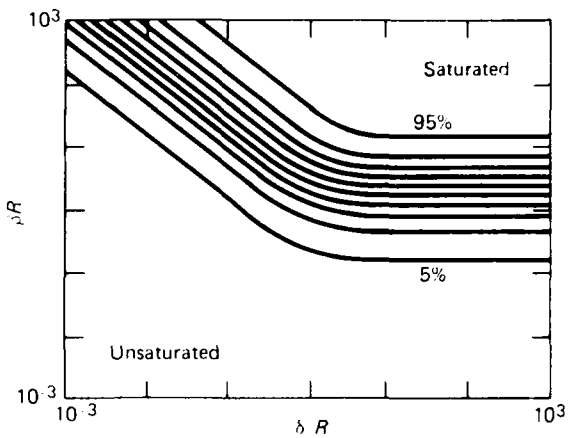


Figure 2 — A topographical map showing contours of equal photothermal saturation plotted as a function of R/μ and δ/R ($\mu = \beta^{-1}$ where β is the optical absorption coefficient). When the OBD signal is saturated, it is insensitive to small changes in β . When it is unsaturated, it is proportional to β .

product κC . Several definitions of TC can be given. In terms of the photothermal signal, S , $TC = [1 - (\delta/S)(\partial S/\partial \delta)]/2$. It can also be expressed in terms of the sample-related frequency dependence of the photothermal signal, which can be measured experimentally.

Figure 2 shows that saturation occurs at high optical absorptions and large thermal diffusion lengths (relative to the pump laser beam radius). Figure 3 indicates that the photothermal signal is dominated by changes in the thermal capacity when optical absorption is high (so that heating occurs mainly at the surface) and thermal conductivity is small (so that the modulated heat travels only a short distance before being attenuated). On the other hand, when heating occurs at a greater depth in the specimen and κ is large (so that the modulated heat flows farther from its source before being attenuated), thermal conductivity becomes dominant. For experimental purposes, the important point to be noted is that the crossover between these regions occurs when the thermal diffusion length and the optical absorption length are equal to the pump beam radius.

Three distinct regions can be seen in Fig. 3, one where the signal depends exclusively on C ($TC = 0$), one where it depends exclusively on κ ($TC = 1$), and a small plateau where it depends on the product κC ($TC = 1/2$). For other values of R/μ and δ/R , the relationship is more complicated. (In photoacoustic imaging, the photoacoustic signal never depends exclusively on κ so that a study of this thermal variable using the photoacoustic technique is more difficult.)

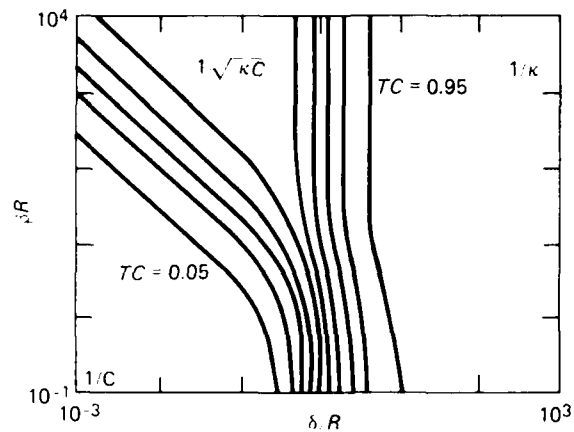


Figure 3 — A topographical map showing contours of equal thermal character (TC) plotted as a function of R/μ and δ/R .

In an optically, or thermally, heterogeneous sample, the values of R/μ and δ/R may vary from point to point on the sample surface. In addition, the ratios can be changed experimentally by varying the value of R and ω . Consequently, as indicated in Figs. 2 and 3, each sample point may have a different sensitivity to small changes in β , κ , and C during a thermal scan, and this sensitivity can be changed experimentally within certain limits by changing R and ω .

These results, which are more fully described in Refs. 7 and 8, provide a convenient guideline for interpreting thermal patterns and help to determine whether features in the patterns can be attributed to changes in a particular physical property. For example, if a feature appears in the photothermal scan at a particular point on the sample surface whose values of R/μ and δ/R lie in the saturated region of Fig. 2, then that photothermal feature must be caused by changes in thermal, not optical, properties. Similar types of conclusions can be drawn when the ratios lie in other regions in Figs. 2 and 3.

SUMMARY AND CONCLUSIONS

Reflective and skimming OBD photothermal imaging methods developed at APL have been used to detect a variety of defects in metals and ceramics. Fatigue and corrosion cracks have been studied in various samples. Surface and near-surface cracks a few micrometers wide are detected easily. OBD photothermal imaging is currently restricted to a laboratory environment, but methods are being investigated that will adapt it for technological applications. Photothermal studies are currently being made on the thermal characteristics of grain boundaries in metal samples.

REFERENCES

- ¹A. C. Boccara, D. Fournier, and J. Badoz, "Thermo-optical Spectroscopy: Detection by the 'Mirage Effect,'" *Appl. Phys. Lett.* **36**, 130 (1980).
- ²J. C. Murphy and L. C. Aamodt, "Optically Detected Photothermal Imaging," *Appl. Phys. Lett.* **38**, 196-198 (1981).
- ³J. C. Murphy and L. C. Aamodt, "Reflective Photothermal Imaging," *J. Phys. Paris* **C6**, 513-517 (1983).
- ⁴L. C. Aamodt and J. C. Murphy, "Photoacoustic Measurements Using a Localized Excitation Source," *J. Appl. Phys.* **52**, 4903-4914 (1981).
- ⁵J. C. Murphy and L. C. Aamodt, "Signal Enhancement in Photothermal Imaging Produced by Three-Dimensional Heat Flow," *Appl. Phys. Lett.* **39**, 519-521 (1981).
- ⁶L. C. Aamodt and J. C. Murphy, "Effect of 3-D Heat Flow near Edges in Photothermal Measurements," *Appl. Opt.* **21**, 111-115 (1982).
- ⁷L. C. Aamodt and J. C. Murphy, "Thermal Effects in Photothermal Spectroscopy and Photothermal Imaging," *J. Appl. Phys.* **54**, 581-591 (1983).
- ⁸L. C. Aamodt and J. C. Murphy, "Generalized Saturation Criteria for Photothermal Measurements," *J. Phys. Paris* **C5**, 115-119 (1983).

This work was supported by NAVSEASYSOM and the Office of Naval Research.

OLDROYD FLUIDS OSCILLATING IN RECTANGULAR DUCTS

V. O'Brien and L. W. Ehrlich

The rectilinear, oscillatory, pressure-driven motion of Oldroyd viscoelastic liquids with complex dynamic viscosity within straight rectangular ducts has been described theoretically. The complementary exact analysis and numerical solutions can be used to infer elastic time constants from laser Doppler velocimeter measurements.

BACKGROUND

Many common fluids like water and air have a simple response to pressure forces; they are called Newtonian. The real shear viscosity, μ , is a constant and there is no elastic response. However, some liquids have a more complex viscoelastic response to forces generated in flowing fluids and they are called non-Newtonian. The response relation is embodied in a "constitutive relation" or "equation of state," in analogy to the ideal gas law. One possible relationship is the Oldroyd three-constant response that incorporates a constant shear viscosity and two time constants related to the elastic response of the fluid that is manifest in frequency-dependent motions.

It was possible to generalize the analysis for parallel oscillatory motion of a Newtonian fluid in rectangular ducts¹ to the class of linear viscoelastic liquids obeying the incompressible Oldroyd model. The new solutions are given as functions of a Stokes number, the ratio of cross-section side lengths, and the two Oldroyd time constants.² Exact analysis and/or numerical approximate solutions by means of finite difference methods allow the prediction of the time-dependent velocity fields that could be measured optically in transparent viscoelastic liquids. Or, inverting the known and unknown aspects, laser Doppler velocimetry³ in rectangular ducts would allow the rheological time constants to be determined by means of the theory.

DISCUSSION

Dynamic Viscosity

The rectilinear oscillatory flow of Newtonian viscous flow in straight round ducts was analyzed long ago.⁴ It was shown to be dependent on a single parameter, a Stokes number $k = a^2 \omega \rho / \eta$, where

η is the (constant, real) shear viscosity of the fluid, ρ is its density, a is the pipe radius, and ω is the frequency (in rad/s) of the oscillation. Oscillatory parallel flow of linearly viscoelastic fluid in round pipes requires only a slight modification in analysis when the shear viscosity is complex.⁷ Under the assumption of an Oldroyd constitutive relation, pipe oscillatory flow depends also on two time constants as well as a Stokes number. Oscillatory flows of viscoelastic fluid in rectangular ducts similarly can be generalized from the Newtonian solutions and offer a scheme to verify the experimental results of round pipe measurements of the Oldroyd constants.⁸

It is assumed that only linear viscoelasticity is required to predict the non-Newtonian flow. Specifically, we assume the three-constant Oldroyd model in which the complex dynamic viscosity is

$$\mu^* = \mu_{\text{ss}} - i\mu_{\text{rel}}, \quad (1)$$

where

$$\mu_{\text{ss}} = \frac{\eta(1 + \lambda_s \lambda_r \omega^2)}{1 + \lambda_s^2 \omega^2}, \quad (1a)$$

$$\mu_{\text{rel}} = \frac{\eta \omega (\lambda_s - \lambda_r)}{1 + \lambda_s^2 \omega^2}, \quad (1b)$$

and relaxation and retardation time constants λ_s , λ_r , respectively, satisfy

$$\lambda_s \rightarrow \lambda_r \neq 0. \quad (1c)$$

Clearly, in the limit $\omega \rightarrow 0$, μ^* corresponds to the shear viscosity of Newtonian fluid in steady flow. The parameters in Eq. 1 can be related to the relaxation function of the fluid through a Fourier transform.

Analysis

The rectilinear incompressible flow everywhere parallel to the bounding walls (Fig. 1) is governed by a one-dimensional momentum equation:

$$\rho \frac{\partial W}{\partial t} = -\frac{dP(t)}{dz} + \mu^* \omega^2 W. \quad (2)$$

Normalizing by the duct half-height b , and assuming that the pressure $P(t)$ and velocity $W(t)$ have harmon-

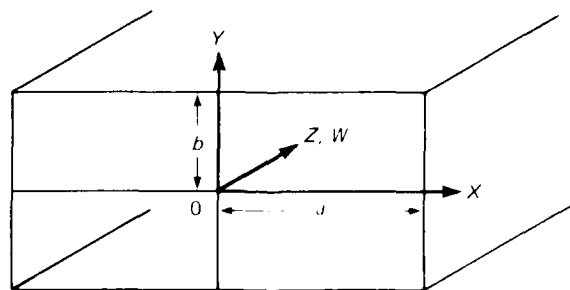


Figure 1 — Rectilinear flow in a straight rectangular duct. $W(X, Y)$

ic factors $e^{-it\omega t}$ that can be factored out, Eq. 2 can be reduced to

$$\left(\frac{\mu^*}{\eta} \omega^2 - \frac{i\omega \rho b^2}{\eta} \right) W^* - \frac{b^2}{\eta} \frac{dP^*}{dz} = -W_{\text{ch}} \text{ (real)}, \quad (3)$$

where P^* is the Z -dependent pressure magnitude, and W_{ch} is a characteristic velocity. (The minus sign is introduced because a positive W velocity corresponds to a negative pressure gradient.) Dividing through by W_{ch} , and setting $w = W^*/W_{\text{ch}}$, $w' = w^* + iw''$, $k = \omega \rho b^2 / \eta$, and $\mu^*/\eta = \mu' - i\mu''$, the nondimensional equation to be solved is

$$[(\mu' - i\mu'') \omega^2 - ik] (w' + iw'') + 1 = 0. \quad (4)$$

The nonslip boundary condition $w = 0$ applies at the walls:

$$x = \pm \frac{a}{b}, \quad y = \pm 1 \quad (a \geq b).$$

By separation of variables,

$$w = w_p \left\{ 1 - 2 \sum_{M=0}^{\infty} \frac{(-1)^M}{p_M} \left[\frac{\cosh \gamma_M x \cos p_M y}{\cosh(\gamma_M a/b)} \right. \right. \\ \left. \left. + \frac{\cos q_M x \cosh \mu_M y}{\cosh \mu_M} \right] \right\}, \quad (5)$$

where

$$p_M = \frac{2M+1}{2}\pi, \quad q_M = \frac{2M+1}{2}\pi \frac{b}{a}.$$

$$\gamma_M = \sqrt{p_M^2 + k^2}, \quad \mu_M = \sqrt{q_M^2 + k^2}.$$

Here,

$$W_F = \frac{1}{ik} = e^{-\frac{i}{2}k^2} (k)^{-1}$$

and

$$k = \frac{ik}{\mu^2 - i\mu^2} = \frac{\rho\omega b^2}{\eta} \frac{i(1 + \lambda_0^2 \omega^2)}{(1 + \lambda_0 \lambda_1 \omega^2) - i\omega(\lambda_0 - \lambda_1)}.$$

The evaluation of an infinite series of terms with complex arguments is tedious even with modern computing programs. An alternative scheme is to start with Eq. 4 and assumed values of λ_0 , λ_1 and compute the flow field directly by a finite-difference approximate solution. Writing out the real and imaginary parts, Eq. 4 separates into

$$\begin{aligned} \mu' A w^+ + (\mu'' A + kI) w^{++} &= 1 \\ (\mu'' A + kI) w^+ + \mu' A w^{++} &= 0 \end{aligned} \quad (6)$$

using A for the matrix operator and I for the identity matrix.

With a mesh of $N \times M$ points to represent the flow area and using the boundary condition that $w^+ = 0$ on the boundary, the matrix equations (6) can be solved readily by a successive overrelaxation technique.

Results

As defined, w is a complex number, but only the real part (w^+) has physical reality. Since $e^{-i\omega t} = (\cos \omega t + i \sin \omega t)$, it suffices for illustration to show the real and imaginary parts of w (w^+ and w^{++} , respectively) along the centerplane of a square duct. They are shown in Figs. 2 and 3 for two values of k for the assumed values $\lambda_0 = 0.3$ s, $\lambda_1 = 0.1$ s, and $\eta = 16$ poise. Also shown for contrast are the corresponding Newtonian w^+ and w^{++} for the same k .

CONCLUSION

Oscillatory rectilinear flow in rectangular ducts offers new prospects for determining material proper-

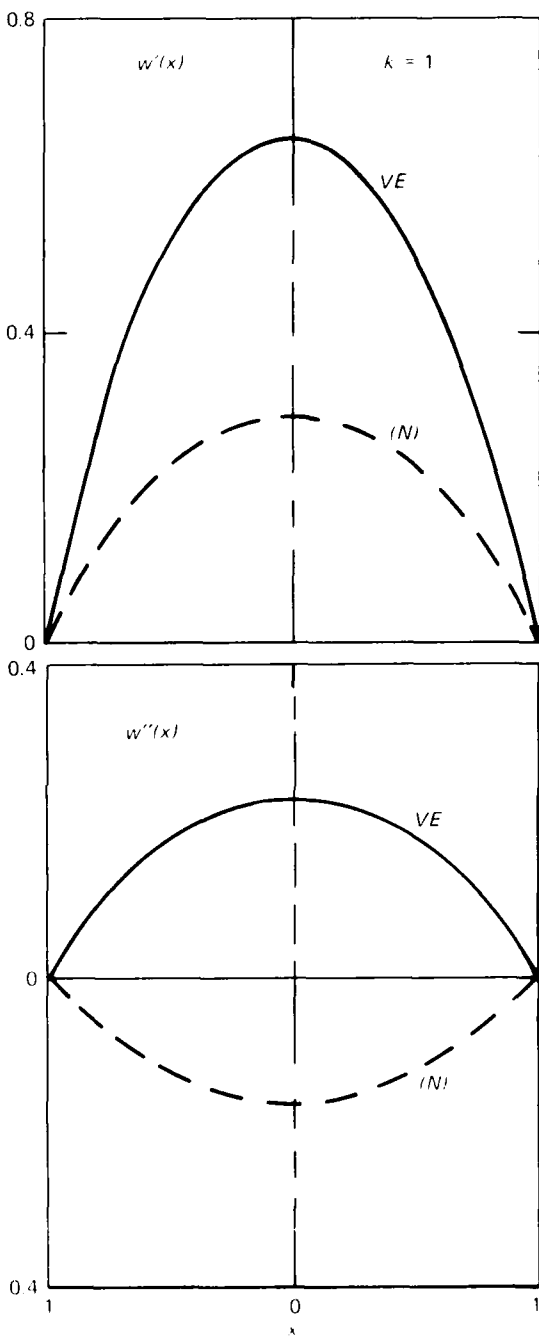


Figure 2 — Real and imaginary parts of w on the centerplanes for $k = 1$ in a square duct for a viscoelastic fluid with $\lambda_0 = 0.3$ s, $\lambda_1 = 0.1$ s (corresponding Newtonian distribution shown for contrast).

ties of viscoelastic fluids that complement oscillatory flow data in round pipes or other apparatus. Although the velocity fields are complicated, harmonic behavior

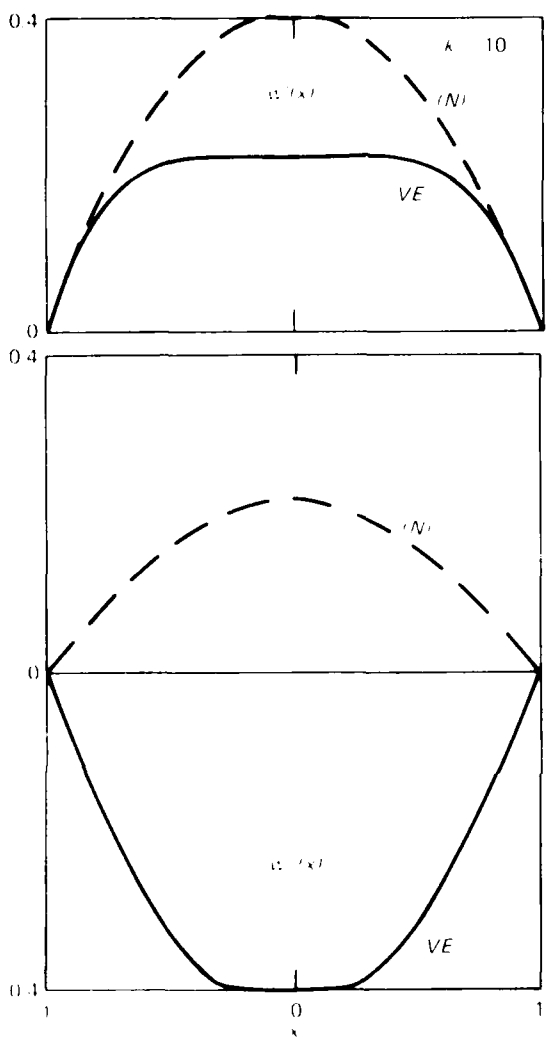


Figure 3 — Real and imaginary parts of w in the centerplanes of a square duct for $k = 10$.

permits the prediction of the flows to be expected as a function of the two Oldroyd time constants. A comparison of velocities obtained by laser Doppler techniques should provide good estimates of the elastic constants.

Let the measured harmonic velocity profiles at a given volume flow steady state be referenced to the maximum velocity in the center of the duct in phase and amplitude. Data taken across the centerplane (or any other line through the center) can be reduced by means of Eq. 6 to give the best-fit real and imaginary parts of the complex viscosity. The basic oscillatory parameter k also depends on b , so that varying the duct cross section provides a check on the frequency-dependent μ^* . The experimental apparatus and data reduction scheme can be calibrated with a Newtonian fluid that has only real viscosity, not dependent on ω .

The numerical scheme can also be applied to ducts of other shapes, but the rectangular ones seem to offer the most practical approach to elastic measurements. In particular, plane walls are optimum for laser Doppler velocity measurements.

REFERENCES

- [1] O'Brien, "Pulsatile Fully Developed Flow in Rectangular Channels," *J. Franklin Inst.* **300**, 225-230 (1975)
- [2] O'Brien and L. W. Hinchliffe, "Rectilinear Oscillatory Viscoelastic Flow in Rectangular Ducts," *J. Non-Newtonian Fluid Mech.* **13**, 33-45 (1983)
- [3] C. B. Barertron, E. E. Mark, and M. H. Friedman, "Pulsatile Flow in a Rectangular Cross Section Bifurcation," in *Proc. 28th Conf. on Engineering in Medicine and Biology*, p. 276 (1975)
- [4] S. L. Grace, "Oscillatory Motion of a Viscous Liquid in a Long Straight Tube," *Philos. Mag.* **5**, 933-939 (1928)
- [5] S. Vela, Ph.D. thesis, University of Minnesota (1964)
- [6] S. Vela, J. W. Kalb, and A. G. Fredrickson, "On Stress Relaxing Solids—Part III: Simple Harmonic Deformation," *J. Am. Inst. Chem. Eng.* **11**, 288-294 (1965)
- [7] J. Harris and R. Maheshwari, "The Measurement of Amplitude and Phase in Oscillatory Fluid Flow in a Tube," *J. Phys. F* **4**, 973-976 (1971)

This work was supported by the U.S. Army CARRADCOM and Independent R&D

BOUNDARY CONDITIONS AND REVERSIBILITY IN DIFFUSION CONTROLLED REACTIONS

L. Monchick

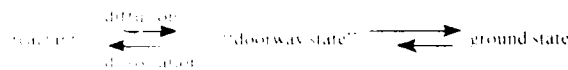
A simple two-state model is explored in which a product newly formed by the reaction of a solid particle and a gaseous reactant relaxes by internal radiationless transitions between its bound states and by redissociation followed by diffusion of the reactants into the solvent. Generally, the matching equations between the internal and external dynamics do not take the form of simple boundary conditions but of a rather more complicated integral relation.

BACKGROUND

The correct modeling of reactions of molecules with surfaces requires knowledge of both the internal and the external dynamics. Historically, the internal dynamics have been modeled by a radiation type boundary condition that has as a consequence that the reaction decays to the equilibrium approximately as $\text{exp}(-\text{constant} \cdot \text{time})$. However, this model has been criticized recently^{1,2} because it replaces a reversible process with an irreversible one not consonant with kinetic theory and because the usual Chapman-Enskog type of kinetic theory cannot be valid just outside the surface.

DISCUSSION

The simplest system³ displaying true reversibility consists of a ground state and a reaction complex or "doorway" state that is formed when the reactants first came together. This can be visualized by the following reaction scheme:



The lengths of the arrows are supposed to indicate the velocity of each step. A mass balance relation can now be set up that relates the net flux into the doorway state, j_{+} , to the flux out of the doorway state, j_{-} :

$$j_{+}(t) = \int dt K(t-t) j_{-}(t) \quad (1)$$

K is a kernel describing the relaxation of the system to equilibrium. For a two-state system, it consists of two exponential decay modes, ϕ_1 is a transmission or reaction probability for entering the reaction zone. The configuration of the reactive system is shown in Fig. 1,

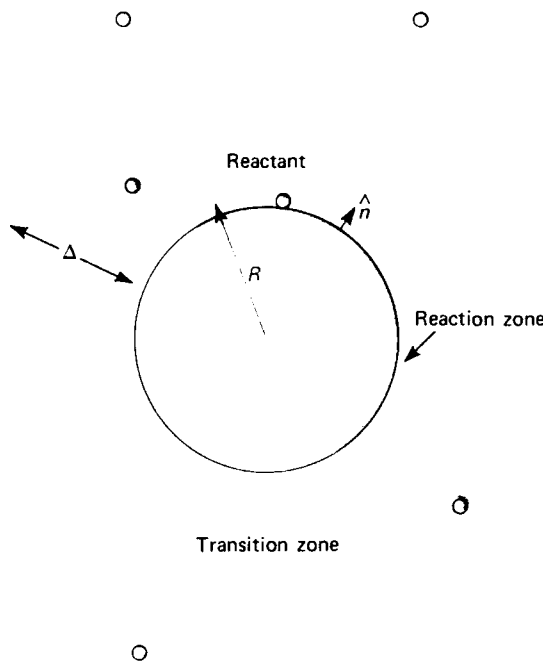


Figure 1 — A spherical particle (crosshatched area) embedded in a gas of reactant molecules (spheres). Three spherical zones are shown concentric with the particle: a reaction zone, a transition zone of width Δ , and an outer zone where the usual gas dynamic laws are valid.

where R is the dimension of the reaction complex. For reaction of a gas with a particle, it would be the radius of the particle plus the width of the reaction zone, which can be taken to be a shell of the thickness of one molecular diameter. The problem is still unsolved unless j_{+} is specified. In the case of a gas, this can be determined by kinetic theory. As a result, the net flux into the reaction complex takes a particularly simple form at sufficiently long times. It is convenient to separate the gas into two regions. The first is the region outside a distance $R + \Delta$ from the center of the particle; here it is a good assumption to describe the gas with ordinary gas kinetic theory. The second is a transition zone, a shell of thickness Δ , where the reaction does not allow this approximation. The net flux into the reaction zone, j_{+} , may be expressed in terms of n_{+} , the average thermal velocity; $n(t)$, the concentration of gaseous reactant just outside the reaction zone; $n_{-}(t)$, a fictitious concentration that would be in equilibrium with the

total amount already reacted; and Δ , the width of the transition zone taken to be several mean free paths thick:

$$\mathbf{j} \cdot \mathbf{j} + \mathbf{j} \approx \frac{\gamma u_n}{4} (n^-(t) - n(t)) + \frac{1}{2} \gamma \left(\frac{R}{R + \Delta} \right)^2 \mathbf{n} \quad (2)$$

\mathbf{n} is a unit vector normal to the particle surface. The numerator is just what physical intuition would have postulated as the correct form: a transmission coefficient times an average arrival rate times the displacement from equilibrium.

The denominator is unexpected and takes its special form for two reasons. One is that the calculation of molecular flux through a surface must take into account the perturbation of the velocity distribution from equilibrium. In the presence of a finite flux \mathbf{j} , this perturbation, according to standard Chapman-Enskog kinetic theory,¹ would be proportional to \mathbf{j} itself. Secondly, Chapman-Enskog theory is not valid at a gas-surface interface,² but can only be applied a suitable distance away. By mass balance, the flux at the edge of the transition zone can be related to the flux at the surface. These two effects account for the form of the denominator of Eq. 2 and introduce several nice features into the theory of diffusion controlled reactions. The geometric factor, $(R/(R + \Delta))^2$, is a Knudsen correction that can account for the rarefaction of the gas; at very low pressures, Δ becomes infinitely large and Eq. 2 goes over into the expected vacuum rate. For more complicated particle shapes, the geometric factor would be replaced by more complicated functional relationships.

At high pressures, Δ vanishes, and it is seen that the transmission coefficient, γ , of the intuitive theory has been replaced by an effective transmission coefficient:

$$\gamma' = \frac{\gamma}{1 - \gamma/2}$$

The difference is not trivial: at $\gamma \approx 1$, neglect of this extra factor would underestimate the reactive flux by a factor of two.

Finally, n^- can be modified to depend also on the degree of relaxation that has taken place in the reaction product. For the two-state theory, only two relaxation modes need be considered, but a more complicated N -state model of the reaction product can be set up³ that, in general, leads to a kernel with N separate relaxation modes.

The two-state model, then, and its extension to include N states, in conjunction with Chapman-Enskog theory, can describe an extremely large range of experimental conditions. It has the virtue of assuming the correct form at both very high and very low pressures and of satisfying kinetic theory and the principle of microscopic reversibility.

REFERENCES

1. Monchick, "Time Delays and Diffusion Controlled Reactions," *J. Chem. Phys.* **62**, 1907-1912 (1975).
2. Northrup and J. T. Hynes, "Coupling of Translational and Reactive Dynamics for a Simple Lattice Model," *J. Stat. Phys.* **18**, 91-105 (1978).
3. Monchick, "Boundary Conditions and Reversibility in Diffusion Controlled Reactions," *J. Chem. Phys.* **78**, 1808-1814 (1983).
4. M. Schell and R. Kapral, "Diffusion Influenced Reactions and Normal Solutions of the Boltzmann Equation," *J. Chem. Phys.* **75**, 915-920 (1981).

This work was supported by Independent R&D.

PATENTS

PATENTS ACTIVITIES

The API Patents Office is responsible for ensuring compliance with contract and grant requirements relative to patent and data rights, as imposed by the various governmental agencies that sponsor work at the Laboratory. In addition to preparing formal disclosures of inventions for the appropriate sponsors, the Patents Office prepares and prosecutes patent applications on behalf of the University and the Department of the Navy.

The following lists indicate the invention disclosures submitted to sponsors, the patent applications prepared and filed in the United States Patent Office, and the previously filed applications that were successfully prosecuted to issuance as patents, during fiscal year 1983.

INVENTION DISCLOSURES

- W. E. Allen and E. J. Porter—*Nickel Cadmium Battery “Dipole” Reconnection Technique*
C. W. Anderson—*Surface Operated Controlled Depth Paravane*
E. Bader and J. H. Higby—*Atmospheric Radio Noise Simulator*
W. C. Baker—*Two-Site Target Cross Correlator*
W. C. Baker—*Programmatic Digital Delay Line*
J. G. Bales—*Electro-Optical Controlled Switch for IBM 3278 9 Channel Internal Communication Line*
B. L. Bales, S. A. Beatty, J. F. Walter, Jr., and T. M. Rankin—*Scenic Simulator*
E. L. Barker—*Radar Display and Distribution System*
R. K. Barker and E. E. Gack—*Integrated Circuit Adaptor*
H. K. Charles, Jr.—*Impermeable Neutron Probe Using Polyimide Dielectric*
D. P. Crawford and J. Papp—*An Improved MINISATIS Handing System*
C. E. Dotsett and R. E. Miller—*Use of Talking Clocks to Time Telephone or Data*
G. E. Finch—*Power Independent Real Time Clock*
J. C. Fritman, R. L. Rouse, and W. H. Zinger—*Solid State Modulator for Microwave Power Tubes*
A. B. Fraser—*Minature Fluorometer*
R. M. Fristrom—*Local Heat Removal from Densely Packed Microchips Using Heat Pipe Methods*
S. H. Gordon—*Dual Function SAT-IR Guided Projectile Seeker*
H. M. Grady and D. N. Quadkinbush—*Paravane System*
S. E. Grenleski and H. B. Land III—*Avoid Skin Friction Measuring Unit*
J. W. Hart and J. S. Hansen—*DCOCH—A Single Superconducting Coil Acting as Both Transmitter and Receiver at 2 Frequencies for Active Electromagnetic Geophysical Prospecting*
R. A. Herle—*Electronic Keyboard*
H. T. Henline—*Wire Wrapping Tool with Cutting Mechanism*
F. K. Hill—*Ultrasonic Technique for Cleaning Ship Hulls*
F. I. Izniski—*A Method and Means for Achieving Image Antenna Element Pattern Stabilization and Frequency Desensitization with Attendant Reduction in Array Mutual Coupling Levels*
F. P. Izniski, J. A. Krill, and W. H. Zinger—*A Sharp Mode Transducer Bend for Overmoded Waveguide*

J. W. Height—*Method and Apparatus for Determining Scatter Coefficients*

H. M. Kincaid and J. M. Vayda—*Method and Apparatus for Determining Frequency Components*

J. E. Kerses—*Fast Radar Frequency Estimator*

J. E. Kerses—*Phase Error Processor Block*

J. E. Kerses—*Small Fast Radar Frequency Processor*

E. H. Kidela—*A Motor Computer Based Research Computer*

J. E. Kincaid—*Method and Apparatus for Reducing Intensity of Radiation at Warm Borders*

J. E. Kincaid—*Technique for Cleaning Laser Mirrors by Escapement*

J. A. Krill and W. H. Zinger—*Space Diversity Radar*

P. E. Lakomy, J. A. Krill, and W. H. Zinger—*A Countermeasure Against Anti-Radiation Missiles (ARM's) and IR Seekers*

D. K. Larson—*Multi Octave Phase Comparator*

J. W. Leight—*Magnetic Ring Enhancer for Sputtering Apparatus*

D. Marsh—*Ship Control Alert System*

J. A. Meyer—*Wire Wrapper with an Adjustable Cutting Device*
C. V. Nelson—*An Automatically Profiling Temperature Sensor for Upper Ocean Measurements*

J. G. Parker and W. D. Stanbro—*Localization of Cancerous Tissue by Monitoring Infrared Fluorescence Emitted by Intravenously Injected Porphyrin Tumor-Specific Markers Excited by Long Wavelength Light*

V. L. Pisacane and S. M. Yionoulis—*Calibration System for the Disturbance Compensation System (DISCOS)*

R. S. Potember, T. O. Poehler, and R. C. Benson—*Optical Storage Switching Device Using Organic Charge Transfer Salts*

W. R. Powell—*Battery Charge Controller for Reduced Water Loss*

A. J. Pue—*Body Motion Decoupling Network for Homing Missiles*

R. A. Quinnell, S. B. Cooper, and R. R. Talbott—*Adaptive Digital Signal Processing System*

J. M. Rankin—*Flight Linear Sled Isolation Servo*

J. M. Rankin—*RAM Fracticide Discriminant*

C. H. Sinex and B. F. Raff—*Expendable Bathyphotometer to Measure Light Attenuation in the Ocean*

W. L. Sternberger—*Cache Memory and Pre-Processor*

W. L. Sternberger—*Synchronized Distributed Analog Multiplexing System*

S. A. Taylor and J. A. Krill—*A Method and Apparatus for Determining the Propagation Diversity of Spread Spectrum Communications*

D. L. Tewell—*STD Bus General Purpose Period Frequency Measurement Board*

R. VonBriesen—*Indefinite Life Pulse Power Supply for Satellite*

C. W. Webster and R. K. Stilwell—*Technique for Impedance Matching Bidirectional Helix Antenna*

W. H. Zinger and J. A. Krill—*A Multiport Rectangular TE₀₁ to Circular TE₀₁ Mode Transducer*

W. H. Zinger and J. A. Krill—*Method for Measuring High Resonator Q's*

PATENT APPLICATIONS

W. H. Avery—*Low Cost Method for Producing Methanol Utilizing OILC Plantships*

R. E. Fischell—*Apparatus for Detecting at Least One Predetermined Condition and Providing an Informational Signal in Response Thereto in a Medication Infusion System*

- R. E. Fischell—*Fluid Handling System for Medication Infusion System*
- R. E. Fischell—*Programmable Control Means for Providing Safe and Controlled Medication Infusion*
- R. E. Fischell—*Refillable Medication Infusion Apparatus*
- J. G. Frink—*Intercomputer Communications Based on Message Broadcasting with Receiver Selection*
- A. F. Hogrete and W. E. Radford—*Coherent Inductive Communications Link for Biomedical Applications*
- E. I. Hottman and J. C. Loessi—*Short-Circuit-Proof Connector Clip for a Multiterminal Circuit*
- D. A. Kitchin—*Synchronous Clock Stopper for Microprocessor Operated in a Power-Limited Environment*
- J. G. Parker and W. D. Stanbro—*Electro-Optical Device for Monitoring Instantaneous Singlet Oxygen Concentration Produced During the Treatment of Cancer by Means of Phototherapy*
- J. G. Parker and W. D. Stanbro—*Localization of Cancerous Tissue by Monitoring Infrared Fluorescence Emitted by Intravenously Injected Porphyrin Tumor-Specific Markers Excited by Long Wavelength Light*
- R. S. Potember, T. O. Poehler, and R. C. Benson—*Optical Storage and Switching Devices Using Organic Charge Transfer Salts*
- M. E. Schmid, R. L. Trapp, and A. F. Davidoff—*Method and Apparatus for Bus Arbitration Using a Pseudo-Random Sequence*
- W. Schneider and R. J. Johns—*Portable pH Data Collector*
- D. M. Silver and N. deHass—*Cryogenic Tank Support System*
- W. H. Zinger and J. A. Krill—*A Multiport Rectangular TE₁₀ to Circular TE₀₁ Mode Transducer*

PATENTS ISSUED

- R. E. Fischell—*Implantable, Programmable Medication Infusion System*, No. 4,373,527
- A. B. Fraser—*Frequency Encoding Closed Loop Circuit with Transducer*, No. 4,408,169
- C. Philippides and W. H. Zinger—*Apparatus for Identifying Coded Information Without Internal Clock Synchronization*, No. 4,395,773
- R. S. Potember, T. O. Poehler, and D. O. Cowan—*Current Controlled Bistable Electrical Organic Thin Film Switching Device*, No. 4,371,883
- T. R. Small—*Superflywheel Energy Storage Device*, No. 4,359,912
- L. E. Stillman—*Deployable Support Structure for Spacecrafts*, No. 4,373,690

PUBLICATIONS AND PRESENTATIONS

PUBLICATIONS

- L. C. Aamodt and J. C. Murphy, "Thermal Effects in Photo-thermal Spectroscopy and Photo-thermal Imaging," *J. Appl. Phys.*, **54**, 581-591 (1983).
- M. H. Acuna and J. K. Alexander (NASA), R. A. Brown (Space Telescope Scientific Inst.), T. W. Hill (Rice Univ.), S. M. Krimigis and L. J. Lanzerotti (API), and G. L. Siscoe (Univ. California), "Physics of the Jovian and Saturnian Magnetospheres," *Space Sci. Rev.*, **34**, 1-24 (1983).
- M. H. Acuna and J. K. Alexander (NASA-Goddard), R. A. Brown (Univ. Arizona), T. W. Hill (Rice Univ.), S. M. Krimigis (API), L. J. Lanzerotti (Bell Labs.), and G. L. Siscoe (Univ. California), "Physics of the Jovian and Saturnian Magnetospheres: Highlights of a Conference Held at the Applied Physics Laboratory, The Johns Hopkins University, October 22-24, 1981," *Space Sci. Rev.*, **35**, 269-292 (1983).
- F. J. Adrian, "Charge Transfer Effects in Surface-Enhanced Raman Scattering," *J. Chem. Phys.*, **77**, 5302-5314 (1982).
- R. H. Andreo, "Closure Hypotheses from the Method of Smoothing for Coherent Wave Propagation in Discrete Random Media," *Opt. Lett.*, **8**, 82-84 (1983).
- R. H. Andreo and R. A. Farrell, "Corneal Small-Angle Light-Scattering Theory: Wavy Fibril Models," *J. Opt. Soc. Am.*, **72**, 1479-1492 (1982).
- J. R. Apel, "A Survey of Some Recent Scientific Results from the Seasat Altimeter," Chap. 20 in *Satellite Microwave Remote Sensing*, Ellis Horwood Ltd., Chichester, England (1983).
- K. B. Baker and R. A. Greenwald (API) and R. T. Tsunoda (SRI International), "Very High Latitude F-Region Irregularities Observed by HF-Radar Backscatter," *Geophys. Res. Lett.*, **10**, 904-907 (1983).
- C. B. Barger, B. H. Nall, and A. N. Jette, "Current Image Diffraction (CID) of Single Crystal Metal Surfaces," *J. Vac. Sci. Technol.*, **A1**, 1130-1133 (1983).
- R. C. Beal, F. M. Monaldo, and D. G. Tilley, "Large and Small Scale Evolution of Digitally Processed SAR Ocean Wave Spectra," *J. Geophys. Res.*, **88**, 1761-1778 (1983).
- R. C. Benson, R. C. Hoffman, R. S. Potember, E. Bourkoff, and T. O. Poehler, "Spectral Dependence of Reversible Optically Induced Transitions in Organometallic Compounds," *Appl. Phys. Lett.*, **42**, 855-857 (1983).
- P. M. Bischoff (JHU) and R. W. Flower (API), "High Blood Pressure in Choroidal Arteries as a Possible Pathogenetic Mechanism in Senile Macular Degeneration," *Am. J. Ophthalmol.*, **96**, 398-400 (1983).
- B. I. Blum, "A Data Model for Patient Management," in *Proc. 4th World Conf. on Medical Informatics*, J. H. Van Bemmel et al., eds., pp. 748-751 (1983).
- B. I. Blum, "An Information System for Developing Information Systems," in *Proc. 1983 National Computer Conf.*, pp. 743-752 (May 1983).
- B. I. Blum, "Clinical Systems Give Basic Benefits," *Eng. Med. Biol. Mag.*, **1**, 28-32 (1982).
- B. I. Blum, "Computer Applications in Medical Care: A State of the Art Survey," in *Proc. Congress on Medical Informatics*, D. A. Lindberg et al., eds., pp. 16-21 (1983).
- B. I. Blum, "The Life Cycle - A Debate over Alternate Models," *ACM SIGSOFT Software Eng. Notes*, **7**, 18-20 (1982).
- B. I. Blum and H. R. Blum, "You Punch in Your Qualifications and It Prints Out Your Program," *MUG Q. VII/4*, 42-45 (1983).
- B. I. Blum (API) and R. C. Houghton, Jr. (NBS), "Rapid Prototyping of Information Management Systems," *ACM SIGSOFT Software Eng. Notes*, **7**, 35-38 (1982).
- B. I. Blum (API) and R. E. Lenhard, Jr. (JHMI), "Displaying Clinical Data for Decision Making," *J. Clin. Eng.*, **8**, 1 (1983).
- B. I. Blum (API) and D. A. B. Lindberg, G. O. Barnett, H. R. Warner, R. E. Lenhard, Jr., and C. J. McDonald (JHMI), "Information Systems and Patient Care," in *Proc. 6th Annual Symp. on Computer Applications in Medical Care*, Washington, pp. 3-7 (1982).
- N. A. Blum, "Mossbauer Study of Magnetism in an Amorphous $\text{Fe}_{40}\text{B}_{60}$ Sputtered Film," *J. Appl. Phys.*, **53**, 7747-7749 (1982).
- J. Bohandy and B. E. Kim, "Anomalous Temperature-Dependent Phosphorescence of Cu Porphyrin in Anthracene," *J. Chem. Phys.*, **78**, 4331-4336 (1983).
- C. A. Boyles, "Coupled Mode Solution for a Cylindrically Symmetric Oceanic Waveguide with a Range and Depth Dependent Refractive Index and a Time Varying Rough Sea Surface," *J. Acoust. Soc. Am.*, **73**, 800-805 (1983).
- W. A. Bryden (API), J. P. Stokes and D. O. Cowan (JHU), T. O. Poehler (API), and A. N. Bloch (Exxon), "Mott Transition in the Solid Solutions HMTSF ($\text{TCNQ}_2\text{FeCl}_4$)," *Mol. Cryst. Liq. Cryst.*, **86**, 281 (1982).
- M. W. Burgan, "Biomedicine: What Does It Mean?" *CBE Views*, **5**, 9-10 (Winter 1982).
- P. F. Bythrow and T. A. Potemra, "The Relationship of Total Birkeland Currents to the Merging Electric Field," *Geophys. Res. Lett.*, **10**, 573-576 (1983).
- J. N. Campbell (JHMI) and R. A. Meyer (API), "Sensitization of Unmyelinated Nociceptive Afferents in the Monkey Varies with Skin Type," *J. Neurophysiol.*, **49**, 98-110 (1983).
- J. N. Campbell (JHMI), R. A. Meyer (API), and S. N. Raja, R. Burke, and J. J. Aryapur (JHMI), "Neural Mechanisms of Hyperalgesia: Effects of Partial Injury to the Receptive Fields of Nociceptive Afferents," *Soc. Neurosci. Abstr.*, **8**, 854 (1982).
- M. Candidi (Istituto Plasma Spazio, Italy), H. W. Kroehl (NOAA), and C.-I. Meng (API), "Intensity Distribution of Dayside of Polar Soft Electron Precipitation and the IMF," *Planet. Space Sci.*, **31**, 489-498 (1983).
- H. K. Charles, Jr., and J. T. Massey (API) and V. B. Mountcastle (JHMI), "Polyimides as Insulating Layers for Implantable Electrodes," in *Extended Abstracts of the First Technical Conf. on Polyimides*, p. 98 (1982).
- H. Y. Chiu and R. C. Benson, "Laser-Induced Decomposition of Sodium Azide," *J. Electron. Spectrosc. Relat. Phenom.*, **29**, 141-146 (1983).
- J. S. Chappell, M. M. Lee, and D. O. Cowan (JHU), T. O. Poehler (API), and A. N. Bloch (Exxon), "Some Infrared Properties of TMTSF 2:1 Salts," *Mol. Cryst. Liq. Cryst.*, **86**, 261 (1982).
- I.-Y. Chiang and D. O. Cowan (JHU), T. O. Poehler (API), and A. N. Bloch (Exxon), "Synthesis of Substituted Tetraselenatulvalenes from Dimethylphosgene Iminium Chloride," *Mol. Cryst. Liq. Cryst.*, **86**, 27 (1982).
- J. E. Coolahan, Jr. (API) and N. Roussopoulos (Univ. Maryland), "Timing Requirements for Time-Driven Systems Using Augmented Petri Nets," *IEEE Trans. Software Eng.*, **SE-9**, 603-616 (1983).
- D. O. Cowan, A. Kini, I.-Y. Chiang, K. Lerstrup, and D. R. Lalham (JHU), T. O. Poehler (API), and A. N. Bloch (Exxon), "The Design, Synthesis, and Characterization of the Molecular Components of Organic Conductors," *Mol. Cryst. Liq. Cryst.*, **86**, 1 (1982).
- R. B. Decker, A. I. Y. Liu, and S. M. Krimigis, "Modeling of the Interaction of Artificially Released Lithium with the Earth's Bow Shock," *Geophys. Res. Lett.*, **10**, 525-528 (1983).
- O. J. Deters and E. F. Mark (API), G. M. Hutchins (JHMI), and C. B. Barger and M. H. Friedman (API), "Secondary

- Flows in Arteric Bifurcations," in *Proc. 36th Conf. on Engineering in Medicine and Biology*, p. 191 (1983).
- G. T. Dincer, D. Richards, E. J. Francis, and W. H. Avery, "Solar Thermal Energy Conversion: Historical Highlights, Status, and Forecast," *J. Energy* **7**, 293-303 (1983).
- G. T. Dincer, D. Richards, E. J. Francis, L. I. Perini, and W. H. Avery (API) and P. J. Ritzcohen (DOE), "OTEC Energy Products and OTEC Plants," in *Solar Engineering*, W. D. Lund, ed., American Society of Mechanical Engineers, New York, pp. 409-419 (1982).
- L. W. Hirsh and M. H. Friedman, "Computer Simulation of Arterial Branch Flow," in *Proc. 4th International Conf. on Mathematical Modelling* (1983).
- C. Feldman, "Fourth European Communities Photovoltaic Solar Energy Conference - A Trip Report," *Johns Hopkins API Tech. Dig.* **3**, 298-300 (1982).
- R. F. Fischell and W. E. Radford (API) and C. D. Saudek (Johns Hopkins Hospital), "A Programmable Implantable Medication System: Applications to Diabetes," in *Proc. 16th Annual Hawaii International Conf. on System Sciences II*, pp. 229-234 (1983).
- R. W. Flower, "A Technique for Fixation of Chronically Implanted Catheters in Cats and Dogs," *J. Appl. Physiol.* **30**, 912-913 (1982).
- S. N. Foner and R. L. Hudson, "Disparate Effects of Rotational Energy Excitation on the Electro-Impact Ionization of Diatomic Molecules: H₂ versus N₂," *Chem. Phys. Lett.* **100**, 559-561 (1983).
- S. N. Foner and R. L. Hudson, "Molecular Beam Mass Spectrometric Studies of Energy Transfer and Chemical Reactions on Heated Surfaces," *J. Vac. Sci. Technol.* **A1**, 1261-1264 (1983).
- J. A. Frantz, D. M. Sunday, and C. R. Thompson, "An Interface to Distribute Hospital Registration Data," in *Proc. 6th Symp. on Computer Applications in Medical Care*, pp. 920-922 (1982).
- A. B. Fraser and R. P. H. Lee, "Miniature Sensitive Fluorometer for Oceanographic Tracer Studies," in *Proc. Oceans 82*, pp. 243-246 (1982).
- E. J. Fremouw (Physical Dynamics, Inc.), C. L. Rino and J. F. Vickrey (SRI International), D. A. Hardy, R. E. Huffman, and F. J. Rich (Air Force Geophysics Lab.), C.-I. Meng, K. A. Potocki, and T. A. Potemra (API), W. B. Hanson and R. A. Heelis (Univ. Texas), and L. A. Wittwer (Defense Nuclear Agency), "The HILLAT Program," *EOS* **64**, 163-170 (1983).
- M. H. Friedman, O. J. Deters, E. F. Mark, and C. B. Bergeron (API) and G. M. Hutchins (JHMI), "Arterial Geometry Affects Hemodynamics. A Potential Risk Factor for Atherosclerosis," *Atherosclerosis* **46**, 226-231 (1983).
- M. H. Friedman, O. J. Deters, E. F. Mark, and C. B. Bergeron (API) and G. M. Hutchins (JHMI), "Geometric Effects on the Hemodynamic Environment of the Arterial Wall: A Basis for Geometric Risk Factors?" in *Fluid Dynamics as a Localizing Factor for Atherosclerosis*, G. Schettler et al., eds., Springer-Verlag, Berlin, pp. 71-78 (1983).
- M. Fristrom, "Comments on Quenching Mechanisms in the Microprobe Sampling of Flames," *Combust. Flame* **50**, 239-242 (1983).
- W. J. Geckle and M. M. Feen, "Evaluation of the Ionospheric Refraction Correction Algorithm for Single-Frequency Doppler Navigation Using TRANE I-II Data," in *IEEE Position Location and Navigation Symp. Record*, pp. 13-21 (1982).
- W. J. Geckle and R. E. Jenkins, "Computer-Aided Measurement of Transverse Axon Sections for Morphology Studies," *Comput. Biomed. Res.* **16**, 287-299 (1983).
- A. P. Georgopoulos, R. Caminiti, and J. F. Kalaska (JHMI) and J. T. Massey (API), "Spatial Coding of Movement: A Hypothesis Concerning the Coding of Movement Direction by Motor Cortical Populations," *Exp. Brain Res.* **7**, 327-336 (1983).
- A. P. Georgopoulos, J. F. Kalaska, and R. Caminiti (JHMI) and J. T. Massey (API), "Interruption of Motor Cortical Discharge Subserving Aimed Arm Movements," *Exp. Brain Res.* **49**, 327-340 (1983).
- A. P. Georgopoulos, J. F. Kalaska, and R. Caminiti (JHMI) and J. T. Massey (API), "On the Relations between the Director of Two-Dimensional Arm Movements and Cell Discharge in Primate Motor Cortex," *J. Neurosci.* **2**, 1527-1537 (1982).
- J. A. Giannini and D. L. Thayer, "Extremely Low Frequency Quasi-Static Propagation Measurements from a Calibrated Electric Field Source in the Ocean," *IEEE Trans. Antennas Propag.* **AP-30**, 825-831 (1982).
- H. E. Gilreath and A. Brandt, "Experiments on the Generation of Internal Waves in a Stratified Fluid," *Proc. 16th Fluid and Plasma Dynamics Conf.* (1983).
- A. D. Goldfinger, "Estimation of Spectra from Speckled Images," *IEEE Trans. Aerosp. Electron. Syst.* **AES-18**, 675-681 (1983).
- J. Goldhirsh, "A Parameter Review and Assessment of Attenuation and Backscatter Properties Associated with Dust Storms over Desert Regions in the Frequency Range of 1 to 10 GHz," *IEEE Trans. Antennas Propag.* **AP-30**, 1121-1127 (1982).
- J. Goldhirsh, "Radar Prediction of Absolute Rain Fade Distributions for Earth-Satellite Paths and General Methods for Extrapolation of Fade Statistics to Other Locations," *IEEE Trans. Antennas Propag.* **AP-30**, 1128-1134 (1982).
- J. Goldhirsh, "Space Diversity Performance Prediction for Earth-Satellite Paths Using Radar Modeling Techniques," *Radio Sci.* **17**, 1400-1410 (1982).
- J. Goldhirsh and J. R. Rowland, "A Tutorial Assessment of Atmospheric Height Uncertainties for High-Precision Satellite Altimeter Missions to Monitor Ocean Currents," *IEEE Trans. Geosci. Remote Sensing* **GE-20**, 418-434 (1982).
- W. L. Goodfellow, Jr., D. T. Burton, W. C. Graves, and L. W. Hall, Jr. (API) and K. R. Cooper (Rutgers Univ.), "Acute Toxicity of Picric Acid and Picramic Acid to Rainbow Trout, *Salmo gairdneri*, and American Oyster, *Crassostrea virginica*," *Water Resour. Bull.* **19**, 641-648 (1983).
- J. L. Green (NASA), N. A. Saffleos (Boston College), D. A. Gurnett (Univ. Iowa), and T. A. Potemra (API), "A Correlation between Auroral Kilometric Radiation and Field-Aligned Currents," *J. Geophys. Res.* **87**, 10,463-10,467 (1982).
- R. A. Greenwald, "Electric Fields in the Ionosphere and Magnetosphere," *Space Sci. Rev.* **34**, 305-315 (1983).
- R. A. Greenwald, "New Tools for Magnetospheric Research," *Rev. Geophys. Space Phys.* **21**, 434-449 (1983).
- M. Gussow, *Basic Electricity*, McGraw-Hill Book Co., New York (1983).
- D. U. Gubser and W. W. Fuller (NRL), T. O. Poehler (API), J. Stokes, D. O. Cowan, and M. Lee (JHU), and A. N. Bloch (Exxon), "Resistive and Magnetic Susceptibility Transitions in Superconducting (TMTSF)₂ClO₄," *Mol. Cryst. Liq. Cryst.* **79**, 225 (1982).
- T. C. Guo and W. W. Guo (API) and L. E. Larsen and J. H. Jacobi (Walter Reed Inst. Res.), "Comments on 'Heat Transfer in Surface-Cooled Objects Subject to Microwave Heating,'" *IEEE Trans. Microwave Theory Tech.* **MIT-31**, 783-785 (1983).
- L. W. Hall, Jr., and D. T. Burton, "Effects of Power Plant Coal Pile and Coal Waste Runoff and Leachate on Aquatic Biota: An Overview with Research Recommendations," *CRC Crit. Rev. Toxicol.* **10**, 287-301 (1982).
- L. W. Hall, Jr., D. T. Burton, and P. R. Abell, "Thermal Responses of Atlantic Silversides (*Menidia menidia*) Acclimated to Constant and Asymmetric Fluctuating Temperatures," *Arch. Hydrobiol.* **94**, 318-325 (1982).

- L. W. Hall, Jr., D. T. Burton, S. L. Margrey, and W. C. Graves, "A Comparison of the Avoidance Responses of Individual and Schooling Juvenile Atlantic Menhaden, *Brevoortia tyrannus*, Subjected to Simultaneous Chlorine and ΔT Conditions," *J. Toxicol. Environ. Health* **10**, 1017-1026 (1982).
- L. W. Hall, Jr., D. T. Burton, S. L. Margrey, and W. C. Graves, "Predicted Mortality of Chesapeake Bay Organisms Exposed to Simulated Power Plant Chlorination Conditions at Various Acclimation Temperatures," in *Proc. 4th Conf. on Water Chlorination: Environmental Impact and Health Effects*, pp. 1005-1017 (1983).
- L. W. Hall, Jr., D. T. Burton, S. L. Margrey, and W. C. Graves, "The Effect of Acclimation: Temperature on the Interactions of Chlorine, ΔT , and Exposure Duration to Eggs, Prolarvae, and Larvae of Striped Bass, *Morone saxatilis*," *Water Res.* **17**, 309-317 (1983).
- L. W. Hall, Jr., D. T. Burton, S. L. Margrey, and W. C. Graves, "The Influence of Spring and Fall Temperatures on the Avoidance Response of Juvenile Atlantic Menhaden, *Brevoortia tyrannus*, Exposed to Simultaneous Chlorine ΔT Conditions," *Water Resour. Bull.* **19**, 283-287 (1983).
- L. W. Hall, Jr., W. C. Graves, D. T. Burton, and S. L. Margrey (APL) and F. M. Hetrick and B. S. Roberson (Univ. Maryland), "A Comparison of Chlorine Toxicity to Three Life Stages of Striped Bass (*Morone saxatilis*)," *Bull. Environ. Contam. Toxicol.* **29**, 631-636 (1982).
- L. W. Hall, Jr., S. L. Margrey, W. C. Graves, and D. T. Burton, "Avoidance Responses of Juvenile Atlantic Menhaden, *Brevoortia tyrannus*, Subjected to Simultaneous Chlorine and ΔT Conditions," in *Proc. 4th Conf. on Water Chlorination: Environmental Impact and Health Effects*, pp. 983-991 (1983).
- J. S. Hansen, D. Bowser, and H. Ko (APL), D. Brenner (Rockwell International) and F. Richer and J. Beatty (Univ. California), "Adaptive Noise Cancellation in Neuromagnetic Measurement Systems," *Il Nuovo Cimento* **2**, 203-213 (1983).
- P. L. Hazan, "Computing and the Handicapped—The Johns Hopkins University First National Search: An Introduction," *Johns Hopkins APL Tech. Dig.* **3**, 226-230 (1982).
- R. F. Henrick, "A Cautionary Note on the Use of Range-Dependent Propagation Models in Underwater Acoustics," *J. Acoust. Soc. Am.* **73**, 810-812 (1983).
- R. F. Henrick and H. S. Burkum, "The Effect of Range Dependence on Acoustic Propagation in a Convergence Zone Environment," *J. Acoust. Soc. Am.* **73**, 173-182 (1983).
- M. I. Hill, "Designing a Mini-RPV for a World Endurance Record," *Astronaut. Aeronaut.* **20**, 47-54 (1982).
- R. S. Hirsh, T. D. Taylor, and M. M. Nadworny, "An Implicit Predictor-Corrector Method for Real Space Chebyshev Pseudospectral Integration of Parabolic Equations," *Comput. Fluids* **11**, 251-254 (1983).
- B. F. Hochheimer, "Second Harmonic Light Generation in the Rabbit Cornea," *Appl. Opt.* **21**, 1516-1518 (1982).
- B. F. Hochheimer and H. A. Kues, "Retinal Polarization Effects," *Appl. Opt.* **21**, 3811-3818 (1982).
- V. L. Hogrefe and W. E. Radford, "Programmable Implantable Medication System (PIMS) Transceiver," in *Proc. 7th International Symp. on Biotelemetry* (Aug 1982).
- I. W. Hunter and S. Favin, "The Thermal Resistance of an Insulating Slab Penetrated by Metal Rods," *J. Heat Transfer* **105**, 208-210 (1983).
- I. W. Hunter, J. R. Kuttler, and S. Favin, "Steady Temperatures in a Wall Penetrated by a Hole and Exposed to Fire on One Side," *Fire Safety J.* **6**, 97-103 (1983).
- R. H. Jackson (Rockwell International) and H. M. South (API), "A Reconfigurable Signal Processor for High Throughput Applications," in *Proc. IEEE International Conf. on Acoustics, Speech, and Signal Processing*, pp. 459-461 (1983).
- A. N. Jette, B. H. Nall, and C. B. Bergeron, "Current Image Diffraction Patterns of Metal Single-Crystal Surfaces," *Phys. Rev. B* **27**, 708-714 (1983).
- E. H. Kidera and S. A. Mack, "Motion Compensation System for Ocean Profiling," *Ocean Eng.* **10**, 201-208 (1983).
- T. J. Kistenmacher and R. Destro, "Polymorphism in Low-Dimensional Materials: X-ray Diffraction Studies on the Temperature Dependence of the Structure of α -Bis(1,2-benzoquinone dioximato)palladium(II)," *Inorg. Chem.* **22**, 2104-2110 (1983).
- S. Koslov, "From Concept to Client: Getting the Product to the User," *Johns Hopkins APL Tech. Dig.* **3**, 263-272 (1982).
- J. A. Krill, R. H. Andreo, and R. A. Farrell, "Variational Calculations of Electromagnetic Scattering from Two Randomly Separated Rayleigh Dielectric Cylinders," *J. Opt. Soc. Am.* **73**, 408-410 (1983).
- J. A. Krill and R. A. Farrell, "The Development and Testing of a Stochastic Variational Principle for Electromagnetic Scattering," in *Proc. URSI Commission F/ESA 1983 Symp.*, pp. 299-307 (1983).
- S. M. Krimigis (APL), G. Haerendel (Max-Planck Inst.-PE), R. W. McEntire (APL), G. Paschmann (Max-Planck Inst.-PE), and D. A. Bryant (Rutherford Appleton Lab.), "The Active Magnetospheric Particle Tracer Explorers (AMPTE) Program," *EOS* **63**, 843-850 (1982).
- S. M. Krimigis and E. C. Roelof, "Low Energy Particle Population," in *Physics of the Jovian Magnetosphere*, A. J. Dessler, ed., Cambridge University Press, New York, pp. 106-156 (1983).
- J. R. Kuttler and V. G. Sigillito, "Frequencies of Limacons and Cardioids that Have Applications to Waveguides and Mitral Valves," *J. Sound Vib.* **84**, 603-605 (1982).
- J. R. Kuttler and V. G. Sigillito, "Vibrational Frequencies of Clamped Plates of Variable Thickness," *J. Sound Vib.* **86**, 181-189 (1983).
- M. M. Lee, J. P. Stokes, and F. M. Wiugul (JHU), T. J. Kistenmacher (APL), D. O. Cowan (JHU), T. O. Poehler (APL), A. N. Bloch (Exxon), and W. W. Fuller and D. U. Gubser (NRL), "Synthesis and Study of Electrochemically Grown Salts of Organic π -Donors," *Mol. Cryst. Liq. Cryst.* **79**, 145 (1982).
- R. E. Lenhard, Jr. (JHMI), B. I. Blum (APL), and J. M. Sunderland, H. G. Braine, and B. Saral (JHMI), "The Johns Hopkins Oncology Clinical Information System," in *Proc. 6th Annual Symp. on Computer Applications in Medical Care*, Washington, pp. 28-43 (1982); also published in *J. Med. Syst.* **7**, 147-174 (1983).
- A. T. Y. Lui (APL), T. E. Eastman (Univ. Iowa), D. J. Williams (APL), and L. A. Frank (Univ. Iowa), "Observations of Ion Streaming during Substorms," *J. Geophys. Res.* **88**, 7753-7764 (1983).
- A. T. Y. Lui and S. M. Krimigis, "Energetic Ion Beam in the Earth's Magnetotail Lobe," *Geophys. Res. Lett.* **10**, 13-16 (1983).
- M. J. Linevsky and N. deHaas, "Optical Thickness Effects in Kinetic Measurements Using Chlorine Atom Resonance Fluorescence," *J. Chem. Phys.* **77**, 6060-6064 (1982).
- K. Makita and C.-I. Meng (APL), and S.-I. Akasofu (Univ. Alaska), "Comparison of the Auroral Electron Precipitations in the Northern and Southern Conjugate Regions by Two DMSP Satellites," in *Proc. 5th Symp. on Coordinated Observations of the Ionosphere and the Magnetosphere in the Polar Regions*, Memoirs of National Inst. of Polar Res., Special Issue No. 26, pp. 149-159 (1983).
- K. Makita and C.-I. Meng (APL) and S.-I. Akasofu (Univ. Alaska), "The Shift of the Auroral Electron Precipitation Boundaries in the Dawn-Dusk Sector in Association with Geomagnetic Activity and Interplanetary Magnetic Field," *J. Geophys. Res.* **88**, 7967-7981 (1983).

- R. A. Makofski, "The Future of Urban Transportation," *Johns Hopkins API Tech. Dig.* **3**, 278-294 (1982).
- L. S. Margulies, "Risk Analysis of Liquefied Natural Gas Transport," *Johns Hopkins API Tech. Dig.* **3**, 325-341 (1982).
- F. E. Mark, O. J. Deters, and M. H. Friedman, "Quasisteadiness of Flow in a Human Coronary Artery Model," in *Mechanics of the Coronary Circulation*, R. E. Mates et al., eds., American Society of Mechanical Engineers, New York, pp. 71-74 (1983).
- B. H. Mauk, "Electromagnetic Wave Energization of Heavy Ions by the Electric 'Phase Bunching' Process," *Geophys. Res. Lett.* **9**, 1163-1166 (1982).
- B. H. Mauk, "Frequency Gap Formation in Electromagnetic Cyclotron Wave Distributions," *Geophys. Res. Lett.* **10**, 635-638 (1983).
- B. H. Mauk, "Helium Resonance and Dispersion Effects on Geostationary Alfvén Ion Cyclotron Waves," *J. Geophys. Res.* **87**, 9107-9119 (1982).
- B. H. Mauk and C.-I. Meng, "Characterization of Geostationary Particle Signatures Based on the 'Injection Boundary' Model," *J. Geophys. Res.* **86**, 3055-3071 (1983).
- C.-I. Meng, "Case Studies of the Storm Time Variation of the Polar Cusp," *J. Geophys. Res.* **88**, 137-149 (1983).
- C.-I. Meng (API) and R. R. Babcock and R. E. Huffman (Air Force Geophysics Lab.), "Ultraviolet Imaging for Auroral Zone Remote Sensing," in *Proc. 21st Aerospace Sciences Meeting*, (1983).
- A. Metropoulos (National Hellenic Res. Foundation) and D. M. Silver (API), "A Qualitative Analysis of Individual Trajectories in the Rotationally Inelastic LiH-He Collision System," *Chem. Phys. Lett.* **93**, 247-252 (1982).
- R. A. Meyer, review of *Pain: A Spike-Interval Coded Message in the Brain* by R. Emmers, *Surg. Neurol.* **18**, 393 (1982).
- R. A. Meyer (API) and J. N. Campbell, S. N. Raja, S. E. MacKinnon, R. Burke, and A. J. Dallon (JHMI), "Neural Activity Originating from a Neuroma in the Baboon," *Soc. Neurosci. Abstr.* **8**, 855 (1982).
- D. G. Mitchell and E. C. Roelof, "Dependence of 50-keV Upstream Ion Events at IMP 7/8 upon Magnetic Field Bow Shock Geometry," *J. Geophys. Res.* **88**, 5623-5634 (1983).
- D. G. Mitchell and E. C. Roelof (API) and T. R. Sanderson, R. Reinhard, and K.-P. Wenzel (European Space Agency), "ISEE IMP Observations of Simultaneous Upstream Ion Events," *J. Geophys. Res.* **88**, 5635-5644 (1983).
- L. Monchick, "Boundary Conditions and Reversibility in Diffusion Controlled Reactions," *J. Chem. Phys.* **78**, 1808-1814 (1983).
- L. Monchick (API) and S. Hess (Univ. Erlangen-Nürnberg), "Diffusion Controlled Reactions of Gases with Surfaces and State Dependent Reactivity. II. Diffusion Slip and Knudsen Corrections," *J. Chem. Phys.* **79**, 2098-2099 (1983).
- K. Moorjani, F. G. Satkiewicz, and T. O. Poehler (API) and D. J. Webb and S. M. Bhagat (Univ. Maryland), "Magnetic Regimes in Amorphous Fe_xB_{100-x}," *Bull. Am. Phys. Soc.* **28**, 414 (1983).
- W. B. Newman, "Acquiring Technical Reports in the Special Library: Another Package for Information Transfer," *Sci. Tech. Libr.* **2**, 45-67 (1982).
- W. B. Newman, "Government Information: Will an Informed Public Be Sacrificed in the Name of Private Enterprise?" *Sci. Tech. Libr.* **3**, 65-67 (1983).
- R. R. Newton, "The Authenticity of Ptolemy's Star Data - II," *Q. J. R. Astron. Soc.* **24**, 27-35 (1983).
- R. R. Newton, "The 400th Anniversary of the Gregorian Calendar," *Johns Hopkins API Tech. Dig.* **3**, 355-357 (1982).
- V. O'Brien, "Bounds and Estimates of Second Normal Stress Difference in Rectilinear Flow," *J. Rheol.* **26**, 499-511 (1982).
- V. O'Brien, "Viscous Flow in an Annulus with Sector Cavity," *J. Fluids Eng.* **104**, 500-504 (1982).
- V. O'Brien and L. W. Ehrlich, "Rectilinear Oscillatory Viscoelastic Flow in Rectangular Ducts," *J. Non-Newtonian Fluid Mech.* **13**, 33-45 (1983).
- V. L. Pisacane, "New Techniques," *Rev. Geophys. Space Phys.* **21** (U.S. National Report to IUGG, 1979-1982), 585-592 (1983).
- V. L. Pisacane and S. M. Yionoulis, "Recovery of Long-Wavelength Mean Gravity Anomalies for the Dedicated Gravitational Satellite (GRAVSAT) Mission," *Acta Astron.* **10**, 9-17 (1983).
- R. S. Potember and T. O. Poehler (API), D. O. Cowan (JHU), A. N. Bloch (Exxon), and P. Brant and F. L. Carter (NRL), "Spectroscopic Properties of Semiconducting Cu-TCNQ Films," *Mol. Cryst. Liq. Cryst.* **86**, 297 (1982).
- R. S. Potember and T. O. Poehler (API), D. O. Cowan (JHU), and F. L. Carter and P. Brant (NRL), "Reversible Field Induced Switching in Copper and Silver Radical-Ion Salts," Chap. VI in *Molecular Electronic Devices*, Marcel Dekker, Inc., New York (1982).
- L. A. Potemra, "Birkeland Currents: Present Understanding and Some Remaining Questions," in *High-Latitude Space Plasma Physics*, D. Hultqvist and T. Hagfors, eds., Plenum Pub. Corp., pp. 335-353 (1983).
- L. A. Potemra (API) and J. N. Barfield (Southwest Research Inst.), "Chapman Conference on Magnetospheric Currents," *EOS* **64**, 518-519 (1983).
- L. E. Proctor (JHMI), R. K. Frazer (API), and R. N. Glackin and C. R. Smith (JHMI), "Recruitment/Decruitment of Caloric Responses: Effect of Anatomical Variables," in *Proc. 8th Extraordinary Meeting of the Barany Society* (1982).
- A. J. Pue, "Operational Concepts for Automated Transportation Systems," *J. Wash. Acad. Sci.* **72**, 66-78 (1982).
- S. N. Raja (JHMI), R. A. Meyer (API), and J. N. Campbell and R. Burke (JHMI), "General Anesthetics Affect the Response of Primary Nociceptive Afferents in Primates," *Soc. Neurosci. Abstr.* **8**, 955 (1982).
- S. E. Ribblett and D. O. Cowan (JHU), A. N. Bloch (Exxon), and T. O. Poehler (API), "New Photoactive Organic Semiconductors: Photoconductivity and Schottky Barrier Studies," *Mol. Cryst. Liq. Cryst.* **85**, 69 (1982).
- E. C. Roelof, H. W. Dodson, and E. R. Hedeman, "Dependence of Radio Emission in Large H_α Flares 1967-1970 upon the Orientation of the Local Solar Magnetic Field," *Solar Phys.* **85**, 339-349 (1983).
- K. H. Sanders, Jr., and W. E. Radford, "The Computer in a Programmable Implantable Medication System (PIMS)," in *Proc. 6th Symp. on Computer Applications in Medical Care*, pp. 682-685 (Oct-Nov 1982).
- F. W. Schenkel and B. S. Ogorzalek (API) and D. L. Paulsen and J. C. Larabee (Air Force Geophysics Lab.), "Satellite Auroral-Ionospheric UV Imager," in *Proc. 21st Aerospace Sciences Meeting* (1983).
- G. Schiffman and D. Tobin (JHU) and W. E. Buchanan (API), "Microcomputer Instruction for the Learning Disabled," *J. Learn. Disabil.* **15**, 557-559 (1982).
- W. Seamone, "The Application of Robotics to the Patient with High Spinal Cord Injury (Quadriplegia): The Robotic Arm Worktable," in *Proc. NATO Advanced Study Institutes on Robotics and Artificial Intelligence* (1983).
- C. Senior and R. M. Robinson (SRI International) and L. A. Potemra (API), "Relationship between Field-Aligned Currents, Diffuse Auroral Precipitation and the Westward Electrojet in the Early Morning Sector," *J. Geophys. Res.* **87**, 10,469-10,477 (1982).
- D. M. Silver (API) and S. Wilson (Univ. Oxford), "Special In-

- variance Properties of $|N + 1/N|$ Padé Approximants in Rayleigh-Schrodinger Perturbation Theory. II. Molecular Interaction Energies," in *Proc. R. Soc. Lond.* **A383**, pp. 477-483 (1982).
- D. W. Simborg, M. G. Chadwick, and Q. E. Whiting-O'Keefe (UCSF) and S. G. Tolchin, S. A. Kahn, and E. S. Bergan (API), "Local Area Networks and the Hospital," *Comput. Biomed. Res.* **16**, 247-259 (1983).
- D. W. Simborg, M. G. Chadwick, and Q. E. Whiting-O'Keefe (UCSF) and S. G. Tolchin, R. L. Stewart, S. A. Kahn, E. S. Bergan, and G. P. Gafke (API), "A Hospital Local Area Communications Network—The First Year's Experience," in *Proc. 6th Annual Symp. on Computer Applications in Medical Care* (1982).
- H. M. South (API) and C. H. Palmer (JHU), "Analysis of Two-Beam Interferometry for Bulk Wave Measurements," *Appl. Opt.* **22**, 2854-2859 (1983).
- L. W. Speiser (Univ. Colorado) and D. J. Williams (API), "Magnetopause Modeling: Flux Transfer Events and Magnetosheath Quasi-Trapped Distributions," *J. Geophys. Res.* **87**, 2177-2186 (1982).
- J. P. Stokes and T. J. Emge (JHU), W. A. Bryden (API), J. S. Chappell and D. O. Cowan (JHU), T. O. Poehler (API), A. N. Bloch (Exxon), and T. J. Kistennacher (API), "(TMTSF)₂(2,5-TCNQBr₂): Structure and Physical Properties," *Mol. Cryst. Liq. Cryst.* **79**, 327 (1982).
- R. J. Taylor and L. B. Richardson, "Ultrasonics as an Alternative to Chlorine for Inhibiting Biofouling," *Johns Hopkins API Tech. Dig.* **3**, 295-297 (1982).
- S. G. Tolchin, E. S. Bergan, and R. L. Stewart (API) and D. W. Simborg, M. G. Chadwick, and Q. E. Whiting-O'Keefe (UCSF), "Progress and Experience in the Implementation of a Hospital Local Area Network at UCSF," in *Proc. 16th Hawaii International Conf. on Systems Sciences II*, pp. 3-13 (1983).
- S. G. Tolchin, S. A. Kahn, R. L. Stewart, E. S. Bergan, and G. P. Gafke, "A Distributed Hospital Information System," *Johns Hopkins API Tech. Dig.* **3**, 342-354 (1982).
- H. Walden (NASA/Goddard) and E. C. Roelof (API), *Numerical Computation of Exponential Matrices Using the Cayley-Hamilton Theorem*, NASA/Goddard TM 83982 (1982).
- D. M. Weintraub (API) and L. A. Russell (STSC, Inc.), eds., in *API 83: Proc. 1983 International Conf. on the Iverson Language*, ACM, New York (1983).
- D. M. Weintraub, "A Flexible Full-Screen Applications Development Workspace Utilizing API Syntax," in *API 83: Proc. 1983 International Conf. on the Iverson Language*, ACM, New York, pp. 187-193 (1983).
- D. J. Williams, "The Earth's Ring Current: Causes, Generation, and Decay," *Space Sci. Rev.* **34**, 223-234 (1983).
- F. Wudl, E. Aharon-Sharon, D. Nalewajek, J. V. Waszczak, W. M. Walsh, Jr., and L. V. Rupp, Jr. (Bell Labs.), P. Chaitin, R. Iacoe, and M. Burns (UCLA), T. O. Poehler (API), and M. A. Beno and J. M. Williams (Argonne National Lab.), "Ditetramethyltetraselenafulvalenium Fluorosulfonate: The Effect of a Dipolar Anion on the Solid State Physical Properties of the (TMTSF)₂X Phase," *J. Chem. Phys.* **76**, 5497-5501 (1982).
- L. J. Zanetti (API), W. Baumjohann (Max-Planck Inst.), and L. A. Potemra (API), "Ionospheric and Birkeland Current Distributions Inferred from the MAGSAT Magnetometer Data," *J. Geophys. Res.* **88**, 4875-4884 (1983).
- F. J. Adrian, "Mechanisms of Surface Enhanced Raman Scattering," Laboratory of Chemical Biodynamics, Univ. California, Berkeley (7 Sep 1982).
- F. J. Adrian, "Possible Direct Singlet-Triplet Charge Transfer Mechanism," Gordon Conf. on Electron Donor-Acceptor Interactions, Meriden, N.H. (16-20 Aug 1982).
- F. J. Adrian, "Spin-Orbit Coupling Mechanism of Electron Spin Resonance Line Broadening in Organic Conductors," JHU Colloq., Baltimore (16 Nov 1982).
- F. J. Adrian, "Surface Enhanced Raman Scattering," JHU Colloq., Baltimore (12 Oct 1982).
- W. H. Avery, "Ocean Thermal Energy Conversion (OTEC): A Major New Source of Fuels and Power," Resources for the Future Meeting, Washington (30 Mar 1983).
- W. H. Avery and D. Richards, "Design of a 160 MW OTEC Plantship for Production of Methanol," OCEANS '83, San Francisco (29 Aug — 1 Sep 1983).
- W. H. Avery, D. Richards, W. G. Niemeyer, and J. D. Shoemaker, "OTEC Energy via Methanol Production," 18th Intersociety Energy Conversion Engineering Conf., Orlando (21-26 Aug 1983).
- C. B. Bergeron, B. H. Nall, and A. N. Jette, "Current Image Diffraction (CID) of Single Crystal Metal Surfaces," 29th National Symp., American Vacuum Soc., Baltimore (17 Nov 1982).
- A. G. Bates, L. J. Rueger, and M. C. Chiu (API), P. Dachel, R. Kunski, and R. Kruger (Bendix), S. C. Wardrip (NASA/Goddard), and V. S. Reinhardt (Bendix), "The NASA/GSFC Hydrogen Maser Program—A Review of Recent Data," 14th Annual PTTI Meeting, Goddard Space Flight Center, Greenbelt, Md. (1 Dec 1982).
- R. C. Beal, "Spaceborne Synthetic Aperture Radar for Oceanography: Five Years after Seasat," JHU/API Colloq. (30 Sep 1983).
- W. G. Berl, "Human Fatalities from Unwanted Fires," Gordon Research Conf., Colby-Sawyer College, New London, N.H. (Aug 1983).
- P. M. Bischoff (JHMI), R. W. Flower (API), and S. D. Wajer (JHMI), "Histologische Studien zur normalen Entwicklung der Netzhautgefasse," Symp. Fruehgeborenen-Retinopathie, Horsaal der Universitatskinderklinik, Inselspital, Bern (3-4 Jun 1983).
- B. I. Blum, "A Microcomputer Based Environment for System Development," 1983 Conf. on Information Sciences and Systems (CISS), JHU, Baltimore (23-25 Mar 1983).
- B. I. Blum, "Changing Information Technology: Application Generators and Consultants," Independent Computer Consultants Assoc. (ICCA '82), Arlington, Va. (5-7 May 1982).
- B. I. Blum, "Computers in Local Public Health Services Delivery: An Introduction," U.S. Conf. of City Health Officers, Washington (13-14 Sep 1982).
- B. I. Blum, "Micro-TEDUM for Program Generation," 12th Annual Meeting, MUMPS Users' Group, San Francisco (31 May-4 Jun 1983).
- B. I. Blum, "Rapid Prototyping of Information Management Systems," Second Software Engineering Symp. on Rapid Prototyping, Columbia, Md. (19-21 Apr 1982).
- B. I. Blum, "System Design Methodology for the MUMPS Environment: A Tutorial," 11th Annual Meeting, MUMPS Users' Group, Denver (7-11 Jun 1982).
- B. I. Blum and J. M. Blum, "MUMPS Program Generation Productivity Measures," 11th Annual Meeting, MUMPS User's Group, Denver (7-11 Jun 1982).
- A. Brandt, "Hydrodynamic Flowfield Imaging," 3rd International Symp. on Flow Visualization, Univ. Michigan, Ann Arbor (6-9 Sep 1983).
- D. L. Burton, "Compensatory Physiological Responses of Estuarine Organisms Exposed to Moderate Temperature

PRESENTATIONS

F. J. Adrian, "Charge Transfer Effects in Surface Enhanced Raman Scattering," 3rd International Conf. on Vibrations at Surfaces, Asilomar, Calif. (1-4 Sep 1982).

- Changes," Seminar, Chesapeake Bay Institute, Shady Side, Md. (1 Sep 1983).
- D. T. Burton, "Power Plant Chlorination," 1982-83 Severn Technical Society Speakers Program, Annapolis (27 Jan 1983).
- H. K. Charles, Jr., "Modern Electronics and Medicine," Armed Forces Communications and Electronics Assoc., Aberdeen Proving Ground, Md. (28 Oct 1982).
- H. K. Charles, Jr., "Multielectrode Microprobes: An Update," 13th Neural Prostheses Workshop, National Inst. of Health, Bethesda (14 Oct 1982).
- S. A. D'Anna (JHMI) and H. A. Kues (APL), "High Resolution Endothelial Photomicrographs," Wilmer Meetings, JHMI, Baltimore (20-22 Apr 1983).
- I. W. Ehrlich, "The Ad-Hoc SOR Method," Elliptic Problem Solvers Meeting, Naval Postgraduate School, Monterey (11 Jan 1983).
- I. W. Ehrlich, "The Ad-Hoc SOR Method—A Local Relaxation Scheme," Meeting, Implicit Methods for PDE's, Los Alamos (26 Jul 1983).
- A. Fisher (APL), Y. Brill (NASA), and L. Osborn (RCA), "The Flight Application of a Pulsed Plasma Microthruster: The NOVA Satellite," 16th International Electric Propulsion Conf., New Orleans (17-19 Nov 1982).
- R. A. Farrell and R. I. McCally, "Light Scattering Analysis Based on Structure in Electron Micrographs," American Physical Society, Los Angeles (21-25 Mar 1983).
- R. A. Farrell, R. I. McCally, and C. B. Bargeron, "CO₂ Laser Damage Thresholds in Rabbit Corneal Epithelium: Deviations from a Simple Critical Temperature Model," Spring Meeting, Association for Research in Vision and Ophthalmology, Sarasota (2-6 May 1983).
- R. E. Fischell, "Animal Implant Results from Artificial Pancreas," The Lecture Group, Baltimore (26 Jan 1983).
- R. E. Fischell, "Human Tissue Stimulator," Disabled American Veterans, Washington (12 Oct 1982).
- R. E. Fischell, "Hypertension Control Systems," Lecture, Cornell Medical College, New York (28 Sep 1983).
- R. E. Fischell, "Implantable Drug Delivery," Univ. Minnesota School of Medicine, Minneapolis (26 Oct 1982).
- R. E. Fischell, "Presentation of Grand Rounds in Endocrinology," Lecture, Univ. Wisconsin School of Medicine, Madison (19 May 1983).
- R. E. Fischell, "Programmable Implantable Medication System," Meeting, Association for the Advancement of Medical Instrumentation, Dallas (23 May 1983).
- R. E. Fischell, "Space Age Technology: Applications in Drug Delivery," Distinguished Lecture, Harvard Medical School, Boston (1-5 Mar 1983).
- R. E. Fischell, "Space Technology Transfer into Medicine," Manned Space Flight Center, Houston (29 Jun 1983).
- R. E. Fischell, "SYMOH-SAMS," Maryland High Blood Pressure Commission, Johns Hopkins Hospital, Baltimore (2 Feb 1983).
- R. E. Fischell, "The Treatment of Diabetes with a Programmable Implantable Medication System," 5th Annual IEEE-EMBS Conf., Columbus (10-12 Sep 1983).
- R. W. Flower, "Oxygen and the Immature Eye: A New Perspective on an Old Problem," 5th Annual Willie Reams Biomedical Lecture, Univ. Richmond (14 Mar 1983).
- R. W. Flower, "A Mechanism of Oxygen Damage to the Immature Retinal Vasculature," ISOTT Meeting, Dortmund, FRG (15-17 Sep 1982).
- R. W. Flower, "Oxygen-Induced Retinopathy," Workshop on Oxygen: In-Depth Study of Pathophysiology, Oak Ridge (30 Jun-1 Jul 1983).
- R. W. Flower, "Perinatal Ocular Vascular Development," JHMI Dept. of Anesthesiology and Critical Care Medicine Lecture Series, Baltimore (3 Jun 1983).
- R. W. Flower (APL) and P. M. Bischoff (JHMI), "Auswirkungen von CO₂ und O₂ auf das Glaskorpergefäß-System: Scanning-EM-Studie bei der Neugeborenen Maus," Symp. Frühgeborenen-Retinopathie, Horsaal der Universitätskinderklinik, Inselspital, Bern (3-4 Jun 1983).
- R. W. Flower (APL) and P. M. Bischoff, R. P. Murphy, and D. S. McLeod (JHMI), "High Speed Choroidal Angiography with Indocyanine Green at the Wilmer Institute," Wilmer Meetings, JHMI, Baltimore (20-22 Apr 1983).
- R. W. Flower (APL) and P. G. Heltne, D. S. McLeod, and S. D. Wajer (JHMI), "Perinatal Retinal Vasculature Development," 5th International Congress of Eye Research, Eindhoven, The Netherlands (3-8 Oct 1982).
- S. N. Foner and R. L. Hudson, "Molecular Beam Mass Spectrometric Studies of Energy Transfer and Chemical Reactions on Heated Surfaces," 29th National Symp., American Vacuum Soc., Baltimore (19 Nov 1982).
- M. H. Friedman, "Geometric Risk Factors for Arteriosclerosis," Institute für Biomedizinische Technik, Zurich (12 Aug 1983).
- M. H. Friedman, "The Interaction of Arterial Geometry and Hemodynamics in Atherogenesis," Imperial College of Science and Technology, London (4 Jun 1982).
- M. H. Friedman, O. J. Deters, F. F. Mark, and C. B. Bargeron (APL) and G. M. Hutchins (JHMI), "Geometric Risk Factors for Atherosclerosis," 6th International Symp. on Atherosclerosis, Berlin (16 Jun 1982).
- M. H. Friedman, O. J. Deters, F. F. Mark, and C. B. Bargeron (APL), and G. M. Hutchins (JHMI), "The Effect of Arterial Geometry on Hemodynamic Stress at the Vascular Wall," Meeting, Federation of American Societies for Experimental Biology, Chicago (12 Apr 1983).
- M. H. Friedman and R. A. Meyer, "Membrane Transport in Concentrated Solutions: Theory and Experiment," NIADDK Mathematical Research Branch Seminar, Bethesda, Md. (5 May 1982).
- J. E. Garey, D. T. Burton, and E. P. Taft, "Marine Biofouling," EPRI Symp. on Condenser Macrofouling Control Technologies State of the Art, Hyannis, Mass. (1-3 Jun 1983).
- W. J. Geckle and M. M. Feen, "Evaluation of the Ionospheric Refraction Correction Algorithm for Single-Frequency Doppler Navigation Using TRANET-II Data," Position Location and Navigation Symp., Atlantic City (6-9 Dec 1982).
- J. A. Giannini, J. S. Hansen, and L. W. Hart, "Experimental Measurements of Temporal Phase Shifts during Solitary Wave-Wave Interactions," 35th Annual Meeting, American Physical Soc. Division of Fluid Dynamics, New Brunswick, N.J. (1982).
- H. E. Gilreath and A. Brandt, "Experiments on the Generation of Internal Waves in a Stratified Fluid," AIAA 16th Fluid and Plasma Dynamics Conf., Danvers, Mass. (12-14 Jul 1983).
- A. D. Goldfinger, R. C. Beal, D. E. Irvine, F. M. Monaldo, and D. G. Tilley, "SAR Calibration: A User's Viewpoint," Alpach Workshop, Graz, Austria (Dec 1982).
- R. A. Greenwald, "High Latitude HF Radar Studies," Air Force Geophysics Lab. Seminar, Hanscom AFB, Mass. (15 Apr 1982).
- R. A. Greenwald, "New Tools for Magnetospheric Research," URSI International Symp. on Radio Probing of the High Latitude Ionosphere and Atmosphere, Fairbanks (9-13 Aug 1982).
- R. E. Hicks, H. K. Charles, Jr., G. D. Wagner, and B. M. Domeneski, "Trends in Medical Electronics Using Surface-Mounted Components and Hybrids," Proc. International Society for Hybrid Microelectronics, Philadelphia (31 Oct-2 Nov 1983).
- D. A. Hurdis, "An Experimental Investigation of the Interaction of Internal Waves with Thermohaline Convection," En-

- gineering Foundation Conf. on Double Diffusion Convection, Santa Barbara, Calif. (Mar 1983).
- G. M. Hutchins (JHMI), M. H. Friedman (API), G. W. Moore (JHMI), and C. B. Bergeron, O. J. Deters, and F. F. Mark (API), "Correlation of Intimal and Medial Thickness with Shear Rate in Human Aortic Bifurcations," 72nd Annual Meeting, International Academy of Pathology, Atlanta (28 Feb 1983).
- G. M. Hutchins and G. W. Moore (JHMI) and M. H. Friedman (API), "Differences in Aortic Geometry in Inbred F344 and LEW Strains of Rats," 67th Meeting, Federation of American Societies for Experimental Biology, Chicago (12 Apr 1983).
- D. E. Irvine, "Uses of Spectral Variability Data," Seasat SAR Workshop on Ocean Wave Spectra, JHU/APL, Laurel, Md. (13-15 Oct 1982).
- C. L. Johnson, "Towed Observation of Free Convection during a Strong Winter Storm," 1982 Fall AGU Meeting, San Francisco (Dec 1982).
- R. J. Klauda, "Overview of Major Ichthyoplankton Programs Conducted in the Hudson River System," 7th Annual Larval Fish Conf., Colorado State Univ., Ft. Collins (17-19 Jan 1983).
- H. W. Ko, "A Modern Magic Carpet: Anomalous Radar Propagation Through Atmospheric Ducts," JHU/APL Colloq. (1 Oct 1982).
- H. W. Ko, "Microwave Propagation Modeling," 7th Joint Working Group on Tropospheric Propagation, Air Force Geophysics Lab., Hanscom AFB (23 Jun 1983).
- S. M. Krimigis, "Hot Ion Plasma and Electron Resonances in Saturn's Magnetosphere: Results from Voyager," Seminar, Applied Physics and Information Science, Univ. California, La Jolla (15 Nov 1982).
- S. M. Krimigis, "Hot, Multicomponent Plasmas in the Magnetospheres of Jupiter and Saturn," American Physical Society Plasma Physics Meeting, New Orleans (1-15 Nov 1982).
- S. M. Krimigis, "Hot, Multicomponent Plasmas in the Magnetospheres of Jupiter, Saturn, and Earth," Seminar, International School for Space Simulations, Kyoto (1 Nov 1982).
- S. M. Krimigis, "Hot, Multicomponent Plasmas in the Magnetospheres of Jupiter and Saturn: Results from Voyager," Astronomy Seminar, Univ. Hawaii (12 Nov 1982).
- H. A. Kues, "The Effects of Pulsed Microwaves on Primate Corneal Endothelium," Bioelectromagnetics Society Meeting, Univ. Colorado, Boulder (Jun 1983).
- H. A. Kues, "Microwaves and the Corneal Endothelium," Guest Lecture, Brooks Air Force Base, San Antonio (Apr 1983).
- H. A. Kues, "Photography as Applied to Research Documentation," Nikon House Educational Lecture Series, Garden City, N.Y. (15 Dec 1982).
- H. A. Kues, "Study of Microwave Induced Corneal Change," ONR AIBS Briefing and Peer Review, Boulder (Jun 1983).
- H. A. Kues, (API) and L.W. Hirst (JHMI), "The Effect of Low Level Microwave Irradiation on the Corneal Endothelium," Bureau of Radiological Health, Rockville, Md. (1 Mar 1983).
- J. S. Lombardo, "A Paravane System for Compensation of Distortions in Towed Arrays," IEEE 16th Electronics and Aerospace Systems Convention, Washington (Jun 1983).
- F. F. Mark and V. O'Brien, "Rectilinear Oscillatory Viscoelastic Flow in Rectangular Ducts," Scientific Conf. on Chemical Defense Research, Chemical Systems Laboratory, Aberdeen Proving Ground, Md. (19 Nov 1982).
- B. H. Mauk and C.-I. Meng, "The Modeling of Geostationary Particle Features Using the 'Injection Boundary' Approach," Univ. New Hampshire Seminar, Durham (7 Oct 1982).
- E. E. McColligan (JHMI) and B. I. Blum (API), "Evaluating an Automated Core Medical Record System for Ambulatory Care," American Medical Informatics Assoc. Meeting, San Francisco (2-5 May 1982).
- C.-I. Meng (API) and R. R. Babcock and R. E. Huffman (Air Force Geophysics Lab.), "Ultraviolet Imaging for Auroral Zone Remote Sensing," 21st AIAA Aerospace Sciences Meeting, Reno (10-13 Jan 1983).
- F. F. Mobley, "Passive Attitude Control," AIAA/NCS Seminar on Spacecraft Attitude Control Systems, Goddard Space Flight Center, Greenbelt, Md. (24 Oct 1983).
- G. W. Moore and G. M. Hutchins (JHMI) and M. H. Friedman (API), "Racial Differences in the Distribution of Major Coronary Artery Branches of the Human Heart," 67th Meeting, Federation of American Societies for Experimental Biology, Chicago (12 Apr 1983).
- J. C. Murphy, "Photothermal Imaging and Microstructural Characterization of Solids," Symp. on Electron and Photo-acoustic Imaging and Spectroscopy, American Vacuum Society, Princeton (16 Mar 1983).
- J. C. Murphy and L. C. Aamodt, "Photothermal Deflection Imaging and Microstructural Characterization of Solids," AAAS Symp. on Thermal Wave Imaging, Detroit (31 May 1983).
- D. E. Nelson and J. W. Sari, "Shock and Bubble Pulse Characteristics of Long Line Charges," Navy Symp. on Underwater Acoustics, Washington (1-3 Nov 1983).
- V. O'Brien, "Flows in Pressure Holes," *J. Non-Newtonian Fluid Mech.* **12**, 383-386 (1983).
- V. O'Brien, "Oblique Instream Streamline Intersections," *Phys. Fluids* **26**, 1379-1380 (1983).
- V. O'Brien, "Oscillatory Flows of Oldroyd Fluids," 3rd Workshop on Numerical Methods in Viscoelastic Fluid Mechanics, Fairlee, Vt. (8 Jun 1983).
- V. O'Brien, "Viscous Flow in an Annulus with a Sector Cavity," ASME, Winter Annual Meeting, Phoenix (18 Nov 1982).
- V. I. Pisacane (API) and D. B. DeBra (Stanford Univ.), "Satellite Technology Developments in Gravity Research," 34th Congress, International Astronautical Federation, Budapest (10-15 Oct 1983).
- T. O. Poehler, "Optical Switching and Memory of Organometallic Charge Transfer Materials," Martin-Marietta Seminar, Baltimore (7 Jan 1983).
- R. S. Potember, "Electronic Devices from Conductive Organics," 1983 Summer Institute for Polymer Science and Technology, New Paltz, N.Y. (17 Jun 1983).
- R. S. Potember, "Optical Switching in Organic Charge-Transfer Complexes," IBM Research Center Colloq., Yorktown Heights, N.Y. (19 Nov 1982); also, Seminar, Wright-Patterson AFB (8 Jul 1983).
- R. S. Potember, "Optical Switching in Organic Semi-Conductor Complexes," International Conf. on the Physics and Chemistry of Synthetic and Organic Metals, Les Arcs, France (15 Dec 1982).
- R. S. Potember and T. O. Poehler, "Erasable Optical Switching in Semiconductor Thin Films," 2nd Workshop on Molecular Electronic Devices, Naval Research Lab., Washington (13 Mar 1983).
- J. F. Smola (API) and N. E. Peterson (NASA/Goddard), "The AMPTE Program—An Overview," STAR Motor Space Symp., Univ. Delaware, Newark (14-15 Sep 1983).
- S. G. Tolchin, "Computer Networks—Architectures and Protocols for Hospital Information Systems," IEEE Tutorial, MEDCOMP 82, Philadelphia (25 Sep 1982).
- S. G. Tolchin, "Computer Networks—Architecture and Protocols for Hospital Information Systems (Tutorial)," 6th Annual Symp. on Computer Applications in Medical Care, Washington (1982).
- R. Turner, R. E. Lee, and R. A. Murphy, "Particle Sizing in a Fuel Rich Ramjet Combustor," American Association for Aerosols Research, Univ. Maryland (19 Apr 1983).
- D. J. Webb and S. M. Bhagat (Univ. Maryland) and K. Moor-

- jani, T. O. Poehler, and F. G. Satkiewicz (API), "Magnetic Resonance in Amorphous Fe_xB_{100-x} Sputtered Films," International Magnetics Conf., Philadelphia (5-8 Apr 1983).
- G. G. Whitworth, J. W. McIntyre, and R. E. Downs, "Time Maintenance of User Satellite Clocks via the Tracking and Data Relay Satellite System," 14th Annual PTTI Meeting, Goddard Space Flight Center, Greenbelt, Md. (30 Nov 1982).
- The following papers were presented at the 1982 Fall AGU Meeting, San Francisco (7-15 Dec 1982):
- K. B. Baker and R. A. Greenwald, "Preliminary Analysis of HF-Radar Signals Backscattered from Very High Latitude E-Region Irregularities;"
 - P. E. Bythrow and T. A. Potemra, "Dawn-Dusk Birkeland Currents, Their Latitudinal Location as a Function of the Interplanetary Medium;"
 - M. Candidi (National Research Council, Italy) and C.-I. Meng (API), "The Polar Cusp Electrons, Geomagnetic Activity and the IMF;"
 - J. F. Carbary and S. M. Krimigis (API) and R. P. Lepping (NASA), "Events in the Interplanetary Medium near Saturn;"
 - M. J. Engebretson (Augsburg College), L. J. Cahill, Jr. (Univ. Minnesota), T. A. Potemra and L. J. Zanetti (API), R. L. Arnoldy (Univ. New Hampshire), and S. B. Mende and T. J. Rosenberg (Univ. Maryland), "The Relationship between Irregular Magnetic Pulsations and Field-Aligned Currents;"
 - R. E. Gold and E. C. Roelof, "Fluctuations in the Coronal Emission of Solar Wind at Fixed Longitudes;"
 - R. A. Greenwald (API), J. P. Villain (Univ. Toulon, France), and K. B. Baker (API), "An AF Radar for Studying E- and F-Region Irregularities in the Auroral Zone and Polar Cap;"
 - S. M. Krimigis, J. F. Carbary, and E. P. Keath (API) and T. P. Armstrong (Univ. Kansas), "Energetic Electron Spectra in Saturn's Magnetosphere;"
 - A. I. Y. Lui and C.-I. Meng, "Magnetic Field Signatures of the Neutral Sheet in the Earth's Magnetotail;"
 - K. Makita (Takushoku Univ., Japan) and C.-I. Meng (API), "The Average Electron Precipitation Pattern during Extremely Quiet Times and Its Dependence on the Magnetospheric Substorm;"
 - B. H. Mauk and C.-I. Meng, "Dynamical Particle 'Injections' as the Source of Geostationary, Quiet Time Particle Spatial Boundaries;"
 - D. G. Mitchell and E. C. Roelof (API) and S. J. Bame (Los Alamos National Lab.), "Solar Wind Iron Abundance Variations at Solar Wind Speeds > 600 km s⁻¹, 1972-1976;"
 - E. C. Roelof and D. G. Mitchell, "Energetic Neutral Atoms (E > 50 keV) from the Ring Current: Simultaneous Measurements by IMP-7 and -8 at $\approx 35 R_E$;"
 - D. Venkatesan (Univ. Calgary) and R. B. Decker, S. M. Krimigis, and E. C. Roelof (API), "Radial Gradient of Cosmic Ray Intensity from a Comparative Study of Voyager 1 and 2 and IMP-8 Data during 1977 Day 268 to 1981 Day 129;"
 - D. J. Williams and L. A. Frank, "An Anomalous Low Altitude Heavy Ion Population;"
 - F. Yasuhara (Chiyoko Univ., Japan), R. A. Greenwald (API), and S.-I. Akasofu (Univ. Alaska), "On the Rotation of the Polar Cap Potential Pattern and Associated Polar Phenomena;"
 - L. J. Zanetti, P. E. Bythrow, T. A. Potemra, K. Makita, and C.-I. Meng, "Ground State of the Earth's Magnetosphere."
- The following papers were presented at the Vought DARPA Semiannual Review Meeting, JHU/APL (15 Mar 1983):
- T. E. Phillips and T. O. Poehler, "Titanium and Tungsten Doped VO₃—Electrical and Optical Properties;"
 - R. S. Potember, T. O. Poehler, and R. C. Benson (API) and R. C. Hoffman (JHU), "Organic Switching Materials."
- The following papers were presented at the American Physical Society Meeting, Los Angeles (22-25 Mar 1983):
- C. B. Bergeron, A. N. Jette, and B. H. Nall, "Current Image Diffraction (CID) of the Basal Plane of Titanium;"
 - W. A. Bryden, T. J. Kistenmacher, and T. O. Poehler, "DBTSF-TCNQF₄: A Mott Insulator with a Sharp High-Temperature Magnetic Transition;"
 - A. N. Jette, B. H. Nall, and C. B. Bergeron, "Bragg Scattering in Low-Energy Current Image Diffraction (CID);"
 - R. S. Potember and T. O. Poehler (API), R. C. Hoffman (JHU), and R. B. Givens and R. C. Benson (API), "Electron Beam Induced Switching in Thin Films of Organometallic Charge Transfer Complexes;"
 - R. S. Potember and T. O. Poehler (API), R. C. Hoffman (JHU), and R. C. Benson (API), "Erasable Optical Switching in Semiconductor Organic Thin Films."
- The following papers were presented at the International Union of Geodesy and Geophysics Meeting, Hamburg, West Germany (15-28 Aug 1983):
- S. A. Mach, "The Two-Dimensional Character of Ocean Microstructure;"
 - J. H. Smart, "Shear Energy Levels in the Upper Ocean;"
 - D. P. Vasholz and L. J. Crawford, "Dye Dispersion in the Oceanic Thermocline."

AUTHOR INDEX

AUTHOR INDEX

A

Aamodt, L. C., 150
Anderson, C. W., 90

B

Ballard, B. W., 77
Baran, S. D., 38
Bargeron, C. B., 107
Benson, R. C., 129
Bischoff, P. M., 104
Bowen, J. I., 93
Bowser, D. A., 109
Brenza, P. T., 63
Buchholz, D. E., 58

C

Charles, H. K., Jr., 129, 135
Chiu, H. Y., 127
Clatterbaugh, C. V., 135
Conn, D. W., 63
Cote, A. J., Jr., 58

D

Daniels, J., 47
Dettmer, E. S., 129
Doty, D. C., 74

E

Ehrlich, L. W., 153

F

Farrell, R. A., 107
Farruggia, G. J., 90
Flower, R. W., 100, 104
Frazer, R. K., 27

G

Gealy, G. S., 16
Goldberg, B., 100
Grant, D. G., 53
Green, W. R., 107
Griffin, M. D., 30, 53
Grunberger, P. J., 58

H

Hansen, J. S., 109
Henshaw, R. M., 77

J

Jenkins, R. E., 139
Johnson, R. E. L., Jr., 93

K

Kerr, J. L., 70
Kershner, D. L., 127
Ko, H. W., 109
Konigsberg, R. L., 50

L

Lundy, R. T., 14
Lutty, G. A., 100

M

McCarthy, R. L., 107
McDonough, R. N., 70
McEvaddy, P. J., 127
McLeod, D. S., 100
Meng, C.-I., 41
Monchick, L., 157
Moore, R. C., 139
Moorjani, K., 146
Murphy, J. C., 146, 150

N

Nelson, R. L., 125
Neradka, V. F., 50
Newman, A. L., 115
Newman, R. W., 122

O

O'Brien, V., 153
O'Connor, J. S., 22
Oden, S. F., 44

P

Perschy, J. A., 44
Persons, D. F., 82
Phillips, C. C., 14
Phillips, T. E., 146
Poehler, T. O., 146
Potocki, K. A., 38

Q

Quinnell, R. A., 125

R

- Ratt, B. E., 70
Rankin, T. M., 50
Riedel, F. W., 24

S

- Schaaf, S. M., 80
Schenkel, F. W., 41
Schwerdtfeger, I. H., 38
Strikwerda, T. E., 53
Stupp, G. B., 24

T

- Thurber, R. E., 19
Twigg, C. A., 74, 125

V

- Van Wie, D. M., 30

W

- Wagner, G. D., 135
Wajer, S. D., 100, 104
Weiermiller, E. G., 47
Weiner, J. A., 129, 135
White, M. E., 30
Wozniak, J. J., 112

Z

- Zaremba, T., 77

END

FILMED

8-85

DTIC